UNIVERSITÀ DEGLI STUDI DI NAPOLI FEDERICO II

PhD IN CHEMICAL SCIENCES

XXXV CYCLE

INNOVATIVE MATERIALS BASED ON ISOTACTIC POLYPROPYLENE: SOLVING THE CONFLICT BETWEEN STRENGTH AND TOUGHNESS IN HETEROPHASIC COPOLYMERS OF POLYPROPYLENE.

SUPERVISOR
PROF. CLAUDIO DE ROSA

EXAMINER
PROF. ANTONIO CARELLA

COORDINATOR
PROF. ANGELINA LOMBARDI

Ph.D. STUDENT
ANGELO GIORDANO

Abstract

The commercial development of isotactic polypropylene (iPP) stands out as a remarkable moment in the evolution of polymeric materials. This innovative material sparked a lot of attention in manufacturing during the last part of the 1950s due to its easy polymerization operating conditions and its versatility in terms of final properties, and, in turn, applications. In fact, given its attractive features, nowadays iPP is extensively used in a wide range of sectors, including electronics, automotive, fibers and filaments, and food packaging. Notwithstanding all the major aspects that make iPP one of the most widely used and synthesized polymers, the biggest drawback of this material relies on its brittleness and low toughness, especially at low temperatures. Over the years, a multitude of approaches has been used to tackle this problem with the goal of enhancing impact strength. One of the employed strategies to increase the toughness consists of incorporating a random rubbery ethylene-propylene copolymer (EPR) directly in the polymerization reactor, by sequentially synthesizing the homopolymer and the rubbery phase in a multiple reactors process, the Catalloy process. This process is, indeed, used on the industrial scale to obtain high-impact iPPs with features that depend on the chemical nature and the relative proportions of the rigid and elastomeric phases. Due to this process and the catalytic system, heterophasic copolymers (HECOs) show a structural complexity due to the presence of the elastomeric phase, which plays a fundamental role in determining the final properties of the product. In fact, since HECOs are obtained using heterogeneous multisite Ziegler-Natta catalysts, they could be characterized by a complex heterogeneous composition, especially regarding the embedded rubbery phase.

The extreme molecular complexity of HECO systems has the consequence that nowadays there are no unequivocal statements about the role played by the different phases on the final properties exhibited by these materials. Therefore, with this Ph.D. project, we set out to further extend the studies carried out so far on these complex reactor blend systems.

Firstly, the properties of HECO samples with different content of rubbery phase and different ethylene concentrations were studied in order to investigate the effect of the EPR phase on the thermoplastic matrix of iPP. Therefore, in Chapter 1, we explored how the elastomeric phase affects the structural, thermal, and mechanical properties of HECO samples. Then, the morphology and melt rheological properties of these samples were studied to evaluate how the elastomeric phase (EPR) is distributed in the thermoplastic matrix and how it affects its relaxation times. Finally, an in-depth study of the thermal behavior of these materials was conducted to explore the effect of the rubbery phase on the crystallization kinetics of iPP.

The exact composition of HECO samples has been studied in detail in Chapter 2 by fractionating the samples in all their components using the methods of boiling solvent fractionation. The isolated different fractions have been characterized in terms of molecular microstructure, ethylene concentration, and crystallization behavior, and their mechanical properties have been analyzed.

Only after this detailed analysis, methods for improving the compatibility between the different components of the HECO copolymer have been studied by using the strategy of adding compatibilizers of different molecular structures and architectures. Therefore, in Chapter 3 we describe the effect of blending HECOs with block, multi-block, and random copolymers as compatibilizers. Remarkable results have been obtained with the use of monodisperse iPP-*b*-PE block copolymers and with random C3C2 copolymers with low ethylene concentrations.

Table of contents

Introduction

Chapter 1

Chapter 2

Chapter 3

INTRODUCTION

Isotactic Polypropylene: polymorphism and its copolymers

In the history of polymeric materials, the commercial development of isotactic polypropylene (iPP) stands out as a special instance. Due to its simple operating conditions in polymerization (in terms of temperature and pressure) as well as its promise in terms of structural, physical, and mechanical properties, this novel material generated a great deal of interest in manufacturing in the second half of the 1950s. The production of polypropylene (PP) takes place by slurry, solution, or gas phase process,[1] in which the propylene monomer is subjected to heat and pressure in the presence of a catalytic system. All these characteristics have made this material successful in interesting market sectors, and currently, isotactic polypropylene is one of the most widely used plastic materials. Indeed, as shown in Figure 1, the worldwide demand for PP has been steadily increasing, reaching close to 75 million tons/year in 2019. This growth is partially due to the versatility of this material, and, hence, the wide range of application fields. Also contributing to this growth are the low cost and wide availability of the monomer, the nontoxicity of the polymer, increasingly efficient and sophisticated catalytic systems, and cost-effective production processes.

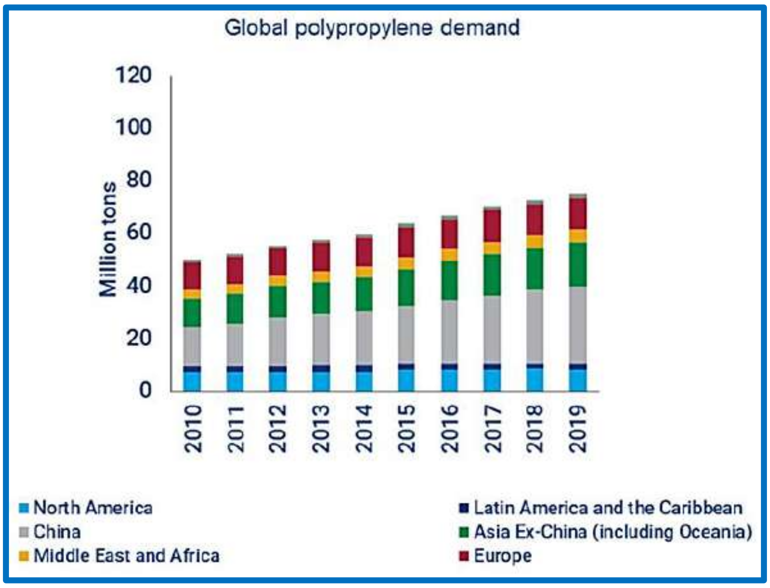

Figure 1: Worldwide polypropylene demand growth in almost 10 years. *(Source: Wood Mackenzie)*

Polypropylene is a highly crystalline thermoplastic polymer with notable differences with respect to polyethylene. These include a lower density, much higher melting point, and higher rigidity and hardness. In addition, PP does not present stress-cracking problems and offers excellent electrical and chemical resistance at higher temperatures. For these reasons, PP is widely used in various applications, including food packaging, automotive, fibers and filaments, healthcare, and electronics. An increase in demand for lightweight materials in automobiles and food packaging is anticipated to drive the PP market in the future. It is estimated, in fact, that PP production will exceed 130 tons per year by 2030.

Polypropylene can be produced with different molecular chain structures under controlled conditions (stereo-specific) but only the isotactic form is largely produced.[2-4] Despite all the important features that make PP one of the largest polymers produced and used, the main weakness related to the highly regular and isotactic structure of the homopolymer is its brittleness (especially at low temperatures) due to both the development of a morphology characterized by large spherulitic superstructures[5] and the glass transition temperature close to room temperature (T_g = -10-0°C). To overcome this drawback, several strategies have been employed over the years with the intention of improving its impact strength.

The properties of iPP in industrial practice are, in fact, routinely modified by statistical copolymerization with other α-olefins[6] (ethylene, 1-butene, 1-hexene, etc...), producing, for example, random copolymers in a wide range of compositions and with different final properties that depend on the comonomer content.[6-9] It is among these copolymers that propylene-ethylene copolymers (C3C2), with an ethylene content of about 50wt%, stand out, and represent an important class of synthetic elastomers belonging to the EPR (Ethylene Propylene Rubber) family since they are essentially amorphous. As early as the 1960s, the possibility of improving the performance of iPP just through the addition of an elastomeric phase was considered. These materials, which are known as heterophasic copolymers,[10-15] were at first produced by mechanical blending of PP and EPR; more recently, however, they can be obtained by the direct synthesis in the polymerization reactor,[16] following the homopolymer production step with a copolymerization step in the presence of ethylene.

1. Isotactic polypropylene: structure and polymorphism

Isotactic polypropylene (iPP) has a complex polymorphic behavior in the solid state, complicated by the presence of structural disorder. Three crystalline forms exist: α, β and γ forms and a mesomorphic form.[17,18] They are characterized by chains in 3_1 helical conformation, with a periodicity of 6.5Å and a sequence of torsion angles $(TG)_n$, where T and G indicate, respectively, dihedral angles in the state *trans* and *gauche*. The commercial iPP that is produced through Ziegler-Natta heterogeneous catalysts based on $MgCl_2$-supported $TiCl_4$ in combination with alkyl-aluminum co-catalysts and Lewis basis as an internal and external donor,[19] crystallizes in the α form in the normal crystallization condition from the melt, from solution and by spinning.[17-20] The γ form, instead, in the case of samples synthesized by Ziegler-Natta catalysts, is obtained by crystallization at high pressure and high temperature, for the low molecular mass fractions and/or stereo-irregular samples and copolymers.[20]

Isotactic polypropylene obtained by homogeneous metallocene catalysts has a different polymorphic behavior from that of Ziegler-Natta commercial samples. Indeed, numerous studies on this issue have shown that the γ-form is obtained more easily than the α-form by crystallization from the melt under normal conditions, even in the case of highly molecular mass and highly stereo-regular samples.[21]

2. Crystalline forms of isotactic polypropylene and their structural analogies

The α-form of iPP may be defined in terms of a monoclinic unit cell (*b* unique axis, chain axis *c* = 6.5Å) having four chains in 3/1 helical conformation, as first postulated by Natta and Corradini[17] and verified by several research.[22-25] Right (R) and left (L) handed helices are projected in a plane perpendicular to the *c*-axis in the packing model depicted in Figure 2. Chains from successive *a*-*c* rows facing one another along *b* are enantiomorphic, and isochiral chains are piled along *a* direction to produce *a*-*c* rows of parallel chains. The vertical dashed lines in Figure 2 show pairs of consecutive *a*-*c* rows facing along *b* which are called "double layers."

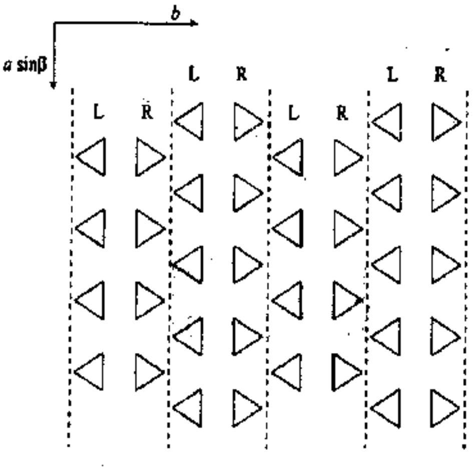

Figure 2. Packing model of right-(R) and left-(L) handed chains of iPP in 3/1 helical conformation (indicated with triangles) in a projection to the normal *c* axis, in the α-form. Vertical dashed lines delimit the double layers. The methyl groups project is located at the vertices of the triangles.

A non-parallel arrangement of the chain axis in the unit cell distinguishes the structural model for the iPP γ-form, which is a rare example of the molecular architecture of synthetic polymer crystals.[26-27] According to the model proposed by Brückner and Meille, chains in 3/1 helical conformation are aligned with axes parallel to the two diagonals of the *ab* face of the face-centered orthorhombic unit cell (a = 8.54, b = 9.93, c = 42.41).[26] In the limit-disordered model with the up/down orientational disorder of isomorphic helices, chain axes create an angle of 81.4° at the interface between successive double layers, and the suggested spatial group is *Fddd*.[26-27] The value of 81.4° is similar to the angle formed among "branched lamellae" in iPP samples crystallized in the α-form.[20] The development of "branched lamellae" in iPP samples crystallized in the α-form is a well-researched phenomenon. It involves daughter lamellae epitaxially growing on lamellae already crystallized in the α-form so that the mother lamellae's a_α- and c_α- axes are oriented parallel to the crystallographic a_α- and c_α-axes of the parent lamellae, respectively (contact plane (0k0)). This results in an angle of roughly 80° at the interface between the chain axes of the mother and daughter lamellae.

The structural model for the γ-form is illustrated in Figure 3A in a projection perpendicular to the diagonal $\mathbf{a}_\gamma+\mathbf{b}_\gamma$, allowing for easy identification of helical chains with an angle of around 80° between them. The structural model provided for the iPP α-form is projected in the plane $a_\alpha \sin\beta_\alpha$-$b_\alpha$ in Figure 3B to enable comparison.

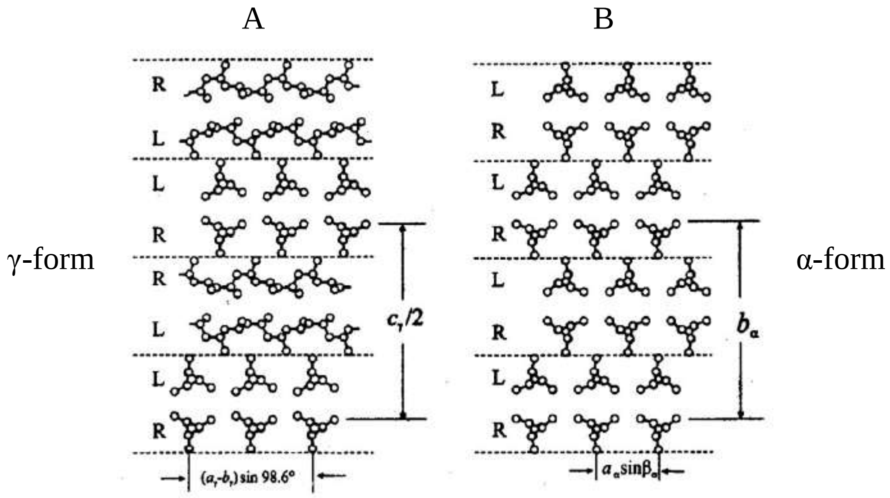

Figure 3. Packing model of iPP chains in the γ-form (A) and in the α-form (B) in projections perpendicular to chain axes for α-form (B) and half of the chain axes for the γ-form (A). "Reprinted (adapted) with permission from {The Oriented γ Form of Isotactic Polypropylene, Auriemma F., De Rosa C., Boscato T., Corradini P., Macromolecules 2001, 34, 4815-4826}. Copyright {2023} American Chemical Society."

Packing models of chains in α and γ forms show strong analogies. In both forms, chains in 3/1 helical conformations (with periodicity ≈ 6.5Å) are organized in double layers. In the α form, the bilayers are stacked along the crystallographic b_α direction with all the chain axes parallel to each other.[17] In the γ-form, the bilayers are stacked along the c_γ direction, and the chain axes in adjacent bilayers are nearly perpendicular to each other (tilted by 81°).[26,27] In the γ-form, the interface between consecutive bilayers presents isomorphic chains, while, in the α form, this interface presents enantiomorphic helices. Therefore, the sequence of helices along the c_γ-axis for the γ-form is |RL|LR|RL|LR…, while along the b_α-axis for the α-form it is |RL|RL|RL|RL…. It is worth noting that the anti-chiral interface between adjacent double layers in the γ-form is similar to that occurring at the interface between mother and daughter lamellae. However, whereas this interface is a structural feature in the γ-form, it is just a morphological feature for the mother/daughter arrangement. The key to understanding the about 80° orientation of chain axes at the interface is the fact that in the α-form the values of cell parameters a_α and c_γ are almost equal.

Both low stereo-regular iPP samples and metallocene-based copolymers crystallize in disordered modifications intermediate between α and γ forms.[28,29] The model of the α/γ disorder has been proposed in ref. 30 and is shown in Figure 4. Consecutive bilayers of chains may face each other with the chain axes either parallel (like in the α-form) or nearly perpendicular (like in the γ-form) (Figure 4). In this model of disordered structure, ordered domains in the α or γ forms are present inside the same crystal, giving rise to a mixture at the molecular level of the α and γ forms (Figure 4).[30]

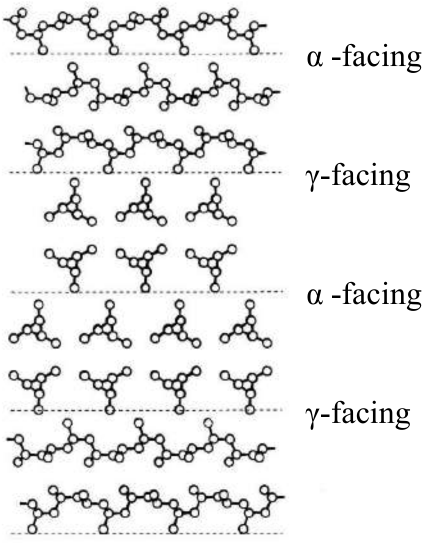

Figure 4. Model of the α/γ disorder occurring in the disordered modification of iPP intermediate between α and γ forms. Consecutive bilayers may face the chain axes either parallel or nearly perpendicular, realizing α-like or γ-like arrangements of the bilayers. The dashed horizontal lines delimit bilayers of chains. “Reprinted (adapted) with permission from {The Oriented γ Form of Isotactic Polypropylene, Auriemma F., De Rosa C., Boscato T., Corradini P., Macromolecules 2001, 34, 4815-4826}. Copyright {2023} American Chemical Society.”

These structural analogies between the α and γ forms result in similar X-ray diffraction profiles of the two polymorphs, as shown in Figure 5. The only remarkable difference is for the third intense diffraction peak that corresponds to d = 4.77Å (2θ = 18.6° Miller indices 130) in the case of α-form and d = 4.43Å (2θ = 20.1° Miller indices 117) in the case of γ-form.

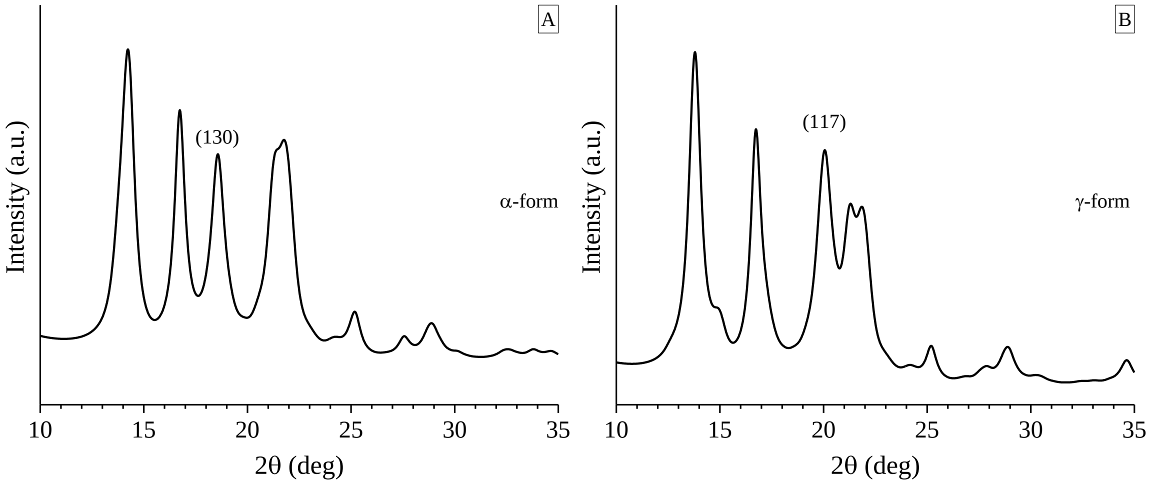

Figure 5. X-ray powder diffraction profiles of iPP samples in the α-form (A) and in γ-form (B).

Compared to the α-form, the polymorph β is characterized by higher impact strength, toughness, and ductility at low temperatures as well as the ability to form micro-voids upon deformation. For this reason, it is commonly used industrially in numerous applications such as pipeline construction, "paper-like" films, uniaxially and biaxially stretched microporous films for gas exchange membranes and porous fibers with high moisture absorption capacity. The β-form can be obtained only under special crystallization conditions, such as in the presence of nucleating agents,[31-34] or through flow crystallization procedures.[35,36] It transforms into the α-form at temperatures greater than 150°C or through stretching procedures. The X-ray diffraction profile of iPP samples crystallized in the β-form is shown in Figure 6. It is characterized by the presence of only two strong reflections, at d = 5.53Å and 4.17Å ($2\theta_{(CuK\alpha)}$ =16° and 21.3°, respectively).

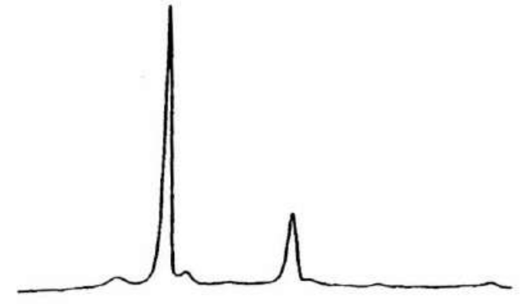

Figure 6. X-ray powder diffraction profile of iPP sample in the β-form.

The crystal structure of β-form of iPP is characterized by an elementary cell with trigonal symmetry with parameters $a = b = 11.05$Å, $c = 6.5$Å, shown in Figure 7. The cell contains three chains of the same chirality in 3/1 helical conformation (the space group is $P3_1$ if the chains are all right-handed spiralized, $P3_2$ in the case of levogyre helices). The chains are characterized by a different azimuthal orientation in the elementary cell, that is, by a different orientation of the ternary helices around the chain axis. The structural peculiarities of such a crystal form reflect a "frustrated" packing pattern,[37] in which the hexagonal surround of two chains in the elementary cell is different from the hexagonal surround of the third chain. It is interesting to note that the resolution of the structure of the β-form of iPP introduced, for the first time in polymer crystallography, the concept of frustration, which underlies many crystal structures of polymers in a helical conformation.

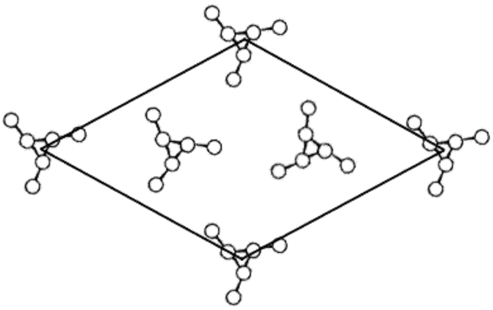

Figure 7. Crystal structure of the β-form of isotactic polypropylene.

The mesomorphic form of iPP is characterized by a degree of order in the relative arrangement of the chains intermediate between that of the crystalline phase and that of the amorphous phase. It is obtained by rapid cooling from the melt, is a metastable form, and is transformed into the crystalline α-form by high-temperature heat treatments.[17]

The X-ray diffraction profile of powders of the mesomorphic form of iPP shows two halos centered at 2θ = 15° and 2θ = 22° (Figure 8).

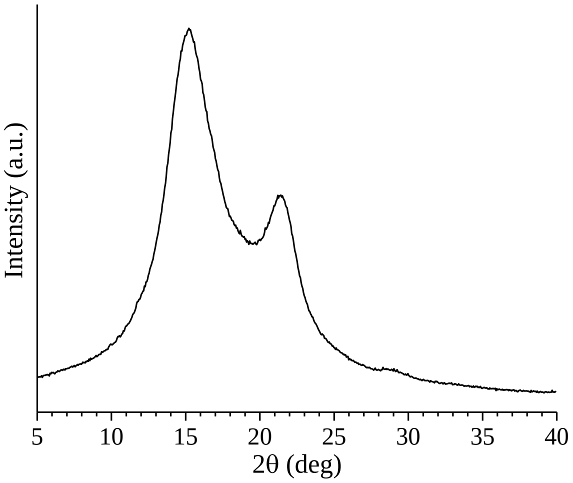

Figure 8. X-ray powder diffraction profile of iPP sample in the mesomorphic form.

Corradini et al.[38] proposed disordered the structural pattern shown in Figure 9 for the mesomorphic phase of iPP that can explain its X-ray diffraction pattern. The results of these analyses indicate that the mesomorphic form of iPP is characterized by small aggregates of parallel chains in 3/1 helical conformation, disordered in lateral packing. In such aggregates of chains, there is some correlation regarding the height and relative orientation of the chains, similar to that of the α-form, although this correlation is completely lost for chains whose axes are a few tens of Angstroms apart.

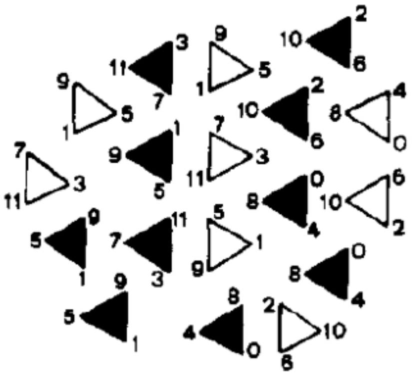

Figure 9. Model of mesomorphic phase packing. In the central part, the chains emulate the α-form packing. Any correlation in the facing of the chains results exclusively local, and is lost rapidly as the distance between the axes of chains increases within a radius of a few tens of Å. The methyl groups are located on the vertices of triangles. The white and black triangles refer to right and left helices, respectively. “Reprinted (adapted) with permission from {On the Structure of the Quenched Mesomorphic Phase of Isotactic Polypropylene, Corradini P., Petraccone V., De Rosa C., Guerra G. Macromolecules, 1986, 19, 2699-2703.}. Copyright {2023} American Chemical Society."

3. Rubbery ethylene-propylene copolymers (EPR)

The easy availability of ethylene and propylene obtained in large quantities from hydrocarbon cracking processes stimulated research for their use in elastomers, as well as being used as thermoplastic materials. Thanks to the school of Professor Natta, around 1955, the synthesis of ethylene-propylene copolymers with elastomeric nature (Ethylene-Propylene Rubber, EPR) was achieved using a Ti-based heterogeneous catalytic system.

This synthesis constituted not only an important achievement from an industrial point of view but also a remarkable discovery from a scientific point of view.

In fact, the principle of making a crystalline polymer amorphous by introducing into the polymer chain, through copolymerization, structural units that disrupt crystallization by making the polymer amorphous or poorly crystalline was used for the first time. These copolymers are characterized by a succession of randomly distributed ethylene and propylene units along the chain.

Among the most interesting physic-chemical properties of EPRs, which allow their wide industrial use, there are:

- low values of glass transition temperature (-60 < T_g > -50°C)
- low specific weight
- good solubility in a wide range of hydrocarbons solvents and good miscibility with paraffinic oils
- high resistance to aging, heat, and ozone thanks to the unsaturations absence
- low cost of starting monomers

These properties allow wide uses of these materials in different sectors of industry from agriculture to textiles and automotive.

Ethylene-Propylene Rubber (EPR) copolymers are also used in the production of so-called Impact Polypropylene Copolymers (IPCs), which has made it possible to further extend the field of application of the iPP because the incorporation of a rubbery fraction into the semi-crystalline polypropylene matrix results in a significant improvement in the material's impact properties, even at low temperatures, without excessively compromising its stiffness.

Among this class of polymeric materials, HECOs (Heterophasic Copolymers) composed of isotactic polypropylene in combination with an ethylene-propylene rubbery copolymer (EPR) take center stage.

The synthesis of Ethylene-Propylene Rubber copolymers is carried out in a fluidized bed reactor with inlet feeds consisting of a well-defined mixture of ethylene and propylene in the gas phase.[39]

The most innovative aspect, related to the solid catalytic component, was the development of a synthesis technology capable of controlling its morphology and porosity while simultaneously generating a uniform distribution of the active centers in the catalyst particle, in order to have control of the polymerization temperature even in the most internal part of the polymer particle, preventing overheating detrimental to the quality of the polymer itself.[40]

The synthesis process uses heterogeneous Ziegler-Natta catalysts, which have a multi-site nature that makes it very difficult, in the case of copolymers, to control the intra-chain and inter-chain distribution of co-monomer units. For this reason, a mixture of chains characterized by a different ethylene-propylene composition is generally obtained, and in addition, within the same chain, the distribution of monomeric units is not uniform as in the case of homogeneous catalysts for which there is greater control over the microstructure, including in terms of regio- and stereo-regularity. The use of heterogeneous catalysts involves, therefore, the presence of ethylene-propylene segments with different crystalline components formed by crystallizable sequences of a polyethylene nature and/or of a polypropylene nature[41-43] with the possibility, consequently, of obtaining a semicrystalline copolymer fraction and a completely amorphous fraction. As an example, the X-ray diffraction pattern of an EPR copolymer sample synthesized with a commercial Ziegler-Natta catalyst and with an ethylene concentration of about 50wt% is shown in Figure 10. It can be seen that, although the concentration of the two comonomers is comparable, the sample has polyethylene-based crystalline components.

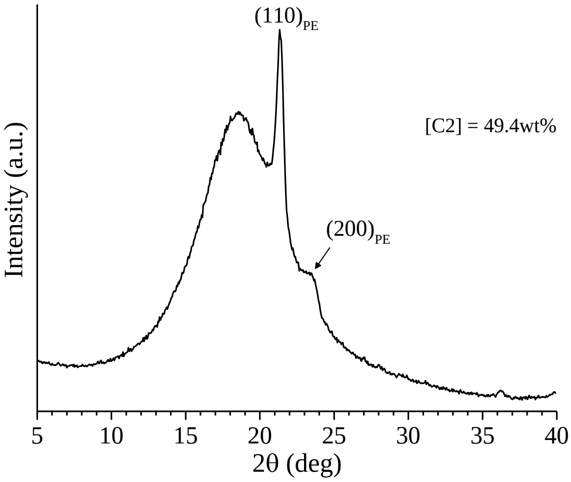

Figure 10. X-ray powder diffraction profile of an EPR copolymer sample synthesized with a Ziegler-Natta catalyst ($TiCl_4/MgCl_2$/Dicyclopentyldimethoxysilane) with an ethylene concentration of about 50wt%.

4. Impact Polypropylene Copolymers

As discussed above, polypropylene (PP) is one of the most widely used commodity plastics due to peculiar characteristics like low density, chemical resistance, and excellent mechanical properties, such as heat resistance, high strength, processability, the possibility to be oriented, and finally low cost. However, PP has low impact strength, especially at low temperatures, which is its major limitation.[44,45] Several methods have been employed to increase its toughness, including adding a nucleating agent to reduce crystal size,[46] mixing with an elastomer,[47] and copolymerizing with α-olefine species.[6] Another strategy is to sequentially synthesize the homopolymer and the rubbery phase in a process, called Catalloy, that employs multiple reactors. Specifically, the iPP is synthesized in the first reactor of this process on spherical catalyst particles, which are subsequently fed into a following reactor for the synthesis of the rubbery copolymer to be embedded in the thermoplastic phase. The rubbery phase is generally constituted by an ethylene/propylene (EP) amorphous or crystalline copolymer. The presence of multiple gas-phase reactors in the production line of the Catalloy process is an effective tool for the preparation of propene-based products with improved properties. The Catalloy process is used on an industrial scale to obtain high-impact resistant iPPs or several types of impact propene-based copolymers.[41,48,49] In general, their characteristics embrace a wide range of applications and rely on the chemical nature of the two phases as well as the relative proportions of the rigid and elastomeric phases. It is possible to create multiphasic systems with super-stiff, super-soft, or stiff and impact materials because of the development of novel polymerization techniques. An increase in the impact resistance and a reduction in the stiffness and hardness of the homopolymer are the main effects of introducing an elastomeric component with a very low Young's modulus.

Heterophasic copolymers show a structural complexity due to the presence of the elastomeric phase, which plays a fundamental role in determining the final product properties. In fact, the rubbery phase can vary in molecular mass, molecular mass distribution, volume, size, and composition and long propene sequences may present a certain percentage of stereo-regularity.[50,51]

The maximum deformation level that may be reached before fracture is controlled by cavitation processes (crazing) or shear-yielding phenomena, which, depending on the temperature and rate of loading, are promoted by the elastomeric particles embedded in the semi-crystalline matrix. While high temperature and slow rate of loading enhance shear yielding, low temperature and rapid loading favor craze formation. The competition of both mechanisms makes it possible to absorb the applied energy, without reaching a critical local stress level able to cause a fracture. These mechanisms operate above the glass transition temperature (T_g) of the dispersed phase and their efficiency is related to the nature of the elastomeric phase, its volume fraction in the system, particle size, and particle size distribution in the thermoplastic matrix. While the size and concentration of the dispersed particles (i.e., their number) define the probability to intercept a fracture line and to activate mechanisms of opposition to its propagation, the rubbery nature determines the behavior at the deformation of the dispersed particles and their capacity to absorb and spread energy. To regulate the size of the particles in the matrix, the molecular mass is essential. To effectively transfer shear stress through a continuous phase and distribute the elastomeric phase in the thermoplastic matrix during the mixing process, the viscosities of the two phases must be in the right proportions.[52,53] In general, the formation of well-dispersed small droplets would be favored by viscosity values of the rubbery phase higher than those of the matrix, whereas if the viscosity of the rubbery phase is lower than that of the matrix, a more coarse dispersion would occur. The surface energy at the interface is another element that plays a role in the stability of a fine dispersion of the two phases. A fine dispersion at the interface would be stabilized by low surface energy. With increasing interfacial energy also coarsening increases. Therefore, the molecular mass may independently govern the viscosity difference between the two phases, whilst the chemical composition of the two phases at the interface controls interfacial energy. In order to avoid affecting the matrix's processability, its molecular mass should generally not be particularly high. Regarding the composition of the elastomeric phase, a copolymer with a high propylene content raises the T_g, which prevents the impact resistance from improving. Instead, with increasing ethylene content in the rubbery phase, the T_g decreases favoring the increase in the impact resistance, even though the risk of the crystallization of long ethylene segments can come into play. In this case, a rubbery particle shows an increased shrinking compared to a completely amorphous particle during the cooling. On the other hand, when a heterophasic copolymer is cooled, iPP matrix crystallization causes a significant volume reduction, which is greater than that of the amorphous rubbery phase, creating a compression stress on the dispersed particles, together with tensions in the matrix.

Consequently, also relatively small deformations may easily determine sufficient stress to craze the matrix. If this is the case, the presence of crystallizable ethylene fraction has a positive effect.

An intrinsic characteristic of the rubbery phase obtained by heterogeneous Ziegler-Natta catalysts consists in the fact that the copolymer has a heterogeneous nature, since it consists of fractions of chains having different comonomer concentrations, different molecular masses, and rather wide molecular weight distributions. Moreover, the distribution of comonomeric units is non-uniform both for different macromolecules (inter-chain) and along the same macromolecule (intra-chain). In the case of ethylene (E)/ propylene (P) rubbery copolymers (EPR), the presence of long and crystallizable ethylene sequences, long and crystallizable propylene sequences, and amorphous E/P segments with a nearly random distribution of E and P units should be considered.

According to a widely recognized model of the Impact Polypropylene Copolymer's (IPC) morphology, the EPR generates droplets that are distributed throughout the homopolymer's matrix.[15,54] The EP copolymer's rubbery droplets experience a kind of microphase separation. As a result, chains containing the longest propene sequences (P-rich) locate at the interphase between the droplets and the iPP matrix, forming a shell-like structure. According to Figure 11, chains with long E sequences (E-rich) are located in the center of the droplets, whereas chains with short EP copolymer segments (rEP), which are distributed almost randomly, are situated between the core and the shell.

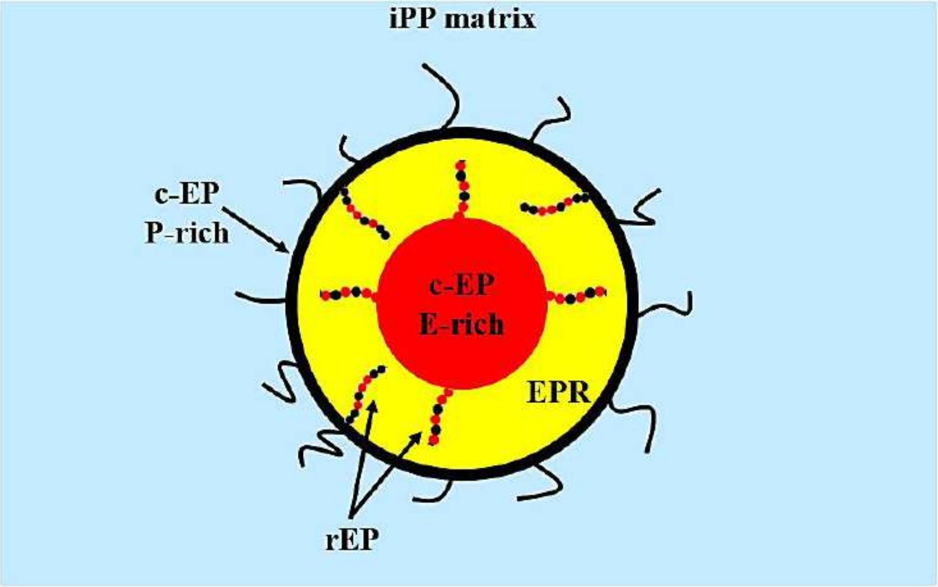

Figure 11. Schematic model of an EPR droplet in the heterophasic morphology of IPC.

The P-rich segments influence the tensile strength because the high content of long P-segments might co-crystallize with the iPP matrix and delay EPR droplet debonding. The E-rich segments, which constitute the EPR droplet core, improve the impact strength because they provide rigidity and promote fracture front propagation through the deep region, enhancing the impact resistance.[15,54-56] Finally, the rEP segments could act as a compatibilizer between the core and shell regions.

5. Industrial production of HECOs

Melt blending of components synthesized in independent processes is a common method to obtain iPP polymer products with improved impact resistance. However, a practical and cost-saving alternative to the mechanical blending of independently synthesized components of industrial relevance consists of the synthesis of the different components in a single process with the use of bulk series reactors, working in the gas phase as it happens in the Catalloy process.[16] In this process the first step consists of the production of the iPP crystalline matrix in the first reactor, while the synthesis of the EP rubbery phase takes place in the successive reactors; by controlling the residence time and monomers feed concentration in the reactors, it is possible to tailor final properties of the product. The entire process is based on the *Reactor Granule Technology (RGT)*[16] and allows to polymerize different monomers in series on the same spherical growing particle, transferring it from one reactor to another. The technology takes advantage of $MgCl_2/TiCl_4$ catalyst spherical particles with a complex porous structure, which is able to replicate their morphology in the final polymer and, simultaneously, generate a uniform distribution of active centers in the catalyst particle. Figure 12 shows SEM images of spherical catalyst particles with two different morphologies (on the left) and of the final polymer (on the right) in which the ability of the catalyst to replicate its morphology in the resulting polymer can be seen. In this way the polymerization temperature is finely controlled, even in the inner part of the polymer, avoiding damage due to overheating.[40] In other words, every single growing polymer particle behaves like a micro-reactor, where it is possible to control not only the morphology but also the tridimensional structure and the ability to homo/copolymerize one or more monomers, to accommodate significant quantities of different phases.

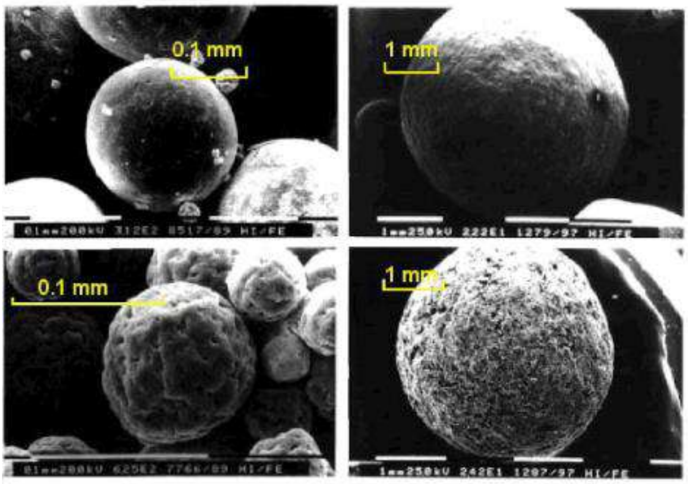

Figure 12. Reactor Granule Technology: SEM micrographs of spherical catalyst particles (left) and final polymer (right) in which is possible to recognize the morphology replication.

The use of this technology allows obtaining homopolymers, random copolymers, and impact heterophasic copolymers, with a good balance of impact/rigidity thanks to the possibility to generate a polypropylene matrix with high crystallinity (isotactic index 99%) in the first step, and a well-dispersed elastomeric phase in the second step exploiting gas phase reactors. Therefore, the HECO systems produced in the Catalloy process are polymeric blends obtained from the synthesis reactor as an already fine dispersion of ethylene-propylene copolymer in an isotactic polypropylene matrix.

6. Goals of the thesis

The main objective of this thesis work is the study of the methods to modify the properties of high impact heterophasic copolymers (HECOs) to obtain structural materials with high tenacity and mechanical resistance. Although it is possible to control the toughness of these products as a function of their application, it is not easy to control the mechanical resistance because toughness and stiffness are generally mutually exclusive in the same material.[57] So, one of the aims of this thesis is to investigate the molecular mechanism underlying the toughness of HECO products with a view to improving their mechanical resistance.

In addition, since these materials are obtained through the use of heterogeneous Ziegler-Natta catalysts, their multi-site nature results in HECO systems being characterized by a complex heterogeneous composition, due to the non-uniform distribution of comonomeric units both inter- and intra-chains within the rubbery EP component. Therefore, the resulting HECO systems could be considered as somewhat mechanically and physically compatible systems, rather than as simple mixtures, in which an iPP matrix includes not only an amorphous rubbery phase, but also semi-crystalline EP copolymers of different ethylene/propylene composition, containing both long crystallizable ethylene and/or propylene sequences and polyethylene chains. On the basis of this intrinsic characteristic of these materials, a further aim of this work is the study of the composition and final properties of each individual component of the heterophasic copolymers and of the relationships between structure, composition and final properties.

Moreover, again, since we are dealing with a complex mixture of macromolecules of different chemical natures, we aim at studying the influence of all these different components on the morphology, relaxation phenomena, and crystallization properties of the thermoplastic matrix of iPP.

Finally, since the elastomeric EPR phase is incompatible with the iPP matrix due to the presence of macromolecules rich in ethylene sequences that are long enough to crystallize, the final properties of HECOs depend on the degree of dispersion of the phase-separated particles of the EPR phase. For this reason, after a detailed study of the compositional heterogeneity of such materials, we aim at studying the methods to improve the dispersion of the EPR phase using different types of compatibilizers. This could be the key to improving the toughness of HECO materials.

In summary, the final aim is to identify the molecular rules that control the level of toughness and strength in HECO samples and to understand the role of each component and their mixture in the toughening and strengthening effect, to obtain materials with tailored levels of damage tolerance for specific applications.

References for the Introduction

1. C. Paulik, C. Tranninger, J. Wang, P. Shutov, D. Mileva, M. Gahleitner, *Macromol. Chem. Phys.* **2021**, *222*, 2100302.

2. L. Barino, R. Scordamaglia, *Macromol. Theory Simul.* **1998**, *7*, 407.

3. G. Morini, E. Albizzati, G. Balbontin, I. Mingozzi, M.C. Sacchi, F. Forlini, I. Tritto, *Macromolecules* **1996**, *29*, 5770.

4. J.C. Chadwick, G. Morini, G. Balbontin, I. Camurati, J.J.R. Heere, I. Mingozzi, F. Testoni *Macromol Chem Phys* **2001**, *202*, 1995.

5. J. Varga, *Journal of materials science* **1992**, *27*, 2557-2579.

6. C. De Rosa, F. Auriemma, O. Ruiz de Ballesteros, L. Resconi, I. Camurati, *Chem. Mater.* **2007**, *19*, 5122-5130.

7. De Rosa, C.; Auriemma, F.; Ruiz de Ballesteros, O.; Resconi, L.; Camurati, I. *Macromolecules*, **2007**, *40*, 6600-6616.

8. C. De Rosa, F. Auriemma, P. Vollaro, L. Resconi, S. Guidotti, I. Camurati, M*acromolecules* **2011**, *44*, 540-549.

9. C. De Rosa, O. Ruiz de Ballesteros, F. Auriemma, R. Di Girolamo, C. Scarica, G. Giusto, S. Esposito, S. Guidotti, I. Camurati, *Macromolecules* **2014**, *47*, 4317-4329.

10. Z. Wang, *J. Appl.Polym. Sci.* **1996**, *60*, 2239-2243.

11. J. Z. Liang, R. K. Y. Li, *J. Appl. Polym. Sci*. **2000**, *77*, 409-417.

12. G. X. Wei, H. J. Sue, J. Chu, C. Huang, K. T. Gong, *Polymer* **2000**, *41*, 2947-2960.

13. Y. S. Thio, A. S. Argon, R. E. Cohen and M. Weinberg, *Polymer* **2002**, *43*, 3661-3674.

14. L. Zhang, C. Li, R. Huang, *J. Polym. Sci. Part B: Polym. Phys* **2004**, *42*, 1656-1662.

15. F. Chen, Y. Shangguan, Y. Jiang, B. Qiu, G. Luo, Q. Zheng, *Polymer* **2015**, *65*, 81-92.

16. G. Cecchin, G. Morini, G. Pelliconi, *Macromol. Symp.* **2001**, *173*, 195-210.

17. G. Natta, P. Corradini, *Nuovo Cimento Suppl*. **1960**, *15*, 40-51.

18. P. Corradini, V. Petraccone, C. De Rosa, G. Guerra, *Macromolecules* **1986**, *19*, 2699-2703.

19. Polypropylene Handbook, Munich: E.P. Moore ed., Hauser publisher, **1996**.

20. S. Brückner, S. Meille, V. Petraccone, B. Pirozzi, *Prog. Polym. Sci* **1991**, *16*, 361-404.

21. R. Thomann, C. Wang, J. Kressler, R. Mulhaupt, *Macromolecules* **1996**, *29*, 8425-8434.

22. M. Hikosaka, T. Seto, *Polymer Journal* **1973**, *5*, 111-127.

23. Z. J. Mencik, *Macromol. Sci., Phys.* **1972**, *B6(1)*, 101.

24. G. Guerra, V. Petraccone, P. Corradini, C. De Rosa, R. Napolitano, B. Pirozzi, G. J. Giunchi, *Polym. Sci., Polym. Phys.* **1984**, *22*, 1029.

25. F. Auriemma, O. Ruiz de Ballestreros, C. De Rosa, P. Corradini, *Macromolecules* **2000**, *33*, 8764-8774.

26. S. Brückner, S. V. Meille, *Nature* **1989**, *340*, 455-457.

27. S. V. Meille, S. Brückner, W. Porzio, *Macromolecules* **1990**, *23*, 4114-4121.

28. F. Auriemma, C. De Rosa, T. Boscato, P. Corradini, *Macromolecules*, **2001**, *34*, 4815-4826.

29. I. L. Hosier, R. G. Alamo, P. Esteso, G. R. Isasi, L. Mandelkern, *Macromolecules*, **2003**, *36*, 5623-5636.

30. F. Auriemma, C. De Rosa, *Macromolecules*, **2002**, *35*, 9057-9068.

31. H. J. Leugering, *Makromolek. Chem.* **1967**, *109*, 204-216.

32. A. Turner-Jones, A. J. Cobbold, *J. Polym. Sci.*, **1968**, *6*, 539.

33. P. Jacoby, B. H. Bersted, W. J. Kissel, C. E. Smith, *J. Polym. Sci. Polym. Phis.Ed*. **1986**, *24*, 461-491.

34. F. L. Binsbergen, B. G. M. De Lange, *Polymer* **1968**, *9*, 23-40.

35. H. J. Leugering, G. Kibsch, *Angew. Makromolek. Chem.* **1973**, *33*, 17.

36. H. Dragaun, H. Hubeny, H. Muschik, *J. Polym. Sci., Polym. Phys. Ed,* **1977**, *15*, 1779.

37. J. C. Wittmann, B. Lotz, P. Smith, *Progress in Colloid & Polymer Science,* **1993**, *92,* 32-38.

38. P. Corradini, V. Petraccone, C. De Rosa, G. Guerra, *Macromolecules,* **1986**, *19*, 2699-2703.

39. P. Prentice, *Polymer* **1982**, *23*, 1189-1192.

40. E. Albizzati, M. Galimberti, *Chimica e l'Industria* **1997**, *79*, 1053-1060.

41. F. M. Mirabella, *Polymer* **1993**, *34*, 1729-1735.

42. T. Usami, Y. Gotoh, H. Unemoto, S. Takayama, *Appl. Polym. Sci.: Appl.Polym. Symp.* **1993**, *52*, 145.

43. B. Ke, *J. Polym. Sci.* **1960**, *42*, 15-23.

44. N. Pasquini, in Polypropylene Handbook 2nd ed., Cincinnati, Ohio, Hanser Verlag **2005**, 307-317.

45. C. De Rosa, F. Auriemma, *J. Am. Chem. Soc.* **2006**, *128,* 11024-11025.

46. K. Premphet, P. Horanont, *Polymer* **2000**, *41,* 9383.

47. R. Greco, C. Mancarella, E. Martuscelli, G. Ragosta, Y. Jinghua, *Polymer* **1987**, *28,* 1929-1936.

48. J. Xu, L. Feng, *Polymer Int.* **1998**, *47,* 433-438.

49. H. Cai, X. Luo, X. Chen, D. Ma, J. Wang, H. Tan, *J. Appl. Polym. Sci.* **1999**, *39*, 6589.

50. Y. Xue, Y. Fan, S. Bo, X. Ji, *Eur. Polym. J.* **2011**, *47*, 1646-1653.

51. Z. Tian, X.P. Gu, G. L. Wu, L.F. Feng, Z.Q. Fan, G.H. Hu, *Ind. Eng. Chem. Res*. **2011**, *50*, 5992-5999.

52. B. Z. Jang, D. R. Uhlmann, J. B. Vander Sande, *J. Appl. Polym. Sci.* **1984**, *29*, 3409-3420.

53. B. Z. Jang, D. R. Uhlmann, J. B. Vander Sande, *J. Appl. Polym. Sci.* **1985**, *30*, 2485-2504.

54. F. Luo, C. Xu, K. Wang, H. Deng, F. Chen, Q. Fu, *Polymer* **2012**, *53*, 1783-1790.

55. C. Zhang, Y. Shangguan, R. Chen, Y. Wu, F. Chen, Q. Zheng, G. Hu, *Polymer* **2010**, *51*, 4969-4977.

56. W. Rungswang, P. Saende, B. Thitisuk, T. Pathaweeisariyakul, W. Cheeyasrirungruang, *J. Appl. Polym. Sci.* **2013**, *128*, 3131-3140.

57. R. O. Ritchie, *Nature Materials* **2011**, *10*, 817-822.

CHAPTER 1

Heterophasic copolymers of isotactic polypropylene

1.1. Materials

A set of six heterophasic copolymers (HECOs) samples, supplied by LyondellBasell Polyolefin laboratories in Ferrara, were analyzed. Samples show different amounts of dispersed phase (EPR) variable between 22 and 32wt% with an ethylene content in the range of 45 and 60wt%. All samples are common HECO, i.e., a biphasic system made of a thermoplastic matrix of iPP and a dispersed rubber phase of EPR except the sample EP3307 which is made of three phases (see Table 1.1). In fact, this sample is made of a thermoplastic matrix of iPP and two dispersed phases, the first one has a content of ethylene equal to 30wt% while the second one contains an amount of ethylene of 60wt% (ratio ≈ 4:7). In addition, a sample of highly stereoregular iPP homopolymer (with [*mmmm*] = 98%), was analyzed.

Table 1.1. iPP content, elastomeric phase content, EPR volume fraction (φ_{EPR}), and ethylene concentration of EPR for the homopolymer and all HECO samples.

Samples	iPP content (wt%)	EPR content (wt%)	φ_{EPR}[a]	[C2] of EPR (wt%)
X19875	100	-	0	-
21588/45	78.0	22.0	0.229	54.0
A1	75.4	24.6	0.256	45.6
B3	71.3	28.7	0.298	60.0
B2	71.0	29.0	0.301	51.0
B1	70.4	29.6	0.307	45.0
EP3307	68.5	31.5 [11.5wt% of C3C2 (C2 = 30wt%); 20wt% of C3C2 (C2 = 60wt%)]	0.326	49.0[b]

(a) EPR volume fraction calculated from $\varphi_{EPR} = \rho_M \, wt_{EPR} / (\rho_M \, wt_{EPR} + \rho_{EPR} \, wt_M)$. ρ_M and ρ_{EPR} are, respectively, the density of the matrix and the EPR phase, while wt_{EPR} and wt_M are the elastomeric phase and matrix content, respectively. $\rho_M = 0.905$ Kg/m^3; $\rho_{EPR} = 0.860$ Kg/m^3.

(b) Value obtained by weight-averaging the contents of the EPR phase for the respective ethylene concentrations of the two phases: $[C2] = ((11.5\times30) + (20\times60))/(31.5)$.

The samples have been produced in the laboratory of Basell Polyolefins in Ferrara using the Catalloy process. Figure 1.1 shows the flow chart of a typical Catalloy plant, in the main part, made up of three reactors.

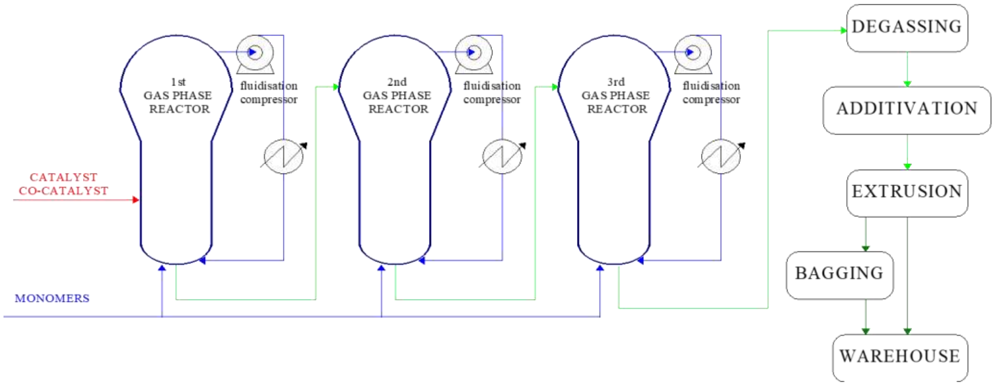

Figure 1.1. Typical Catalloy plant flow chart.

The process consists of the synthesis of the highly isotactic iPP homopolymer in the first reactor. Then, ethylene and propylene monomers are introduced in the successive reactors in the gas phase and, appropriately changing the feed monomers ratio, the EPR copolymer is synthesized in the second or other following reactors, forming soft particles embedded in the crystalline iPP matrix. The process allows obtaining various kinds of copolymers of the desired composition, acting on the monomers feed composition, type of catalyst, temperature, and reaction time. The whole process relies on the use of the reactor granule technology, that is of spherical particles of $MgCl_2/TiCl_4$ catalyst, having a complex porous structure able to replicate their morphology in the final morphology of the produced polymer. Catalyst stereoselectivity is controlled by adding a Lewis base (external donor) dicyclopentyldimethoxysilane, whose molecular structure is shown in Figure 1.2.

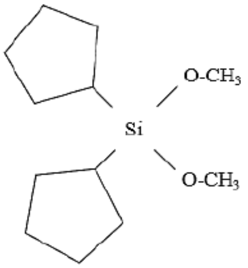

Figure 1.2. External donor D (dicyclopentyldimethoxysilane) used for the synthesis of the HECO samples studied.

This donor is used also to improve the comonomers distribution in the rubbery fraction and to ensure a high stereoregularity of the homopolymer or copolymer chains.

The mechanism of the polymer growth around the catalyst particle, sketched in Figure 1.3, may be summarized as follows:[1]

- The catalyst grain (macroparticles) is made up of microparticles of $MgCl_2$ and larger clusters of microparticles (sub-particles) (Figure 1.3A);
- The major contributor to catalyst porosity derives from macro-voids formed by the interstitial spaces among the sub-particles;
- Active sites are localized at the surface of the microparticles;
- The catalyst explosion starts in the early stage of polymerization; early polymerization breaks the macroparticle catalyst in its components, micro, and sub-particles. (Figure 1.3B);
- The polymer grain reproduces the morphology of the catalyst grain: monomer diffuses in the bulk of the catalyst and forms a polymer shell (micro-globule) around every catalyst microparticle (Figure 1.3B);
- Polymer micro-globules tend to agglomerate in order to form bigger and thicker clusters (sub-globules) (Figure 1.3C);
- During the polymerization, catalyst microparticles undergo further fragmentation and tend to migrate from the bulk to the polymer sub-globule surface, where the polymerization reaction keeps continuing.

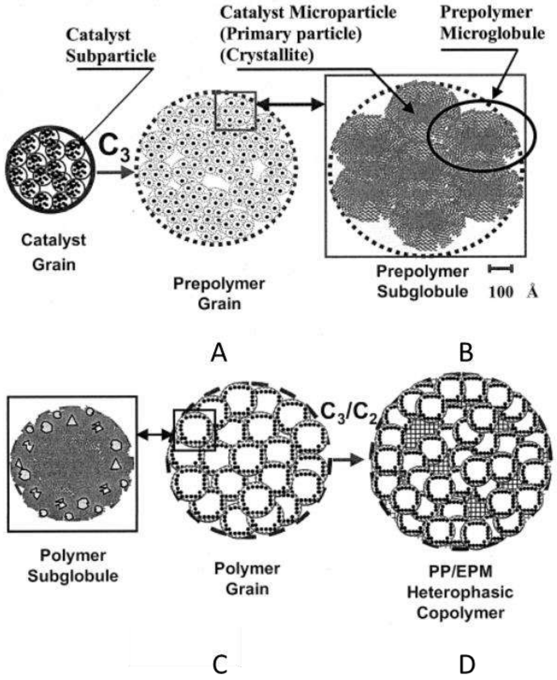

Figure 1.3. Polypropylene growing mechanism around spherical $MgCl_2/TiCl_4$ catalyst particle: pre-polymerization step (A,B), main polymerization step (C), and successive copolymerization of the ethylene-propylene copolymer (D). Reprinted from Polypropylene product innovation by reactor granule technology, Cecchin C., Morini G., Pelliconi A., Macromol. Symp., 173, 195-209, 2001, with permission from Wiley (2023).

According to this model, the grains of the polymer reproduce the shape, dual hierarchy, and porosity of the grain of the catalyst, while the grains increase the size during polymerization. Therefore, it is possible to predict, design, and tailor the shape, size, and porosity of the macroparticles of the catalyst to obtain a specific product and/or process.

In conclusion, “Catalloy” heterophasic copolymers are materials with peculiar physical and mechanical properties obtained in a controlled way that is not reproducible by another type of plant.

1.2. Polymer characterization: Structural (WAXS), thermal (DSC), and mechanical properties

Samples that have not been thermally and mechanically treated in any way (as-prepared samples), i.e., as supplied by Basell Polyolefin, were characterized by structural and thermal analysis in order to obtain information about the structure, the crystallinity, and the thermal behavior.

Wide-angle X-ray diffraction profiles were recorded with an Empyrean automatic powder diffractometer (PANalytical), using nickel filtered Cukα radiation (λ = 1.5418Å). Thermal analysis was performed with a differential scanning calorimeter Mettler Toledo (DSC-822) in a flowing N_2 atmosphere. A scanning rate of 10 °C/min was used to record the first heating, cooling, and second heating scans.

In order to study the mechanical properties, films of the homopolymer and all samples shown in Table 1.1 were obtained through the compression molding technique using a hydraulic press. The temperature at which the samples were melted was chosen based on DSC thermograms and, in particular, a temperature of about 40°C above the melting temperature was selected. The samples were placed between either two Teflon sheets or two aluminum sheets before being placed between the press plates. After holding samples in the press at 200°C for five minutes, they were cooled by three different procedures:

1. slow cooling from the melt to 25°C by circulating cold water between the press plates with a cooling rate of about 10°C/min. Samples were previously placed between two Teflon sheets;
2. rapid cooling from the melt down to 10°C by rapidly immersing (quenching) the sample in a thermostatic water/ice bath. Samples were previously placed between two Teflon sheets;
3. rapid cooling from the melt to 10°C by quenching the sample into a thermostatic water/ice bath. Samples were previously placed between two sheets of aluminum foil.

Stress-strain curves were recorded according to *A.S.T.M.* D882-83 standard, with the aim to understand how the rubbery phase content and the ethylene concentration of the EPR phase influenced the mechanical parameters. Analyses of mechanical properties were performed at room temperature and at T = -20°C.

1.2.1. Structural and thermal characterization of as-prepared samples

The X-ray powder diffraction profiles of all as-prepared samples are reported in Figure 1.4. The structural characterization shows that all samples crystallize in the α-form of isotactic polypropylene as evidenced by the presence of the peaks at $2\theta = 14°$, 16.9°, 18.6°, and 21.3° corresponding to the $(110)\alpha$, $(040)\alpha$, $(130)\alpha$ and $(111)\alpha$ reflections of the α-form of the iPP.[2-6] However, for sample B3, i.e., the sample with the highest ethylene content of the elastomeric phase, a low-intensity shoulder is present at $2\theta = 23.5°$ corresponding to the reflection $(200)_{PE}$ of the orthorhombic form of polyethylene[7] suggesting the presence of quite long ethylene sequences in the EPR phase that are able to crystallize. In addition, for the sample EP3307, it is possible to note the presence of the peak at $2\theta = 16°$, corresponding to the $(110)_\beta$ reflection of the β form of iPP,[8-10] which indicates the presence in this sample of a certain amount of crystals of the β form. At low and high values of 2θ, there are also very narrow Bragg reflections (≈ 9.5° and 29°) ascribable to the presence of the talc.

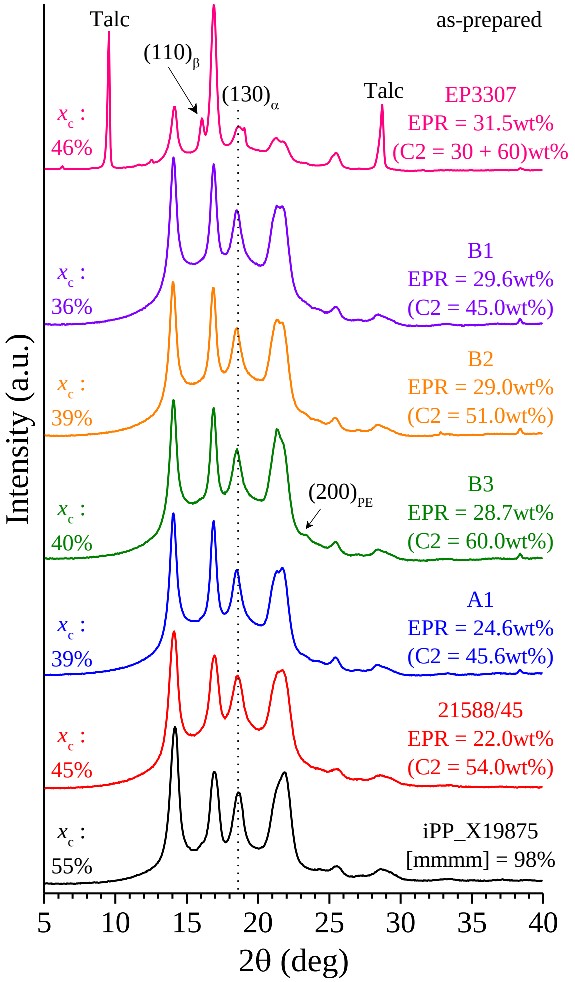

Figure 1.4. X-ray diffraction patterns of the as-prepared homopolymer and of all HECO samples.

Figure 1.5 shows the DSC thermograms of the first heating (A), cooling (B), and second heating (C) of the analyzed samples. In the thermograms of the HECO samples, in addition to the main melting peaks at about 165-170°C and crystallization peaks at about 120°C, corresponding to the melting and crystallization of the α-crystals of the thermoplastic matrix of iPP, there is a low-enthalpy peak at lower temperatures ($T_m \approx 120°C$, $T_c \approx 100°C$). These peaks may be attributed to the melting and crystallization of defective polyethylene crystals (PE-like) that are generated from longer ethylene sequences that belong to the EPR copolymer of the rubbery phase. The presence of such ethylene sequences, which are long enough to crystallize, is due to the use of a Ziegler-Natta catalyst, which, because of multiple heterogeneous sites, produces copolymers having a non-uniform distribution of comonomer units, both inter-, and intra-chain.

Table 1.2 shows the thermal parameters obtained from DSC thermograms of Figure 1.5, while Figure 1.6 reports the crystallization and melting (from 2nd heating) temperatures and enthalpies as a function of both EPR content and the ethylene concentration of the rubbery phase.

The crystallization temperature of PE-like crystals increases as the ethylene concentration of the EPR phase increases (Figure 1.6A, bottom red trend). However, these values also depend on the EPR content. In fact, the temperature first increases and then decreases for further increases in the elastomeric phase content (Figure 1.6A, bottom black trend). Nevertheless, if we focus on samples with a similar elastomeric phase content (≈ 29wt%) it is possible to conclude that this decrease is strongly dependent on the ethylene concentration. In general, no trend is observed for the melting temperatures of PE-like crystals as a function of the EPR content and the ethylene concentration of the EPR phase. Moreover, the crystallization and melting enthalpies of PE-like crystals slightly increase as the ethylene concentration increases (Figure 1.6C,F). However, these values also depend on the EPR content. In fact, they first increase and then decrease for further increases in the rubbery phase content (Figure 1.6B,E). Still, even in this case, a significant influence of ethylene concentration remains. In fact, the further decrease in enthalpies of melting and crystallization can be attributed to a decrease in ethylene concentration for samples with similar EPR content. Finally, the lower melting enthalpy of the PE-like crystals for sample EP3307 can also be attributed to the fact that there is a low copolymer content with an ethylene concentration of 60wt% (see Table 1.1).

Regarding the thermoplastic iPP matrix, no trends are observed for the crystallization and melting temperatures (Figure 1.6A,D) and enthalpies (Figure 1.6B,C,E,F) as a function of both the ethylene concentration and the rubbery content.

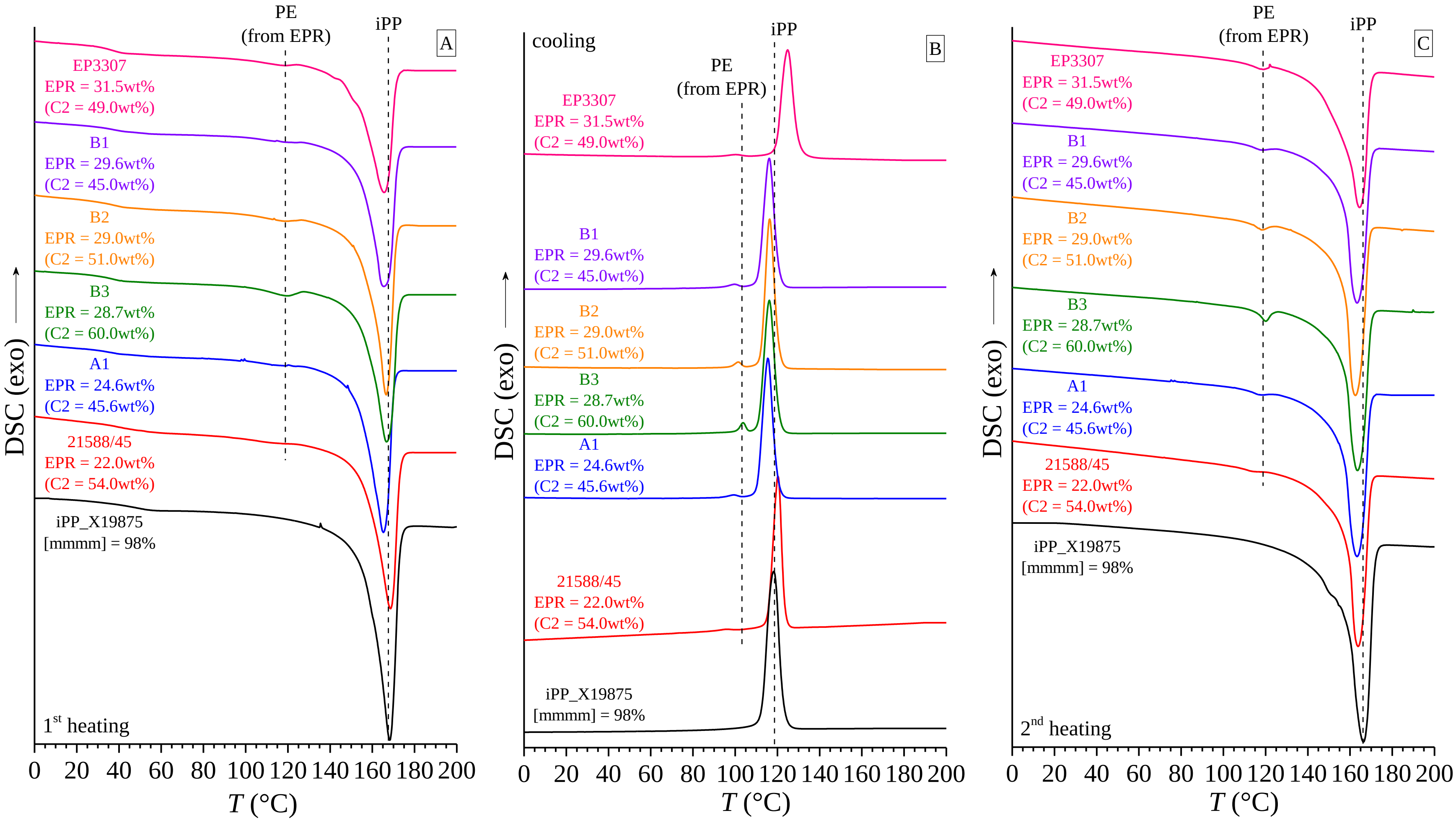

Figure 1.5. Comparison of DSC thermograms of first heating (A), cooling (B), and second heating (C) of all "as-prepared" samples.

Table 1.2. Values of melting temperatures and enthalpies recorded in first heating (T_m^I and ΔH_m^I), crystallization temperatures and enthalpies (T_c, ΔH_c), and melting temperatures and enthalpies recorded in second heating (T_m^{II}, ΔH_m^{II}) of iPP homopolymer and all HECO samples. Subscripts "1" and "2" refer to the values for PE-like and α-form crystals, respectively.

Sample	T_{m1}^{I} (°C)	ΔH_{m1}^{I} (J/g)	T_{m2}^{I} (°C)	ΔH_{m2}^{I} (J/g)	T_{c1} (°C)	ΔH_{c1} (J/g)	T_{c2} (°C)	ΔH_{c2} (J/g)	T_{m1}^{II} (°C)	ΔH_{m1}^{II} (J/g)	T_{m2}^{II} (°C)	ΔH_{m2}^{II} (J/g)
iPP	-	-	168.3	98.8	-	-	118.2	112.4	-	-	166.3	112.6
21588/45 **EPR = 22.0wt%** **C2 = 54.0wt%**	113.3	1.5	168.6	72.4	96.0	2.4	120.2	76.5	114.6	6.0	163.7	83.4
A1 **EPR = 24.6wt%** **C2 = 45.6wt%**	-	-	165.3	74.7	99.4	3.3	115.4	83.3	117.9	7.2	163.3	84.0
B3 **EPR = 28.7wt%** **C2 = 60.0wt%**	119.3	4.3	166.8	71.0	103.8	6.2	116.2	79.5	120.1	9.0	163.6	79.2
B2 **EPR = 29.0wt%** **C2 = 51.0wt%**	118.0	2.3	166.6	71.9	101.4	4.1	116.4	80.2	118.2	7.8	162.6	79.8
B1 **EPR = 29.6wt%** **C2 = 45.0wt%**	-	-	165.4	72.0	99.8	3.5	116.1	78.9	118.2	7.2	163.2	78.6
EP3307 **EPR = 31.5wt%** **C2 = 49.0wt%**	117.6	2.0	165.6	66.2	100.4	3.5	124.8	77.5	118.6	4.0	164.4	75.6

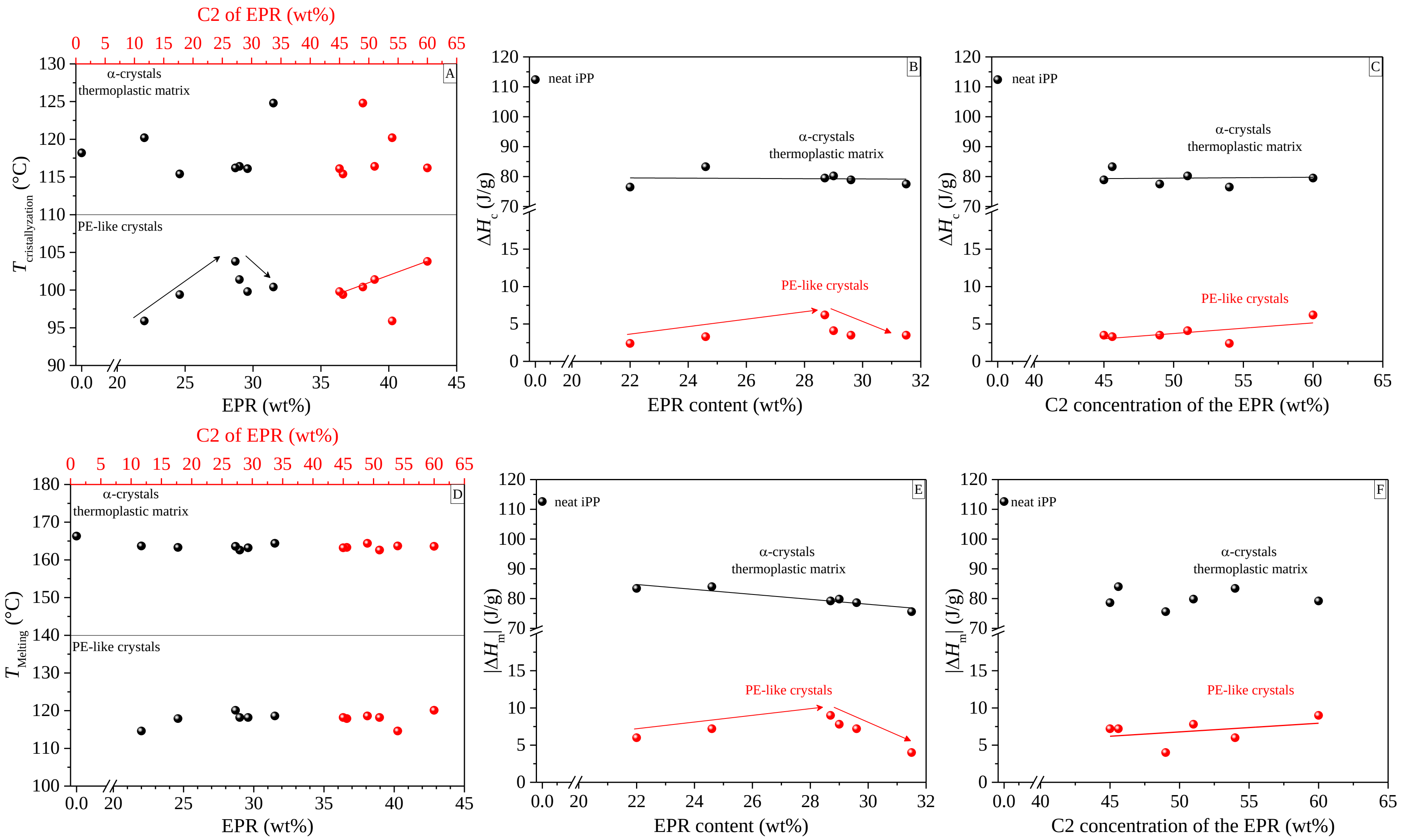

Figure 1.6. Crystallization (A) and melting temperatures from second heating thermograms (D) of the iPP matrix and EPR dispersed phase as a function of the EPR content and of the ethylene concentration of EPR of all as-prepared HECO samples. Crystallization (B) and melting enthalpies from second heating thermograms (E) of the thermoplastic matrix and rubbery phase as a function of the EPR content. Crystallization (C) and melting enthalpies from second heating thermograms (F) of the iPP matrix and elastomeric phase as a function of the ethylene concentration of the EPR. In addition, all values for the homopolymer are reported as well.

1.2.2. Structural analysis and mechanical properties recorded at room temperature of samples crystallized from the melt by slow cooling

The X-ray powder diffraction profiles of all compression molded films obtained by slow cooling from the melt are reported in Figure 1.7. All samples crystallize in the α-form of isotactic polypropylene. However, it is also possible to note the presence of the low-intensity peak at $2\theta = 20.1°$, corresponding to the reflection $(117)_{\gamma}$[2,11-13] which indicates, for all samples, the presence of a small amount of iPP crystals in the γ form. For the sample EP3307, at low and high values of 2θ, there are still very narrow Bragg reflections (≈ 9.5° and 29°) ascribable to the presence of the talc.

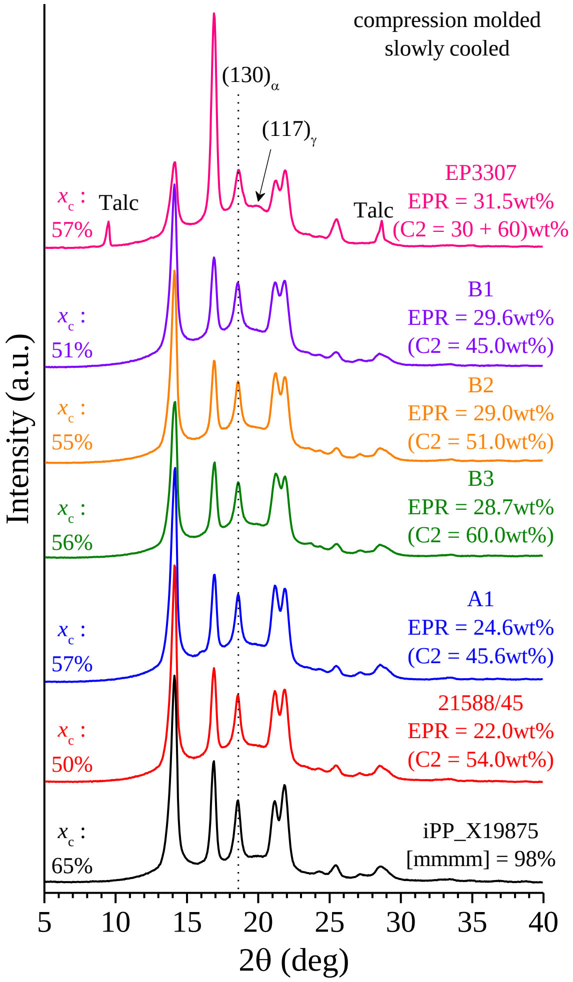

Figure 1.7. X-ray diffraction patterns of the compression molded films of the homopolymer and of all HECO samples obtained by slow cooling from the melt to record stress-strain curves at room temperature. The diffraction profiles were recorded a $T = 25°C$.

An analysis of mechanical properties was performed on all compression-molded films of samples shown in Table 1.1, recording stress-strain curves with the aim to understand how the rubbery phase content and the ethylene concentration of the EPR phase affect the ductility, the strength, and the stiffness of the HECOs samples.

Figure 1.8 shows the stress-strain curves of all HECOs recorded at room temperature on films of samples obtained by slow cooling from the melt. The stress-strain curve of the homopolymer is also shown for comparison. The values of the mechanical parameters evaluated from the stress-strain curves of Figure 1.8 are reported in Table 1.3.

The analysis reveals that the introduction of a rubbery phase leads to an improvement of the ductility and a reduction of the strength in comparison with the mechanical properties of highly isotactic polypropylene. Overall, we can note that the ductility increases, and the strength decreases with increasing the EPR content.

The mechanical parameters of HECOs are reported in Figure 1.9 as a function of the content and the composition of the EPR phase. In more detail, we can see that the ductility (Figure 1.9A) of samples with a similar EPR content decreases as the ethylene concentration increases, while the tensile strength (Figure 1.9B) and stiffness (Figure 1.9C) decrease as the EPR content increases. In addition, for samples with a similar rubbery phase content, the tensile strength increases as the ethylene concentration increases, due probably to the presence of PE-like crystals which can offer greater resistance to deformation. Regarding Young's modulus (Figure 1.9C), although generally the values decrease as the EPR content increases, they also depend on the crystallinity index of samples.

Finally, the fact that the strain at break (Figure 1.9A) decreases as the ethylene concentration increases, with a loss in ductility, could be due to the presence of macromolecules belonging to the elastomeric phase that contain long ethylene sequences able to crystallize forming PE-like crystals. This results in lower ductility due to the incompatibility between PE and iPP.[14,15]

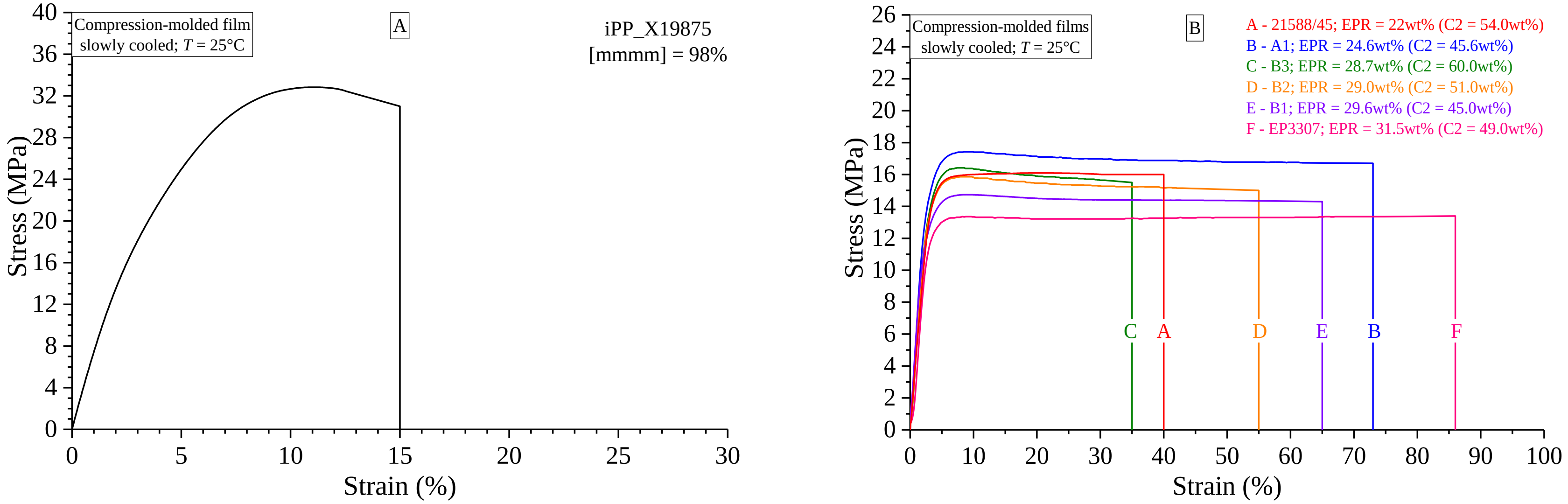

Figure 1.8. Stress-strain curves at *T* = 25°C of compression-molded films of the homopolymer (A) and all HECOs (B) crystallized by slow cooling from the melt.

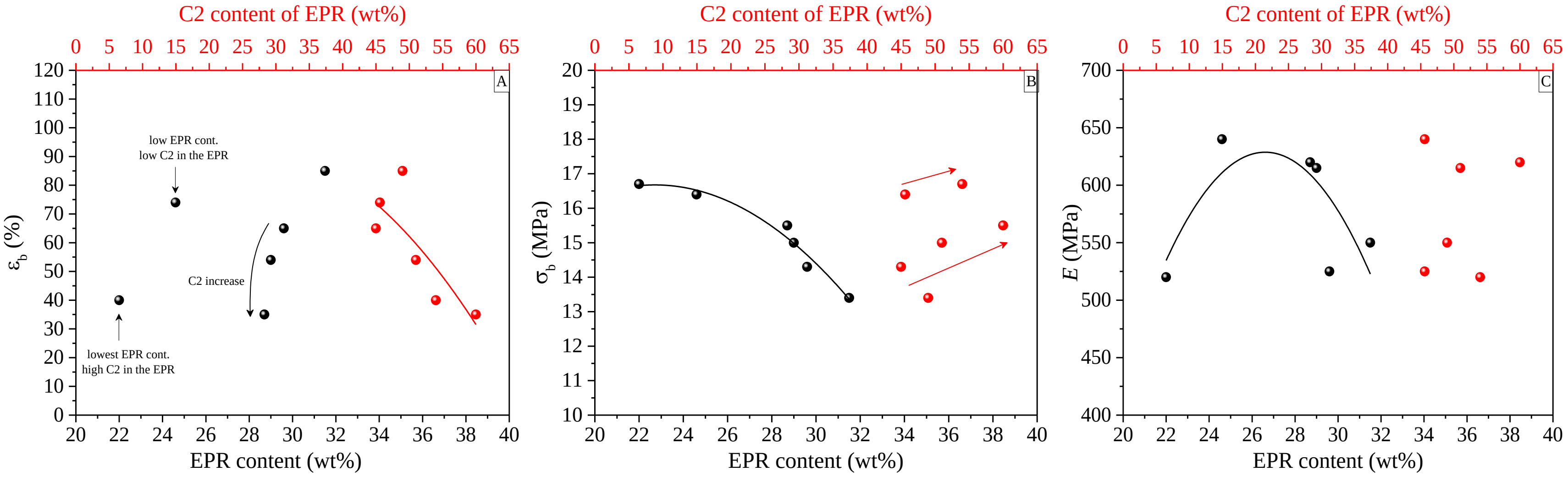

Figure 1.9. Deformation at break (A), stress at break (B), and Young's modulus (C) as a function of the EPR content and of the ethylene concentration of the EPR derived from stress-strain curves reported in Figure 1.8.

Table 1.3. Values of strain (ε_b) and stress (σ_b) at break, Young's modulus (E), and degree of crystallinity (x_c) of compression-molded films crystallized by slow cooling from the melt of iPP homopolymer and all HECO samples obtained from the analysis at T = 25°C of Figure 1.8.

Sample	EPR (wt%)	C2 (EPR) (wt%)	ε_b (%)	σ_b (MPa)	E (MPa)	x_c[(a)] (%)
iPP	-	-	15 ± 1	31 ± 1	770 ± 20	65
21588/45	22.0	54.0	40 ± 15	16.7 ± 0.3	520 ± 30	50
A1	24.6	45.6	75 ± 7	16.4 ± 0.3	640 ± 25	57
B3	28.7	60.0	35 ± 3	15.5 ± 0.2	620 ± 30	56
B2	29.0	51.0	55 ± 9	15.0 ± 0.4	615 ± 15	55
B1	29.6	45.0	65 ± 8	14.3 ± 0.2	525 ± 25	51
EP3307	31.5	49.0	85 ± 5	13.4 ± 0.2	550 ± 25	57

(a) Values evaluated from X-ray diffraction profiles of Figure 1.7.

1.2.3. *Structural analysis and mechanical properties recorded at low temperature of samples crystallized by slow cooling from the melt*

Since HECOs are widely used in artifacts that must be durable even at low temperatures, an analysis of mechanical properties, was conducted at the temperature of -20°C to understand whether the introduction of the elastomeric phase improved the mechanical performances of the iPP even at low temperatures. New compression molded films crystallized by slow cooling from the melt were prepared for recording the stress-strain curves at low temperature. Figure 1.10 shows the X-ray powder diffraction profiles of these new compression molded films. All samples crystallize in the α-form of iPP. However, in all samples there is also the presence of the low-intensity peak at $2\theta = 20.1°$, corresponding to the reflection $(117)_\gamma$ and, for the iPP and B3 samples, is even possible to note the presence of the peak at $2\theta = 16°$, corresponding to the reflection $(110)_\beta$ of the β form of iPP.

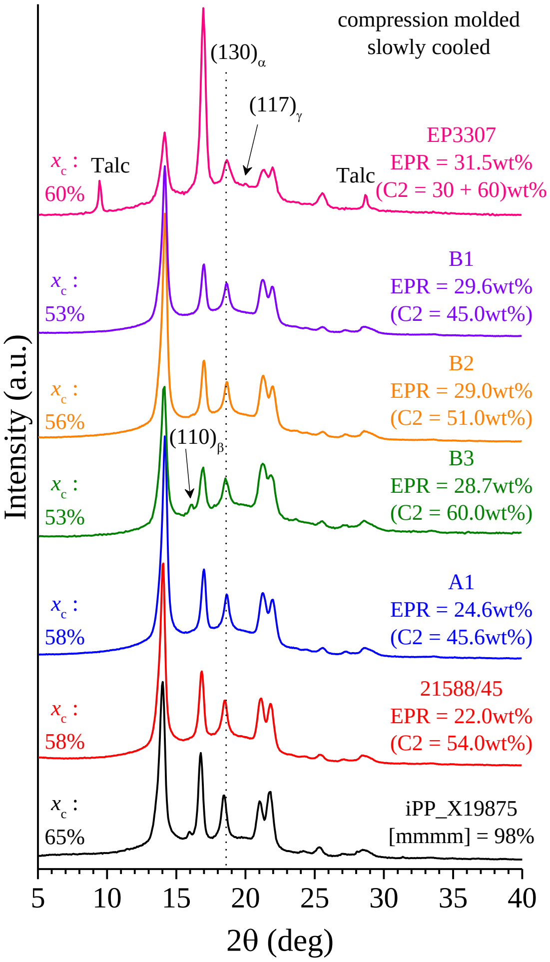

Figure 1.10. X-ray diffraction patterns of the compression molded films of the homopolymer and of all HECO samples obtained by slow cooling from the melt to record stress-strain curves at T = -20°C. The diffraction profiles were recorded a T = 25°C.

Figure 1.11 shows the stress-strain curves of the homopolymer and all HECOs recorded at T = -20°C on film of samples obtained by slow cooling from the melt. The values of the mechanical parameters evaluated from the stress-strain curves of Figure 1.11 are reported in Table 1.4.

Surprisingly, the analysis of the mechanical properties performed on all HECO samples shows that the ductility improves at lower temperatures with even an increase in stiffness and mechanical strength. In other words, the presence of the elastomeric phase extends the application range of isotactic polypropylene and allows these materials to be used even at low temperatures given their good mechanical properties. In fact, it is evident from Figure 1.11A that the iPP specimen remains very brittle at low temperatures, and, when compared with the curve in Figure 1.8A, it is clear that low-temperature stretching results in increased stresses involved for all strain values.

Figure 1.12 shows the mechanical parameters obtained from Figure 1.11B as a function of the elastomeric phase content and the ethylene concentration of the EPR. It is possible to see that the ductility is influenced both by the content and the composition of the rubbery phase. In fact, the strain at break increases as the elastomeric phase content increases. However, for samples with very similar EPR content (about 29wt%), ductility is intrinsically affected by the ethylene concentration; in fact, it decreases as the ethylene concentration increases. Overall, an increase in the ethylene concentration has a negative effect on the strain at break (Figure 1.12A). The latter result should be, also in this case, related to the weak interfacial adhesion between the iPP and PE-like crystals.

As for the tensile strength (Figure 1.12B) and for the stiffness (Figure 1.12C), an increase in the EPR content leads to a decrease in the stress at break and Young’s modulus values, respectively. In general, it seems that the ethylene concentration has no particular effect on these two mechanical parameters and Young’s modulus values are still dependent on the crystallinity of samples.

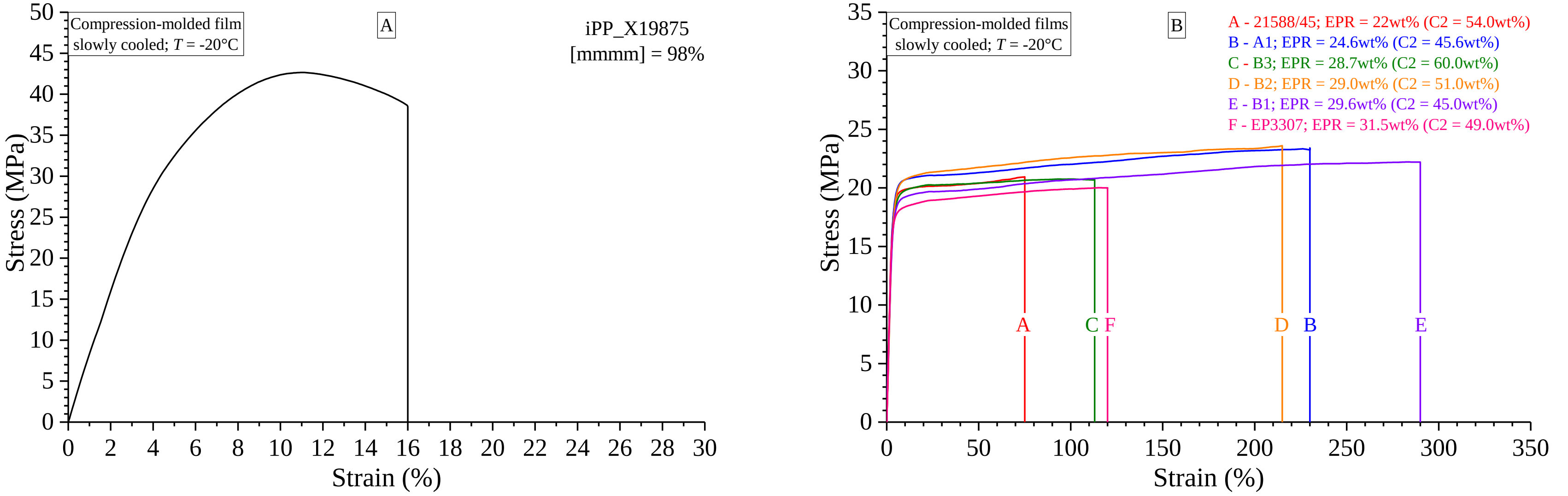

Figure 1.11. Stress-strain curves at *T* = -20°C of compression-molded films of the homopolymer (A) and all HECOs (B) crystallized by slow cooling from the melt.

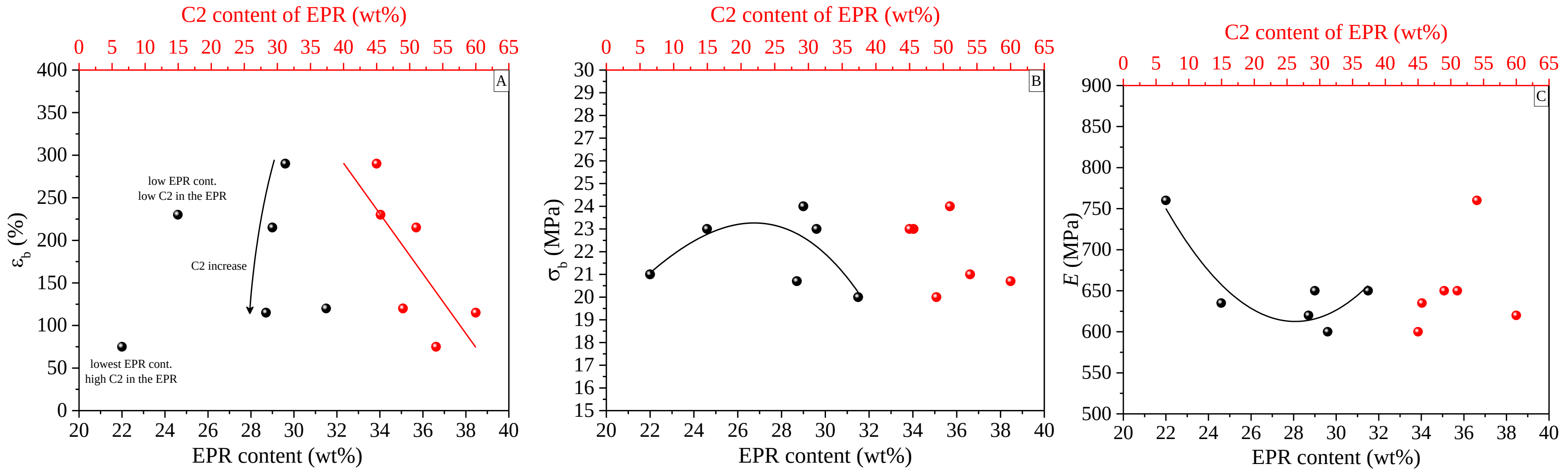

Figure 1.12. Deformation at break (A), stress at break (B), and Young's modulus (C) as a function of the EPR content and of the ethylene concentration of the EPR derived from stress-strain curves reported in Figure 1.11.

Table 1.4. Values of strain (ε_b) and stress (σ_b) at break, Young's modulus (E), and degree of crystallinity (x_c) of compression-molded films crystallized by slow cooling from the melt of iPP homopolymer and all HECO samples obtained from the analysis at T = -20°C of Figure 1.11.

Sample	EPR (wt%)	C2 (EPR) (wt%)	ε_b (%)	σ_b (MPa)	E (MPa)	x_c[(a)] (%)
iPP	-	-	16 ± 2	38 ± 3	835 ± 75	65
21588/45	22.0	54.0	75 ± 10	21 ± 2	760 ± 50	58
A1	24.6	45.6	230 ± 10	23 ± 2	735 ± 75	58
B3	28.7	60.0	115 ± 15	21 ± 1	620 ± 70	53
B2	29.0	51.0	215 ± 25	24 ± 1	650 ± 30	56
B1	29.6	45.0	290 ± 60	23 ± 2	600 ± 60	53
EP3307	31.5	49.0	120 ± 15	20 ± 1	650 ± 30	60

(a) Values evaluated from X-ray diffraction profiles of Figure 1.10.

1.2.4. Structural analysis and mechanical properties recorded at room temperature of samples crystallized by quenching (ice/water bath and Teflon sheets)

The X-ray powder diffraction profiles of compression molded films obtained by rapid cooling from the melt down to 10 °C i.e., quenching the sample in a thermostatic ice/water bath, are reported in Figure 1.13. It is worth pointing out that all samples were previously placed between two Teflon sheets. Despite the rapid cooling from the melt, the diffraction profiles show that all samples are still crystalline, and they crystallize in the α-form of isotactic polypropylene. The development of α-form crystals is favored by the substrate within the sample was sandwiched to obtain the compression-molded film. In fact, Teflon has a low thermal transmission coefficient that does not allow the sample to be obtained in the iPP mesomorphic form even though the sample was quenched from the melt. In addition, only for sample EP3307, it is also possible to notice the presence of the low-intensity peak at $2\theta = 20.1°$, corresponding to the reflection $(117)_\gamma$.

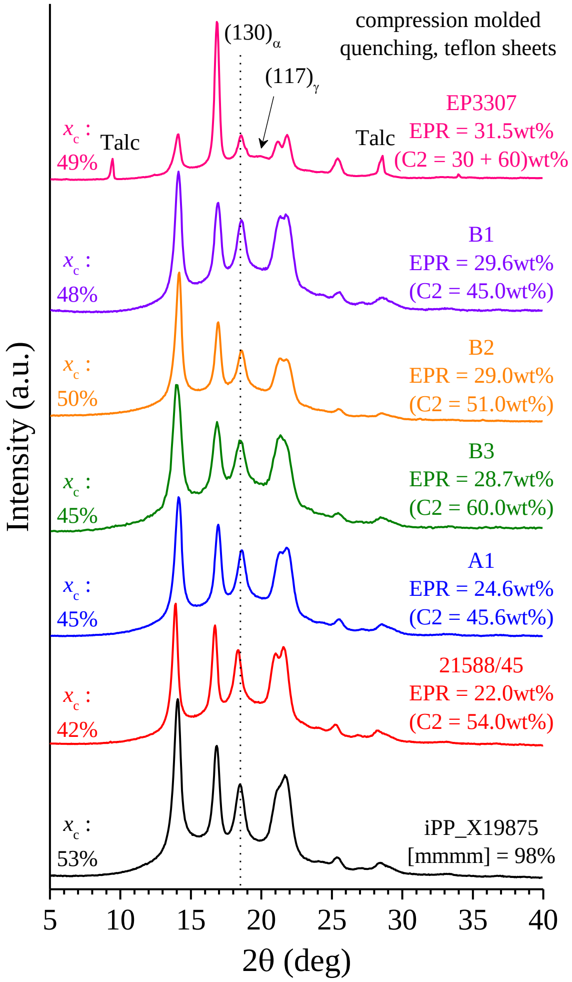

Figure 1.13. X-ray diffraction patterns of the compression molded films of the homopolymer and of all HECO samples obtained by rapidly cooling the melt in an ice/water bath at 10 °C to record stress-strain curves at room temperature. The diffraction profiles were recorded a $T = 25°C$.

Figure 1.14 shows the stress-strain curves of all HECOs recorded at room temperature on films of sample obtained by quenching the melt in an ice/water bath at 10°C. The stress-strain curve of the homopolymer is also shown for comparison. The values of the mechanical parameters evaluated from the stress-strain curves of Figure 1.14 are reported in Table 1.5. Figure 1.15 shows the mechanical parameters as a function of the elastomeric phase content and the ethylene concentration of the EPR.

First of all, from Figure 1.14A, it is possible to see how the different cooling method for obtaining the compression-molded film radically changes the mechanical properties of the homopolymer (compare with Figure 1.8A). Although X-rays profiles (Figures 1.7, 1.13) showed the same α-form crystallinity of iPP, the sample obtained by quenching is much more ductile, strong, and tough with just a slight decrease in the mechanical strength. This result would be attributed to the effect of the cooling rate on the morphology and crystallinity degrees. In fact, the increase of the cooling rate results in smaller and less perfect iPP spherulites.[16-19]

As far as the mechanical properties of HECOs, we can see that the ductility increases with increasing the EPR content but, nevertheless, is intrinsically affected by the ethylene concentration. The strain at break, in fact, decreases as the ethylene concentration increases. However, the ductility of all HECO samples is lower if compared to the mechanical behavior of the neat iPP. This result could be due to the fact that the rubbery particles, in this case, act as an obstacle to the elongation for higher strain values of the thermoplastic matrix.

In addition, it is possible to notice in all stress-strain curves of samples obtained by rapid cooling from the melt, the presence of the yielding point for low strain values ($\varepsilon \approx 10\%$) not observed when the same polymers were obtained by slow cooling from the melt (see Figure 1.8B). This peculiar behavior could arise from the necessity of applying a higher stress to release the macromolecules of the amorphous phase frozen in a glassy domain with a consequent increase of the segmental mobility of the amorphous phase.

In comparison to the homopolymer sample it can be seen that the presence of the rubbery particles, on the one hand, facilitates the onset of the plastic deformation, according to the much lower stress at yielding values exhibited from HECOs than iPP sample (see Table 1.5), but, on the other hand, leads to a decrease in the deformation at break values in comparison to the homopolymer sample. Finally, the values of the Young's modulus decrease with increasing rubbery phase content, and no particular trends are observed as a function of the ethylene concentration.

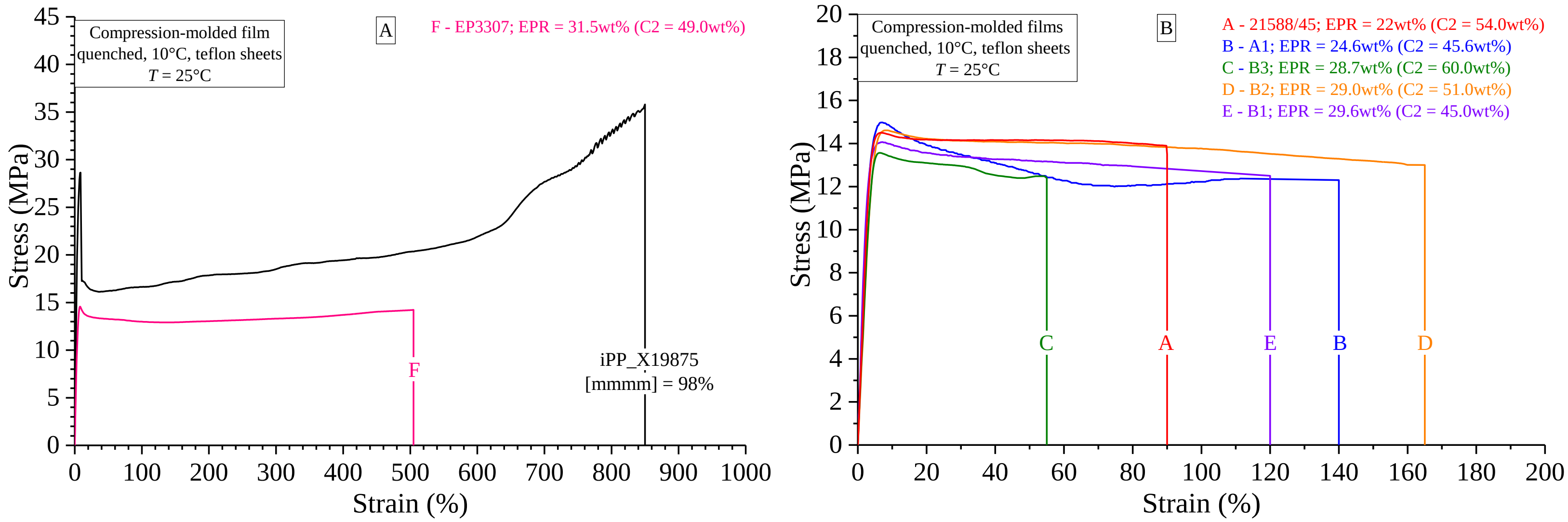

Figure 1.14. Stress-strain curves at *T* = 25°C of compression-molded films of the homopolymer and EP3307 (A) and all HECOs (B) crystallized by quenching the melt down to 10°C.

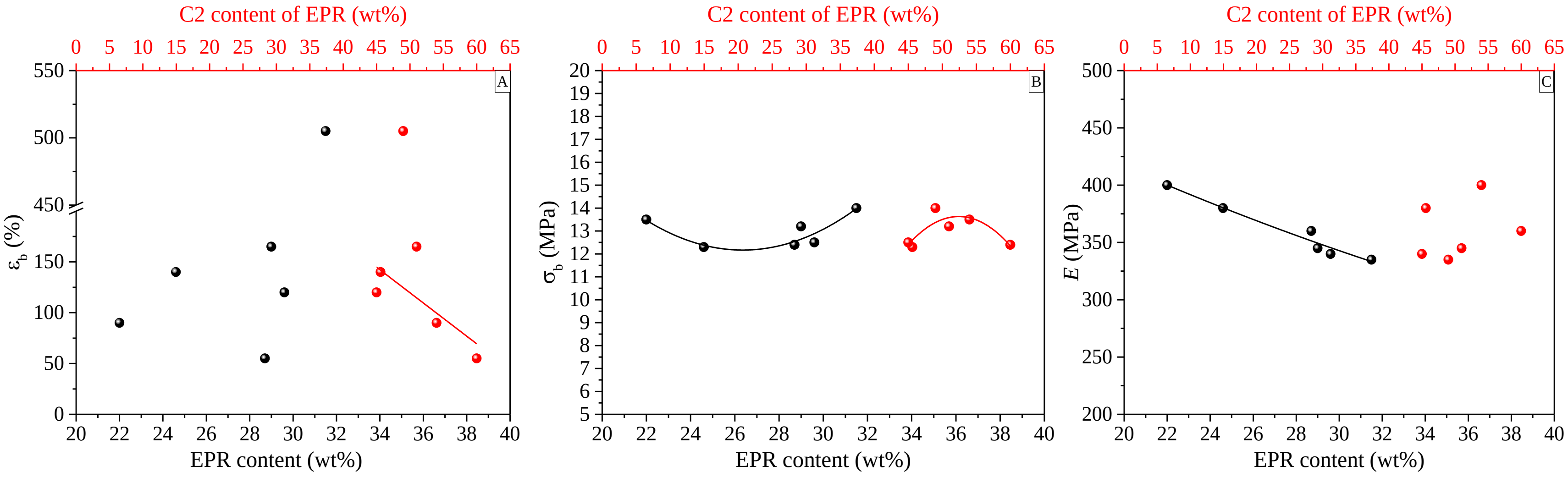

Figure 1.15. Deformation at break (A), stress at break (B), and Young's modulus (C) as a function of the EPR content and of the ethylene concentration of the EPR derived from stress-strain curves reported in Figure 1.14.

Table 1.5. Values of strain (ε_b) and stress (σ_b) at break, Young's modulus (E), strain (ε_y) and stress (σ_y) at the yield point and degree of crystallinity (x_c) of compression-molded films crystallized by quenching the melt down to 10°C of iPP homopolymer and all HECO samples obtained from the analysis at T = 25°C of Figure 1.14.

Sample	EPR (wt%)	C2 (EPR) (wt%)	ε_b (%)	σ_b (MPa)	ε_y (%)	σ_y (MPa)	E (MPa)	x_c[(a)] (%)
iPP	-	-	850 ± 25	36 ± 1	9 ± 1	30 ± 2	665 ± 25	53
21588/45	22.0	54.0	90 ± 25	14 ± 1	7 ± 1	15 ± 1	400 ± 40	42
A1	24.6	45.6	140 ± 50	12 ± 1	7 ± 1	15 ± 1	380 ± 30	45
B3	28.7	60.0	55 ± 25	12 ± 1	7 ± 1	14 ± 1	360 ± 20	45
B2	29.0	51.0	165 ± 40	13 ± 1	8 ± 1	15 ± 1	345 ± 15	50
B1	29.6	45.0	120 ± 20	13 ± 1	7 ± 1	14 ± 1	340 ± 15	48
EP3307	31.5	49.0	505 ± 85	14 ± 1	8 ± 1	15 ± 1	335 ± 25	49

(a) Values evaluated from X-ray diffraction profiles of Figure 1.13.

1.2.5. Structural analysis and mechanical properties recorded at low temperature of samples crystallized by quenching from the melt (ice/water bath and Teflon sheets)

New compression molded films crystallized by quenching from the melt were prepared for recording the stress-strain curves at low temperatures. The X-ray powder diffraction profiles of these new compression molded films obtained by rapid cooling from the melt down to 10°C (quenching samples in a thermostatic ice/water bath) are reported in Figure 1.16. It is worth underlining that all samples were previously placed between two Teflon sheets. Despite the rapid cooling from the melt, the diffraction profiles show that all samples are still crystalline, and they crystallize in the α-form of isotactic polypropylene. Only samples A1 and B1 are less crystalline, and probably contain a small amount of the mesomorphic form, In the diffraction profile of the sample EP3307 the characteristic peaks of talc are still evident.

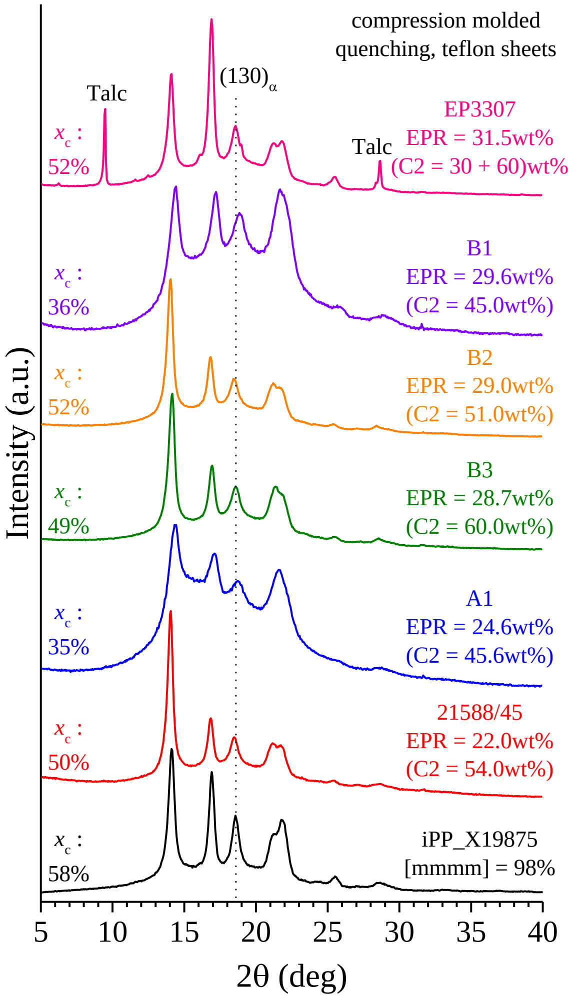

Figure 1.16. X-ray diffraction patterns of the compression molded films of the homopolymer and of all HECO samples obtained by rapidly cooling the melt in an ice/water bath to record stress-strain curves at T = -20°C. The diffraction profiles were recorded a T = 25°C.

Figure 1.17 shows the stress-strain curves recorded at *T* = -20°C of the films obtained by quenching from the melt of the homopolymer and all HECOs (samples of Figure 1.15). The values of the mechanical parameters evaluated from the stress-strain curves of Figure 1.17 are reported in Table 1.6.

The analysis performed at low temperatures on the homopolymer sample shows a completely different behavior with respect to that previously found for the same sample analyzed at room temperature (see Figure 1.14A). In fact, even though the sample has been crystallized by quenching from the melt, it exhibits a very brittle behavior at low temperature, similar to that of the sample obtained by slow cooling from the melt, both at room temperature and at low temperature (see Figures 1.8A and 1.11A).

On the other hand, the stress-strain curves at low temperature of the quenched samples of HECO of Figure 1.17B shows that all the specimens are much more ductile than the homopolymer sample and even more ductile than the analogous quenched HECO samples stretched at room temperature (see Figure 1.14).

Figure 1.18 shows the mechanical parameters obtained from Figure 1.17B as a function of the elastomeric phase content and the ethylene concentration of the EPR. For samples with similar content of the EPR phase, it appears that ε_b values increase for a slight increase of the amount of the elastomeric phase but decrease as the ethylene concentration of the rubbery phase increases. This result could be related to the weak interfacial adhesion between the iPP matrix and PE-like crystals.

The values of stress at break also seem to depend on the concentration of ethylene at low temperatures. In fact, the tensile strength increases as the ethylene content increases, indicating that the presence of long ethylene sequences in macromolecules belonging to the rubbery phase slightly increases the stiffness at -20°C probably because small polyethylene crystals develop under stretching and oppose an additional resistance to the plastic deformation at low temperatures.

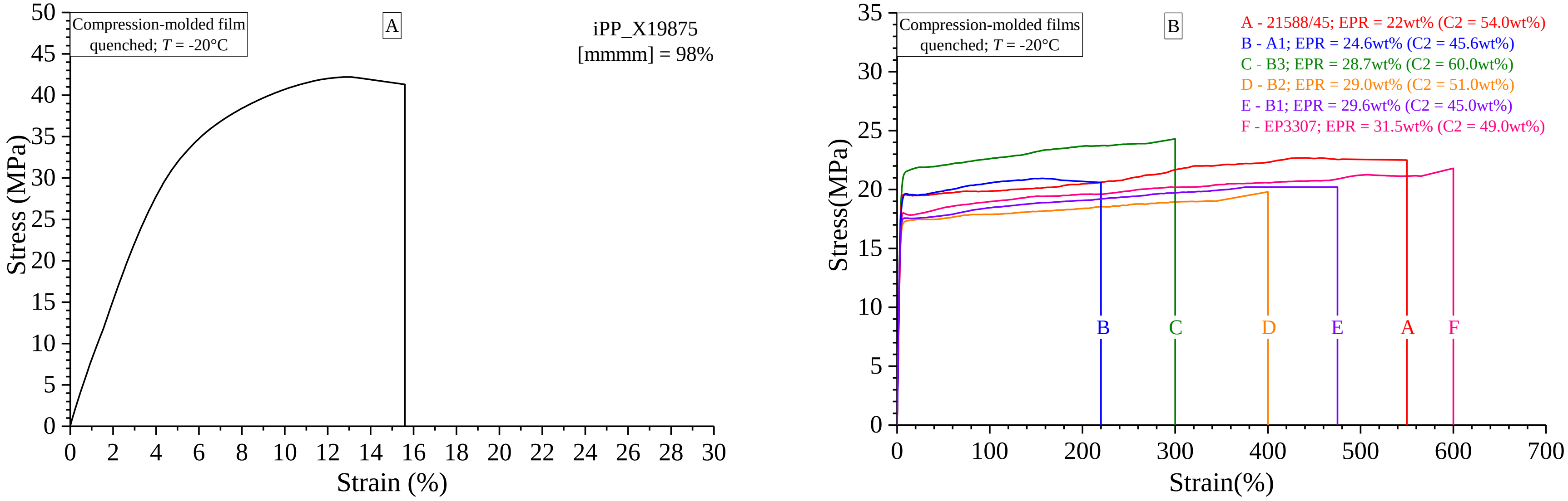

Figure 1.17. Stress-strain curves at *T* = -20°C of compression-molded films of the homopolymer (A) and all HECOs (B) crystallized by quenching the melt down to 10°C.

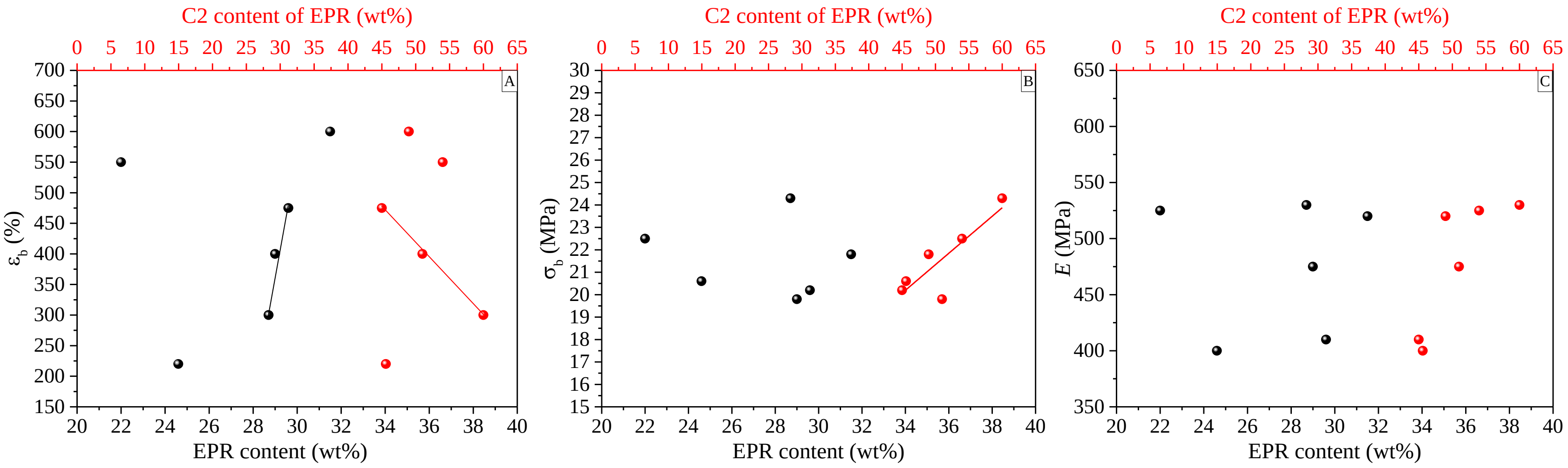

Figure 1.18. Deformation at break (A), stress at break (B), and Young's modulus (C) as a function of the EPR content and of the ethylene concentration of the EPR derived from stress-strain curves reported in Figure 1.17.

Table 1.6. Values of strain (ε_b) and stress (σ_b) at break, Young's modulus (E), strain (ε_y) and stress (σ_y) at the yield point and degree of crystallinity (x_c) of compression-molded films crystallized by quenching the melt down to 10°C of iPP homopolymer and all HECO samples obtained from the analysis at T = -20°C of Figure 1.17.

Sample	EPR (wt%)	C2 (EPR) (wt%)	ε_b (%)	σ_b (MPa)	ε_y (%)	σ_y (MPa)	E (MPa)	x_c[(a)] (%)
iPP	-	-	15 ± 1	41 ± 1	-	-	770 ± 35	58
21588/45	22.0	54.0	550 ± 30	23 ± 1	7 ± 2	20 ± 1	525 ± 50	50
A1	24.6	45.6	220 ± 40	21 ± 1	8 ± 2	20 ± 1	400 ± 50	35
B3	28.7	60.0	300 ± 45	24 ± 2	4.0 ± 0.5	22 ± 1	530 ± 50	49
B2	29.0	51.0	400 ± 105	20 ± 3	3.5 ± 0.5	17 ± 1	475 ± 60	52
B1	29.6	45.0	475 ± 60	20 ± 1	8 ± 1	17 ± 2	410 ± 50	36
EP3307	31.5	49.0	600 ± 80	22 ± 1	7 ± 1	18 ± 1	520 ± 25	52

(a) Values evaluated from X-ray diffraction profiles of Figure 1.16.

1.2.6. Comparison of mechanical properties of slowly cooled and quenched samples (ice/water bath and Teflon sheets) at T = 25°C and T = -20°C

Figure 1.19 shows a comparison of stress-strain curves recorded at room temperature and -20 °C of all HECO samples for films obtained by slow and rapid cooling from the melt. In general, samples obtained by quenching (dash-dotted lines) are more ductile but with lower stresses involved throughout the strain range than the same samples obtained by slow cooling from the melt (solid lines), both at room temperature and at -20 °C. Moreover, the mechanical properties of the samples at T = -20°C (see blue lines) are even improved with respect to the analogous samples deformed at room temperature (see red lines). In fact, all specimens deformed at low temperatures exhibit higher values of strain and stress at break than the same specimens stretched at T = 25°C, both for samples crystallized by slow and rapid cooling from the melt.

So, the tensile analysis showed that all HECO samples not only preserve toughness properties even at low temperature, but in many cases both toughness and ductility improve at low temperature, in addition to also exhibiting an increase in the overall mechanical strength. This surprising result is probably due to the fact that some fractions of the EPR rubbery phase, that exhibit a mechanical behavior with a viscous flow at room temperature, are characterized by a much more deformability without viscous flow at low temperature.

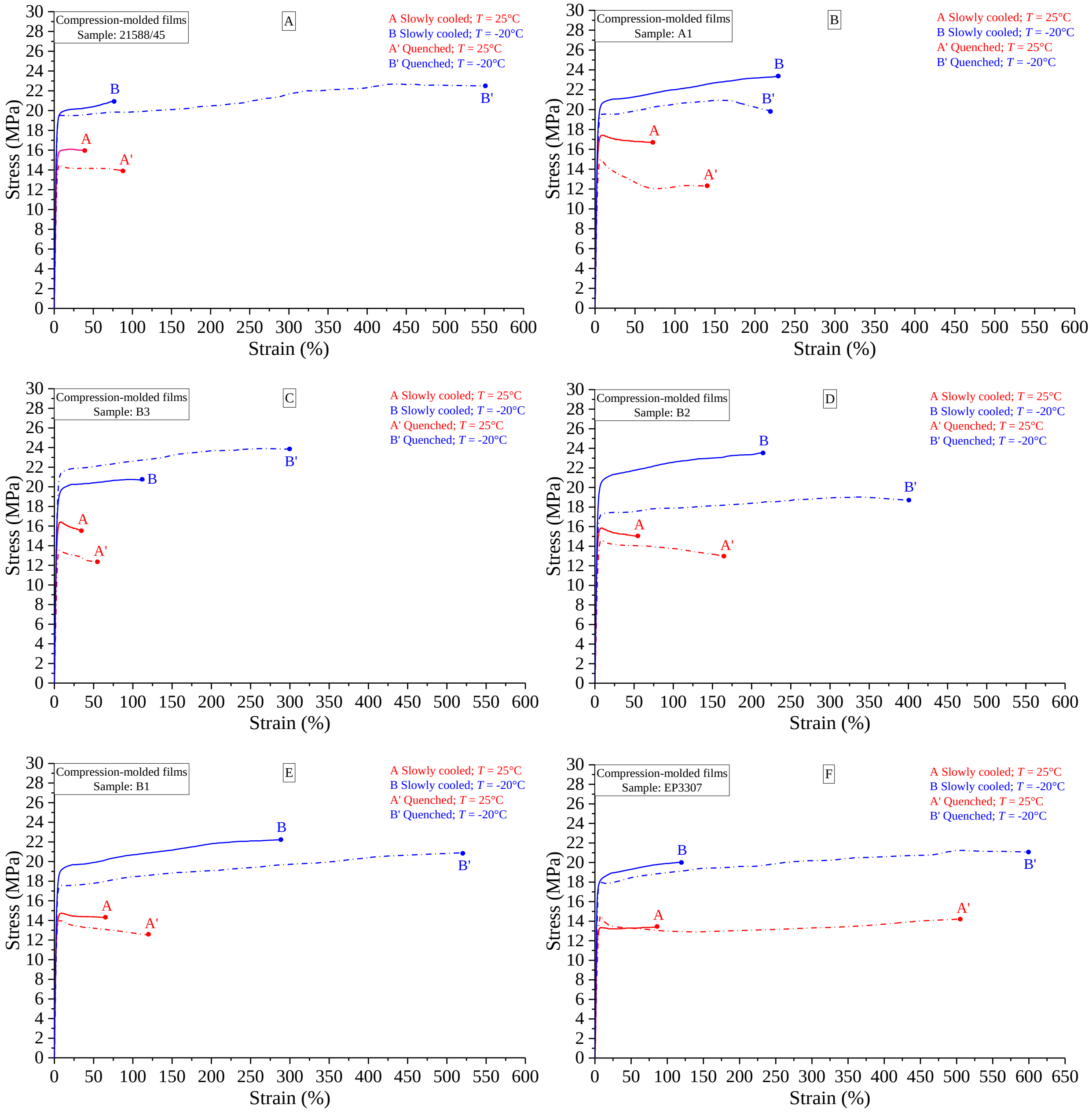

Figure 1.19. Comparison of stress-strain curves at T = 25°C (red lines) and T = -20°C (blue lines) of all compression-molded films of HECOs crystallized by quenching (dash-dotted lines) and slow cooling (solid lines) from the melt.

1.2.7. Structural and thermal analysis and mechanical properties recorded at room temperature of quenched samples crystallized in the mesophase (ice/water bath and sheets of aluminum foil)

It is widely known that iPP crystallizes in the mesomorphic form when the sample is rapidly quenched from the melt to low temperatures (typically 0°C).[20] In fact, under these conditions, the crystallization of the stable α form is prevented and the disordered mesomorphic form is favored.[21] The resulting mesomorphic form exhibits a disordered structure with a degree of order intermediate between that of the α form and the disorder of the amorphous phase. In order to investigate whether the presence of the elastomeric phase had an influence on obtaining the mesomorphic form of iPP, HECO samples, and the homopolymer were placed between two sheets of aluminum foil, placed in the press at $T = 200°C$ for 5 min, and then roughly cooled in an ice-water bath at 10°C. In these conditions, the iPP homopolymer crystallizes in the mesomorphic form.

The X-ray powder diffraction profiles of all compression molded films obtained by quenching the samples from the melt are reported in Figure 1.20. Almost all samples crystallize in the mesomorphic form of the iPP, as indicated by the presence of the two broad reflections at $2\theta = 16$ and 22°, typical of the mesomorphic form. So, unlike the compression-molded films of samples obtained between two Teflon sheets - whose diffraction profiles are shown in Figures 1.13 and 1.16 - films obtained by placing the samples between two aluminum foils crystallize in the mesomorphic form of iPP. This result arises from the fact that aluminum is intrinsically characterized by a high thermal transmission coefficient, which allows effective rapid cooling of the sample from the melt. Nevertheless, although several tests were done both at 10°C and also by quenching the sample in a thermostatic bath at 0°C, the formation of the pure mesomorphic form was not observed for the sample EP3307. This result could be inferred from the presence of talc which probably inhibits the formation of the mesophase and acts as a nucleating agent for the development of α-form crystals.

From Figure 1.20 it is evident that the halo at $2\theta = 22°$ in the diffraction profiles of HECOs is more intense than that in the diffraction profile of the homopolymer. Since the (110) reflection of polyethylene is located in the same 2θ region, this result demonstrates the crystallization of macromolecules belonging to the elastomeric phase containing long ethylene sequences forming PE-like crystals.

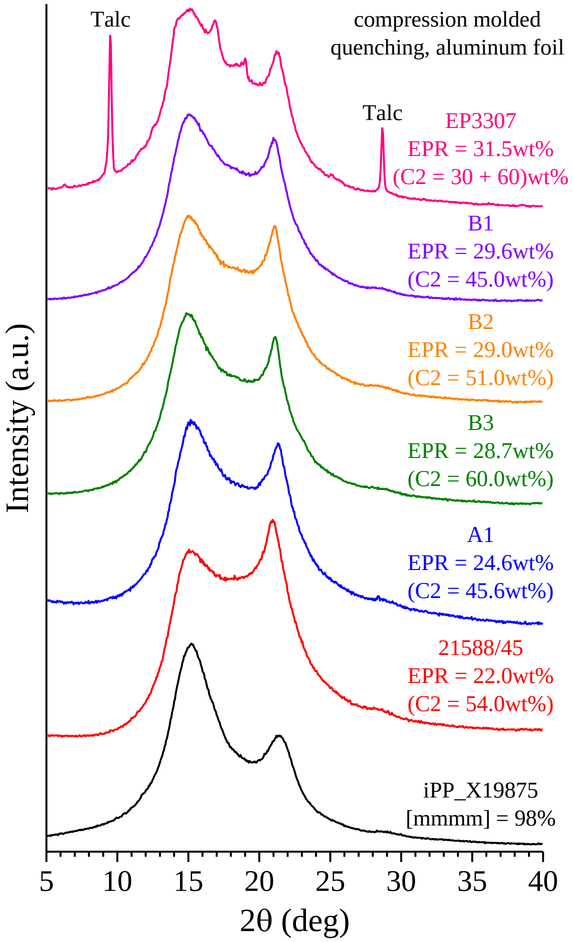

Figure 1.20. X-ray diffraction patterns of the compression molded films of the homopolymer and of all HECO samples obtained by quenching the melt in an ice/water bath and using aluminum foil. The diffraction profiles were recorded a *T* = 25°C.

DSC thermograms of all samples of HECO crystallized in the mesomorphic form of iPP are reported in Figure 1.21. The DSC curves show in all samples the presence of a low-enthalpy endothermic peak at nearly 45°C, a low-enthalpy exothermic peak at 90-100°C, and a high-temperature melting peak (≈ 165°C). The endothermic peak at about 45°C represents the conventional "annealing peak" as a result of the relaxation of the stiff amorphous phase at the interfaces between the mesomorphic domains and the bulk amorphous, and/or due to transition-related processes that occur before the melting of the mesophase and the subsequent recrystallization. The exothermic peak (≈ 90-100°C) corresponds to the mesomorphic-α crystals transition while the high-enthalpy endothermic peak is attributed to the melting of the α-form crystals formed during heating from the mesomorphic form.[22-25]

In addition, especially for samples B2 and B3 with high ethylene concentration and high EPR content, a small endothermic peak due to the melting of defective polyethylene crystals (PE-like) belonging to the elastomeric phase is also visible.

Figure 1.22 shows the melting temperatures and enthalpies as a function of the EPR content and the ethylene concentration of the rubbery phase. The transition temperature and the melting temperature seem not to be dependent on the EPR content and the ethylene concentration.

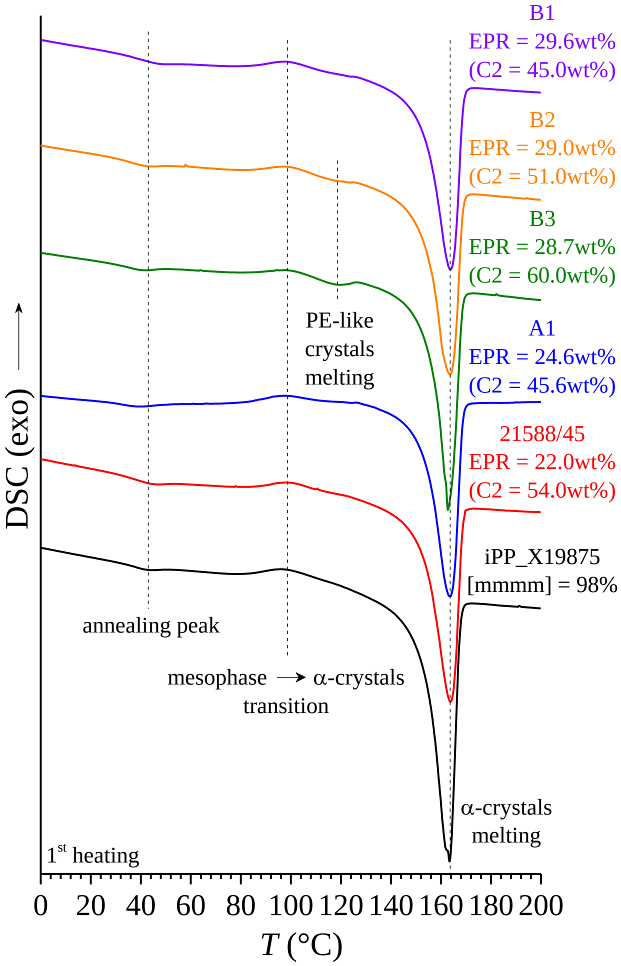

Figure 1.21. DSC thermograms of the compression molded films of the homopolymer and of all HECO samples obtained by quenching the melt in an ice/water bath and using aluminum foil. The thermogram of the sample EP3307 is not showed since the pure mesomorphic form was not obtained.

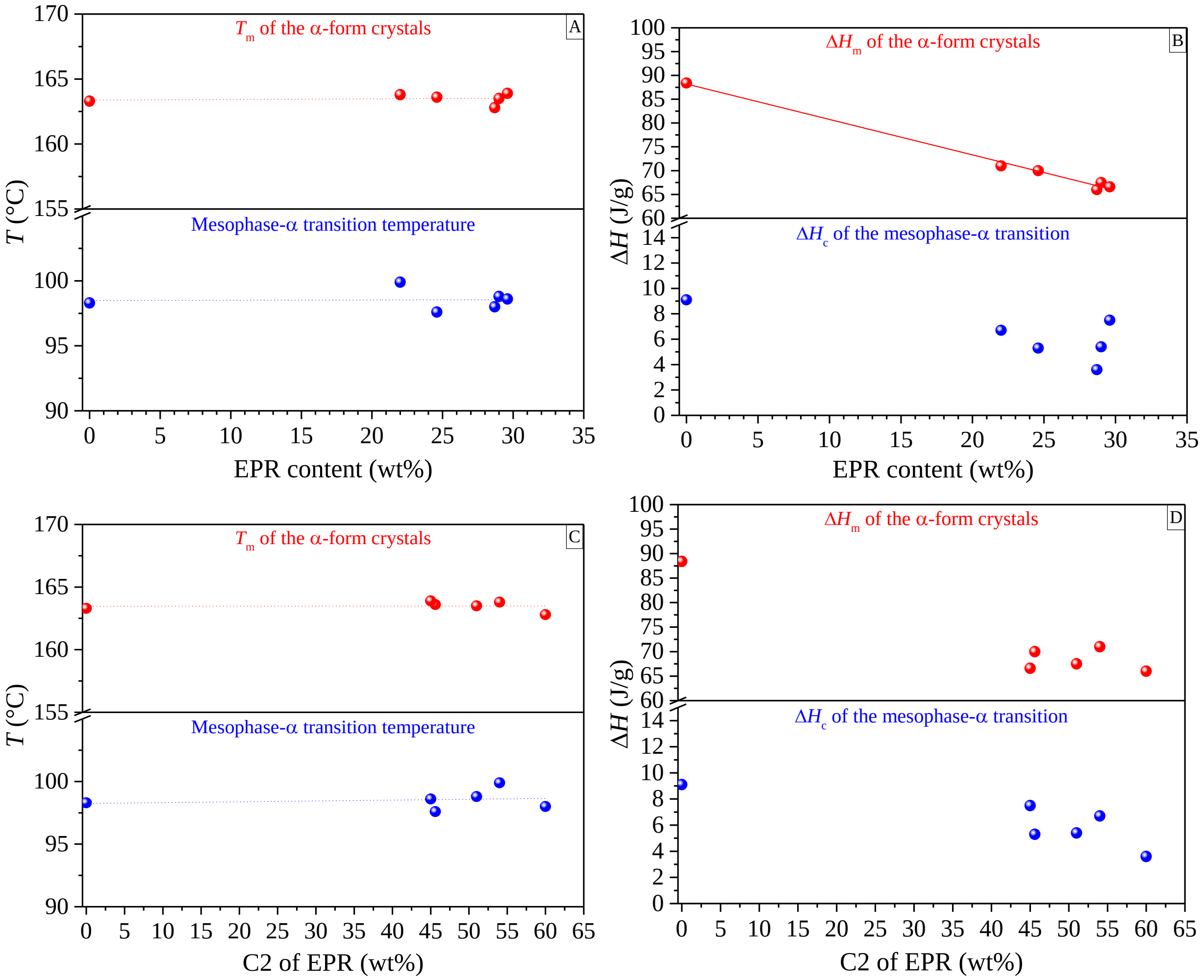

Figure 1.22. Melting and transition temperatures (A,C) and enthalpies (B,D) of the homopolymer and iPP matrix of HECOs as a function of the EPR content (A,B) and of the ethylene concentration of EPR (C,D).

Figure 1.23 shows the stress-strain curves of all samples crystallized in the mesomorphic form of iPP recorded at T = 25°C. The values of the mechanical parameters evaluated from stress-strain curves of Figure 1.23 are reported in Table 1.7. Figure 1.24 shows the mechanical parameters as a function of the elastomeric phase content and the ethylene concentration of the EPR. The analysis of mechanical properties shows that all the samples are very ductile with strain-at-break values between 500 and 900% and that the HECO samples are less ductile and with lower stress involved throughout the deformation range than the homopolymer. As expected, the presence of the rubbery phase produces lower values of stress. Moreover, the lower ductility of the mesophase in the HECO compared to the homopolymer could be related to the presence of the EPR phase and the consequent presence of phase-separated domains.

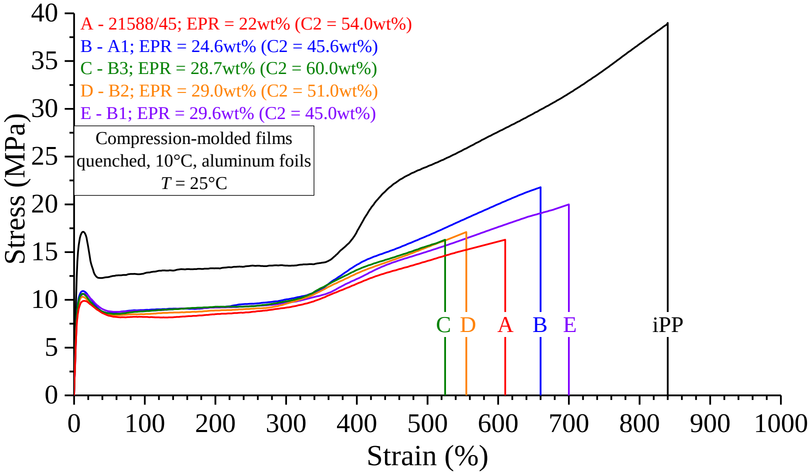

Figure 1.23. Stress-strain curves at *T* = 25°C of compression-molded films of the homopolymer and all HECOs crystallized in the mesomorphic form. The stress-strain curve of the sample EP3307 was not recorded since the pure mesomorphic form was not obtained.

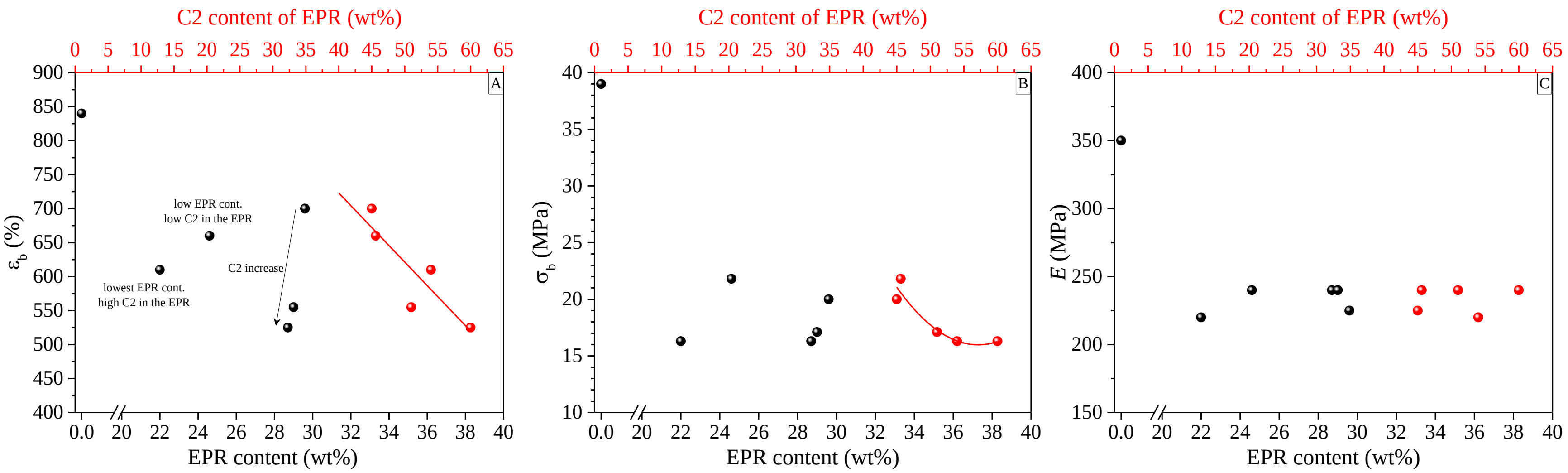

Figure 1.24. Deformation at break (A), stress at break (B), and Young's modulus (C) as a function of the EPR content and of the ethylene concentration of the EPR derived from stress-strain curves reported in Figure 1.23.

Table 1.7. Values of strain (ε_b) and stress (σ_b) at break, Young's modulus (*E*), strain (ε_y) and stress (σ_y) at the yield point of compression-molded films crystallized in the mesomorphic form of all HECO samples obtained from the analysis at *T* = 25°C of Figure 1.23.

Sample	EPR (wt%)	C2 (EPR) (wt%)	ε_b (%)	σ_b (MPa)	ε_y (%)	σ_y (MPa)	*E* (MPa)
iPP	-	-	840 ± 60	39 ± 4	13 ± 1	17 ± 1	350 ± 15
21588/45	22.0	54.0	610 ± 60	16 ± 1	14 ± 1	10 ± 1	220 ± 5
A1	24.6	45.6	660 ± 40	22 ± 1	13 ± 1	11 ± 1	240 ± 5
B3	28.7	60.0	525 ± 25	16 ± 1	12 ± 1	11 ± 1	240 ± 5
B2	29.0	51.0	555 ± 25	17 ± 1	12 ± 1	10 ± 1	240 ± 5
B1	29.6	45.0	700 ± 40	20 ± 1	15 ± 1	11 ± 1	225 ± 5

1.3. Study of the crystal morphology by Polarized Optical Microscopy (POM)

In this section a study of the crystal morphology of the homopolymer sample and all HECOs with different content of the elastomeric phase and different ethylene concentration of the EPR by using polarized optical microscopy (POM) will be discussed. For POM analysis, a small amount of the sample was sandwiched between two optical microscopy coverslips and then melted onto a hot-stage Kofler, in order to obtain films of the thickness ≈ 500-800μm. Successively, in order to understand the differences in the mechanical behavior reported in Figures 1.8 and 1.14, samples were subjected to two different crystallization procedures to obtain specimens slowly cooled from the melt and by quenching.

To ensure that samples crystallized slowly from the melt, the following temperature program was adopted through the use of a Linkam hot-stage:

- Heating up to 200°C at 10°C/min heating rate;
- Cooling down to 25°C at 5 °C/min cooling rate.

On the other hand, to rapidly crystallize samples from the melt, after melting the sample on the Kofler hot-stage, the coverslips were quickly dipped in an ice-water bath at 10°C.

1.3.1. Crystal morphology of samples slowly cooled from the melt

Polarized optical microscopy (POM) images of samples of iPP homopolymer and of HECO slowly crystallized from the melt at cooling rate of 5 °C/min are reported in Figures 1.25-1.27 at two different magnifications 20X (Figures 1.25A-C - 1.26A-C - 1.27A) and 40X (Figures 1.25A'-C' - 1.26A'-C' - 1.27A'). POM images of the homopolymer show that the sample crystallizes in the classic spherulitic morphology typical of a highly stereoregular iPP sample. On the other hand, POM images of HECOs reveal that all samples form spherulites with irregular boundaries and shapes and, in general, these spherulites have roughly the same size of those of the homopolymer. However, unlike the morphology of the pure iPP sample, all HECO samples show more or less circular dark areas, probably corresponding to non-birefringent particles. Such particles could presumably be attributed to the amorphous fractions of the elastomeric phase. Overall, no banded spherulites appear due to PE crystallization, indicating that the rubbery phase does not contain very long ethylene sequences able to crystallize independently.

iPP [mmmm] = 98%

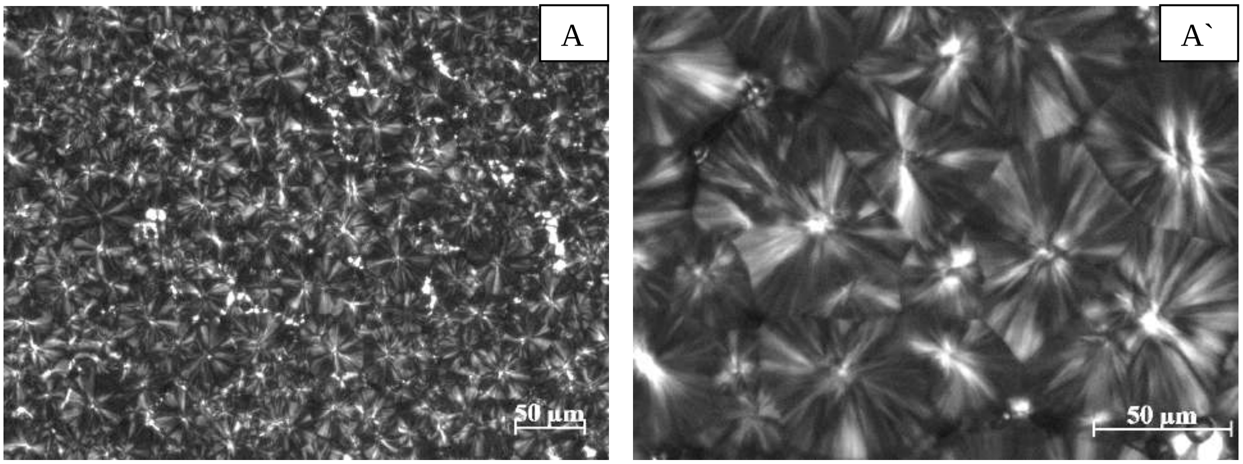

21588/45; EPR = 22wt%, C2(EPR) = 54.0wt%

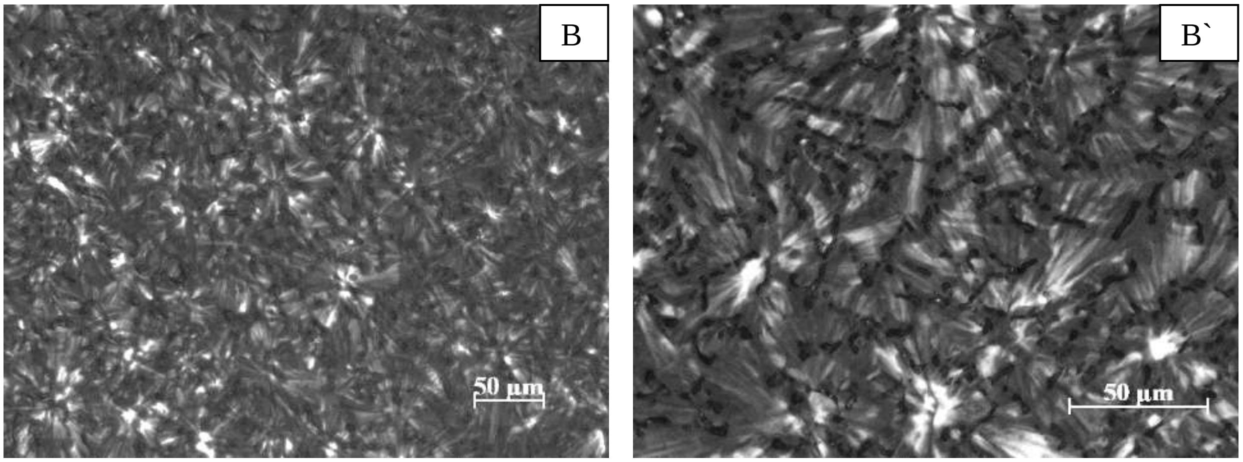

A1; EPR = 24.6wt%, C2(EPR) = 45.6wt%

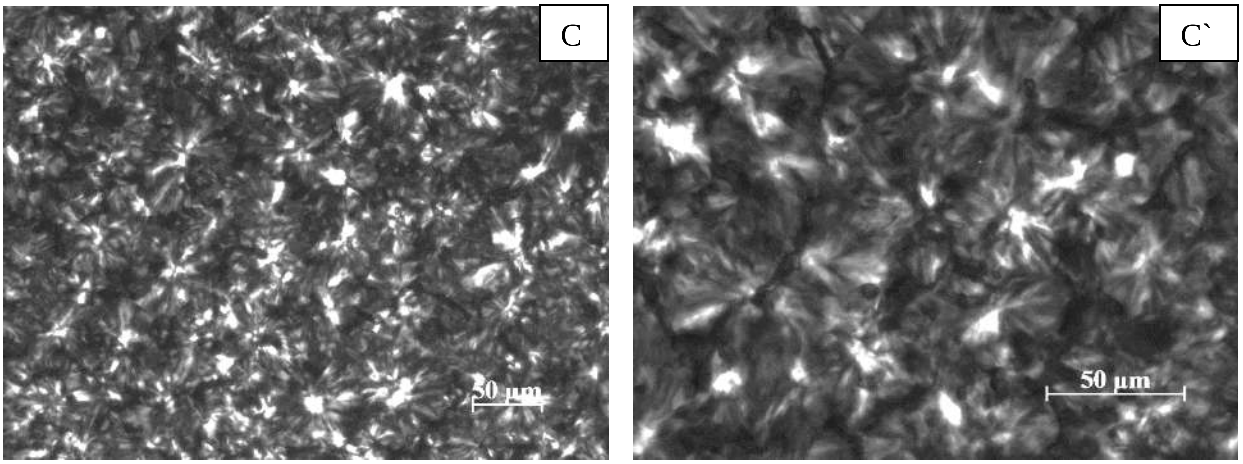

Figure 1.25. POM images of slowly cooled homopolymer sample (A,A'), and HECO samples 21588/45 with EPR = 22.0wt% and C2(EPR) = 54.0wt% (B,B'), and A1 with EPR = 24.6wt% and C2(EPR) = 45.6wt% (C,C'). The dashed letters refer to the highest magnification images.

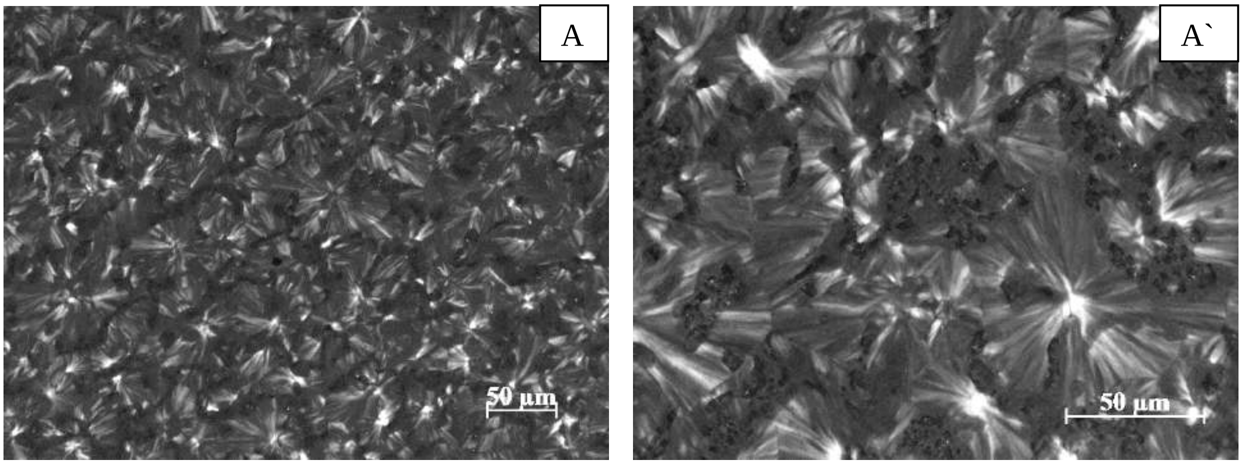
B3; EPR = 28.7wt%, C2(EPR) = 60.0wt%

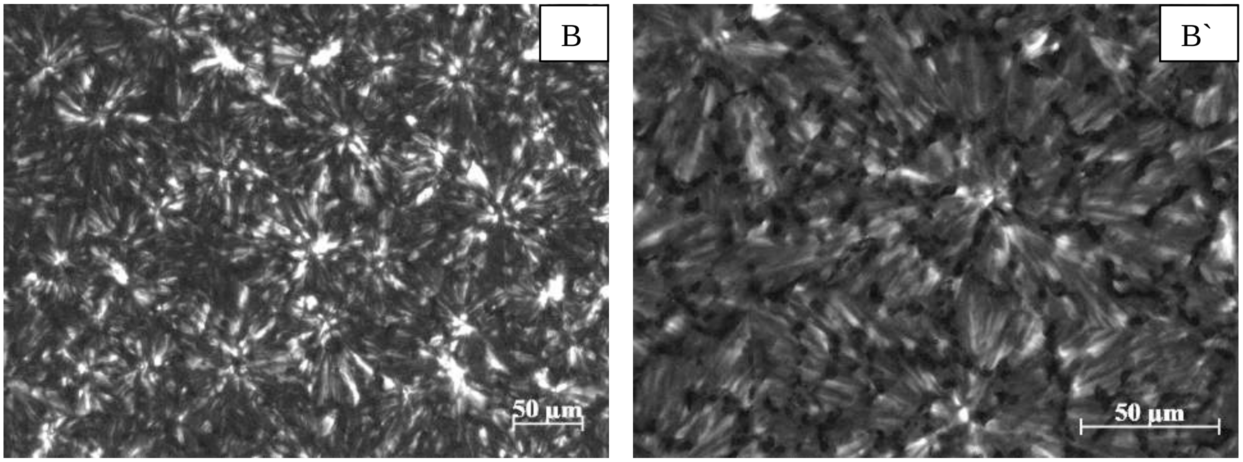
B2; EPR = 29.0wt%, C2(EPR) = 51.0wt%

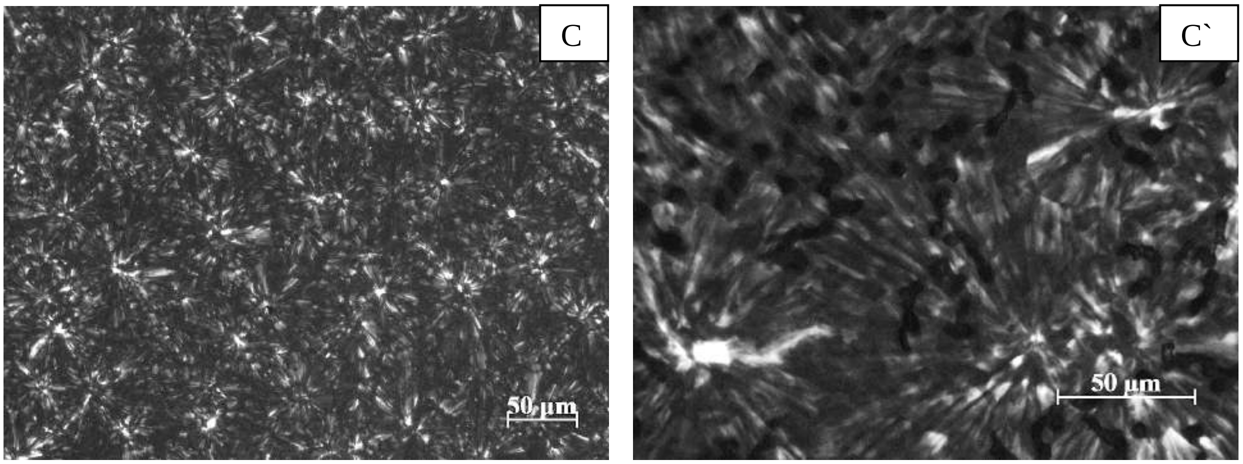
B1; EPR = 29.6wt%, C2(EPR) = 45.0wt%

Figure 1.26. POM images of slowly cooled HECO samples B3 with EPR = 28.7wt% and C2(EPR) = 60.0wt% (A,A'), B2 with EPR = 29.0wt% and C2(EPR) = 51.0wt% (B,B'), and B1 with EPR = 29.6wt% and C2(EPR) = 45.0wt% (C,C'). The dashed letters refer to the highest magnification images.

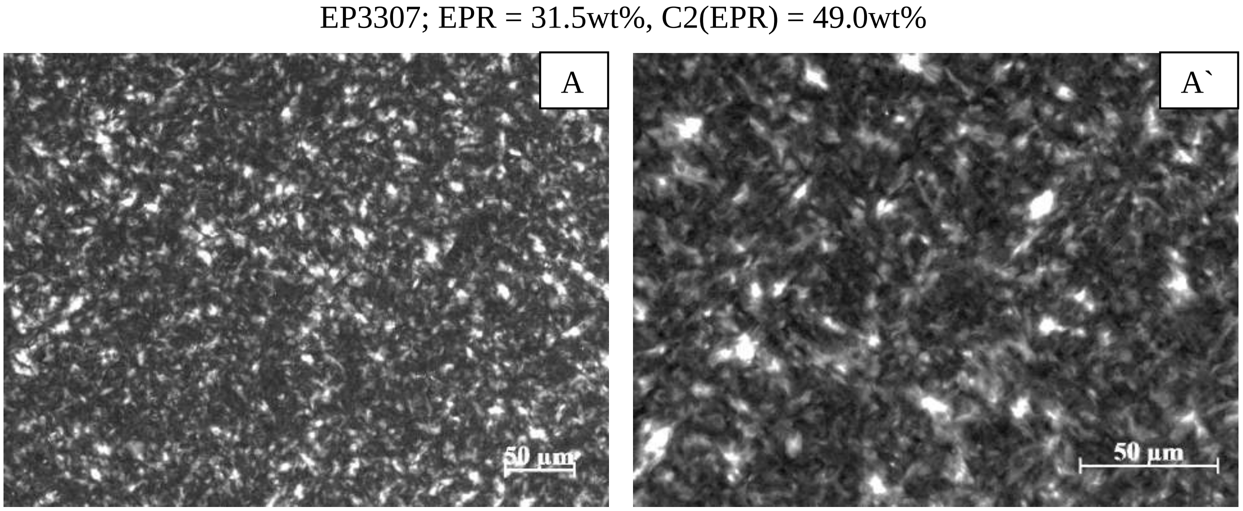

Figure 1.27. POM images of slowly cooled HECO sample EP3307 with EPR = 31.5wt% and C2(EPR) = 49.0wt% (A,A’). The dashed letter refers to the highest magnification image.

1.3.2. Crystal morphology of samples crystallized in the α form by quenching

POM images of samples of the iPP homopolymer and of HECO quenched from the melt in a thermostatic ice-water bath at 10°C are reported in Figures 1.28-1.30 at two different magnifications 20X (Figures 1.28A-C - 1.29A-C – 1.30A) and 40X (Figures 1.28A’-C’ - 1.29A’-C’ - 1.30A’). These samples are crystallized in the α form of iPP, as the samples of the Figure 1.13. The POM images of all samples show the presence of needle-like crystals (best seen in 40X magnification images), with the presence of small needle-shaped entities that are more or less birefringent. However, for the sample EP3307, very small crystalline entities with little birefringence are observed, along with birefringent spots probably attributable to the presence of additives. Since X-ray analysis showed the presence of talc (see Figure 1.4), these spots can most likely be ascribed to the presence of this filler.

iPP [mmmm] = 98%

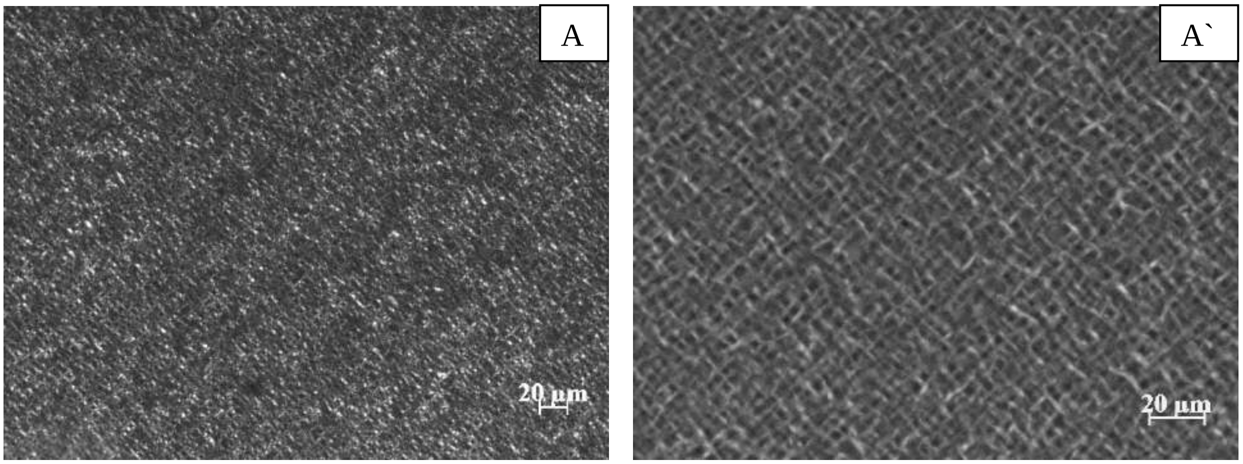

21588/45; EPR = 22wt%, C2(EPR) = 54.0wt%

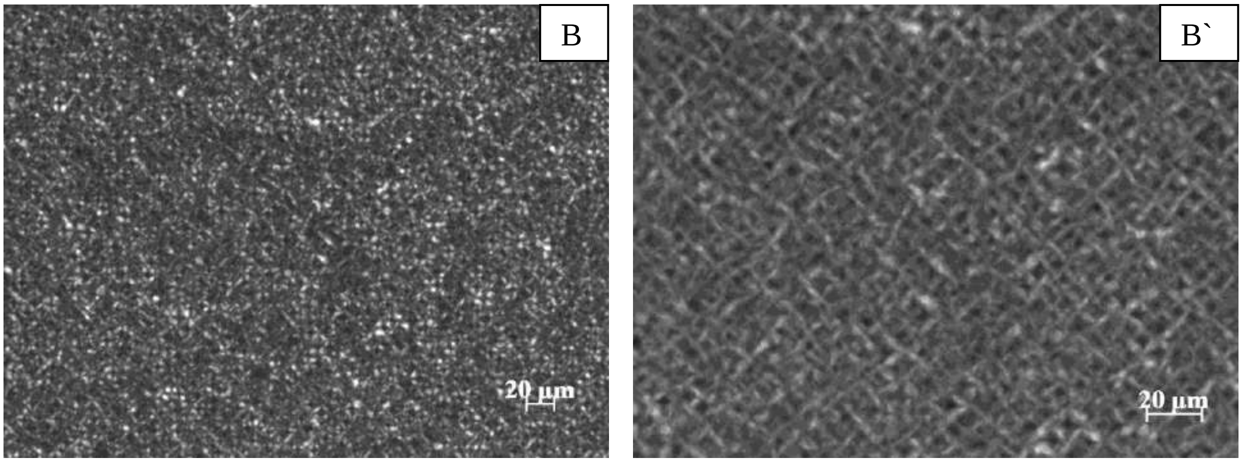

A1; EPR = 24.6wt%, C2(EPR) = 45.6wt%

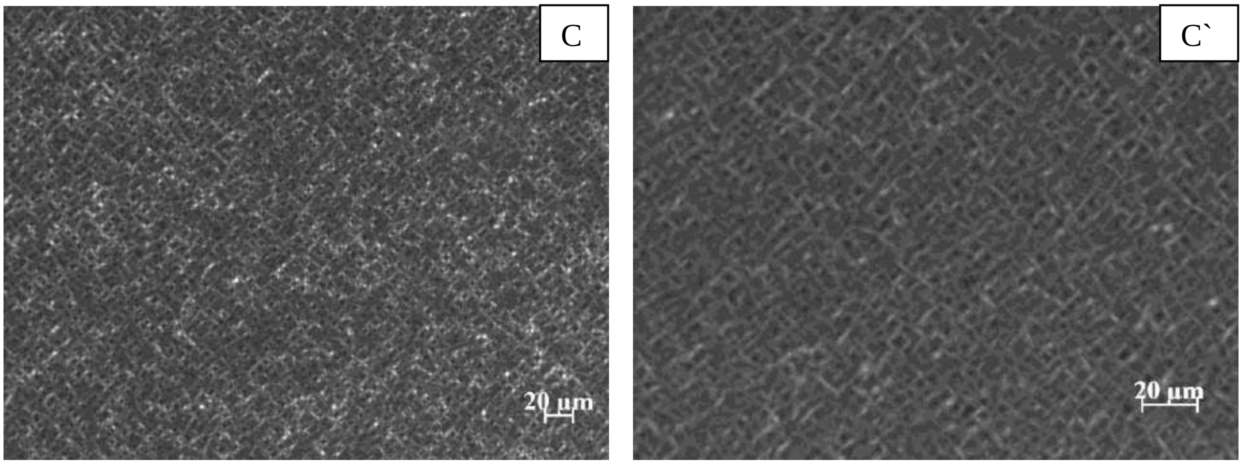

Figure 1.28. POM images of quenched homopolymer sample (A,A’), and HECO samples 21588/45 with EPR = 22.0wt% and C2(EPR) = 54.0wt% (B,B’), and A1 with EPR = 24.6wt% and C2(EPR) = 45.6wt% (C,C’). The dashed letters refer to the highest magnification images.

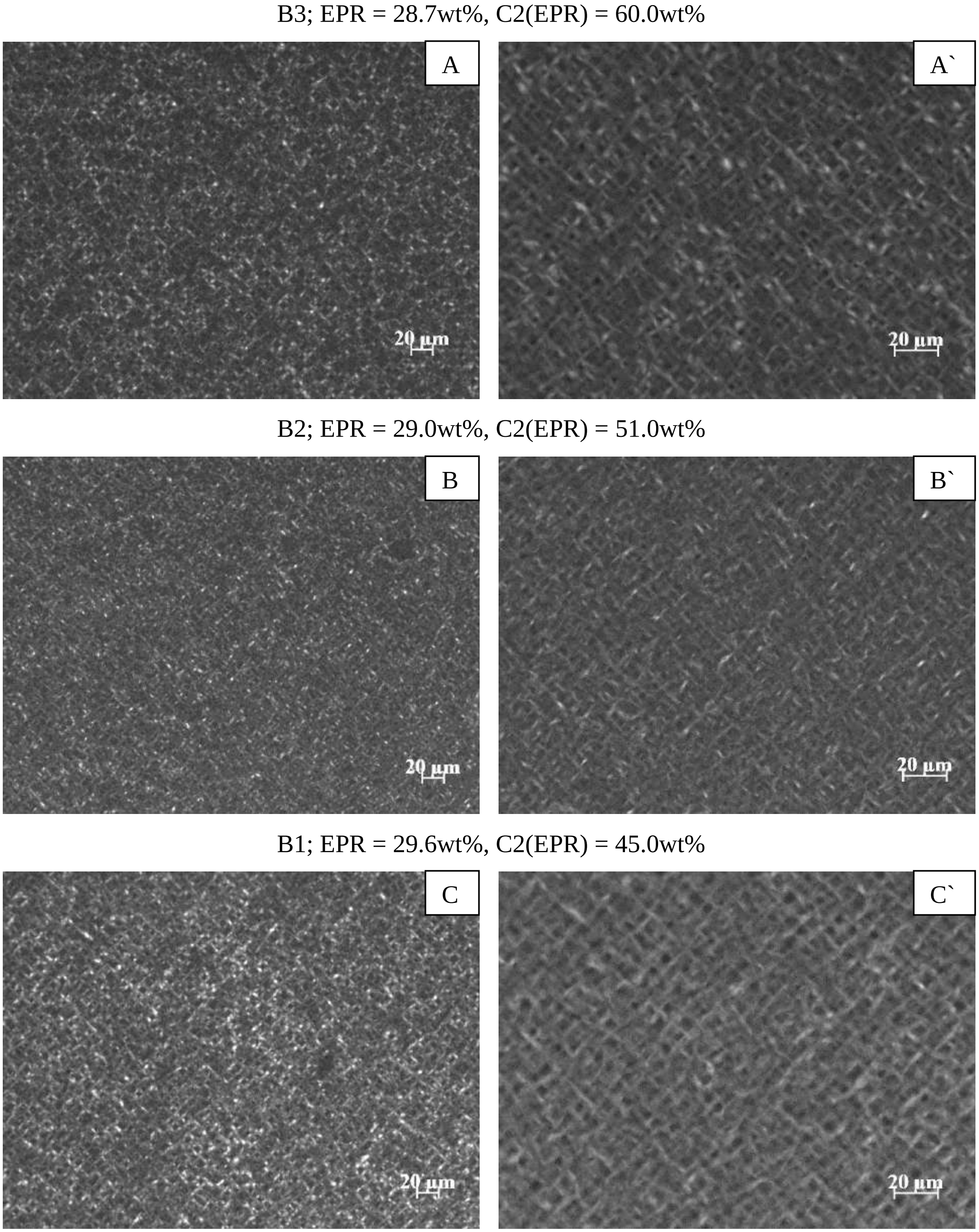

Figure 1.29. POM images of quenched HECO samples B3 with EPR = 28.7wt% and C2(EPR) = 60.0wt% (A,A'), B2 with EPR = 29.0wt% and C2(EPR) = 51.0wt% (B,B'), and B1 with EPR = 29.6wt% and C2(EPR) = 45.0wt% (C,C'). The dashed letters refer to the highest magnification images.

EP3307; EPR = 31.5wt%, C2(EPR) = 49.0wt%

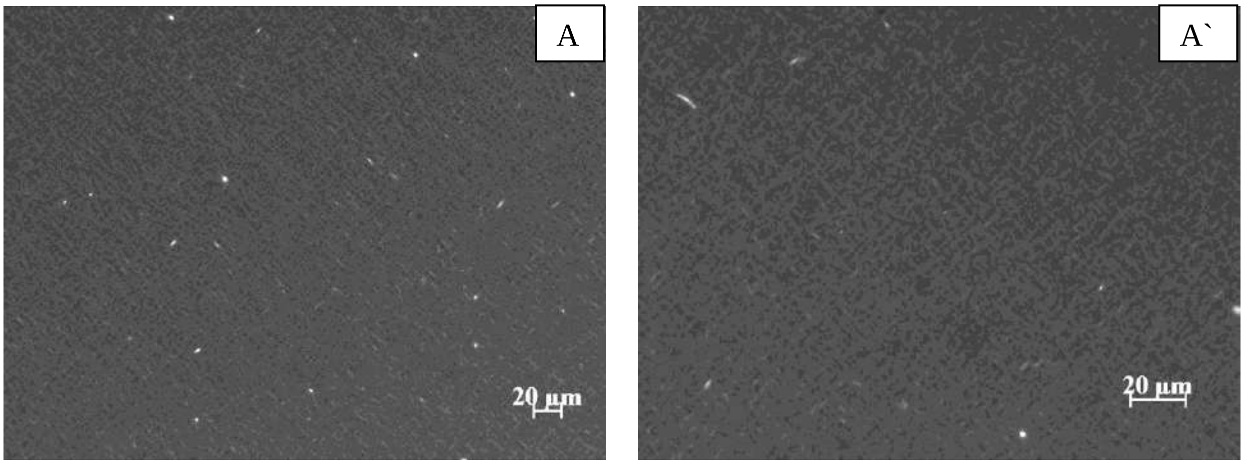

Figure 1.30. POM images of quenched HECO sample EP3307 with EPR = 31.5wt% and C2(EPR) = 49.0wt% (A,A'). The dashed letter refers to the highest magnification image.

Through the morphological analysis, we can be able to explain the difference in the mechanical behavior of samples crystallized by the two different cooling methods described above. In fact, since samples obtained by quench exhibit a needle-like morphology and are also less crystalline (given the lower birefringence and low values of crystallinity degrees shown in Tables 1.4,1.6), they present higher ductility and lower mechanical strength than samples that crystallize in the spherulitic morphology and with higher values of crystallinity degrees (see Tables 1.3,1.5).

Overall, the main result of the POM analysis is that the presence of the rubbery phase does not greatly influence the morphology of iPP at least regarding the size of the crystalline structures. In fact, in the case of samples obtained by slow cooling the melt, large spherulites are obtained. Moreover, in the case of samples crystallized by quenching the melt, the formation of needle-like crystals, typical of samples rapidly crystallized from the melt, is not disturbed by the presence of the elastomeric phase. At the same time, for samples obtained by slow cooling from the melt, the addition of the EPR phase resulted in a less regular spherulite texture with less sharp spherulite boundaries.

PARAGRAPH 1.4, PAGES 60-87 : EMBARGOED

1.5. Study of crystallization kinetics by Fast Scanning Chip Calorimetry (FSC)

In order to verify whether the presence of the EPR copolymer influences the crystallization kinetics of iPP, isothermal and non-isothermal crystallization experiments were carried out by fast scanning chip calorimetry (FSC) technique.

Mettler Toledo's power-compensation differential scanning chip calorimeter Flash DSC 1 was used to analyze the crystallization behavior of all samples (Greifensee, Switzerland). The Huber TC100 Intracooler (Offenburg, Germany) was linked to the main instrument, allowing the sensor-support temperature to be controlled at -90°C for investigations requiring fast cooling. At a flow rate of 40 mL/min, nitrogen gas was used to purge the sample environment. Using an SLEE rotary microtome (Mainz, Germany), samples were obtained by microtoming portions with a thickness of 8μm from the available pellets. Using a scalpel and a stereomicroscope, the sections' lateral sizes were then decreased to 50–100μm before being adhered to the UFS 1 sensor's membrane. A tiny piece of gold leaf atop a thin silicone-oil film was used as the contact medium to increase the thermal contact between the sensor membrane and the sample, thereby allowing for sample shrinkage and expansion without placing pressure on the membrane.[26] According to the instrument operating instructions, the sensor was calibrated, and the temperature was adjusted before the samples were applied. Crystallization was examined using FSC in the cooling range of 1-3000 K/s for non-isothermal experiments and at temperatures between 0-110°C for isothermal crystallization measurements.

1.5.1. Non-isothermal crystallization experiments

The homopolymer and all HECOs sets of rate-normalized FSC cooling and successive heating curves are shown in Figures 1.55-1.61 as examples of the non-isothermal crystallization studies that were carried out. Red, green, and blue color coding are used to identify or mark the various phase transitions for the formation of iPP α-crystals, iPP mesophase formation, and crystallization of macromolecules rich in long ethylene sequences (EPC particles), respectively. In order not to lose important visual information about the crystallization processes involved in all samples, the strategy of showing a limited number of curves recorded at different cooling rate values for all cooling thermograms was chosen. However, for the heating curves, the thermograms recorded at the heating rate of 1000 K/s, after the cooling processes were performed in the cooling range of 1 to 3000 K/s, are shown. The values of the peak crystallization temperatures evaluated from

Figures 1.55A-1.61A, and the normalized enthalpy of melting evaluated from Figures 1.55B-1.61B, are reported in Figures 1.55C,D-1.61C,D as a function of the cooling rate. This last information (normalized enthalpy of melting) was gathered by integrating the FSC-heating curves that covered the final α-crystals melting, the mesophase to α-crystal transition, and the iPP mesophase formation. Because of the difficulty in isolating its contribution, integration also includes the melting phenomenon of the EPC particles in the case of HECO samples. Data are, then, normalized in the range 0-1 because the mass of FSC samples is unknown.

In the case of the iPP sample (Figure 1.55A), slow cooling at rates up to about 500 K/s allows only the formation of α-crystals, and the crystallization temperature decreases with the increasing cooling rate (Figure 1.55C). In the 200-700 K/s cooling rate range, a further exothermic phenomenon can be seen at lower temperatures. In fact, if the formation of α-crystals at high temperatures is incomplete, further cooling allows the formation of the mesophase in the range temperature 5-25°C with temperature values increasing as the cooling rate decreases. However, the transition enthalpy of the mesophase formation process is rather low and for higher cooling rates smoothly overlaps the glass transition at the low-temperature side. When cooling the melt faster than 700 K/s any ordering process is suppressed.

Regarding HECO samples, it is possible to detect separated exothermic phenomena corresponding to the crystallization of the iPP matrix and ethylene-propylene crystalline (EPC) particles (Figures 1.56A-1.61A). The iPP-matrix crystallizes qualitatively like the homopolymer, at least in case of low cooling rates up to around 100 K/s. Nevertheless, for almost all HECOs, from the cooling rate of 80 K/s and up to 400 K/s it is possible to notice an exothermic phenomenon in the 40-50°C temperature range, which in the case of the homopolymer is absent or at least hidden in the broad crystallization peak. This phenomenon could still be associated with the formation of α-crystals of the thermoplastic matrix in agreement with the fact that as the cooling rate increases the enthalpy of the peak at higher temperatures (≈ 75°C) decreases while that of the peak at lower temperatures (≈ 45°C) increases. Indeed, this is not the only possible explanation. In fact, since these samples derive from a synthesis process that uses Ziegler-Natta catalysts, there could be fractions of macromolecules belonging to the EPR copolymer rich in long propylene sequences that could crystallize. We do not exclude that these low-temperature crystallization phenomena could be associated with the formation of more imperfect α-crystals belonging to the C3C2 copolymer dispersed in the thermoplastic matrix.

In any case, from the rate of 200-300 K/s, α-crystals formation is incomplete, and further cooling allows the formation of the mesophase, whose enthalpy increases against that associated with the crystallization of the α-form crystals. Nevertheless, for samples B3 and EP3307, the mesophase formation at around room temperature is not observed during the cooling, indicating that all macromolecules capable of crystallizing during cooling, form α-crystals. Overall, for further increases in cooling rate and for values above 700 K/s, any ordering process is suppressed for the iPP matrix but not for the crystalline components (EPC) present in the EPR throughout the examined cooling rate range.

The data of Figure 1.55B-1.61B serve as examples demonstrating the different crystallization and melting behaviors of neat iPP and heterophasic copolymers. In the case of the homopolymer, fast cooling completely suppressed crystallization and ordering processes. For this reason, subsequent heating to above the glass transition temperature first causes exothermic mesophase formation at around 30°C, followed by exothermic transformation of the mesophase into α-crystals at around 100°C and finally endothermic melting of the crystals formed during heating. Decreasing the cooling rate to below about a few hundred K/s allows crystallization and ordering during cooling, and consequently, on subsequent heating, the mesophase formation at around 30°C is reduced until it disappears completely for cooling rate values of 200 K/s.

Qualitatively similar behavior is detected for the iPP-matrix in the heterophasic samples. However, in addition to the iPP-matrix-related transitions, additional melting occurs around 120°C, associated with the presence EPC particles.

Figures 1.55D-1.61D confirm this observation. In fact, for high cooling rates, the homopolymer sample exhibits zero global enthalpy values, indicating that there is no crystalline organization after cooling the melt. As the cooling rate decreases, the formation of α-form crystals is promoted, and the enthalpy increases until it reaches the maximum value. However, in the case of the heterophasic copolymer samples, for high values of cooling rate, the value of ΔH_m is not zero. We argue this result by taking into consideration the presence of the crystalline components belonging to the rubbery phase (EPC). In fact, since the crystallization of these macromolecules is never suppressed even for high cooling rates, during the subsequent heating scans there is a contribution to the overall enthalpy from the melting peak of the EPC that causes the enthalpy to be nonzero.

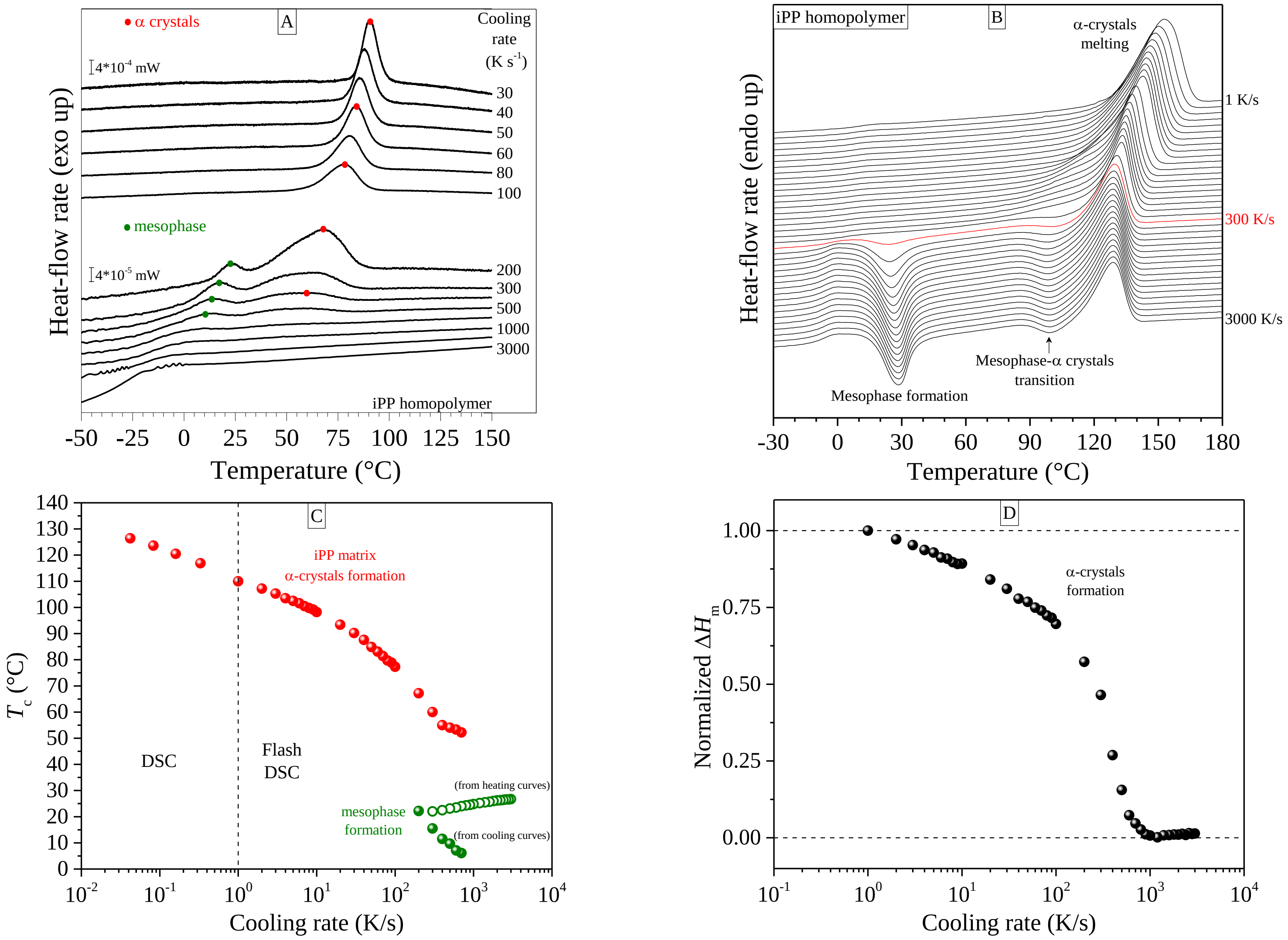

Figure 1.55. Sets of rate-normalized FSC cooling curves, with the exothermic heat-flow rate directed upwards (A) and successive FSC heating curves recorded at 1000 K/s with the exothermic heat-flow rate directed downwards (B) of the homopolymer sample. In picture B, the values 1, 300, and 3000K/s indicate, as an example, the cooling rates used in the previous cooling steps. Peak crystallization temperature (C) and normalized overall enthalpy of melting (D) as a function of the cooling rate. T_c values obtained from independent classic DSC experiments at four different cooling rates are also shown in picture C.

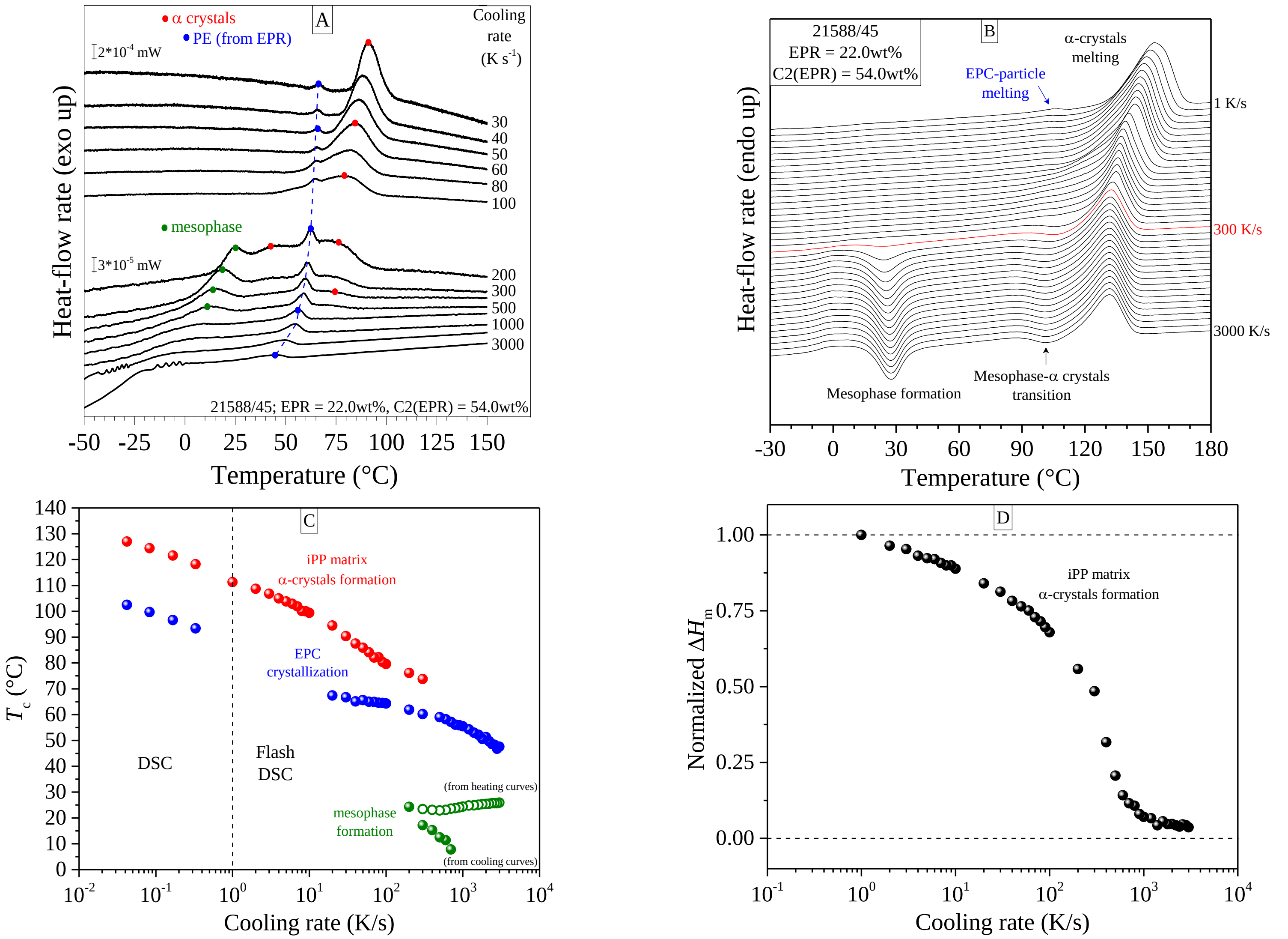

Figure 1.56. Sets of rate-normalized FSC cooling curves, with the exothermic heat-flow rate directed upwards, (A) and successive FSC heating curves recorded at 1000 K/s with the exothermic heat-flow rate directed downwards, (B) of the HECO sample 21588/45. In picture B, the values 1, 300, and 3000K/s indicate, as an example, the cooling rates used in the previous cooling steps. Peak crystallization temperature (C) and normalized overall enthalpy of melting (D) as a function of the cooling rate. T_c values obtained from independent DSC experiments at four different cooling rates are also shown in picture C.

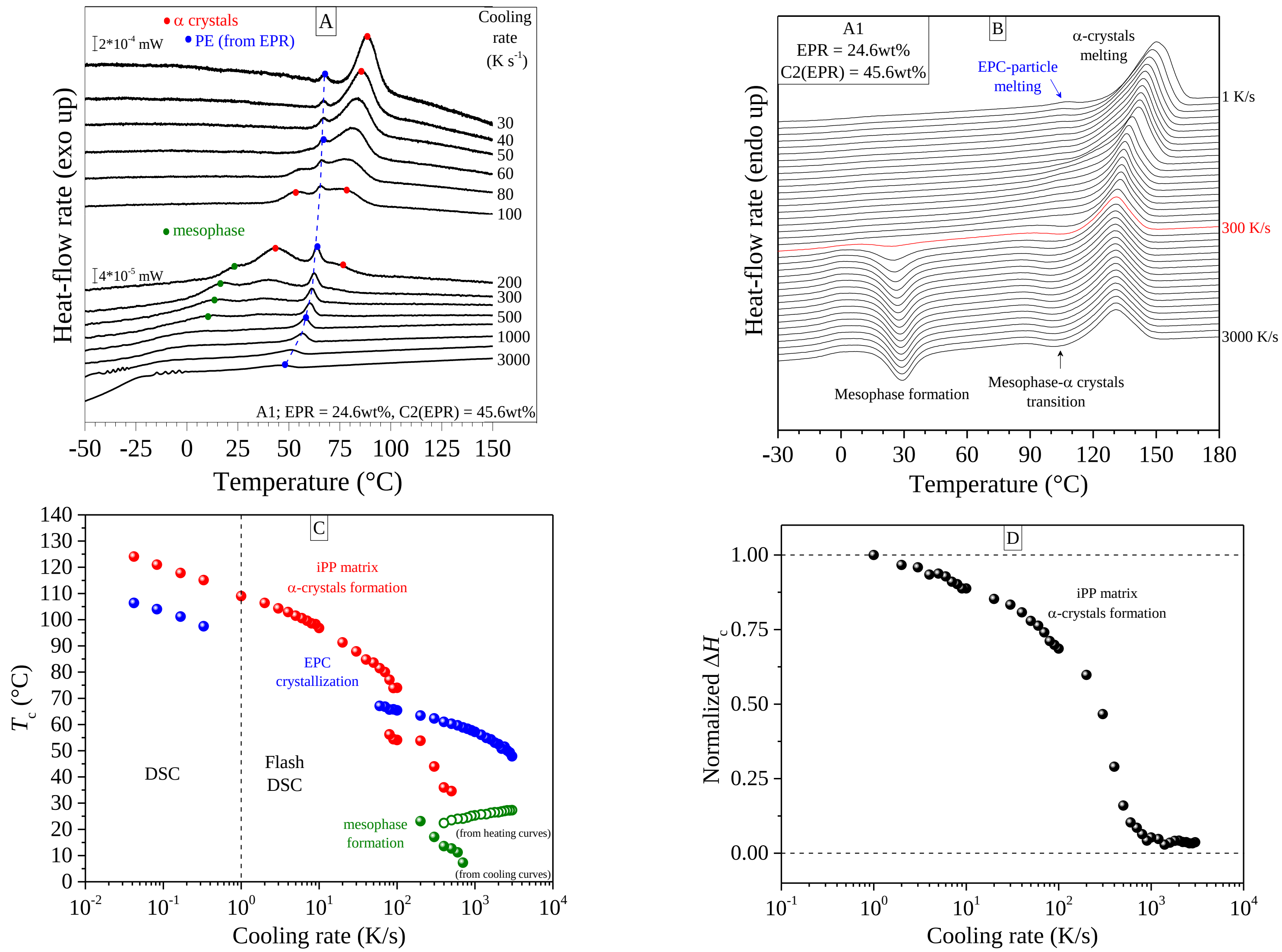

Figure 1.57. Sets of rate-normalized FSC cooling curves, with the exothermic heat-flow rate directed upwards, (A) and successive FSC heating curves recorded at 1000 K/s with the exothermic heat-flow rate directed downwards, (B) of the HECO sample A1. In picture B, the values 1, 300, and 3000K/s indicate, as an example, the cooling rates used in the previous cooling steps. Peak crystallization temperature (C) and normalized overall enthalpy of melting (D) as a function of the cooling rate. T_c values obtained from independent DSC experiments at four different cooling rates are also shown in picture C.

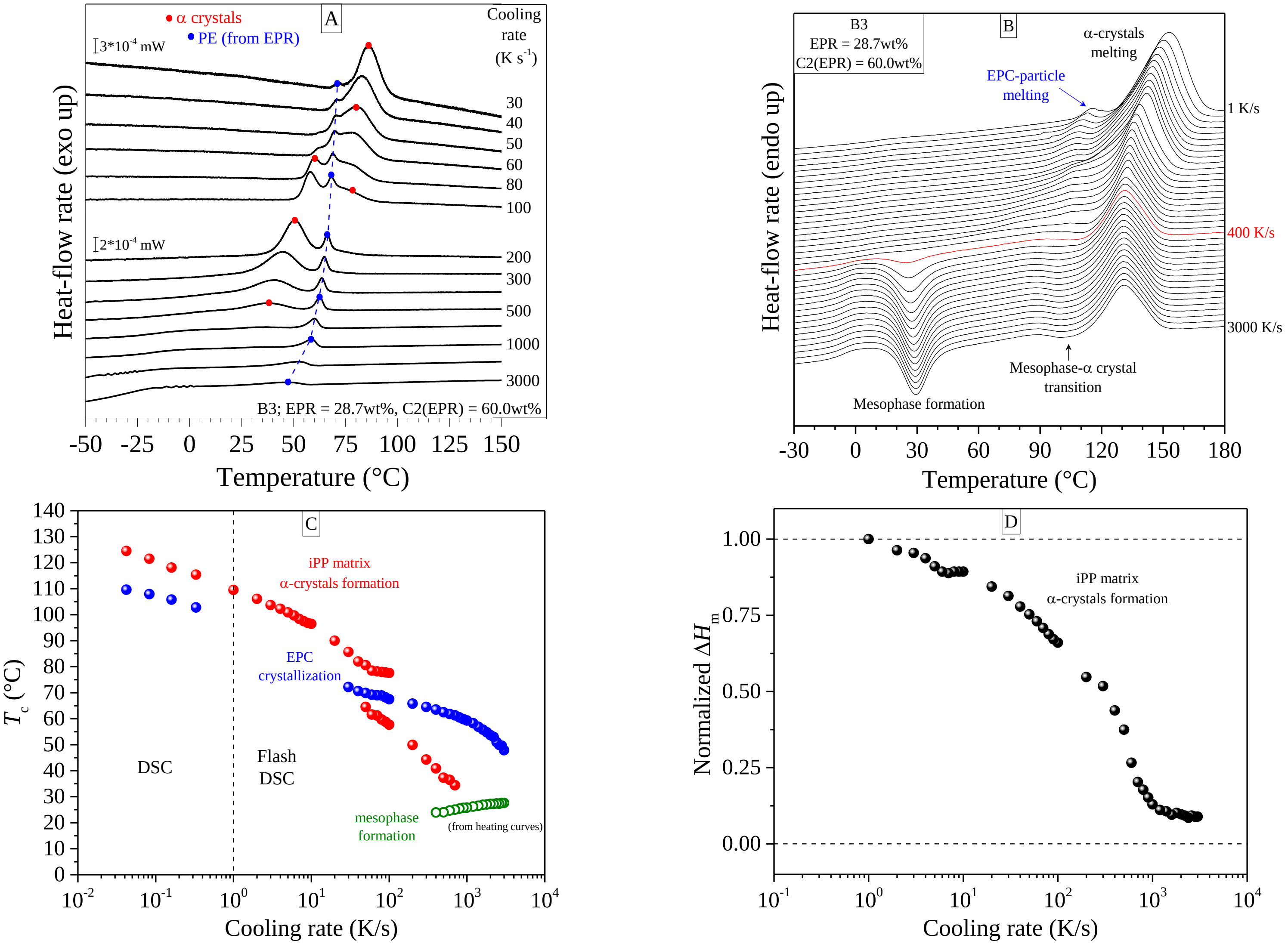

Figure 1.58. Sets of rate-normalized FSC cooling curves, with the exothermic heat-flow rate directed upwards, (A) and successive FSC heating curves recorded at 1000 K/s with the exothermic heat-flow rate directed downwards, (B) of the HECO sample B3. In picture B, the values 1, 400, and 3000K/s indicate, as an example, the cooling rates used in the previous cooling steps. Peak crystallization temperature (C) and normalized overall enthalpy of melting (D) as a function of the cooling rate. T_c values obtained from independent DSC experiments at four different cooling rates are also shown in picture C.

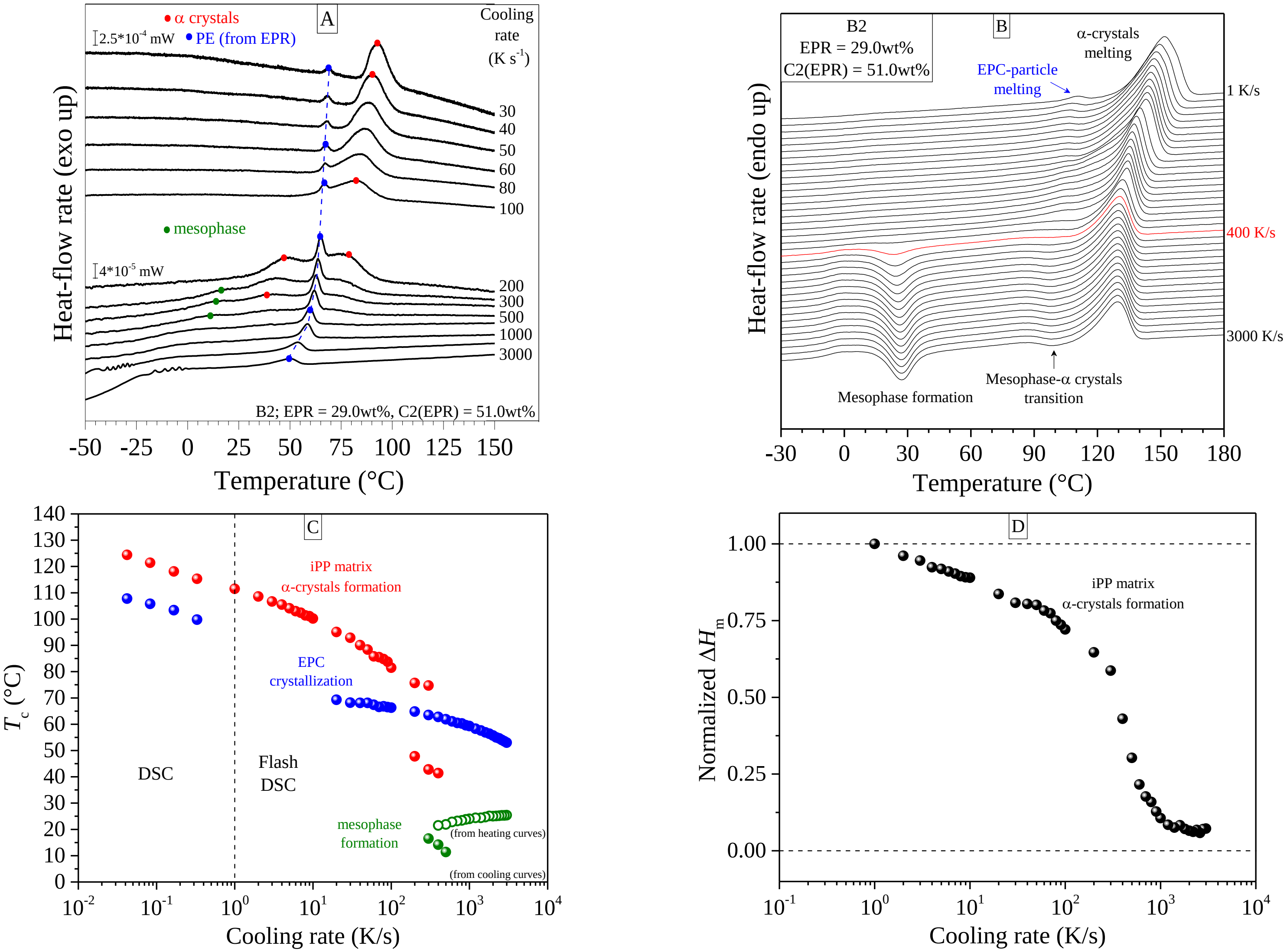

Figure 1.59. Sets of rate-normalized FSC cooling curves, with the exothermic heat-flow rate directed upwards, (A) and successive FSC heating curves recorded at 1000 K/s with the exothermic heat-flow rate directed downwards, (B) of the HECO sample B2. In picture B, the values 1, 400, and 3000K/s indicate, as an example, the cooling rates used in the previous cooling steps. Peak crystallization temperature (C) and normalized overall enthalpy of melting (D) as a function of the cooling rate. T_c values obtained from independent DSC experiments at four different cooling rates are also shown in picture C.

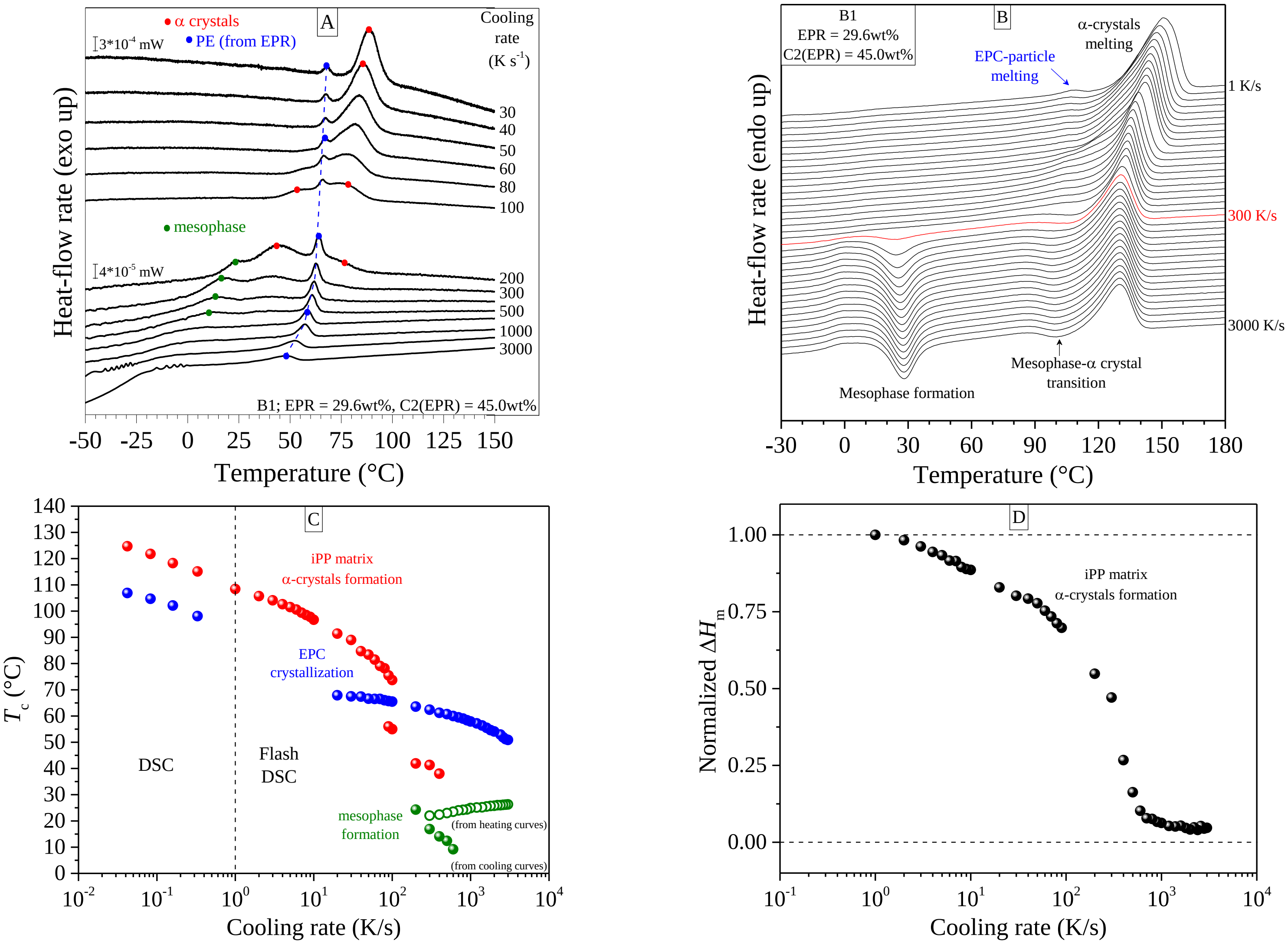

Figure 1.60. Sets of rate-normalized FSC cooling curves, with the exothermic heat-flow rate directed upwards, (A) and successive FSC heating curves recorded at 1000 K/s with the exothermic heat-flow rate directed downwards, (B) of the HECO sample B1. In picture B, the values 1, 300, and 3000K/s indicate, as an example, the cooling rates used in the previous cooling steps. Peak crystallization temperature (C) and normalized overall enthalpy of melting (D) as a function of the cooling rate. T_c values obtained from independent DSC experiments at four different cooling rates are also shown in picture C.

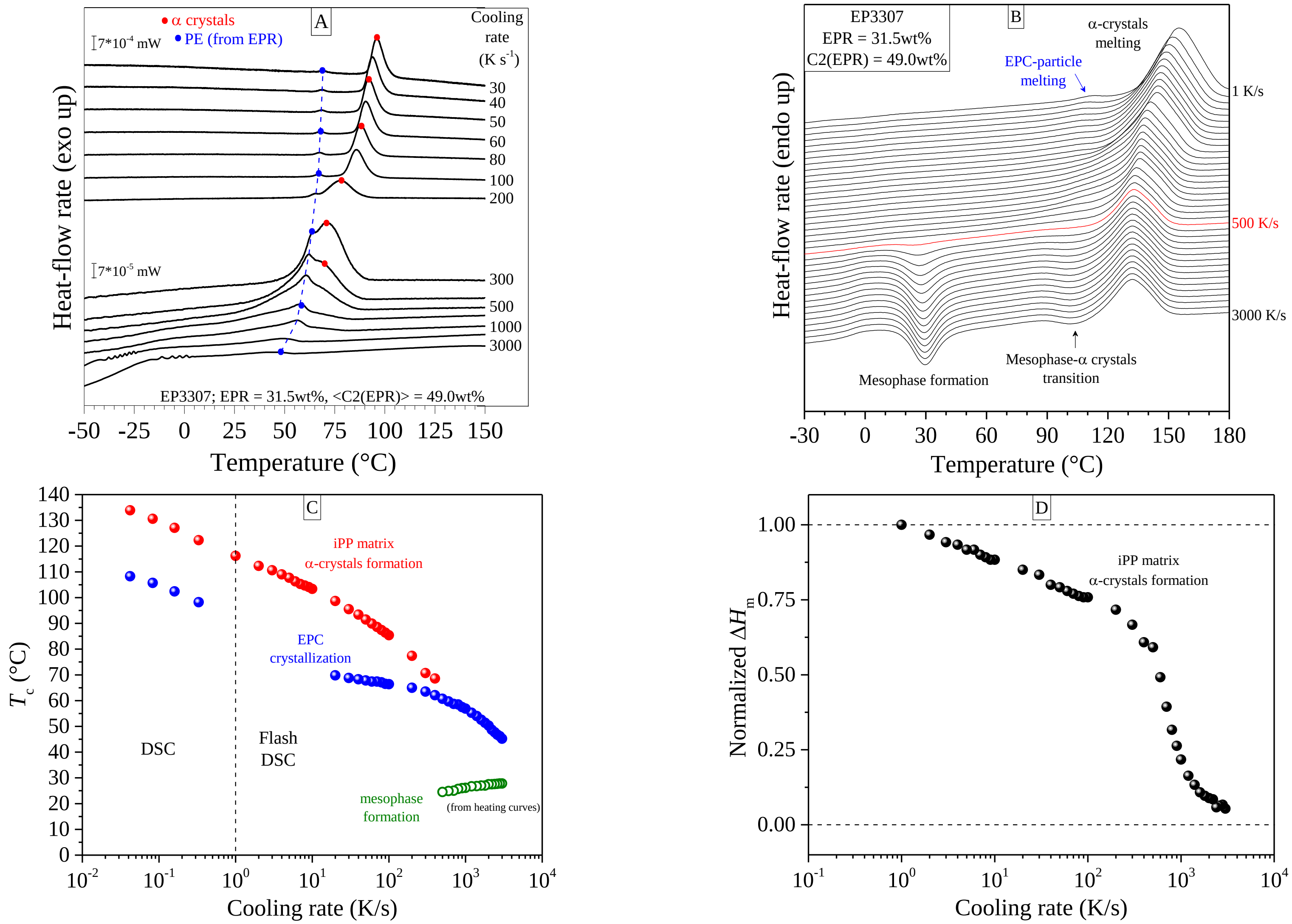

Figure 1.61. Sets of rate-normalized FSC cooling curves, with the exothermic heat-flow rate directed upwards, (A) and successive FSC heating curves recorded at 1000 K/s with the exothermic heat-flow rate directed downwards, (B) of the HECO sample EP3307. In picture B, the values 1, 500, and 3000K/s indicate, as an example, the cooling rates used in the previous cooling steps. Peak crystallization temperature (C) and normalized overall enthalpy of melting (D) as a function of the cooling rate. T_c values obtained from independent DSC experiments at four different cooling rates are also shown in picture C.

As an example, Figure 1.62 shows a comparison for the peak crystallization temperatures as a function of the cooling rate for the homopolymer and HECO samples with similar EPR content but different ethylene concentration of the elastomeric phase. For the lowest cooling rate values and more precisely in the range of 1-100 K/s, the crystallization temperature of the iPP matrix of the heterophasic samples is similar to that of the homopolymer. However, the presence of the elastomeric phase results in a change in the melting temperature of the alpha-form crystals of the thermoplastic matrix. In fact, for higher cooling rate values, it can be observed that the T_c of the iPP matrix is lower than that of the neat sample. Overall, the presence of the rubbery phase prevents, during the cooling, the formation of the mesomorphic form in favor of the crystallization of the α form. In fact, by increasing the ethylene concentration of the elastomeric phase, the formation of the mesophase is suppressed. Finally, despite the different concentration of the elastomeric phase, the three HECO samples show similar crystallization temperatures of the crystalline segments of EPC.

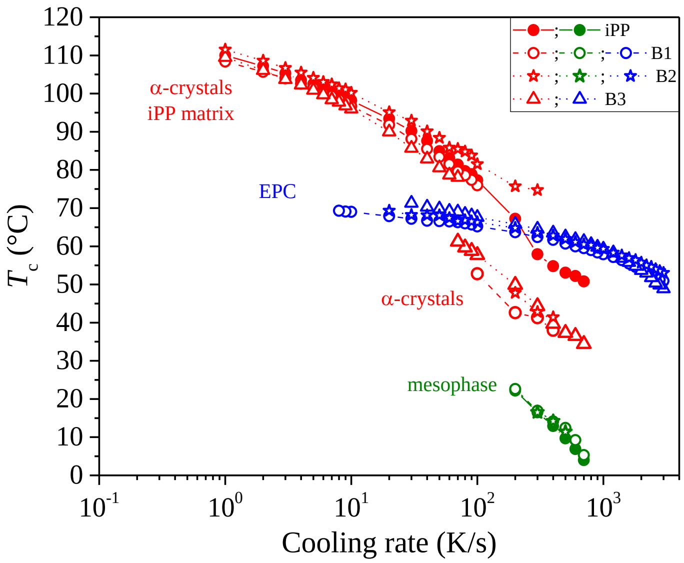

Figure 1.62. Peak crystallization temperature of iPP homopolymer and HECOs B1 (EPR = 29.6wt%, C2(EPR) = 45.0wt%), B2 (EPR = 29.0wt%, C2(EPR) = 51.0wt%), and B3 (EPR = 28.7wt%, C2(EPR) = 60.0wt%) as a function of the cooling rate.

1.5.2. Isothermal crystallization experiments

To get quantitative information regarding the typical characteristic times of the formation of the various crystalline/ordered phases, isothermal crystallization experiments were carried out. Figures 1.63-1.69 show sets of FSC crystallization isotherms of the homopolymer and all HECO samples. The analysis of neat iPP reveals, as expected, high-temperature α-crystal formation and low-temperature mesophase formation associated to heterogeneous and homogeneous nucleation mechanisms, respectively, according to the previous study of neat iPP.[27-31] The maximum rate of the mesophase development is seen at temperatures close to room temperature, while crystallization of the α-form is fastest in the temperature range of 50 to 80°C.

For HECO samples, more intricate crystallization events can be observed. Besides the phenomena observed in the neat iPP of the high-temperature crystallization of α form and low-temperature mesophase formation, various other crystallization events occur, at identical temperatures, in the range of crystallization temperatures between 50 and 70°C, especially for samples with high ethylene concentration. Since this phenomenon is related to the ethylene content in the EPR phase and because the non-isothermal experiments evidenced the crystallization of EPC particles in the range 50-70°C (Figures 1.56C-1.61C), we assume that peaks at lowest crystallization time correspond to the crystallization of rich-ethylene macromolecules belonging to the rubbery EPR phase.

Figures 1.63C-1.69C provide a representation of the temperature dependence of the crystallization kinetics evaluated from crystallization peak times of Figure 1.63A-1.69A. The common bimodal temperature dependency of the crystallization rate is replicated for neat iPP (Figure 1.63A).[27-31] When crystallization temperatures are high, heterogeneous crystal nucleation associated with the formation of lamellar α-crystals predominates, whereas when crystallization temperatures are low, homogeneous crystal nucleation associated with the formation of a nodular mesophase prevails.[32-35] The nucleation scheme changes at around 50°C.

In the case of almost all HECO samples, it is possible to notice the presence of three different temperature ranges. In fact, as far as the iPP-matrix crystallization, all samples show a trimodal distribution of the crystallization rate with an additional rate maximum between those related to the crystallization of the α-form and mesophase in the neat iPP. The only exception is the sample EP3307 for which only two domains are still visible.

In the temperature range of about 110-70°C, only the crystallization of the thermoplastic iPP matrix occurs, since the crystallization in the EPC particles proceeds at much lower temperatures, as evidenced by the non-isothermal experiments.

At temperatures between 70-40°C, the crystallization rate increases compared to the high-temperature crystallization process and passes through an additional maximum before the homogeneous nucleation process becomes effective. The increase in the crystallization rate could be correlated with the crystallization of the EPC particles. In fact, it appears that if the crystallization in the EPC particles occurs before the crystallization of α-crystals, there is an increase in the crystallization rate of the iPP-matrix with a decrease in the characteristic crystallization time. Low-temperature crystallization of the iPP-matrix proceeds via homogeneous nucleation in the temperature range of 40-0°C.

Finally, the triphasic sample EP3307, shows a two-domain trend similar to that of the homopolymer. However, much lower characteristic crystallization times are observed for this HECO sample than for the neat iPP, thus with an increased crystallization rate. This result could be attributed to a nucleating effect by the macromolecules rich in long crystalline ethylene sequences belonging to the EPR copolymer with an ethylene concentration of 60wt%. In fact, regarding the temperature range 110-70°C, the presence of the EPR phase in the molten state has a strong effect on the characteristic crystallization times of the iPP matrix. In fact, the characteristic crystallization times of α-form crystals decrease compared with the homopolymer sample revealing an important nucleating effect of EPC particles on the thermoplastic matrix. On the other hand, since the domain within the 40-70°C temperature range is not observed, it is possible that the copolymer with [C2] = 30wt%, belonging to the triphasic sample, has a positive effect on the crystallization kinetics of the thermoplastic matrix probably due to a good matrix-EPC interfacial adhesion.

In conclusion these data indicate that the presence of the elastomeric phase can significantly change the crystallization kinetics of the isotactic polypropylene.

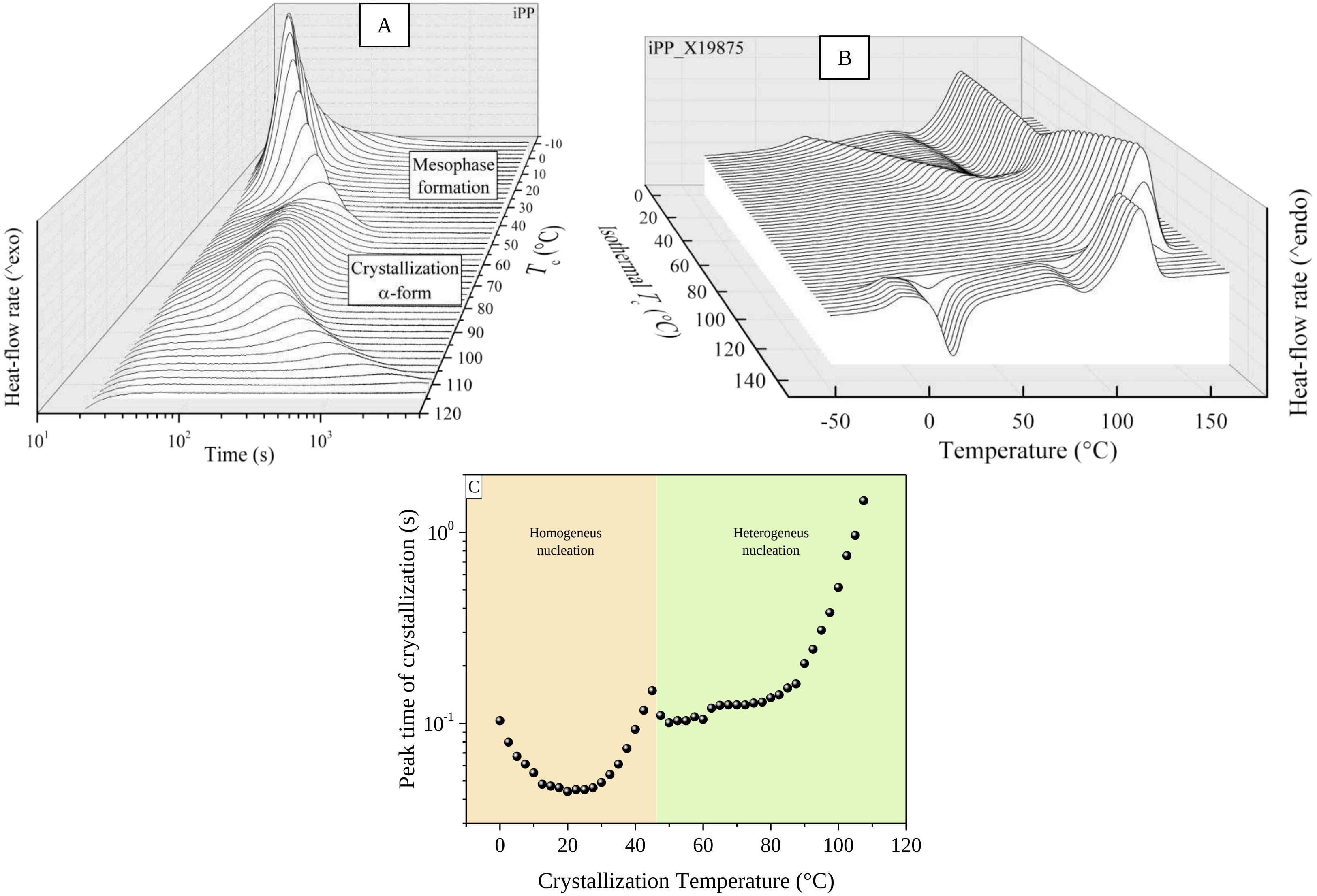

Figure 1.63. Sets of FSC crystallization isotherm, with the exothermic heat-flow rate directed upwards, (A) and successive FSC heating curves recorded at 1000 K/s, with the exothermic heat-flow rate directed downwards, (B) of the homopolymer sample. Peak time of crystallization as a function of the crystallization temperature (C) in the entire analyzed temperature range between 0 and 110°C.

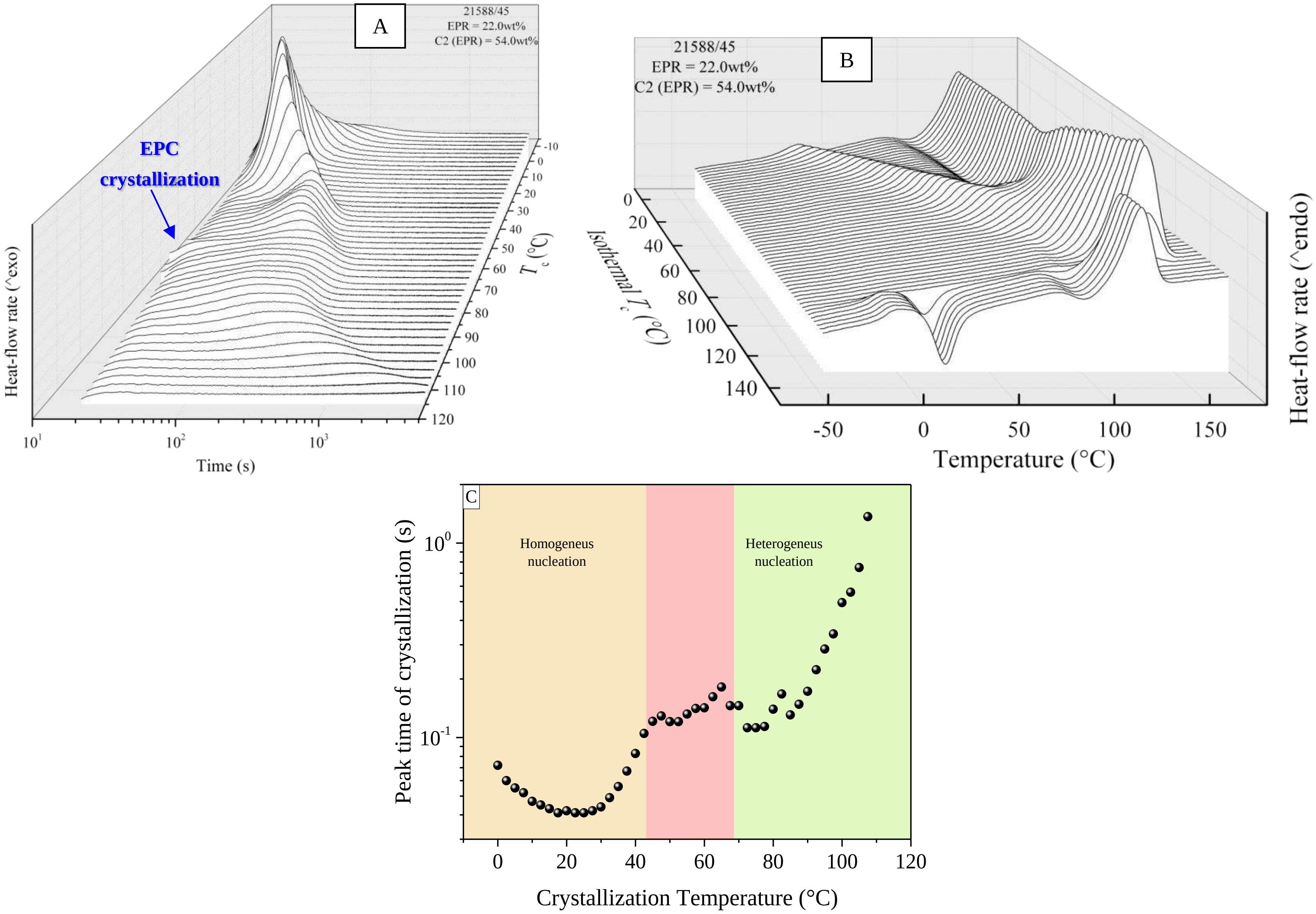

Figure 1.64. Sets of FSC crystallization isotherm, with the exothermic heat-flow rate directed upwards, (A) and successive FSC heating curves recorded at 1000 K/s, with the exothermic heat-flow rate directed downwards, (B) of the HECO sample 21588\45. Peak time of crystallization as a function of the crystallization temperature (C) in the entire analyzed temperature range between 0 and 110°C.

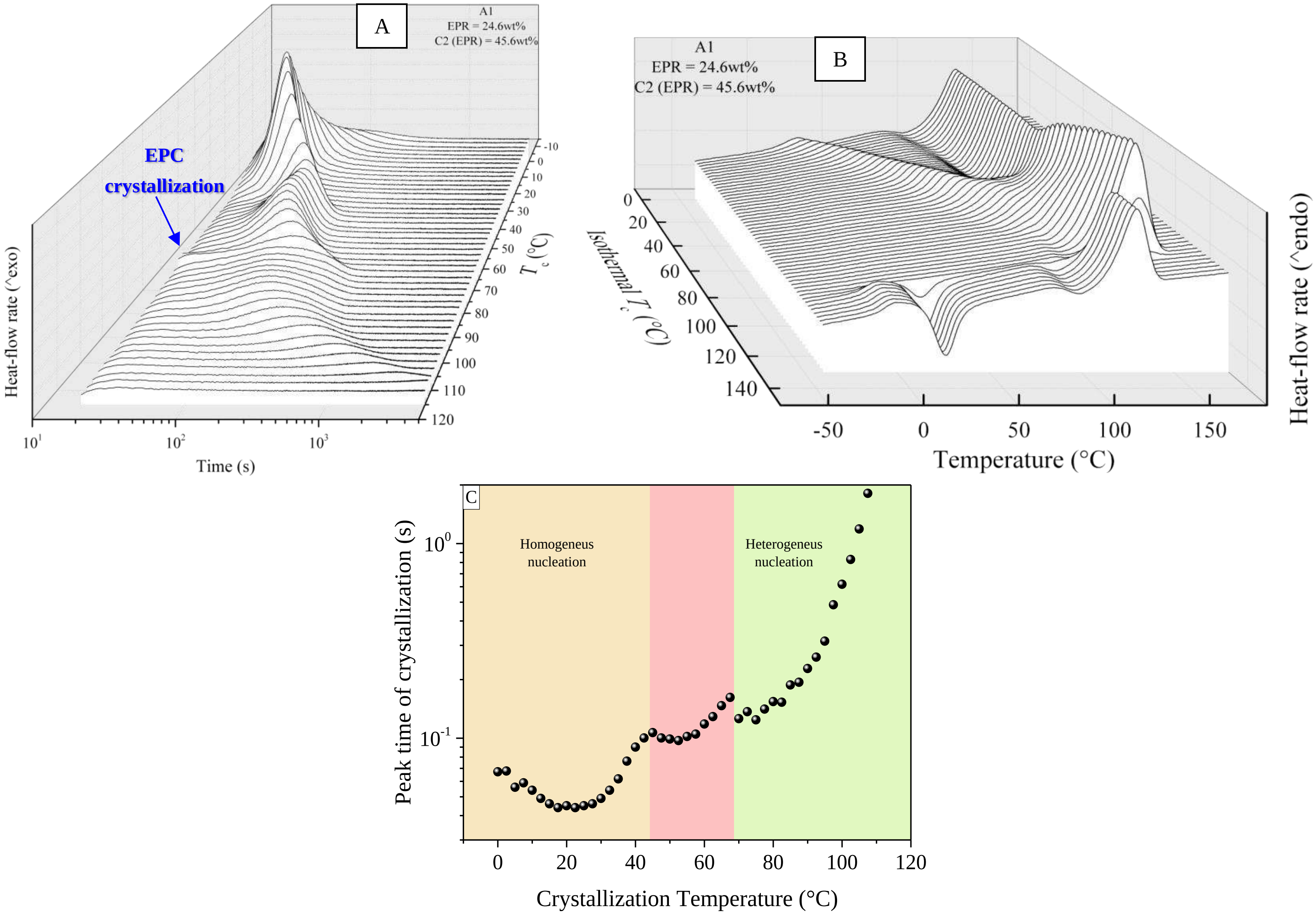

Figure 1.65. Sets of FSC crystallization isotherm, with the exothermic heat-flow rate directed upwards, (A) and successive FSC heating curves recorded at 1000 K/s, with the exothermic heat-flow rate directed downwards, (B) of the HECO sample A1. Peak time of crystallization as a function of the crystallization temperature (C) in the entire analyzed temperature range between 0 and 110°C.

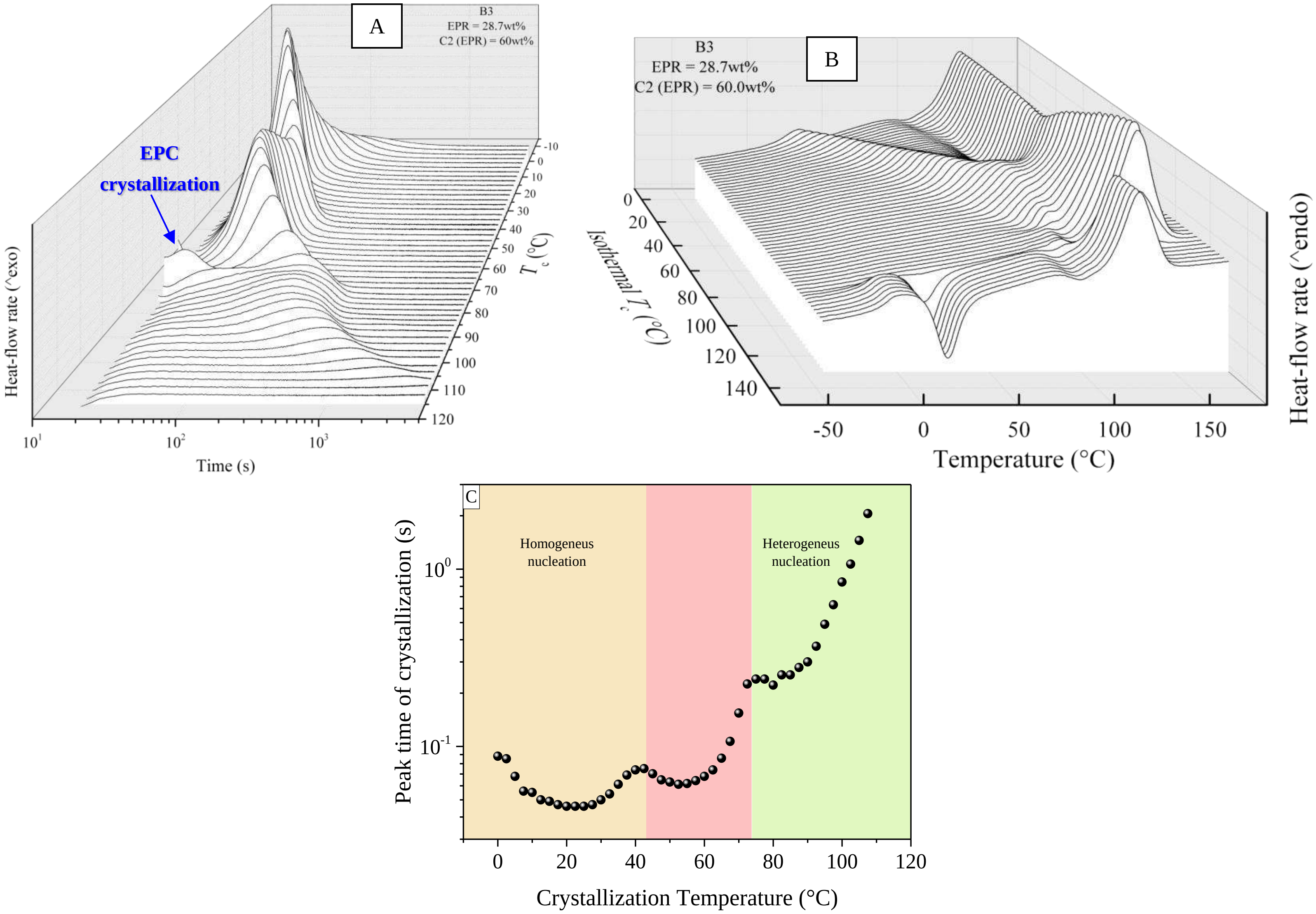

Figure 1.66. Sets of FSC crystallization isotherm, with the exothermic heat-flow rate directed upwards, (A) and successive FSC heating curves recorded at 1000 K/s, with the exothermic heat-flow rate directed downwards, (B) of the HECO sample B3. Peak time of crystallization as a function of the crystallization temperature (C) in the entire analyzed temperature range between 0 and 110°C.

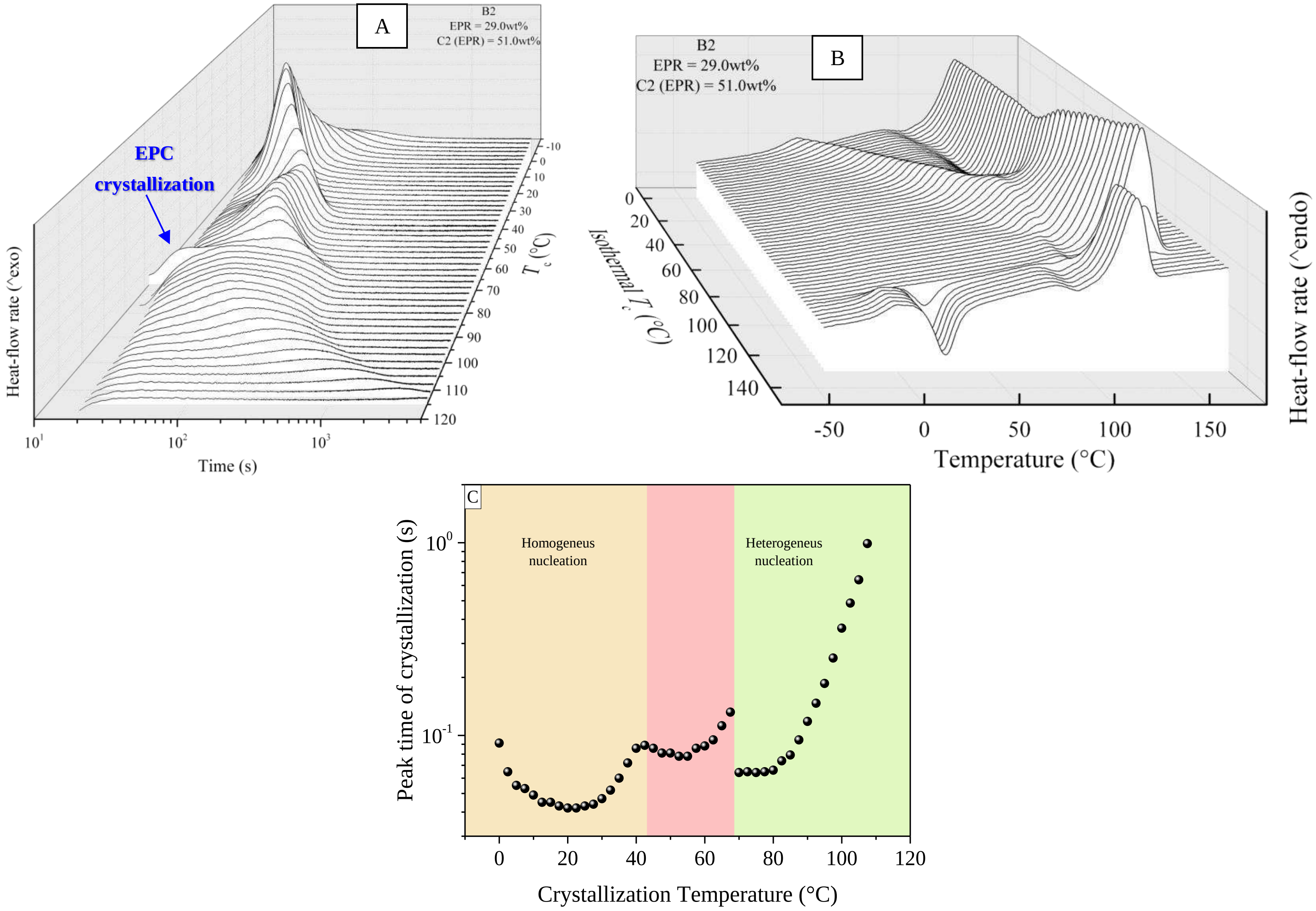

Figure 1.67. Sets of FSC crystallization isotherm, with the exothermic heat-flow rate directed upwards, (A) and successive FSC heating curves recorded at 1000 K/s, with the exothermic heat-flow rate directed downwards, (B) of the HECO sample B2. Peak time of crystallization as a function of the crystallization temperature (C) in the entire analyzed temperature range between 0 and 110°C.

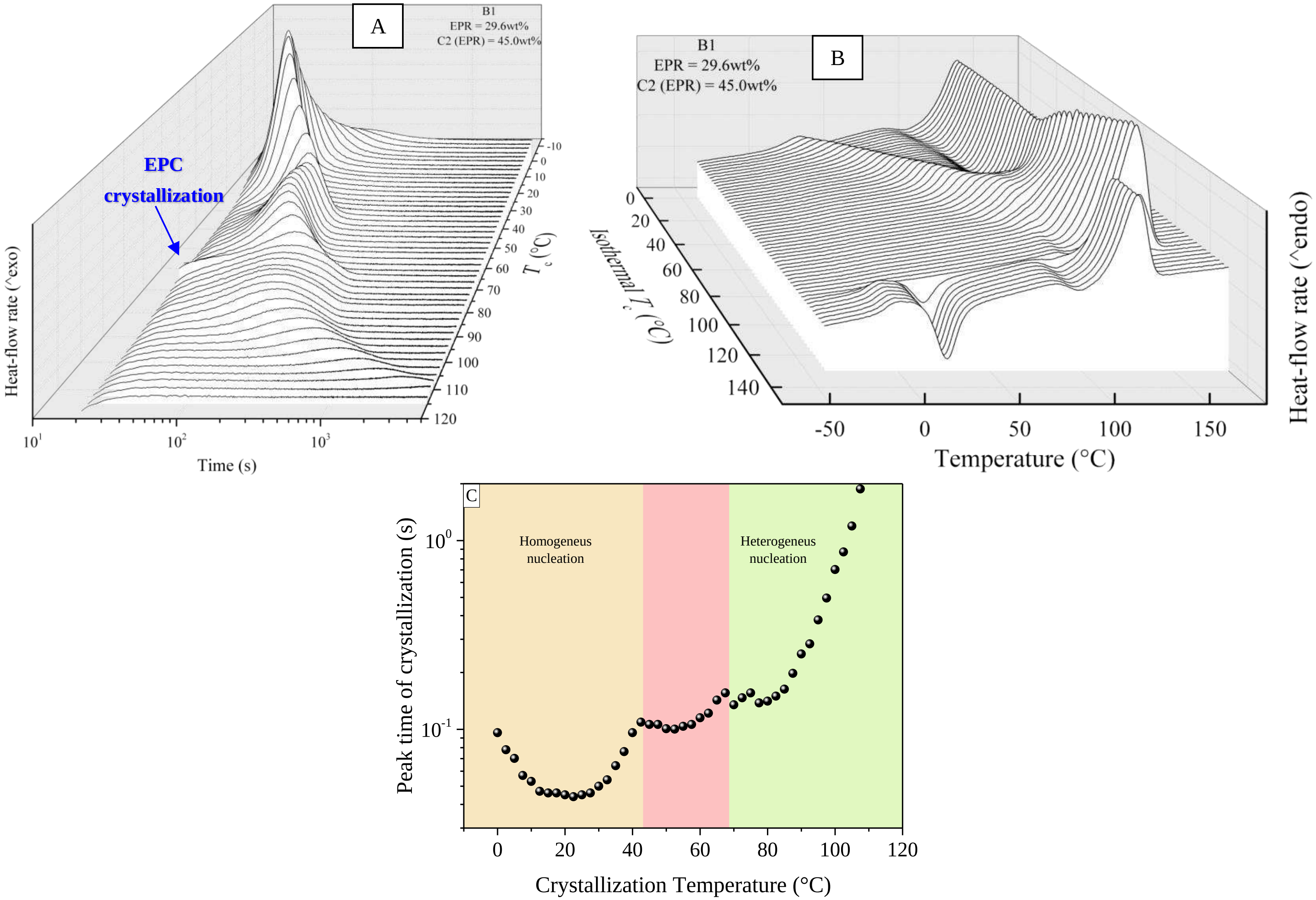

Figure 1.68. Sets of FSC crystallization isotherm, with the exothermic heat-flow rate directed upwards, (A) and successive FSC heating curves recorded at 1000 K/s, with the exothermic heat-flow rate directed downwards, (B) of the HECO sample B1. Peak time of crystallization as a function of the crystallization temperature (C) in the entire analyzed temperature range between 0 and 110°C.

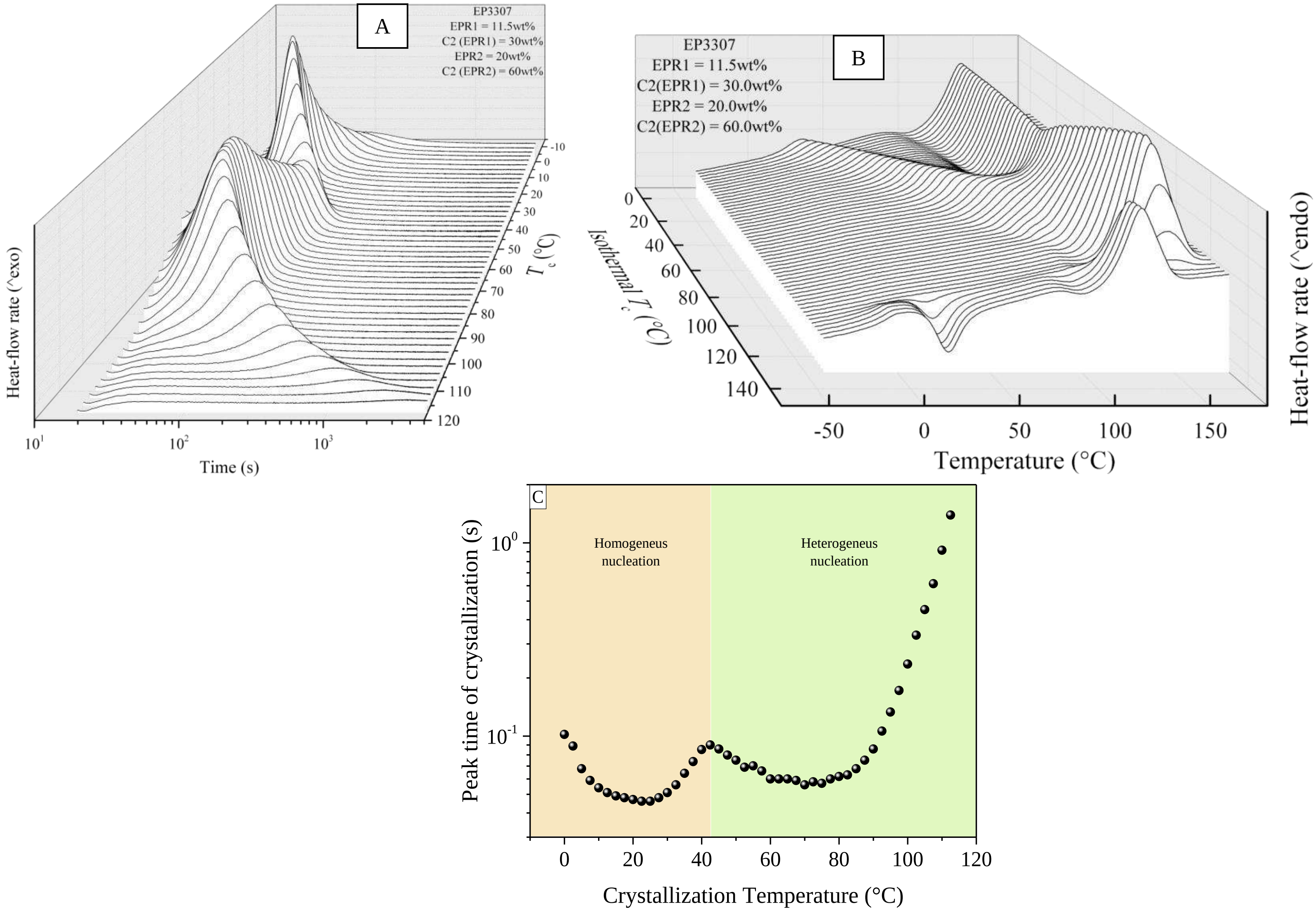

Figure 1.69. Sets of FSC crystallization isotherm, with the exothermic heat-flow rate directed upwards, (A) and successive FSC heating curves recorded at 1000 K/s, with the exothermic heat-flow rate directed downwards, (B) of the HECO sample EP3307. Peak time of crystallization as a function of the crystallization temperature (C) in the entire analyzed temperature range between 0 and 110°C.

In order to consider only the effect of the ethylene concentration of the elastomeric phase on the crystallization rate of the thermoplastic matrix, a comparison of crystallization time as a function of isothermal crystallization temperatures is shown in Figure 1.70 only for samples with the same rubbery phase content and for the homopolymer. It is apparent that as the ethylene concentration increases, in the thermal range from 40 to 70°C, the crystallization rate of the iPP matrix increases suggesting that the presence of the crystalline EPC particles act as a nucleating agent for the α-form crystals. Figure 1.62 supports this hypothesis since it is well evident that those EPC particles crystallize in the 45-70°C range temperature.

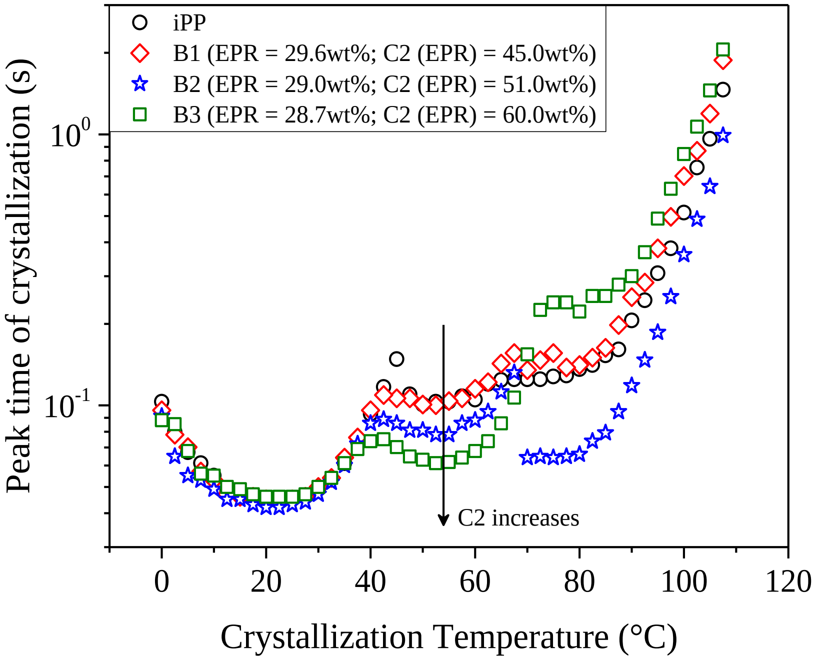

Figure 1.70. Peak time of crystallization as a function of the crystallization temperature in the entire analyzed temperature range between 0 and 110°C for the homopolymer and HECO samples with the similar EPR content and different ethylene concentration of the rubbery phase.

1.6. Study of viscoelastic properties by Dynamic Mechanical Thermal Analysis (DMTA)

To evaluate how the rubbery phase influenced the relaxation phenomena of the iPP matrix, the viscoelastic properties both of HECO samples and the iPP homopolymer were studied. For an overall thermomechanical profile, the viscoelastic properties of all compression-molded samples, obtained by slow cooling from the melt, were studied by Dynamic Mechanical Thermal Analysis with a TTDMA dynamic mechanical analyzer by Triton. Measurements were carried out in single cantilever bending mode geometry, imposing a frequency of 1Hz and displacement amplitude of 0.02mm while heating samples at a rate of 5°C/min in the temperature range -100-150°C.

Temperature dependence of the (in phase) storage modulus, G', the (out phase) loss modulus, G'', and the damping factor, tanδ (G''/G') for all HECO samples is shown in Figure 1.71.

The storage modulus for all HECO samples is, as expected, lower than that of the homopolymer throughout all temperature range, due to the presence of the rubbery phase. In addition, for the homopolymer, a main slope change in the -10 to 25°C temperature range, associated to the glass transition of the iPP, is observed. For HECOs samples, on the other hand, two main slope changes are observed, one in the -60 to -30°C temperature range and the other in the -10 to 25°C range, associated to the glass transition of the EPR phase and iPP, respectively.

From the tanδ values of Figure 1.70C three different transition phenomena can be distinguished:[36]

- the α-transition in the range -60 to -40°C corresponding to the glass transition of the amorphous EPR;
- the β-transition or glass transition at about 10°C for the amorphous phase of the semicrystalline iPP;
- the α_c-transition between 90 and 120°C, which is associated to other molecular rearrangements. In particular, this transition develops as a result of conformational defects diffusing from the crystalline phase to the interphase between the crystalline and amorphous phases. Therefore, it is assumed that this transition has an impact on both crystalline and amorphous phases.

The relative intensity of the peak attributed to the T_g of the elastomeric phase, increases with increasing elastomeric phase content while the relative magnitude assigned to the T_g of the iPP decreases with increasing EPR content.

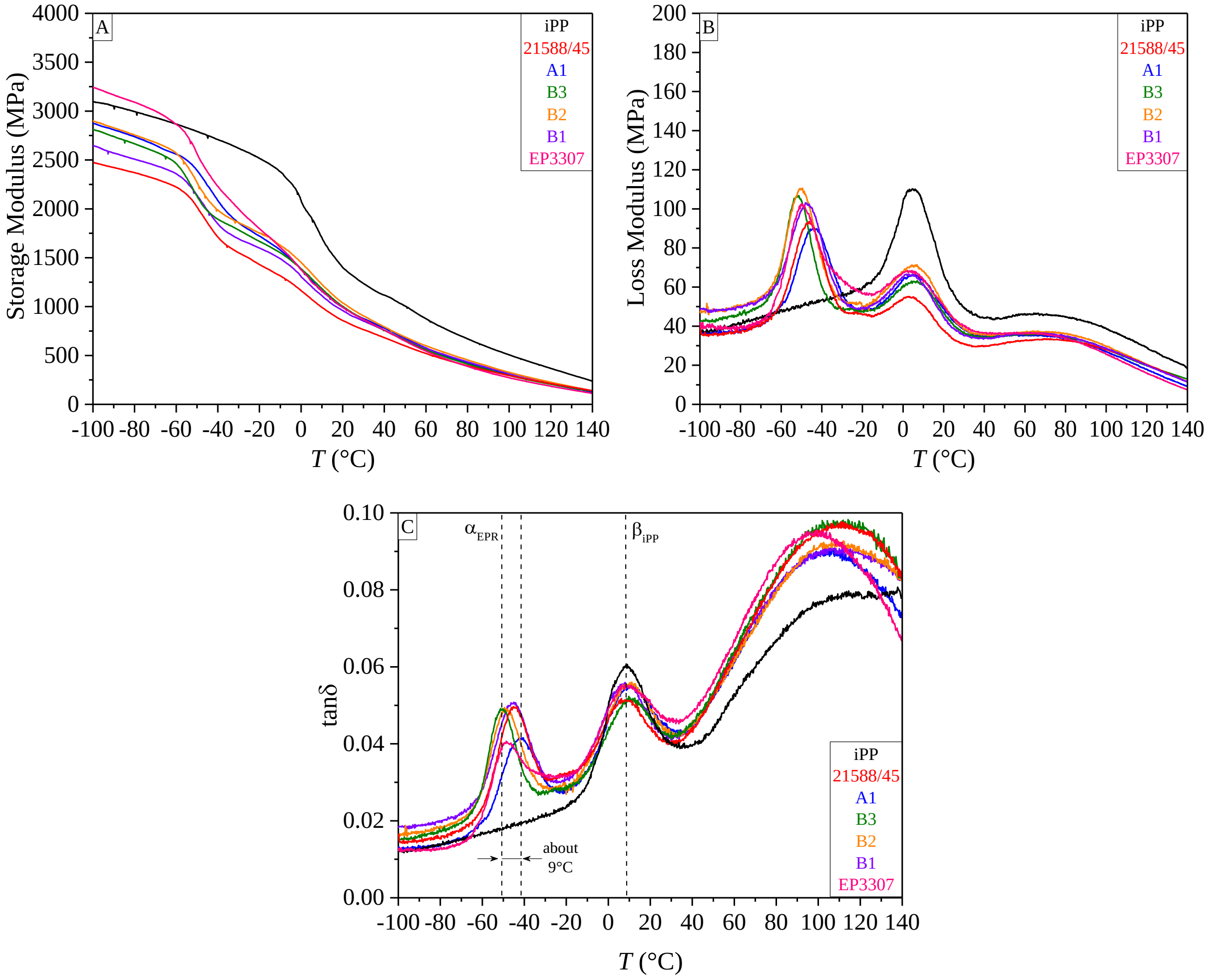

Figure 1.71. Temperature dependence of the storage modulus (A), the loss modulus (B), and the damping factor (C) for the homopolymer and all HECO samples.

The values of T_g are reported in Figure 1.72 as a function of the content of the EPR phase and ethylene concentration of the EPR phase. The glass transition temperature of the iPP thermoplastic matrix seems to be independent on the ethylene concentration and the EPR content, while the T_g of the rubbery phase generally decreases as the ethylene concentration increases. Since the T_g of iPP seems to be not influenced by the presence of EPR it could be possibly concluded that there is no significant bulk interaction between iPP and EPR. Finally, by plotting the values of the storage modulus at 23°C as a function of the rubbery phase content (see Figure 1.72B), it is evident the decrease of the stiffness of HECO samples compared to the homopolymer, even though there is no significant change as the EPR content increases.

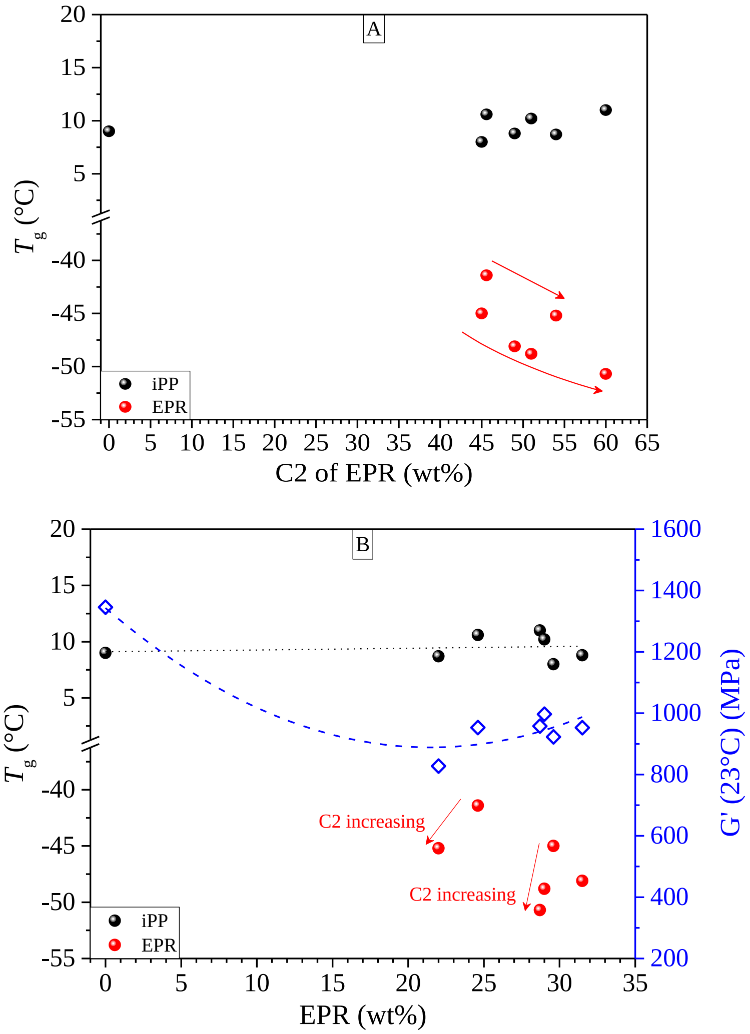

Figure 1.72. Glass transition temperature as a function of the ethylene concentration of the elastomeric phase (A) and of the EPR content (B) for the homopolymer and all HECO samples. Picture B also shows values of the storage modulus evaluated at *T* = 23°C.

1.7. Study of rheological properties

The rheological properties of all materials were also studied using an ARES 2000 Rheometer (TA Instruments, Newcastle, DE, USA) equipped with an environmental test chamber. The sample environment was purged with dry air, and measurements were performed in parallel-plate geometry. The diameters of the upper and lower plates were 8 and 25 mm, respectively. The responses of samples, in the linear viscoelastic shear oscillation, were evaluated in a frequency range of 0.1-250 rad/s, setting the strain amplitude at 1% and the gap distance between the two plates at 250 μm. Since the melting temperature of the iPP sample and the highest melting temperatures of HECOs were about 165°C, all rheological tests were performed in a temperature range of 15-35°C higher than the melting temperature of the iPP component. In particular, the analysis was conducted at three different temperatures, choosing T = 180, 190, and 200°C.

Before diving into the discussion, it is worth mentioning that, since polymers show a viscoelastic behavior, we need to measure the conservative modulus G' for the elastic component and the dissipative modulus G" for the viscous component.

The values of the dynamic moduli (G', G'') versus the angular frequency, for all samples and at different temperatures, are shown in Figures 1.73-1.79. Dynamic moduli G'(ω) and G''(ω) increase with increasing frequency that corresponds to the decrease of time of measurement. In particular, at low frequency G'' > G' suggesting that all samples have a liquid-like behavior or, in other word, show a viscous response to the applied stress and the dissipative modulus prevails over the elastic modulus. With the increase of the angular frequency both moduli increase until a cross-over point (ω_c) is reached. The cross-over point defines the beginning of the rubbery plateau and corresponds to an average relaxation time. For values of the angular frequency higher than ω_c, the elastic modulus prevails over the dissipative modulus, G' > G'', and the material show a solid-like elastic behavior indicating entanglement effects.

More specifically, in the case of the homopolymer (Figure 1.73) and sample EP3307 (Figure 1.79), the crossover point is reached for low values of angular frequency. For all other HECO samples (Figures 1.74-1.78) the crossover point is reached at higher values of angular frequency and the value of the storage modulus (G') merely overlaps with the value of the loss modulus (G") after ω_c.

The value of the cross-over point ω_c is related to the relaxation time ($\tau_c = 2\pi\omega_c^{-1}$). Therefore, since the values of ω_c are much higher for HECOs than for the homopolymer, the introduction of the rubbery phase produces a decrease of the relaxation time of iPP.

Moreover, in almost all cases of Figures 1.73-1.79, besides the normal decrease of both moduli with increasing temperature, the value of ω_c increases with increasing the experimental temperature, resulting in a decrease of the relaxation time. Therefore, higher values of operating temperature favor the relaxation phenomena of the materials.

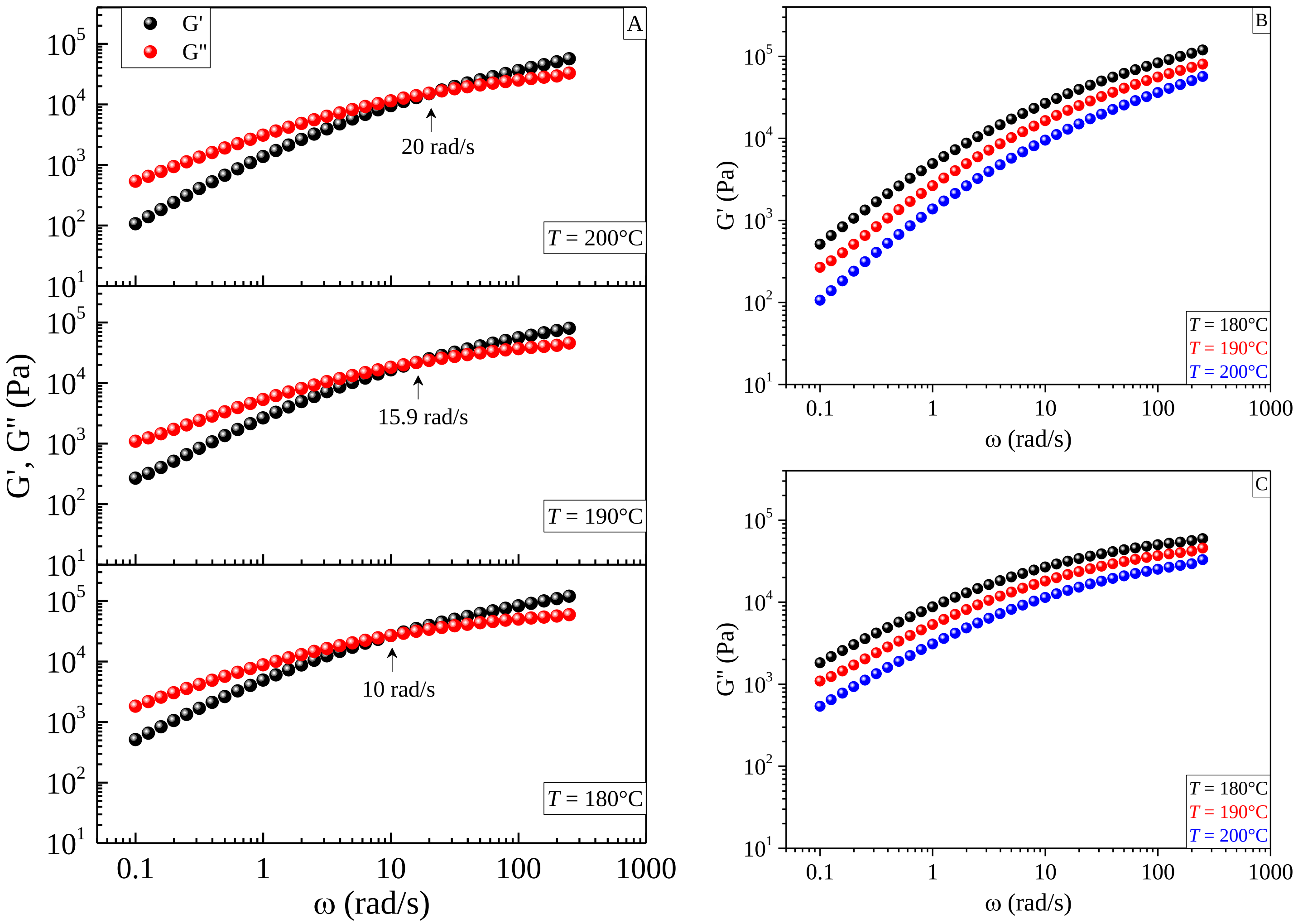

Figure 1.73. Storage modulus (G’) and loss modulus (G’’) versus angular frequency for the homopolymer sample at *T* = 180, 190 and 200°C. Arrows indicate the cross-over point values.

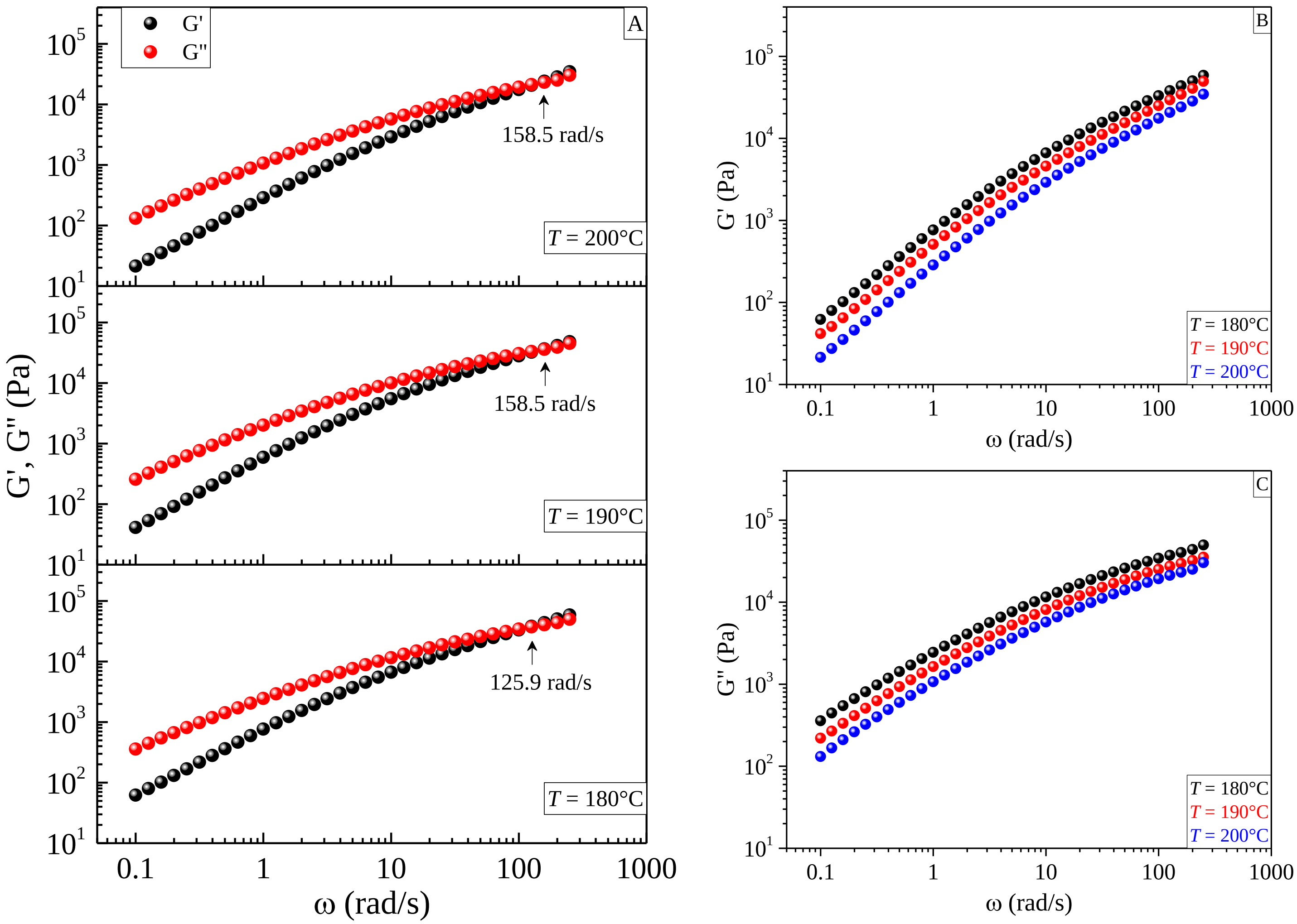

Figure 1.74. Storage modulus (G') and loss modulus (G'') versus angular frequency for the HECO sample 21588/45 (EPR = 22.0wt%; C2 = 54.0wt%) at *T* = 180, 190 and 200°C. Arrows indicate the cross-over point values.

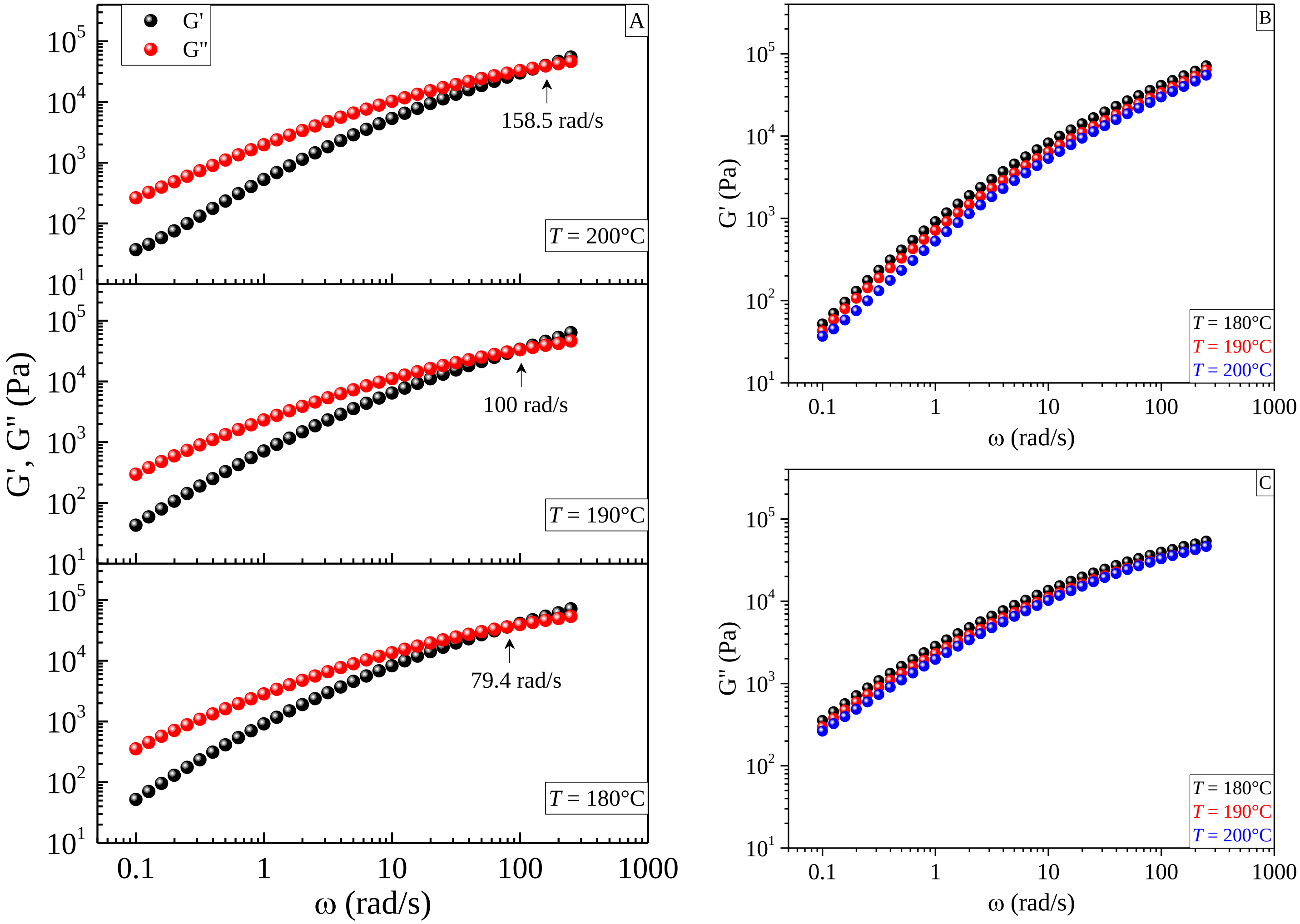

Figure 1.75. Storage modulus (G') and loss modulus (G'') versus angular frequency for the HECO sample A1 (EPR = 24.6wt%; C2 = 45.6wt%) at *T* = 180, 190 and 200°C. Arrows indicate the cross-over point values.

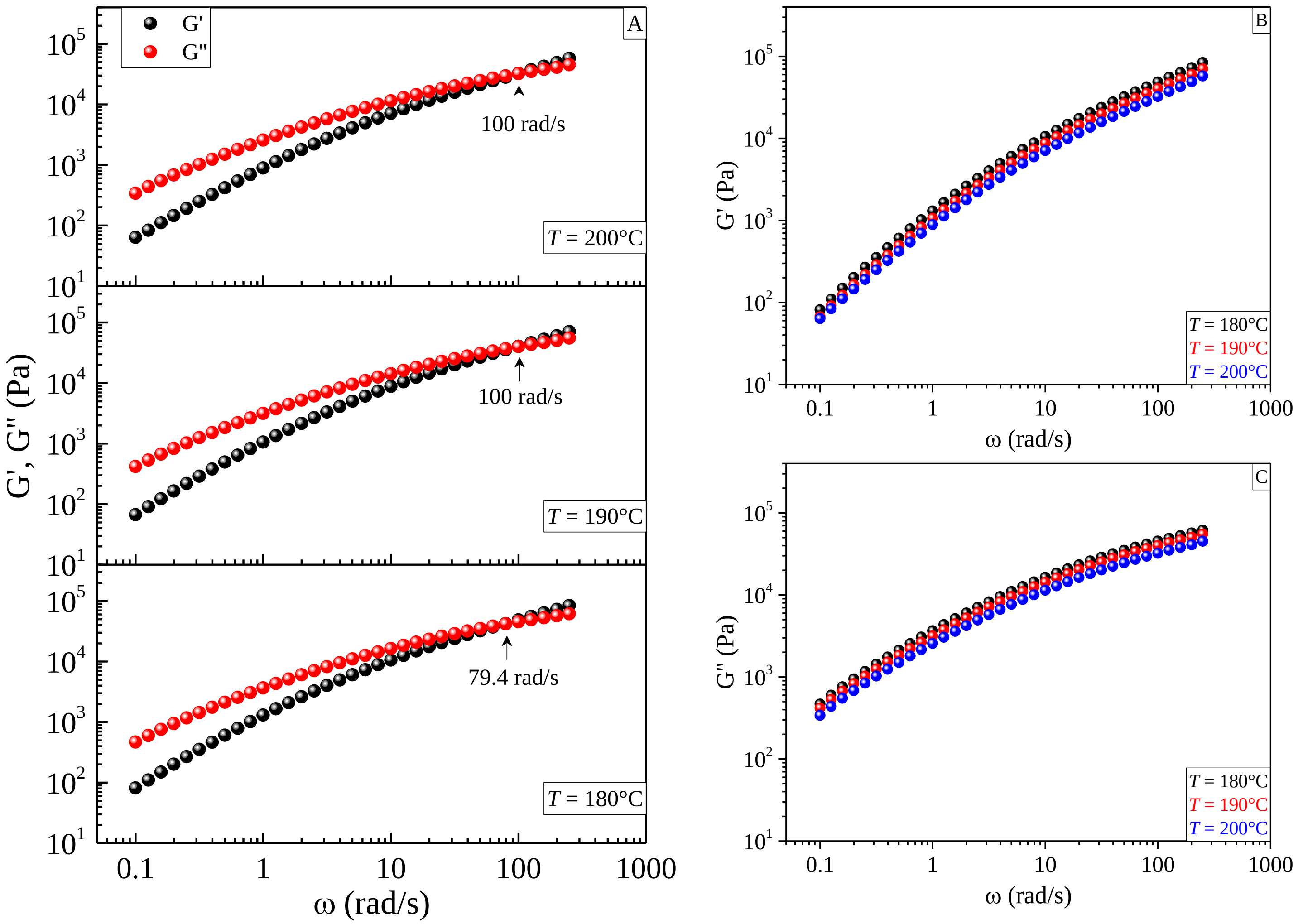

Figure 1.76. Storage modulus (G’) and loss modulus (G’’) versus angular frequency for the HECO sample B3 (EPR = 28.7wt%; C2 = 60.0wt%) at *T* = 180, 190 and 200°C. Arrows indicate the cross-over point values.

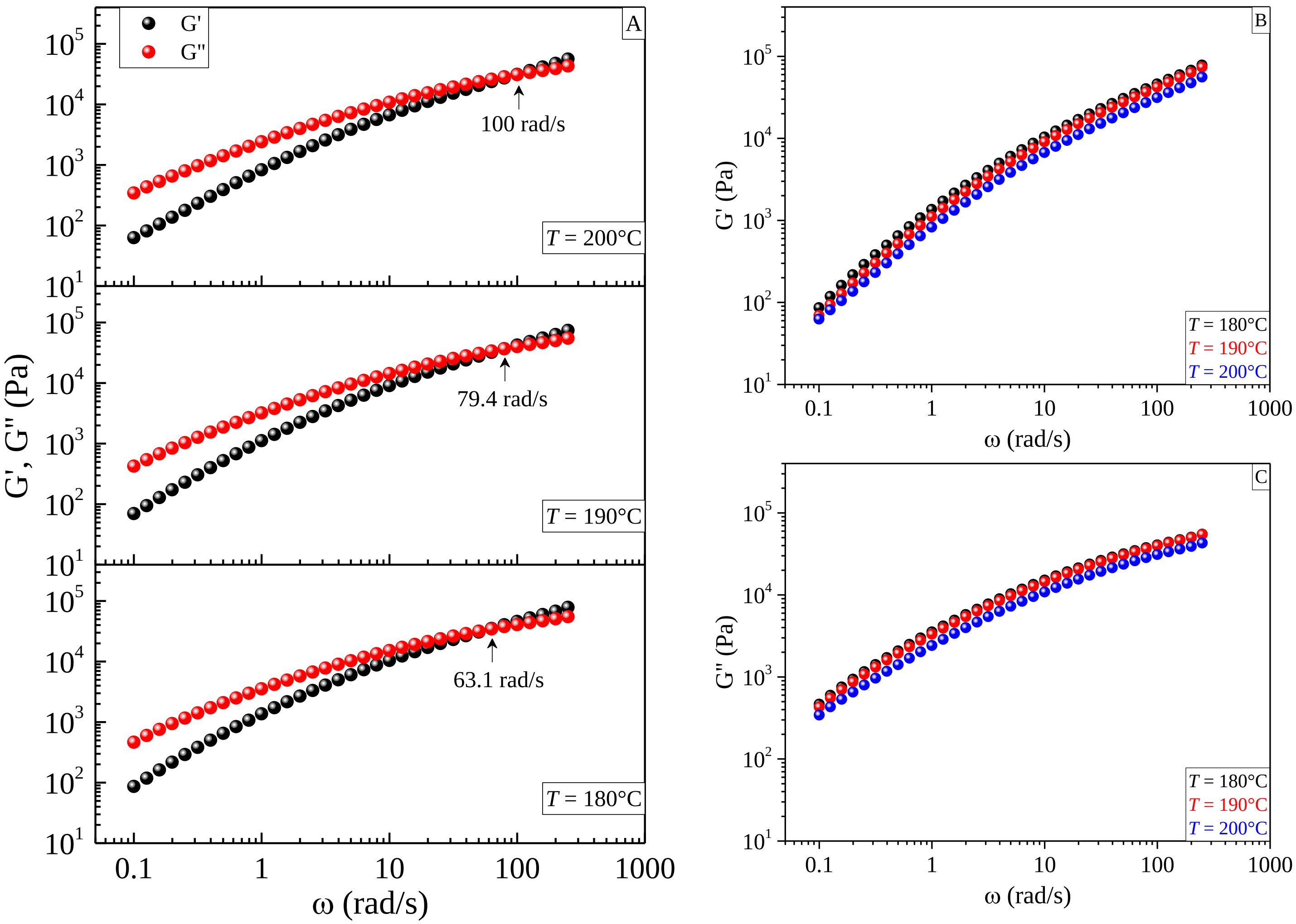

Figure 1.77. Storage modulus (G') and loss modulus (G'') versus angular frequency for the HECO sample B2 (EPR = 29.0wt%; C2 = 51.0wt%) at *T* = 180, 190 and 200°C. Arrows indicate the cross-over point values.

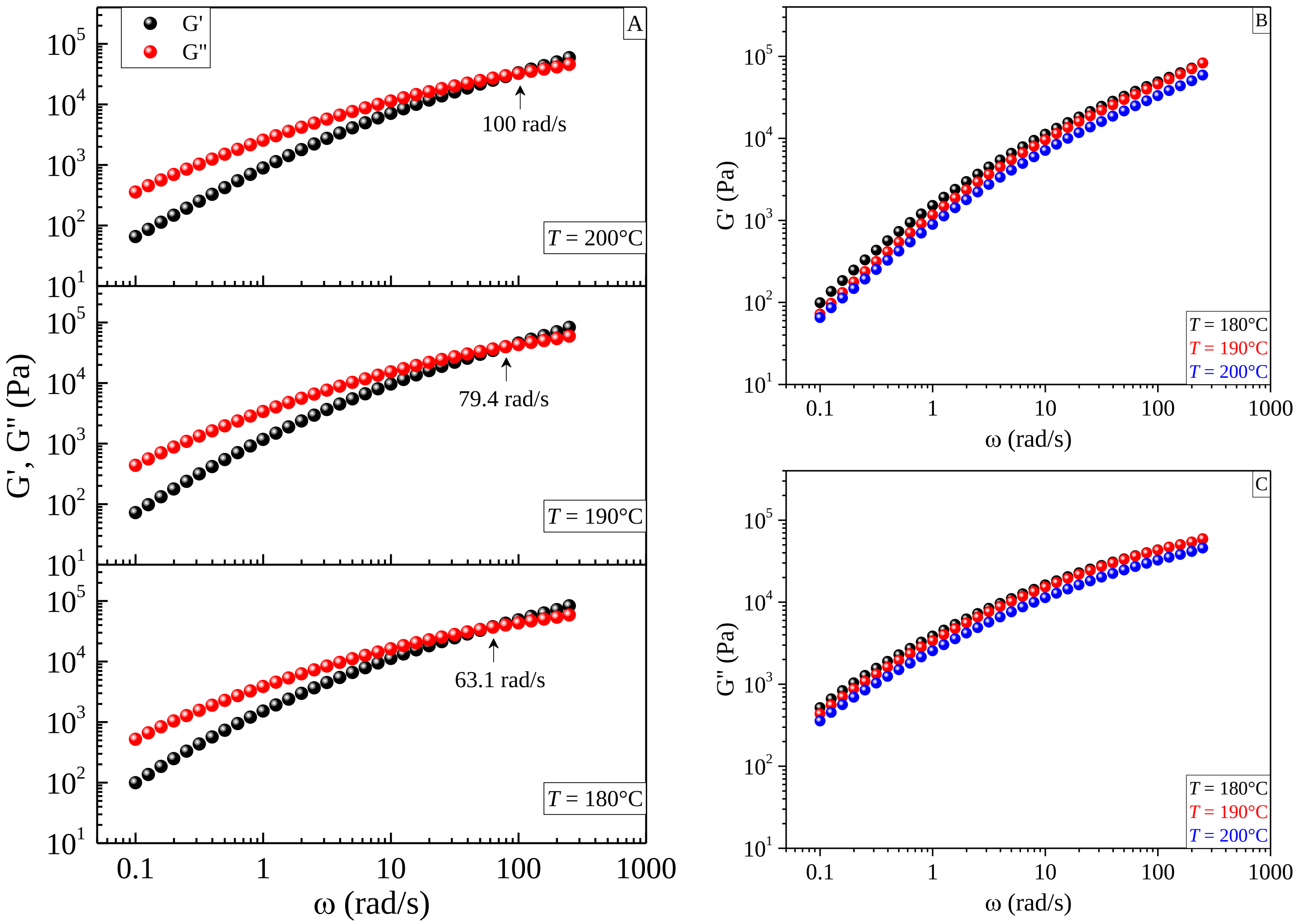

Figure 1.78. Storage modulus (G’) and loss modulus (G’’) versus angular frequency for the HECO sample B1 (EPR = 29.6wt%; C2 = 45.0wt%) at *T* = 180, 190 and 200°C. Arrows indicate the cross-over point values.

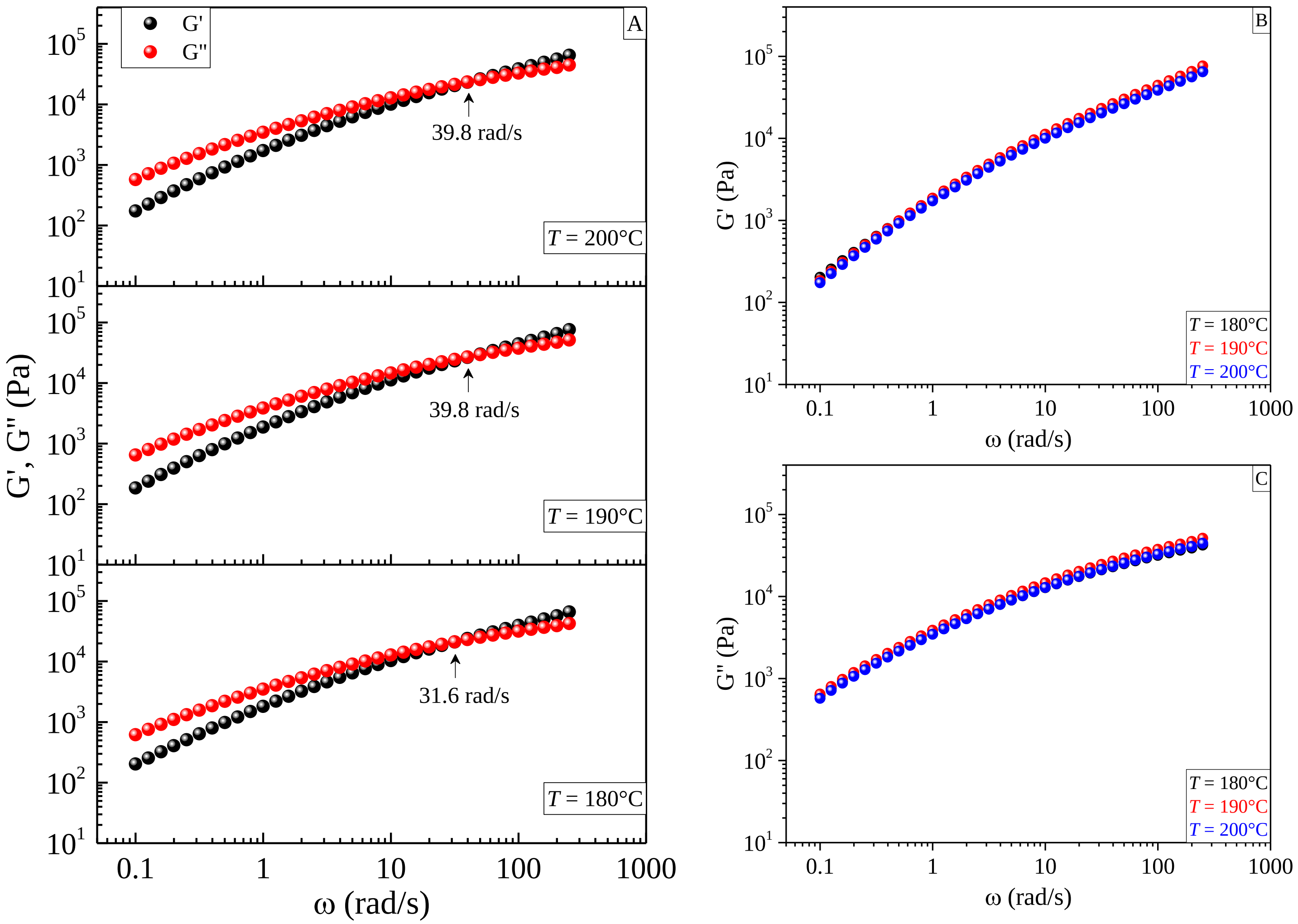

Figure 1.79. Storage modulus (G') and loss modulus (G'') versus angular frequency for the HECO sample EP3307 (EPR = 31.5wt%; C2 = 49.0wt%) at *T* = 180, 190 and 200°C. Arrows indicate the cross-over point values.

Figure 1.80 shows, as an example, a comparison of the moduli obtained at the operating temperature of 190°C. In general, it can be observed that all HECO samples have, especially for low-frequency values, values of moduli lower than those of the homopolymer. However, the decrease is not proportional to the content of the elastomeric phase. In fact, sample 21588/45 (see red trend), which has the lowest content of rubbery phase, shows values of moduli lower than those of the sample EP3307 (see pink trend), which has a total elastomeric phase content of 31.5wt%. The fact that sample EP3307 exhibits moduli values that are very similar to those of the homopolymer could be related to the fact that the third phase (C3C2 = 30wt%) acts as a compatibilizer for the sample examined ensuring greater homogeneity among the different components.

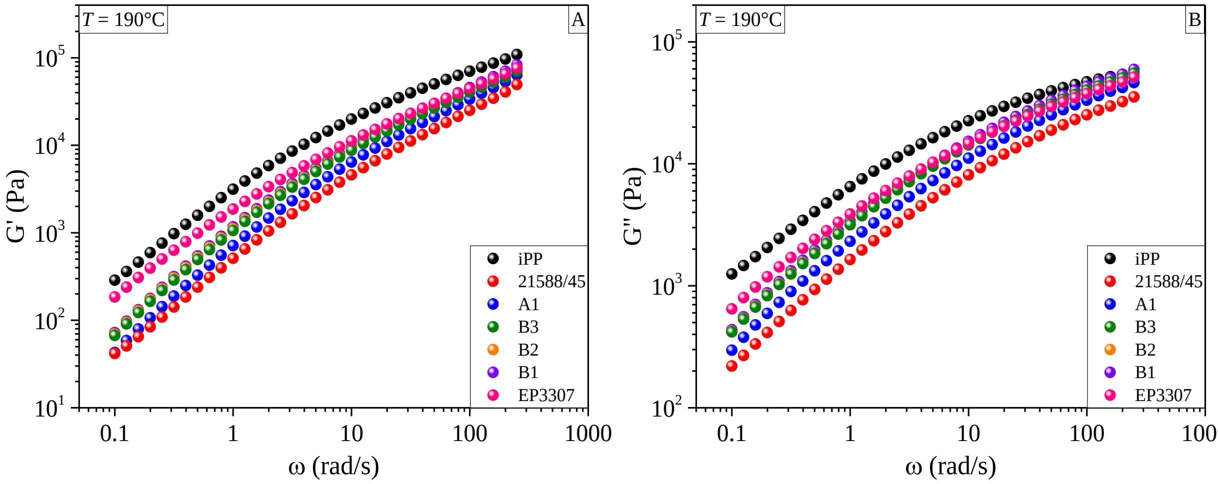

Figure 1.80. Storage modulus, G’, (A) and loss modulus, G’’, (B) versus angular frequency for the homopolymer and all HECO samples at *T* = 190 °C.

Figure 1.81 shows the complex viscosities of all HECO samples and that of the iPP homopolymer obtained at three different temperatures. All samples follow the same trend with values of the complex viscosity decreasing as the frequency increases until roughly reaching the same value at high frequency. However, at lower frequencies, they differ due to differences in the compositions and interactions among the HECO components. In particular, the homopolymer sample has higher complex viscosity values than those of the HECO samples probably because the elastomeric phase has a much lower viscosity than that of the iPP. Nonetheless, with the increasing of the operating temperature the homopolymer shows the same viscosity trend of the other samples. In addition, it can be seen that samples with approximately the same elastomeric phase content (for example the samples with EPR ~ 29wt%) show identical complex viscosity values throughout the frequency range, which decrease with decreasing the percentage of rubbery phase. Therefore, the decrease in complex viscosity values is not proportional to rubbery phase content. In fact, sample 21588/45, which has the lowest elastomeric phase content, exhibits the lowest viscosity value.

Overall, samples do not show strong variations in terms of complex viscosity, suggesting that they approximately have comparable molecular weights.

In order to derive some important rheological parameters, it is necessary to reach Newtonian viscosity plateau. As the Newtonian viscosity plateau cannot be determined directly in the investigated angular frequency range, it is calculated by applying the Carreau-Yasuda model:[37]

$$\eta^* = \eta^*_0\,[1 + (\lambda\omega)^a]^{\left(\frac{n-1}{a}\right)}$$

where η^*_0 is the zero-shear complex viscosity ($\omega \approx 0$), λ is a characteristic relaxation time of the fluid, and *n* is the power-law index. The parameter "a" describes the breadth of the transition region between the Newtonian viscosity plateau and the power-law region. The relaxation time (λ) is represented as: $\lambda = \eta^*_0 / \tau^*$), where τ^* is the shear stress at the transition between Newtonian and power-law regions.

For all HECOs it was possible to apply the Carreau-Yasuda model but for the homopolymer the model did not converge, and a reliable estimate of the rheological parameters was not possible. The data of complex viscosity are fitted in Figure 1.81 with the Carreau-Yasuda and the zero-shear complex viscosity η^*_0 is evaluated by the extrapolation to zero frequency.

The zero-shear complex viscosity and characteristic relaxation time values, extrapolated by the Carreau-Yasuda model for all HECOs, are listed in Table 1.8.

Figure 1.82 shows the values of zero-shear complex viscosity evaluated as a function of both EPR content and ethylene concentration of the EPR. From Figure 1.82A, it can be seen that η^*_0 increases linearly as the content of the dispersed EPR phase increases. On the other hand, no trends are recognizable as a function of the ethylene content (Figure 1.82B) but, in general, the zero-shear complex viscosity is almost constant for samples with the same EPR content and different concentrations of ethylene in the EPR phase. This suggests that zero-shear complex viscosity depends on the EPR content and is independent on the ethylene concentration.

However, the EPR content is not the only factor that controls the viscosity of HECOs because it also depends on the microstructure of different components constituting the elastomeric phase. Indeed, Tian et al.[38] have investigated the roles of ethylene-propylene segmented copolymer (EPS) in high-impact polypropylene copolymers (IPCs) from the viewpoints of rheology. They found that an increase in the EPS content (with a high length of PP sequences) leads to a decrease in the interfacial tension among the various components of a HECO system, confirming the compatibilizing roles of EPS in IPCs.[38]

According to the findings of Tian et al. we could explain why the triphasic sample (EPR = 31.5wt%) has zero-shear complex viscosity values higher than the other samples. In fact, the presence of the C3C2 copolymer at low ethylene concentration (high length of propylene sequences) could have a compatibilizing effect that enhances the dispersion of the EPR phase in the thermoplastic iPP matrix.

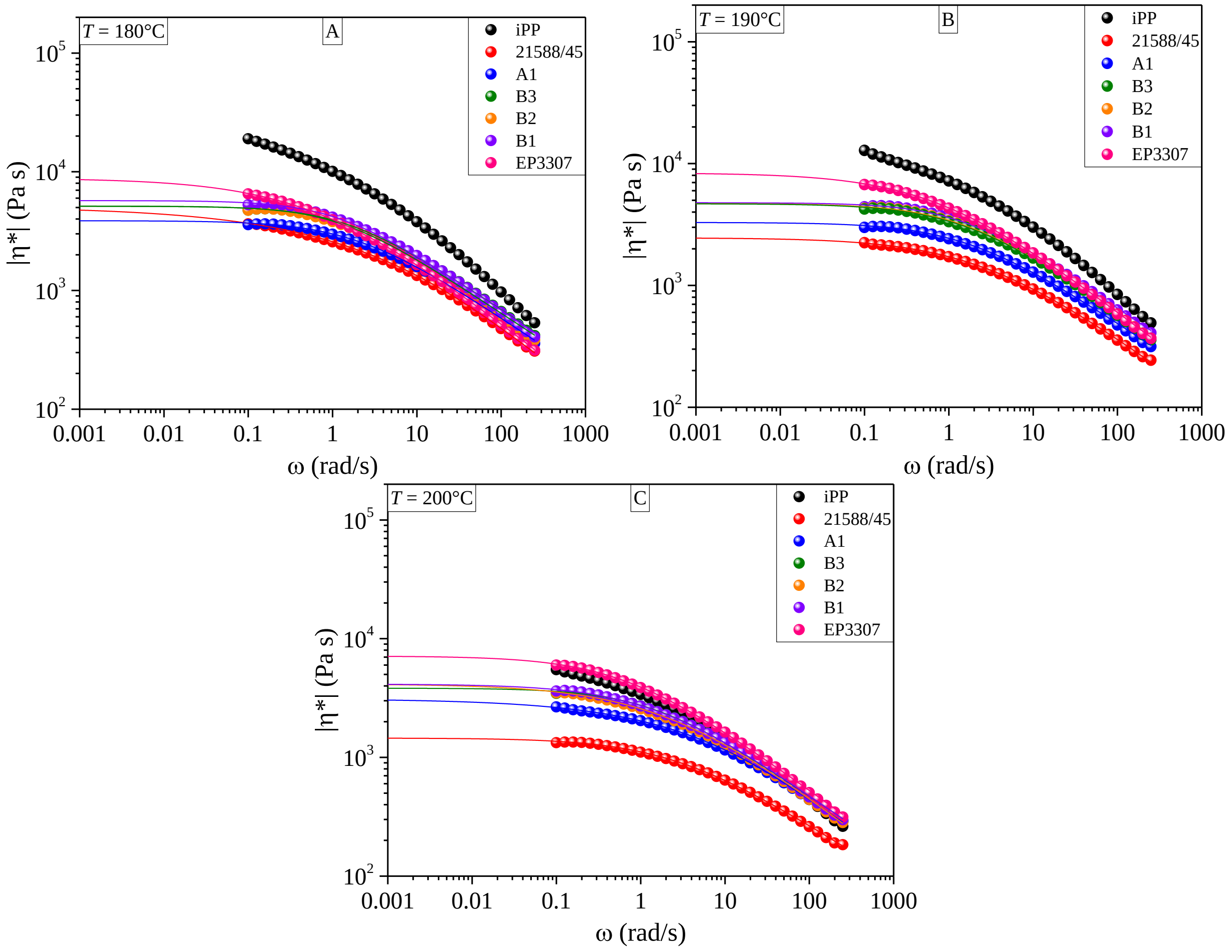

Figure 1.81. Complex viscosity versus angular frequency of the homopolymer and all HECO samples at *T* = 180°C (A), 190°C (B) and 200°C (C).

Table 1.8. Zero-shear complex viscosity and characteristic relaxation time obtained from the Carreau-Yasuda model for all HECO samples.

Samples	**EPR (wt%)**	**C2 (EPR) (wt%)**	**η^*_0 (kPa s)**			**λ (s)**		
			180°C	190°C	200°C	180°C	190°C	200°C
21588/45	22.0	54.0	50.8	24.6	14.6	0.026	0.387	0.382
A1	24.6	45.6	38.7	32.9	30.6	0.498	0.595	0.100
B3	28.7	60.0	51.2	46.8	38.3	0.682	0.594	0.706
B2	29.0	51.0	51.4	47.0	41.5	0.812	0.671	0.422
B1	29.6	45.0	57.1	47.7	41.4	0.881	0.696	0.665
EP3307	31.5	49.0	88.3	83.8	71.4	1.31	1.31	1.53

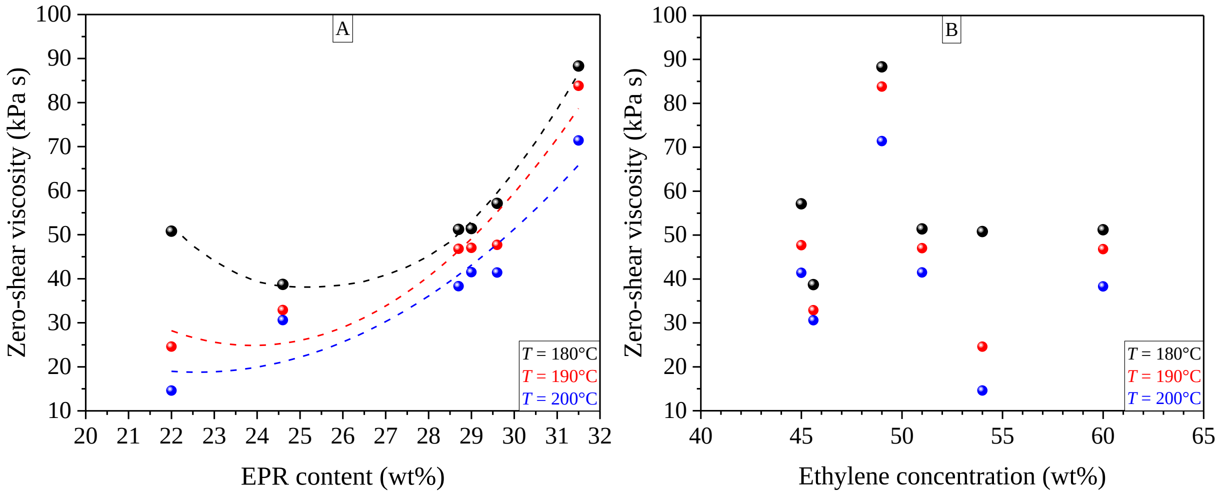

Figure 1.82. Zero-shear viscosity as a function of the EPR content (A) and ethylene concentration of the rubbery phase (B).

PARAGRAPH 1.8, PAGES 125-152 : EMBARGOED

References for Chapter 1

1. C. Cecchin, G. Morini, A. Pelliconi, *Macromol. Symp.* **2001**, *173*, 195-209.

2. G. Natta, P. Corradini, *Nuovo Cimento Suppl*. **1960**, *15*, 40.

3. S. T. Hikosaka M., *Polym. J*. **1973**, *5*, 111.

4. Z. J. Mencik, *Macromol. Sci., Phys.* **1972**, *B6*, 101.

5. G. Guerra, V. Petraccone, P. Corradini, C. De Rosa, R. Napolitano, B. Pirozzi and G. J. Giunchi, *Polym. Sci*., *Polym. Phys*. **1984**, *22*, 1029.

6. F. Auriemma, O. Ruiz de Ballestreros, C. De Rosa and P. Corradini, *Macromolecules* **2000**, *33*, 8764.

7. Bunn C. W.; *Trans Faraday Soc*, **1939**, *35*, 482.

8. S.V. Meille, D.R. Ferro, S. Brückner, A.J. Lovinger, F.J. Padden, *Macromolecules* **1994**, *27*, 2615.

9. B. Lotz, S. Kopp, D.L. Dorset, C. R. *Acad. Sci. (Paris), Ser. IIB* **1994**, *319*, 187.

10. D.L. Dorset, M.P. McCourt, S. Kopp, M. Schumacher, T. Okihara, B. Lotz, *Polymer* **1998**, *39*, 6331.

11. S.V. Meille, S. Brückner, *Nature*, **1989**, *340*, 455-457.

12. S.V. Meille, S. Brückner, W. Porzio, *Macromolecules* **1990**, *23*, 4114-4121.

13. S. Brückner, S.V. Meille, V. Petraccone, B. Pirozzi, *Progr. in Polymer Science* **1991**, *16*, 361-404.

14. F.S. Bates, G.H. Fredrickson, *Macromolecules* **1994**, *27*, 1065-1067.

15. F.S. Bates, *Science* **1991**, *251*, 898-905.

16. R. Greco, G. Ragosta, *J. Mater. Sci*. **1988**, *23*, 4171-4180.

17. O. Ibhadon, *J. Appl. Polym. Sci*. **1998**, *69*, 2657-2661.

18. A. van der Wal, J.J. Mulder, R.J. Gaymans, *Polymer* **1998**, *39*, 5477-5481.

19. M. Elmajdoubi, T. Vu-Khanh, *Theoretical and Applied Fracture Mechanics* **2003**, *39*, 117–126.

20. C. De Rosa, F. Auriemma, R. Di Girolamo, O. Ruiz de Ballesteros; *J. Polym. Sci., Part B: Polym. Phys.* **2014**, *52*, 677.

21. I. Coccorullo, R. Pantani, G. Titomanlio; *Polymer* **2003**, *44*, 307.

22. R. Androsch, *Macromolecules* **2008**, *41*, 533–535.

23. D. Mileva, R. Androsch, E. Zhuravlev, C. Schick, *Macromolecules* **2009**, *42*, 7275–7278.

24. R. Androsch, M.L. di Lorenzo, C. Schick, B. Wunderlich, *Polymer* **2010**, *51*, 4639–4662.

25. D. Mileva, R. Androsch, E. Zhuravlev, C. Schick, B. Wunderlich, *Thermochim. Acta* **2011**, *522*, 100–109.

26. A. Wurm, A. Herrmann, M. Cornelius, E. Zhuravlev, D. Pospiech, R. Nicula, C. Schick, *Macromol. Mater. Eng.* **2015**, *300*, 637–649.

27. A. Toda, R. Androsch, C. Schick, *Polymer* **2016**, *91*, 239–263.

28. F. de Santis, S. Adamovsky, G. Titomanlio, C. Schick, *Macromolecules* **2007**, *40*, 9026–9031.

29. R. Androsch, M.L. di Lorenzo, C. Schick, B. Wunderlich, *Polymer* **2010**, *51*, 4639–4662.

30. C. Silvestre, S. Cimmino, D. Duraccio, C. Schick, *Macromol. Rapid Comm.* **2007**, *28*, 875–881.

31. D. Mileva, J. Wang, M. Gahleitner, K. Jariyavidyanont, R. Androsch, *Polymers* **2020**, *12*, 1683

32. C.C. Hsu, P.H. Geil, H. Miyaji, K. Asai, *J. Polym. Sci. Polym. Phys.* **1986**, *24*, 2379–2401.

33. T. Ogawa, H. Miyaji, K. Asai, *J. Phys. Soc. Jpn.* **1985**, *54*, 3668–3670.

34. Q. Zia, R. Androsch, H.J. Radusch, S. Piccarolo, *Polymer* **2006**, *47*, 8163–8172.

35. Q. Zia, R. Androsch, H.J. Radusch, E. Ingoliç, *Polym. Bull.* **2008**, *60*, 791–798.

36. C. Grein, K. Bernreitner, M. Gahleitner, *J. Appl. Pol. Sci.* **2004**, *93*, 1854–1867.

37. K. Yasuda, R. C. Armstrong, R. E. Cohen, *Rheol. Acta* **1981**, *20*, 163−178.

38. Z. Tian, L. F. Feng, Z. Q. Fan, G. H. Hu, *Ind. Eng. Chem. Res.* **2014**, *53*, 11345-11354.

39. A.J. Müller, M.L. Arnal, *Prog Polym Sci* **2005**, *30*, 559.

40. B. Fillon, J. Wittmann, B. Lotz, A. Thierry, *J. Polym Sci Pol Phys* **1993**, *31*, 1383.

41. D.J. Blundell, A. Keller, A.J. Kovacs, *J. Polym Sci B Polym Lett* **1966**, *4*, 481.

42. A.J. Müller, R.M. Michell, R.A. Pérez, A.T. Lorenzo, *European Polymer Journal* **2015**, *65*, 132–154.

43. L. Sangroniz, D. Cavallo, A. J. Müller, *Macromolecules* **2020**, *53*, 4581−4604.

44. J.Xu, Y. Ma, W. Hu, M. Rehahn, G. Reiter, *Nat. Mater.* **2009**, *8*, 348−353.

45. B. O. Reid, M. Vadlamudi, A. Mamun, H. Janani, H. Gao, W. Hu, R.G. Alamo, *Macromolecules* **2013**, *46*, 6485−6497.

46. M. J. Muthukumar, *Chem. Phys.* **2016**, *145*, 031105.

47. X. Chen, A. Mamun, R.G. Alamo, *Macromol. Chem. Phys.* **2015**, *216*, 1220−1226.

48. B. Fillon, J.C. Wittmann, B. Lotz, A. Thierry, *J. Polym. Sci., Part B: Polym. Phys.* **1993**, *31*, 1383−1393.

49. D. Cavallo, L. Gardella, G. Portale, A.J. Müller, G.C. Alfonso, *Polymer* **2013**, *54*, 4637−4644.

50. G. Reiter, *Chem. Soc. Rev*. **2014**, *43*, 2055−2065.

51. F. Su, X. Li, W. Zhou, S. Zhu, Y. Ji, Z. Wang, Z. Qi, L. Li, *Macromolecules* **2013**, *46*, 7399−7405.

52. N. Zaldua, J. Maiz, A. de la Calle, S. García-Arrieta, C. Elizetxea, I. Harismendy, A. Tercjak, A.J. Müller, *Polymers* **2019**, *11*, 1680.

53. A.T. Lorenzo, M.L. Arnal, J.J. Sánchez, A.J. Müller, J. *Polym. Sci., Part B: Polym. Phys.* **2006**, *44*, 1738-1750.

54. R.M. Michell, A. Mugica, M. Zibitur, A.J. Müller, *Adv. Polym. Sci*. **2016**, *276*, 215-256.

Chapter 2

PAGES 156-218 : EMBARGOED

CHAPTER 3

Blends of heterophasic copolymers with random and block copolymers

As revealed by the analyses performed in Chapter 2, a heterophasic copolymer is composed of the thermoplastic matrix of isotactic polypropylene (iPP) as the main component and multiple fractions with different microstructures and final properties. Among the different fractions extracted from heterophasic copolymers, families of macromolecules with ethylene concentration as high as 70mol% and with polyethylene (PE)-like microstructure have been found.

Despite their strong similarity in terms of hydrocarbon composition, samples of iPP and PE are immiscible with each other.[1,2] This phenomenon is accentuated if the two starting polymers are synthesized with heterogeneous catalysts involving chains with different molecular mass and molecular mass distribution and different microstructures. This results in a separation between the two phases that inhibits good interfacial interaction and gives bad mechanical properties to the final blends.[3,4] To improve the mechanical properties of blends and overcome this limitation, different types of additives, including amorphous copolymers[5-7] and semi-crystalline block and multi-block copolymers,[8] have been used as compatibilizers of blends of the two starting homopolymers. More recently, the strategy of using block copolymers (iPP-*b*-PE) or multi-block copolymers (iPP-*b*-PE-*b*-iPP-*b*-PE), synthesized with a hafnium-based isoselective catalyst,[8] has been chosen in order to increase the degree of interpenetration between the chemically identical blocks of the copolymer and the two starting homopolymers in the molten state and increase the interfacial adhesion between iPP and PE.[9-11] According to Ref. 8, employing block copolymers, with a greater effect using tetrablock copolymers, allows for morphological control, turning brittle materials into blends that are mechanically resilient. Based on these results obtained on iPP/PE blends and considering that HECO samples are reactor blends of iPP and a heterogeneous C3C2 copolymer, we apply the same strategy of using compatibilizers of the two phases to improve the mechanical properties of HECOs. Copolymers of different natures and microstructures, produced with different catalysts and synthetic technologies, were used as possible compatibilizers. More specifically, the following random and block copolymers have been used:

- Monodisperse di-block copolymers obtained by living organometallic catalysis based on hafnium isoselective catalyst and with the operating conditions described in ref. 8;
- Polydisperse multi-block copolymers synthesized by chain-shuttling technology;[12]

- Random C3C2 copolymers produced by using a zirconium-based metallocene catalyst.

Finally, in order to test whether other polymer additives could also work in blends with isotactic polypropylene, we also studied blends of iPP with isotactic ethylene/1-butene copolymers (C2C4) and with another elastomeric phase consisting of a very high molecular weight sample of poly(1-octene) (PO).

3.1. Methods

Blends of HECO samples and copolymers of different natures were prepared by dissolving a certain amount of the two selected components in xylene (mixture of isomers), at its boiling temperature and under stirring, keeping to a HECO/copolymer ratio of 95:5wt or 90:10wt%. In contrast, for iPP/C2C4 and iPP/PO blends, blends with different iPP/additive ratios were prepared. Specifically, blends with the isotactic ethylene/1-butene copolymers were prepared at 30wt% C2C4 copolymer with the aim of emulating the iPP/C3C2 ratios of a standard heterophasic copolymer, while in the case of blends with poly(1-octene) (PO), different samples were prepared at 10, 30, and 40wt% of the PO rubbery phase. The dissolution process was interrupted when all the components of the mixture were completely solubilized resulting in a clear solution (about 2 hours). After this time, the still-hot solution was quickly poured into cold methanol in order to allow the polymer coagulation, filtered, and dried in a vacuum oven at 60°C until reaching a constant weight.

All samples were, then, analyzed to study their structural, thermal, and mechanical properties. X-ray diffraction patterns were recorded at room temperature with Ni-filtered Cu K_α radiation ($\lambda = 1.5418$ Å). The powder diffraction profiles were obtained with an automatic PANalytical Empyrean diffractometer. The voltage and the current adopted for the test were 40 kV and 40 mA, respectively. The diffraction profiles were recorded through a continuous scan of the diffraction angle 2θ, in a range of 5-40° with a speed of 0.02°/s ($\Delta 2\theta = 0.1°$ and $\Delta t = 5$s). The degree of crystallinity x_c has been evaluated from the X-ray diffraction profiles by the ratio between the crystalline diffraction area (A_{cr}) and the total area of the diffraction profile (A_{tot}):

$$x_c = \frac{A_{cr}}{A_{tot}} \cdot 100 = \frac{A_{tot} - A_{am}}{A_{tot}} \cdot 100$$

The crystalline diffraction area has been obtained from the total area of the diffraction profile by subtracting the diffraction halo of the amorphous phase (A_{am}) after scaling and subtraction of a straight baseline.

Calorimetric measurements have been performed with the DSC822 calorimeter by Mettler Toledo, in a flowing N_2 atmosphere at a scan rate of 10°C/min. All samples were first heated up to the melting from -40°C to 200°C (first heating scan), then cooled from 200°C to -40°C (cooling scan), and finally heated again from -40°C to 200°C (second heating scan).

Mechanical tests were performed at room temperature on melt crystallized compression-molded films with a Zwicky tester machine (by Zwick Roell), following the standard test method for tensile properties of thin plastic sheeting ASTM D882. Rectangular specimens 100 mm long and 5 mm wide, cut from the compression-molded films by using a die-cutter, have been stretched up to the break while recording the stress-strain curves to determine mechanical tensile parameters, such as the stress and strain at breaking (σ_b and ε_b) and, eventually, at yield point (σ_y and ε_y). The values of Young's modulus (E) have been determined in independent experiments. The analysis was conducted on compression-molded samples crystallized from the melt with slow-controlled conditions (about 10°C/min). The reported stress-strain curves and the values of mechanical properties are averaged over at least five independent experiments.

3.2. Block copolymers by living catalysts

Block copolymers (BCPs) are composed of chemically diverse macromolecules that are covalently bonded and have an architecture that is either linear or nonlinear and that tends to segregate into various microdomains, with the spontaneous formation of different nanostructures,[13-17] as a result of their mutual repulsion. Ionic, radical, and ring-opening metathesis polymerization (ROMP) are three common methods for creating BCPs with specific topologies and monodisperse molecular weights. These techniques allow for the uninterrupted sequential enchainment of monomer units, offer fine molecular weight control, and allow for the synthesis of a broad variety of polymeric structures. However, with these techniques, crystalline BCPs composed of stereoregular polyolefins cannot be produced. Only recently, several stereoselective catalysts able to promote the stereoselective and living polymerization of olefins have been discovered and novel block copolymers based on stereoregular polypropylene and polyethylene with different architectures have been produced.[18-24] In particular, living catalytic polymerization allows for the synthesis of semicrystalline block copolymers by the successive addition of monomers and/or end-functionalized macromolecules.[20-24]

In this work, samples of isotactic polypropylene-*block*-polyethylene (iPP-*b*-PE) and isotactic polypropylene-*block*-linear-low-density polyethylene (iPP-*b*- LLDPE) were used, which were synthesized by living polymerization with a Hf-based post-metallocene catalyst reported in Figure 3.1.

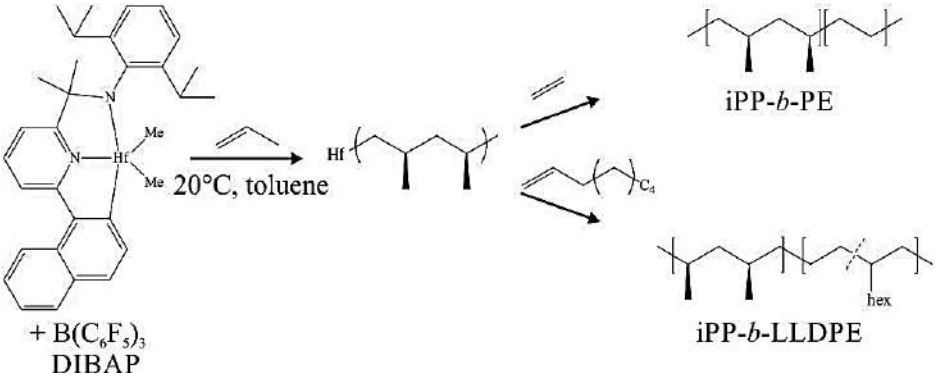

Figure 3.1. Structure of the hafnium complex used as a catalyst for the preparation of the iPP-*block*-PE and iPP-*block*-LLDPE block copolymer samples and the scheme of the sequential polymerization procedure.

Table 3.1 shows the main characteristics of the block copolymers used for the preparation of blends (5wt% of compatibilizer). All the block copolymers have high molecular mass ($180 < M_w < 280$ kDa) and a weight fraction of ethylene (f(C2)) varying between 20 and 90wt%.; in particular, the JME-V-256 copolymer sample has a high ethylene content (about 90wt%) while the other samples have an ethylene content varying between 20 and 35wt%. Copolymers RDG-1-138 and RDG-1-166 have the same molecular mass of the iPP block ($M_n \approx 95$kDa) and a different length of the PE block ($M_n = 50$kDa and 86kDa, respectively). The JME-V-54 copolymer has a high molecular mass iPP block ($M_n = 120$kDa) and a low molecular mass LLDPE block ($M_n = 35$kDa) while the JME-V-256 sample has a short iPP block ($M_n = 31$kDa) and a long LLDPE block ($M_n = 180$kDa). The LLDPE block corresponds to a random ethylene-1-octene copolymer with a 1-octene concentration of 1.5mol% (f(C8)).

Table 3.1. Main characteristics of iPP-*b*-PE and iPP-*b*-LLDPE block copolymers used as compatibilizers for HECOs.

Sample	Type	M_n (kDa)	M_w (kDa)	PDI	f(C8) (mol%)	f(C2) (wt%)	M_n (iPP) (kDa)	M_n (PE) (kDa)
RDG-1-138	iPP-*b*-PE	144.7	188.1	1.30	-	31	94.6	50.1
RDG-1-166		180.6	227.6	1.26	-	36	94.6	86
JME-V-54	iPP-*b*-LLDPE	155	201.5	1.3	1.5	23	120	35
JME-V256		211	274.3	1.3	1.5	86	31	180

3.2.1. Effect of iPP-b-PE copolymers in blend with HECOs

Figure 3.2 shows DSC thermograms (Figure 3.2A), X-ray diffraction profiles of samples crystallized from the melt (Figure 3.2B), and stress-strain curves (Figure 3.2C) of samples of the iPP-*b*-PE block copolymers RDG-1-138 and RDG-1-166. Thermal analysis (Figure 3.2A) reveals that samples exhibit thermograms with a single intense peak of both melting (T_m ≈ 130°C) and crystallization (T_c ≈ 106-109°C) indicating that the two blocks of iPP and PE, melt and crystallize at about the same temperature and the two phenomena overlap.

The diffraction profiles (Figure 3.2B) show that the two samples exhibit crystallinity from both isotactic polypropylene and polyethylene as evidenced by the simultaneous presence of the $(110)_\alpha$, $(040)_\alpha$, and $(130)_\alpha$ reflections characteristic of the α-form of isotactic polypropylene and the $(110)_{PE}$ and $(200)_{PE}$ reflections characteristic of the orthorhombic form of polyethylene. In addition, the samples crystallized from the melt also exhibit the reflection located at values of $2\theta \approx 20°$ characteristic of the γ form of iPP indicating that, actually, these samples crystallize in a mixture of α and γ form crystals. From the stress-strain curves shown in Figure 3.2C, it can be deduced that the two samples exhibit excellent mechanical properties with high deformation at break with a marked strain-hardening phenomenon. In addition, the samples are characterized by high tensile and mechanical strength, and moderate yielding stress values in agreement with the crystallinity indices evaluated by the diffraction profiles in Figure 3.2B.

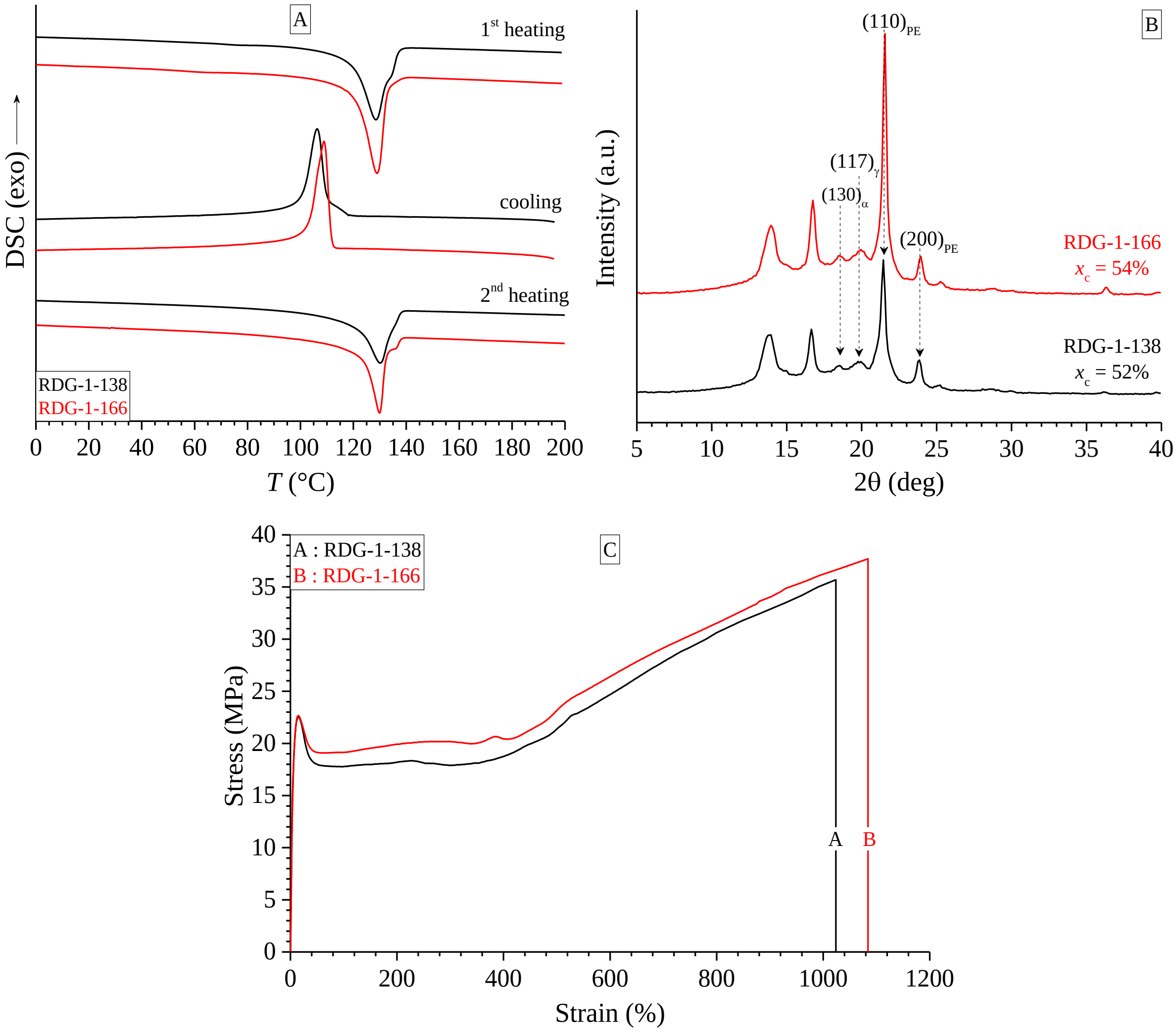

Figure 3.2. DSC thermograms (A), X-ray powder diffraction patterns of compression-molded films (B), and stress-strain curves (C) of iPP-*b*-PE block copolymer samples RDG-1-138 and RDG-1-166.

In order to investigate the possible compatibilizing effect of block copolymers, four of the six available HECO samples shown in Table 1.1 of Chapter 1 were selected. Specifically, we chose two samples with similar content of rubbery phase (≈ 29wt%) but different ethylene concentrations of EPR, that is, the samples B1 (C2 = 45.0wt%) and B3 (C2 = 60.0wt%), the sample EP3307 with the two C3C2 copolymers (EPR1 = 11.5wt% and EPR2 = 20.0wt%), and the sample with the lowest elastomeric phase content, 21588/45 (EPR = 22.0wt%).

The X-ray powder diffraction profiles recorded on all blends, as obtained immediately after the blending process, are reported in Figure 3.3. The diffraction profiles show that all samples crystallize in the α-form of isotactic polypropylene as evidenced by the presence of the peaks at 2θ = 14°, 16.9°, 18.6°, and 21.3° corresponding to the (110)α, (040)α, (130)α and (111)α reflections of the α-form of the iPP. In addition, all samples also present a low-intensity peak at 2θ ≈ 23.5° corresponding to the reflection $(200)_{PE}$ of the orthorhombic form of polyethylene.

This implies that there is also a small amount of polyethylene crystals in all samples, due to the crystallization of PE from the EPR phase of the HECO samples and/or due to the contribution of the PE block of the block copolymer samples. However, in the pure HECO samples, this reflection of PE is clearly observed only in the diffraction profile of the sample B3 with the highest ethylene concentration (Figure 1.4). Therefore, the presence of the compatibilizer, probably, favours the crystallization of macromolecules of the EPR phase rich in long ethylene sequences.

For blends of sample EP3307, in addition, at low and high values of 2θ, there are also very narrow Bragg reflections (≈ 9.5° and 29°) ascribable to the presence of the talc.

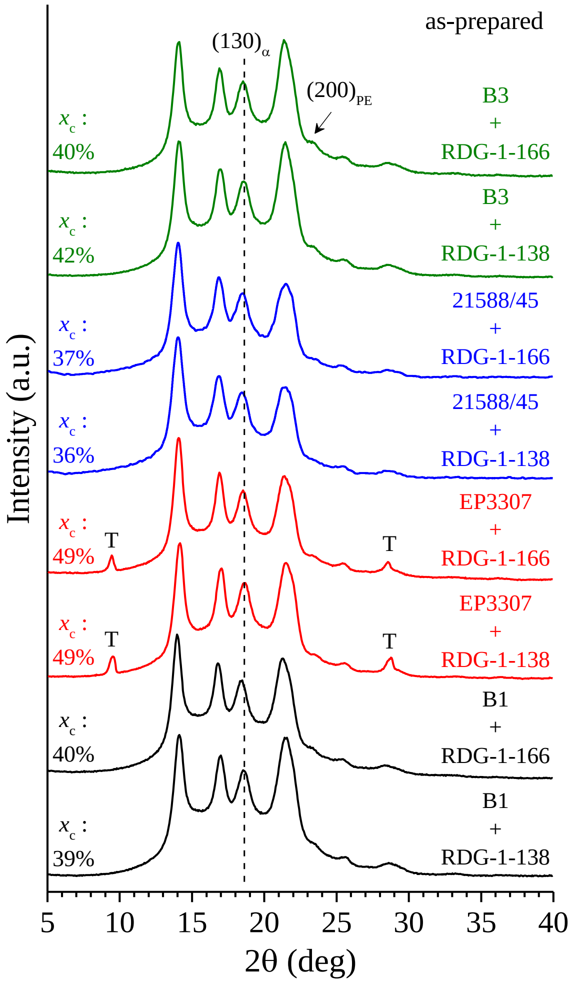

Figure 3.3. X-ray powder diffraction patterns of all the "as-prepared" blends of HECO samples with the iPP-*b*-PE copolymers.

Figure 3.4 shows the DSC thermograms of the first heating (A), cooling (B), and second heating (C) of the analyzed blend samples. In the heating thermograms, in addition to the main melting peaks at about 165-170°C corresponding to the melting of the α-crystals of the thermoplastic matrix of iPP, there are low-enthalpy melting peaks at lower temperatures (T_m ≈ 120°C) attributable to the melting of defective polyethylene crystals. This implies that the melting of crystals belonging to the two different phases of compatibilized HECO copolymers occurs independently of each other. On the other hand, for almost all samples, except samples B3 and EP3307, a single crystallization peak in the cooling thermograms is observed. Since the thermal analysis performed on the non-compatibilized HECO samples had shown the presence of two distinct crystallization peaks, one at a higher temperature attributable to the iPP matrix and one at a lower temperature related to the crystallization of polyethylene-like crystals (see Figure 1.5, Chapter 1), we can conclude that the addition of the iPP-*b*-PE samples produces an increase of the crystallization temperature of PE from the EPR and the PE crystallization peak almost overlaps with the crystallization peak of the iPP matrix. In other words, the two phases crystallize at about the same temperature and the two phenomena superimpose.

Table 3.2 shows the thermal parameters obtained from DSC thermograms of Figure 3.4, while Figure 3.5 reports the crystallization and melting (from 2nd heating thermograms) temperatures of the EPR phase of all HECOs before and after the addition of 5wt% of iPP-*b*-PE copolymers. From the data shown in Table 3.2, it is evident that after the addition of the compatibilizers, the values of the crystallization and melting temperatures of the thermoplastic matrices of the investigated samples do not experience great changes. However, as becomes even more evident from Figure 3.5, the addition of the block copolymers greatly affects the thermal properties of the elastomeric phase in terms of melting and crystallization temperature values. In fact, the addition of the compatibilizer results in an increase in the crystallization temperature of the PE-like crystals of the rubbery phase by about 11-14°C compared to the non-compatibilized sample. This result implies that the polyethylene-like crystals develop earlier and almost concomitantly with the iPP crystals. Probably, this finding is synonymous with compatibilization occurring in the molten state between the two phases that constitute a heterophasic copolymer as a result of an increase in physical junctions between chemically identical blocks in the mixture. This result could also be facilitated by a nucleating effect of iPP crystals on PE.

Consequently, also the melting temperatures evaluated from thermograms of the second heating are affected by the addition of the compatibilizer. In fact, values of T_m increase in the range of 4-10°C indicating PE-like crystals with greater lamellar thicknesses that melt at higher temperatures.

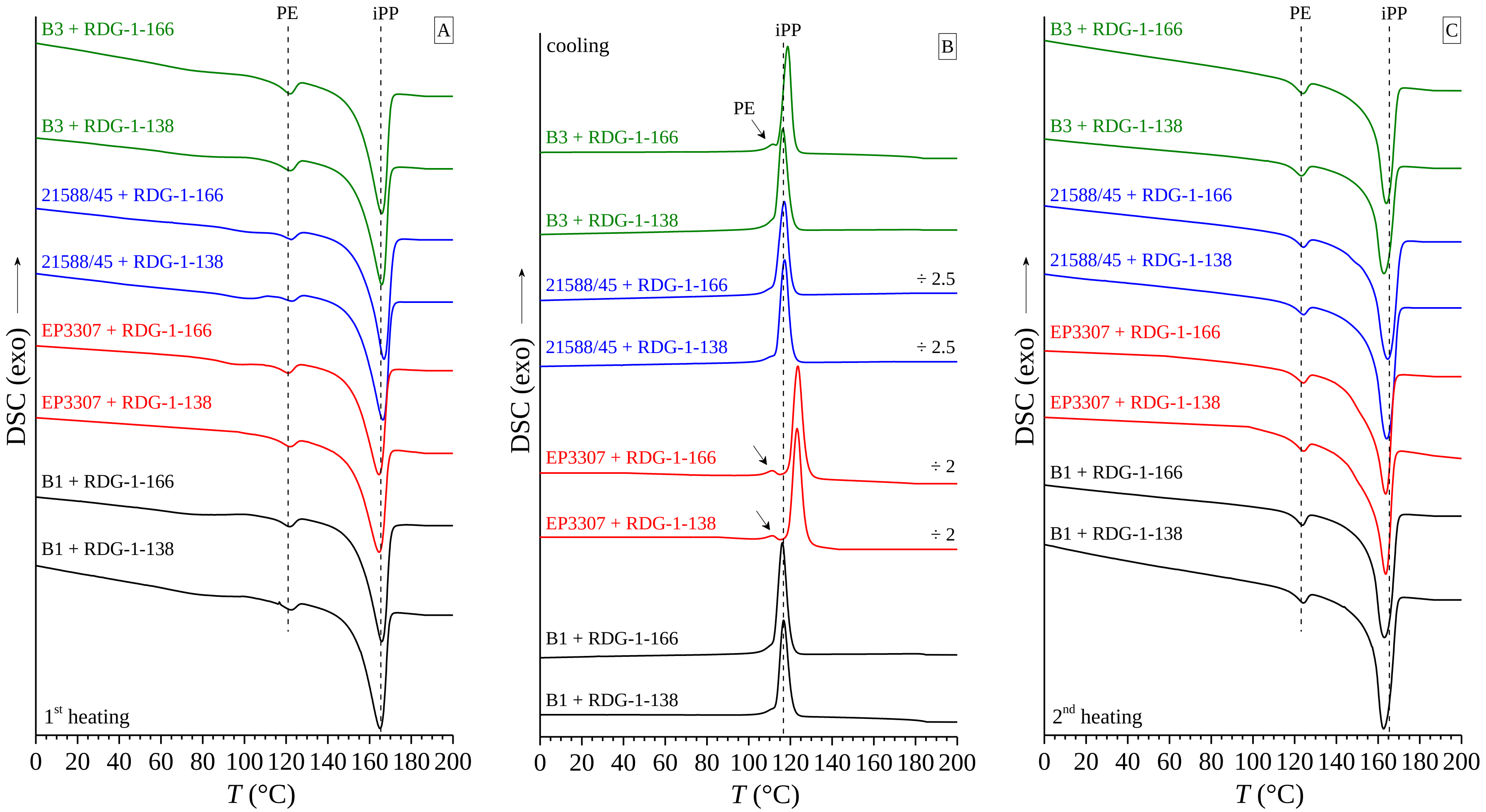

Figure 3.4. Comparison of DSC thermograms of first heating (A), cooling (B), and second heating (C) of all "as-prepared" blends of HECOs with iPP-*b*-PE copolymers.

Table 3.2. Values of melting temperatures and enthalpies recorded in first heating (T_m^I and ΔH_{mTOT}^I), crystallization temperatures and enthalpies (T_c, ΔH_c), and melting temperatures and enthalpies recorded in second heating (T_m^{II}, ΔH_{mTOT}^{II}) of iPP-*b*-PE copolymer samples, non-compatibilized HECO samples and blends of HECOs with iPP-*b*-PE block copolymer samples. Subscripts “1” and “2” refer to values for PE and α-form crystals, respectively.

Sample	T_{m1}^I (°C)	T_{m2}^I (°C)	ΔH_{mTOT}^I (J/g)	T_{c1} (°C)	T_{c2} (°C)	ΔH_c (J/g)	T_{m1}^{II} (°C)	T_{m2}^{II} (°C)	ΔH_{mTOT}^{II} (J/g)
RDG-1-138	129	134	105.4	106	106	86.5	130	136	89.1
RDG-1-166	129	-	112.3	109	109	89.1	130	136	92.1
B1	-	165.4	72.0	99.8	116.1	82.4	118.2	163.2	85.8
B1 + RDG-1-138	122.1	165.1	83.3	110.8	116.7	77.6	124.1	162.6	86.1
B1 + RDG-1-166	121.6	165.8	75.9	110.7	116.2	75.7	123.7	163.0	77.4
EP3307	117.6	165.6	68.2	100.4	124.8	81.0	118.6	164.4	79.6
EP3307 + RDG-1-138	113.6	164.5	69.7	114.2	127.4	76.2	124.6	163.7	70.6
EP3307 + RDG-1-166	113.7	164.4	65.9	111.2	127.9	74.9	124.7	163.6	69.3
21588/45	113.3	168.6	73.9	96.0	120.2	78.9	114.6	163.7	89.4
21588/45 + RDG-1-138	122.6	166.5	82.6	110.0	117.2	76.8	124.3	164.1	85.5
21588/45 + RDG-1-166	122.4	166.9	78.8	110.0	117.0	75.6	124.2	164.6	82.0
B3	119.3	166.8	75.3	100.4	116.2	85.7	120.1	163.6	88.2
B3 + RDG-1-138	121.9	166.0	74.8	111.5	116.3	79.0	123.3	162.8	81.6
B3 + RDG-1-166	121.7	165.7	79.7	111.7	118.7	84.8	123.7	163.9	81.9

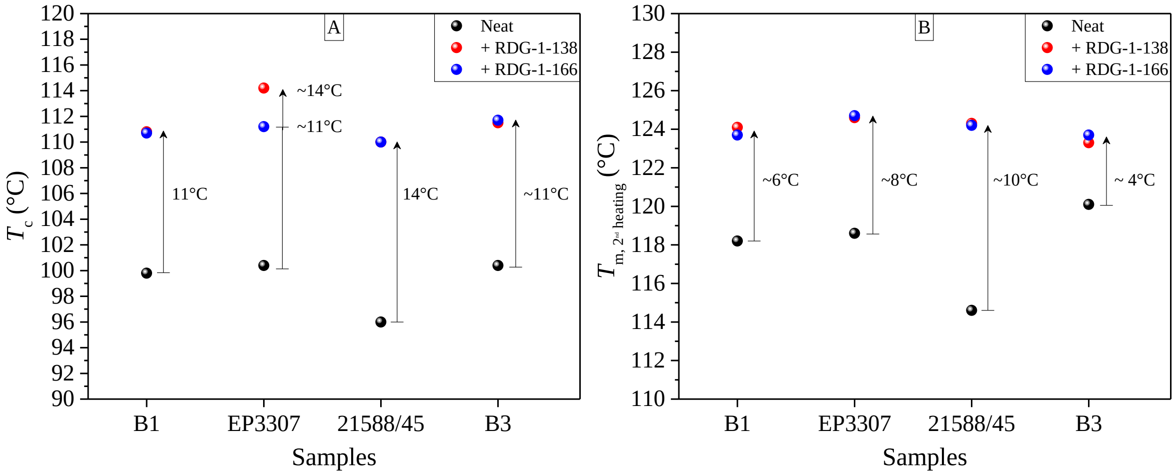

Figure 3.5. Crystallization (A) and melting temperatures from second heating thermograms (B) of PE crystals from the EPR phase of all HECO samples before and after adding iPP-*b*-PE samples as compatibilizers.

To evaluate the effect of compatibilizers on the HECO samples, an analysis of mechanical properties was performed on all compression-molded films of blends, recording stress-strain curves. The X-ray powder diffraction profiles of all compression molded films obtained by slow cooling from the melt are reported in Figure 3.6. The diffraction profiles show that all samples crystallize in the α-form of isotactic polypropylene. However, for the blend B3 + RDG-1-138 it is also possible to notice the presence of the peak at $2\theta = 16°$, corresponding to the reflection $(110)_\beta$ of the β-form of iPP. For blends of the sample EP3307 is still possible to note Bragg reflections due to the talc.

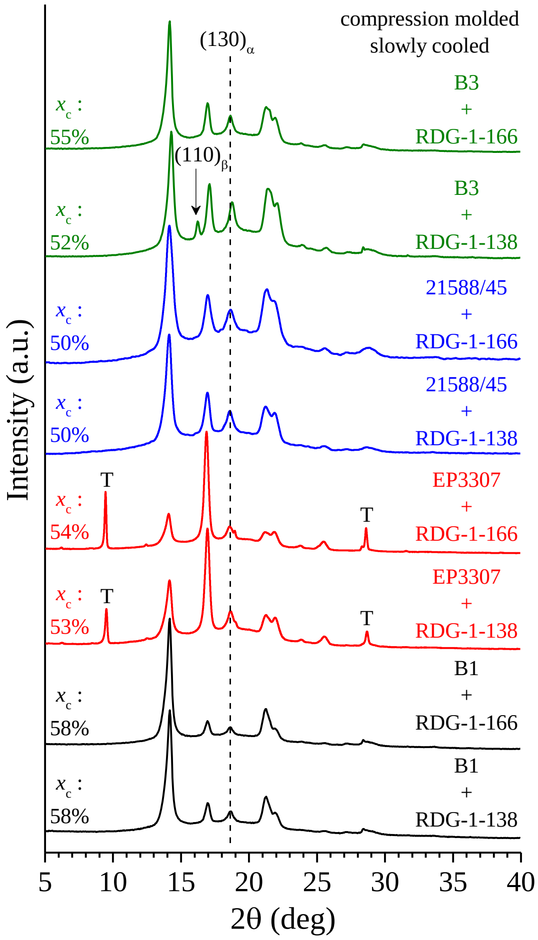

Figure 3.6. X-ray powder diffraction profiles of the compression molded films of blends of HECO samples with iPP-*b*-PE block copolymers.

Figure 3.7 shows the stress-strain curves of all blends recorded at room temperature on compression-molded films crystallized by slow cooling from the melt. For completeness, the stress-strain curves of the non-compatibilized samples are also shown in Figure 3.7. The values of the mechanical parameters evaluated from the stress-strain curves of Figure 3.7 are reported in Table 3.3.

It is evident from Figure 3.7A that the introduction of block copolymers into sample B1 does not produce an improvement of ductility, compared to the un-compatibilized sample. If we refer to the fractionation data reported in Chapter 2, it can be seen that sample B1 has an ethylene-rich fraction percentage (F4, C2 = 72.7mol%) of only 4wt%. This means that, overall, the macromolecules rich in long ethylene sequences are very dilute in the system, and, probably, the "PE" block of iPP-*b*-PE copolymers is unable to establish an interaction with this fraction of macromolecules. It could, therefore, be possible that the introduction of 5wt% of the iPP-*b*-PE copolymer sample contributes to increasing the degree of incompatibility in the HECO sample leading to a worsening of its mechanical properties.

On the other hand, the introduction of the iPP-*b*-PE copolymers in samples EP3307 (Figure 3.7B), 21588/45 (Figure 3.7C), and B3 (Figure 3.7D) leads to, in almost all cases, significant improvements to the strain-at-break of the HECO samples. Such materials are, in fact, composed of macromolecule fractions rich in a very high polyethylene-like microstructure that is in the range of 8-25wt%. An increase, therefore, in the concentration of these fractions in HECO copolymers could be the reason for a good compatibilizing effect by the block copolymers. This result is consistent with the fact that sample EP3307, which has a total percentage of F4 and F5 fraction of about 25wt%, undergoes the most effective enhancement when mixed with the block copolymers. In particular, sample RDG-1-166 seems to make the best improvements to sample EP3307 and also to samples 21588/45 and B3. This outcome is related to the fact that sample RDG-1-166 has a higher average molecular mass (and thus length) of the PE block than sample RDG-1-138 (see Table 3.1). Accordingly, samples with a longer polyethylene block are required for a block copolymer of the iPP-*b*-PE type to act as an efficient compatibilizer. In short, the addition of the compatibilizer promotes interfacial adhesion between the two chemically different phases by tending to accumulate at the interface of the two separate phases. In recent studies,[8,27] a model of interfacial adhesion of iPP/HDPE blends in the presence of compatibilizers of the iPP-b-PE nature has been proposed, which involves the two-block copolymer forming physical junctions with the two starting homopolymers by increasing their number of entanglements in the molten state. During cooling, co-crystallization of the two blocks with the crystalline lamellae of the homopolymers occurs at the amorphous interface of the two phases, locking them together and resulting in improvements in mechanical properties.

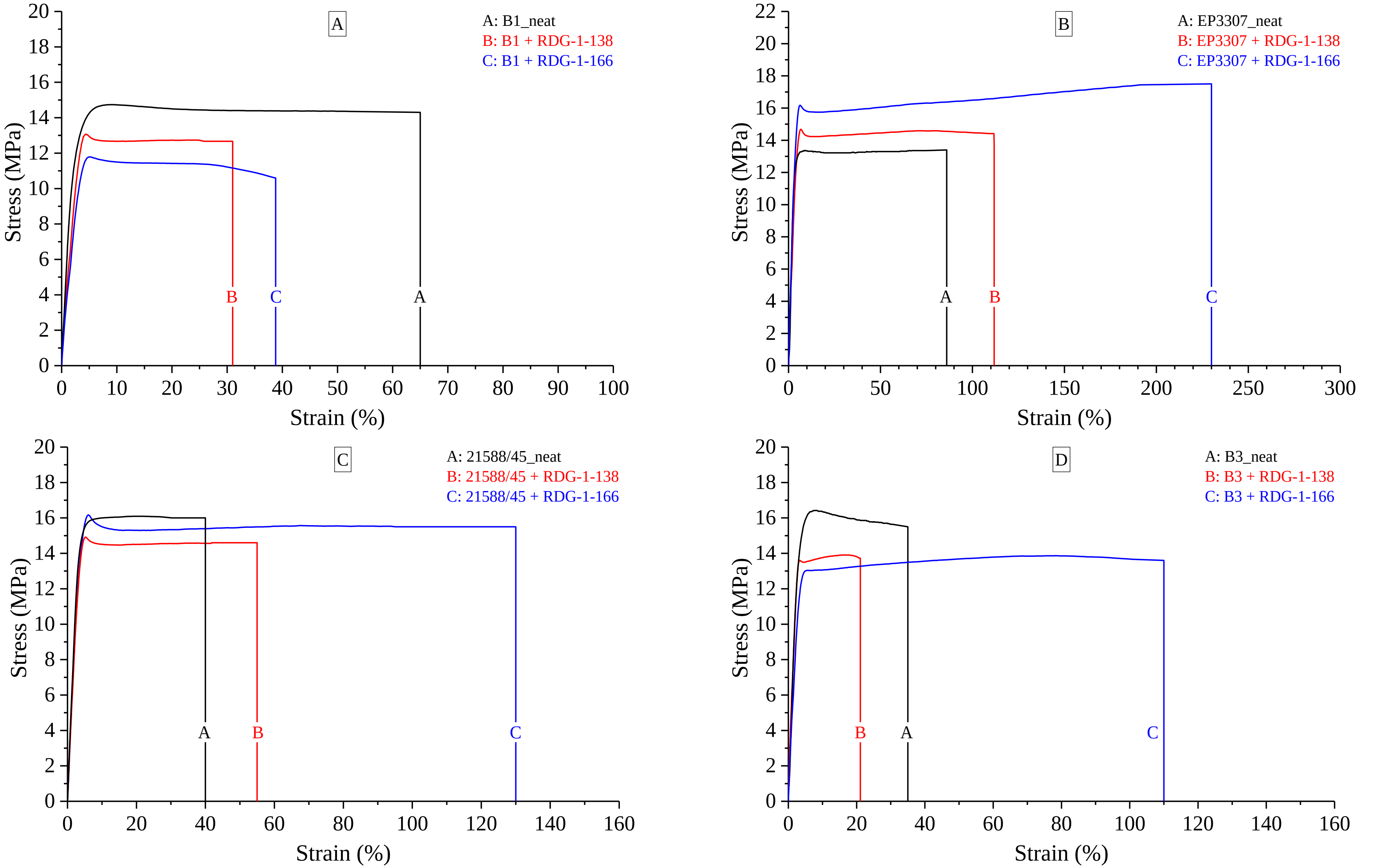

Figure 3.7. Stress-strain curves recorded at *T* = 25°C of compression-molded films of pure samples of HECO B1 (A), EP3307 (B), 21588/45 (C), and B3 (D) and of blends of the same HECO with iPP-*b*-PE block copolymer samples.

Table 3.3. Values of strain (ε_b) and stress (σ_b) at break, Young's modulus (E), strain (ε_y) and stress (σ_y) at the yield point and degree of crystallinity (x_c) of compression-molded films crystallized by slow cooling from the melt of iPP-*b*-PE copolymer samples, non-compatibilized HECO samples and blends of HECOs with block copolymer samples.

Sample	ε_b **(%)**	σ_b **(MPa)**	ε_y **(%)**	σ_y **(MPa)**	E **(MPa)**	x_c[a] **(%)**
RDG-1-138	1025 ± 55	36 ± 1	16.0 ± 0.8	23.0 ± 0.5	400 ± 35	52
RDG-1-166	1085 ± 70	38 ± 1	16 ± 0.5	23.0 ± 0.6	355 ± 20	54
B1	65 ± 8	14.3 ± 0.2	-	-	525 ± 25	55
B1 + RDG-1-138	30 ± 5	12.4 ± 0.7	4.4 ± 0.3	13.1 ± 0.5	460 ± 10	58
B1 + RDG-1-166	40 ± 5	11.1 ± 0.6	5.3 ± 0.7	11.8 ± 0.5	390 ± 20	58
EP3307	85 ± 5	13.4 ± 0.2	-	-	550 ± 25	57
EP3307 + RDG-1-138	110 ± 30	14.4 ± 0.5	6.8 ± 0.4	14.4 ± 0.5	340 ± 40	53
EP3307 + RDG-1-166	230 ± 40	17.8 ± 0.7	6.4 ± 0.5	16.2 ± 0.9	435 ± 45	54
21588/45	40 ± 15	16.7 ± 0.3	-	-	520 ± 30	54
21588/45 + RDG-1-138	55 ± 10	14.6 ± 0.2	5.0 ± 0.3	15.0 ± 0.3	465 ± 35	50
21588/45 + RDG-1-166	130 ± 35	15.5 ± 0.2	5.9 ± 0.3	16.2 ± 0.5	460 ± 50	50
B3	35 ± 3	15.5 ± 0.2	-	-	620 ± 30	56
B3 + RDG-1-138	21 ± 1	13.7 ± 0.9	3.3 ± 0.2	13.6 ± 0.8	450 ± 30	52
B3 + RDG-1-166	110 ± 20	13.6 ± 0.3	5.5 ± 0.1	14.0 ± 0.5	445 ± 20	55

a) Values evaluated from X-ray powder diffraction profiles of Figure 3.2B, Figure 3.6, and Figure 1.7.

3.2.2. Effect of iPP-b-LLDPE copolymers in blend with HECOs

Figure 3.8 shows DSC thermograms (Figure 3.8A), X-ray diffraction profiles of samples crystallized from the melt (Figure 3.8B), and stress-strain curves (Figure 3.8C) of samples JME-V-54 and JME-V-256 of the iPP-*b*-LLDPE block copolymers. The DSC heating curves of samples (Figure 3.8A) exhibit two main endothermic peaks at about 105 and 130°C for both the first and second heating scans. Peaks at higher temperature values are due to the melting of the iPP block, whilst peaks at lower temperatures correspond to the melting of the LLDPE block. These data are consistent with the fact that the enthalpies of peaks at a lower temperature (≈ 105°C) increase as the molecular mass of the LLDPE block increase and those of peaks at higher temperatures (≈ 130°C) decrease with the decreasing of the iPP-block length (see Table 3.1).

The DSC thermograms recorded during the cooling from the melt present only one exothermic phenomenon indicating that the two blocks of iPP and LLDPE crystallize at the same temperature.

The X-ray powder diffraction profiles of compression-molded film of samples slowly crystallized from the melt (Figure 3.8B) reveal that the iPP block of sample JME-V-54 crystallizes in a disordered modification of α and γ forms as indicated by the co-presence of both $(130)_{\alpha}$ and $(117)_{\gamma}$ Bragg reflections at $2\theta = 18.6°$ and 20.1°, respectively. In the case of the sample JME-V-256 the iPP block crystallizes in the α or γ forms but the amorphous halo of LLDPE-block in the range of $2\theta = 18\text{-}20°$ does not allow to observe the presence of the $(130)_{\alpha}$ and $(117)_{\gamma}$ reflections. The polyethylene phase crystallizes in both BCPs in the orthorhombic form as evidenced by the presence of the (110) and (200) reflections at $2\theta =$ 21.4° and 23.9°, respectively.

From the stress-strain curves shown in Figure 3.8C, it appears that the two BCP samples exhibit good mechanical properties with high values of stress and strain at break. However, the sample JME-V-54 is more strong and more ductile probably due to the presence of the longer crystalline iPP-block.

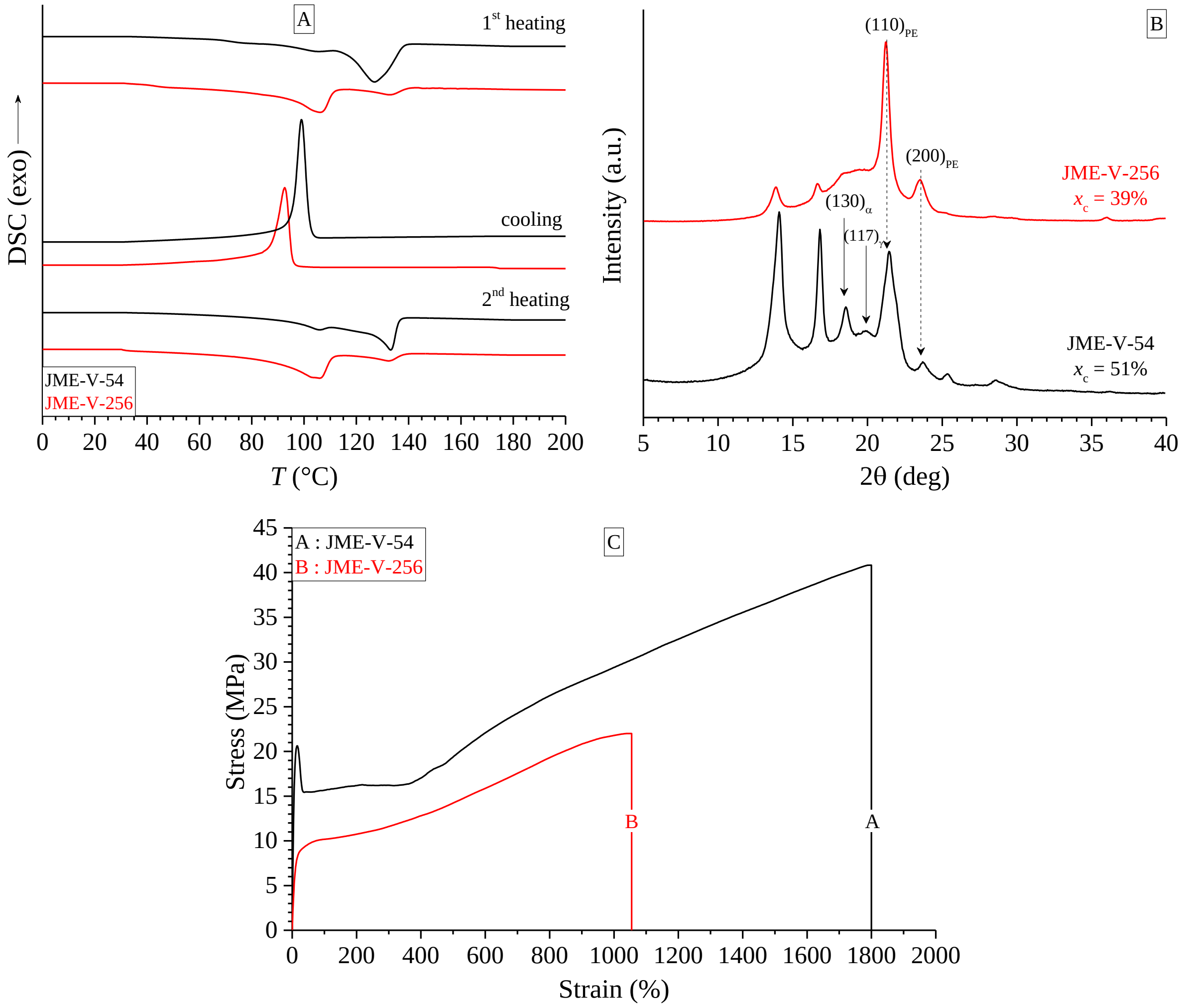

Figure 3.8. DSC thermograms (A), X-ray powder diffraction patterns of compression-molded films (B), and stress-strain curves (C) of iPP-*b*-LLDPE block copolymer samples JME-V-54 and JME-V-256.

The X-ray powder diffraction profiles recorded on all blends of HECOs with iPP-*b*-LLDPE copolymers, as obtained immediately after the blending process, are reported in Figure 3.9. The diffraction profiles show that all samples crystallize in the α-form of isotactic polypropylene as evidenced by the presence of the peaks at $2\theta = 14°$, 16.9°, 18.6°, and 21.3° corresponding to the $(110)_\alpha$, $(040)_\alpha$, $(130)_\alpha$ and $(111)_\alpha$ reflections of the α-form of the iPP. In addition, in all samples, a low-intensity peak at $2\theta \approx 23.5°$, corresponding to the $(200)_{PE}$ reflection of the orthorhombic form of polyethylene, is also present, due to the crystallization of PE from the EPR phase and/or the LLDPE blocks of the block copolymers. Also in this case, the presence of the compatibilizer probably favors the crystallization of polyethylene crystals from the chains belonging to the EPR phase.

For blends of sample EP3307, it is still possible to recognize Bragg reflections ($2\theta \approx 9.5°$ and 29°) ascribable to the presence of the talc.

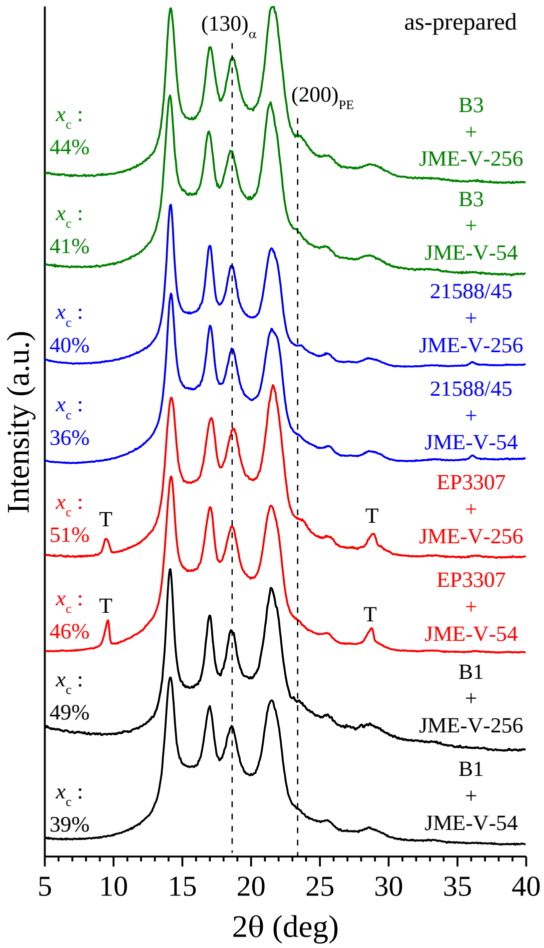

Figure 3.9. X-ray powder diffraction patterns of all the "as-prepared" blends of HECO samples with iPP-*b*-LLDPE copolymers.

Figure 3.10 shows the DSC thermograms of the first heating (A), cooling (B), and second heating (C) of the analyzed blends of HECOs with iPP-*b*-LLDPE copolymers. In the heating thermograms of samples, there are low-enthalpy melting peaks at lower temperatures ($T_m \approx 120°C$) that are related to the melting of imperfect polyethylene crystals in addition to the major melting peaks at around 165-170°C that correspond to the melting of α-crystals of the thermoplastic matrix of iPP. In contrast, a single crystallization peak is observed in almost all samples cooling thermograms. We can infer that the addition of iPP-*b*-LLDPE copolymers favors the crystallization of the PE-like crystals with an increase in the crystallization temperature so that the crystallization peak of PE in the DSC cooling scans almost overlaps with the crystallization peak of the iPP matrix. In fact, the thermal analysis performed on the non-compatibilized HECO samples (Figure1.5, Chapter 1) had shown the presence of two distinct crystallization phenomena, one at a higher temperature related to the iPP matrix and one at a lower temperature related to the crystallization of polyethylene-like crystals.

Table 3.4 shows the thermal parameters obtained from DSC thermograms of Figure 3.10, while Figure 3.11 reports the crystallization temperatures of the EPR phase of all HECOs before and after the addition of 5wt% of iPP-*b*-LLDPE copolymers.

From the data shown in Table 3.4, it can be seen that after the addition of the compatibilizers, in almost all cases, the crystallization temperatures relative to the thermoplastic matrix change slightly (2°C on average) from the values obtained for the samples without compatibilizers. This implies that the addition of the block copolymers causes a slight acceleration in the development of alpha-form crystals. However, the most significant result is related to the crystallization temperatures of the PE crystals. In fact, as is even more evident from Figure 3.11, the introduction of 5wt% of the iPP-b-LLDPE copolymers results in an increase of T_c of 5-17°C compared to samples without compatibilizer, and the most significant effect occurs on sample B1. This finding suggests that polyethylene crystals originate quicker and roughly simultaneously with iPP crystals. This outcome is probably related to effective compatibilization, in the molten state between the two phases that constitute a heterophasic copolymer.

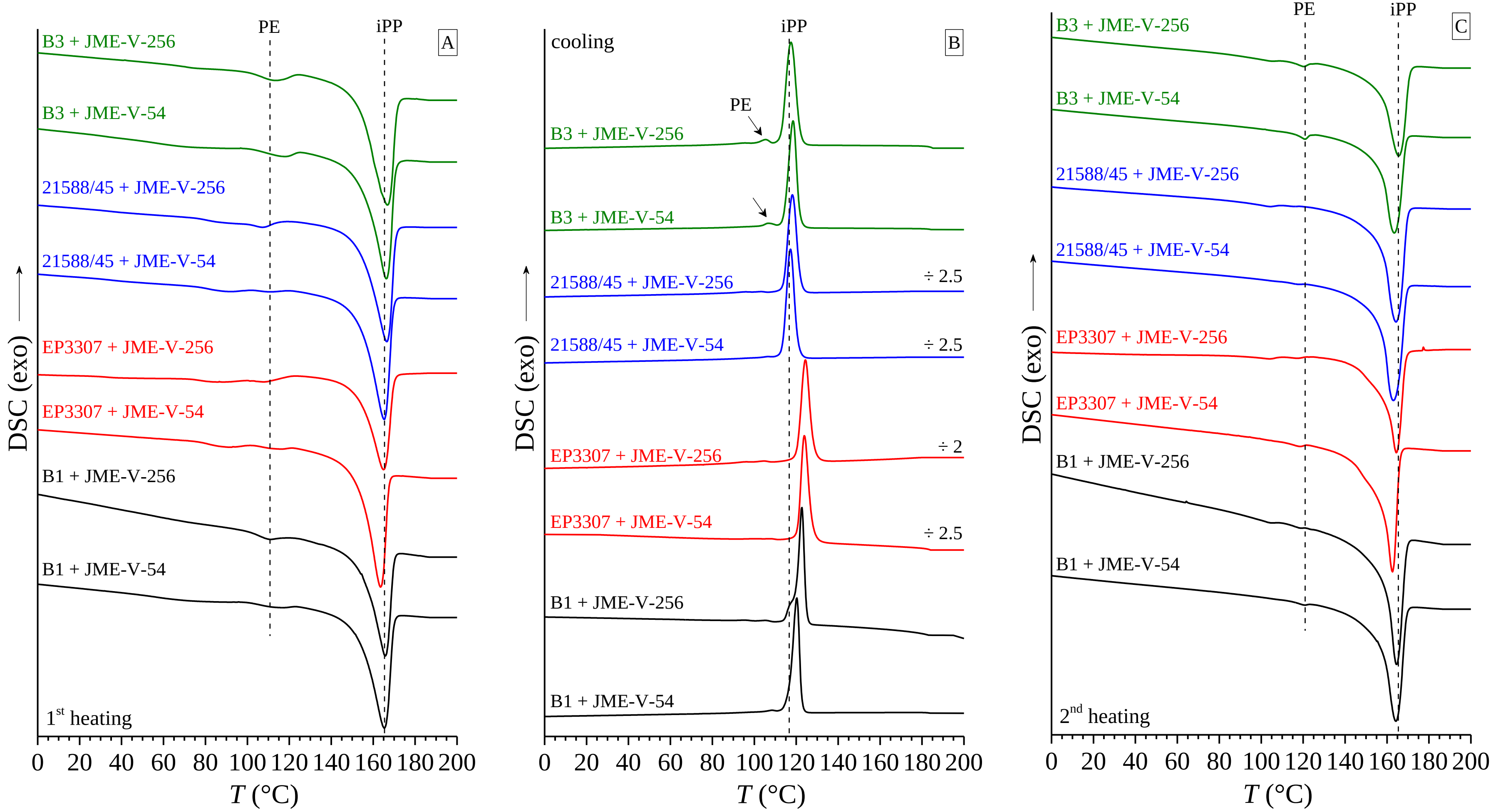

Figure 3.10. Comparison of DSC thermograms of first heating (A), cooling (B), and second heating (C) of all "as-prepared" blends of HECOs with iPP-*b*-LLDPE copolymers.

Table 3.4. Values of melting temperatures and enthalpies recorded in first heating (T_m^{I} and ΔH_{mTOT}^{I}), crystallization temperatures and enthalpies (T_c, ΔH_c), and melting temperatures and enthalpies recorded in second heating (T_m^{II}, ΔH_{mTOT}^{II}) of iPP-*b*-LLDPE copolymer samples, non-compatibilized HECO samples and blends of HECOs with block iPP-*b*-LLDPE copolymer samples. Subscripts "1" and "2" refer to values for PE and α-form crystals, respectively.

Sample	T_{m1}^{I} (°C)	T_{m2}^{I} (°C)	ΔH_{mTOT}^{I} (J/g)	T_{c1} (°C)	T_{c2} (°C)	ΔH_c (J/g)	T_{m1}^{II} (°C)	T_{m2}^{II} (°C)	ΔH_{mTOT}^{II} (J/g)
JME-V-54	104	127	94.2	99	99	76.2	106	133.2	69.6
JME-V-256	106	133	53.6	92.6	92.6	75.5	106	132.7	55.0
B1	-	165.4	72.0	99.8	116.1	82.4	118.2	163.2	85.8
B1 + JME-V-54	113.3	165.2	72.2	108.4	120.4	74.5	120.6	164.2	74.2
B1 + JME-V-256	110.4	165.8	77.4	116.9	122.8	75.6	118.4	164.5	82.1
EP3307	117.6	165.6	68.2	100.4	124.8	81.0	118.6	164.4	79.6
EP3307 + JME-V-54	116.3	163.4	61.3	108.0	127.8	77.0	118.6	162.6	70.8
EP3307 + JME-V-256	86.7; 108.5	164.9	66.1	104.5	124.4	70.0	104.3; 117.7	164.5	72.1
21588/45	113.3	168.6	73.9	96.0	120.2	78.9	114.6	163.7	89.4
21588/45 + JME-V-54	110.0	165.2	75.0	106.5	117.3	74.7	117.4	163.1	82.9
21588/45 + JME-V-256	106.8	166.5	81.5	103.0	118.2	75.0	104.0	164.3	81.4
B3	119.3	166.8	75.3	100.4	116.2	85.7	120.1	163.6	88.2
B3 + JME-V-54	117.1	166.3	77.2	106.7	118.5	76.1	120.9	163.4	75.5
B3 + JME-V-256	112.6	166.8	75.1	105.4	117.5	77.1	120.3	165.6	70.2

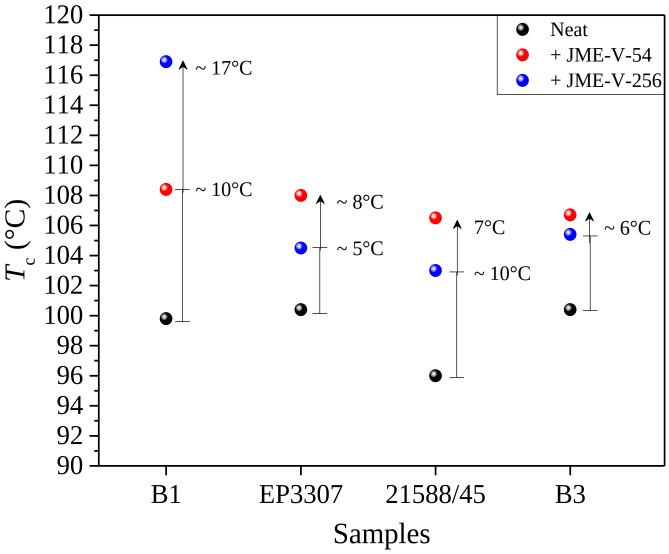

Figure 3.11. Crystallization temperatures of the EPR phase of all HECO samples before and after adding iPP-*b*-LLDPE samples as compatibilizers.

The X-ray powder diffraction profiles of all compression molded films obtained by slow cooling from the melt are reported in Figure 3.12. The diffraction profiles show that all samples crystallize in the α-form of isotactic polypropylene. However, for blends of B3 with JME-V-54 and JME-V-256, there is also the presence of the peak at 2θ = 16°, corresponding to the reflection $(110)_\beta$ of the β-form of iPP.

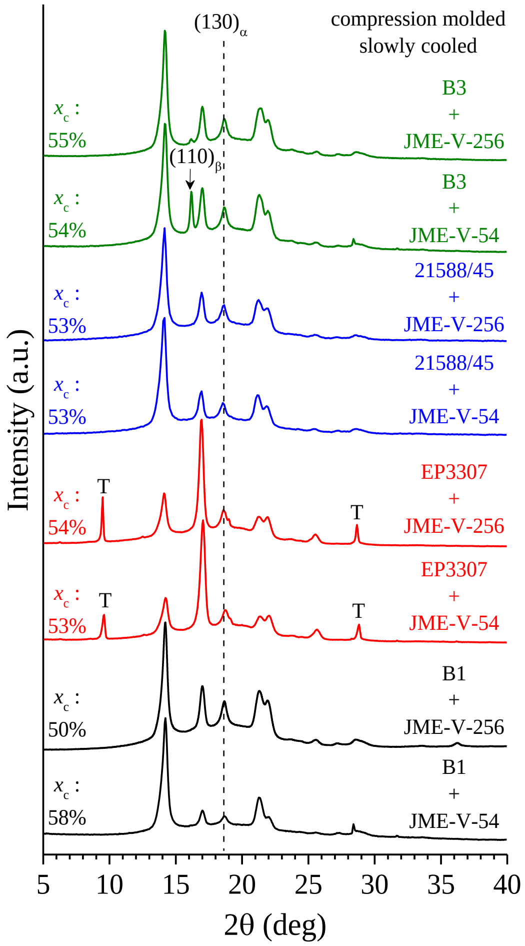

Figure 3.12. X-ray powder diffraction patterns of the compression molded films of blends with iPP-*b*-LLDPE copolymers.

Figure 3.13 shows the stress-strain curves of pure HECO samples and blends of HECOs with iPP-b-LLDPE copolymer samples, recorded at room temperature on films of samples obtained by slow cooling from the melt. The values of the mechanical parameters evaluated from the stress-strain curves of Figure 3.13 are reported in Table 3.5.

It is evident from Figure 3.13B,C that the introduction of both block copolymers into sample EP3307 and 21588/45, respectively, does not give improvements in ductility, compared to the non-compatibilized samples. Similarly, the introduction of the sample JME-V-54 does not produce an improvement for samples B1 and B3 (Figures 3.13A, D, respectively). This result can be attributed to the fact that the LLDPE block in this copolymer sample is not long enough to exert a good compatibilizing effect.

However, the introduction of the sample JME-V-256, with a very high LLDPE-block length, in samples B1 (Figure 3.13A) and B3 (Figure 3.13D) leads to great improvements in their ductility. Hence, samples with a longer LLDPE block are required for a block copolymer of the iPP-*b*-LLDPE type to act as an efficient compatibilizer.

On balance, nevertheless, block copolymers of the iPP-*b*-LLDPE type were found to be less efficient in compatibilizing HECO samples than block copolymers of the iPP-*b*-PE type, suggesting that in HECO samples there are macromolecule families with a much more PE-like rather than LLDPE-like microstructure.

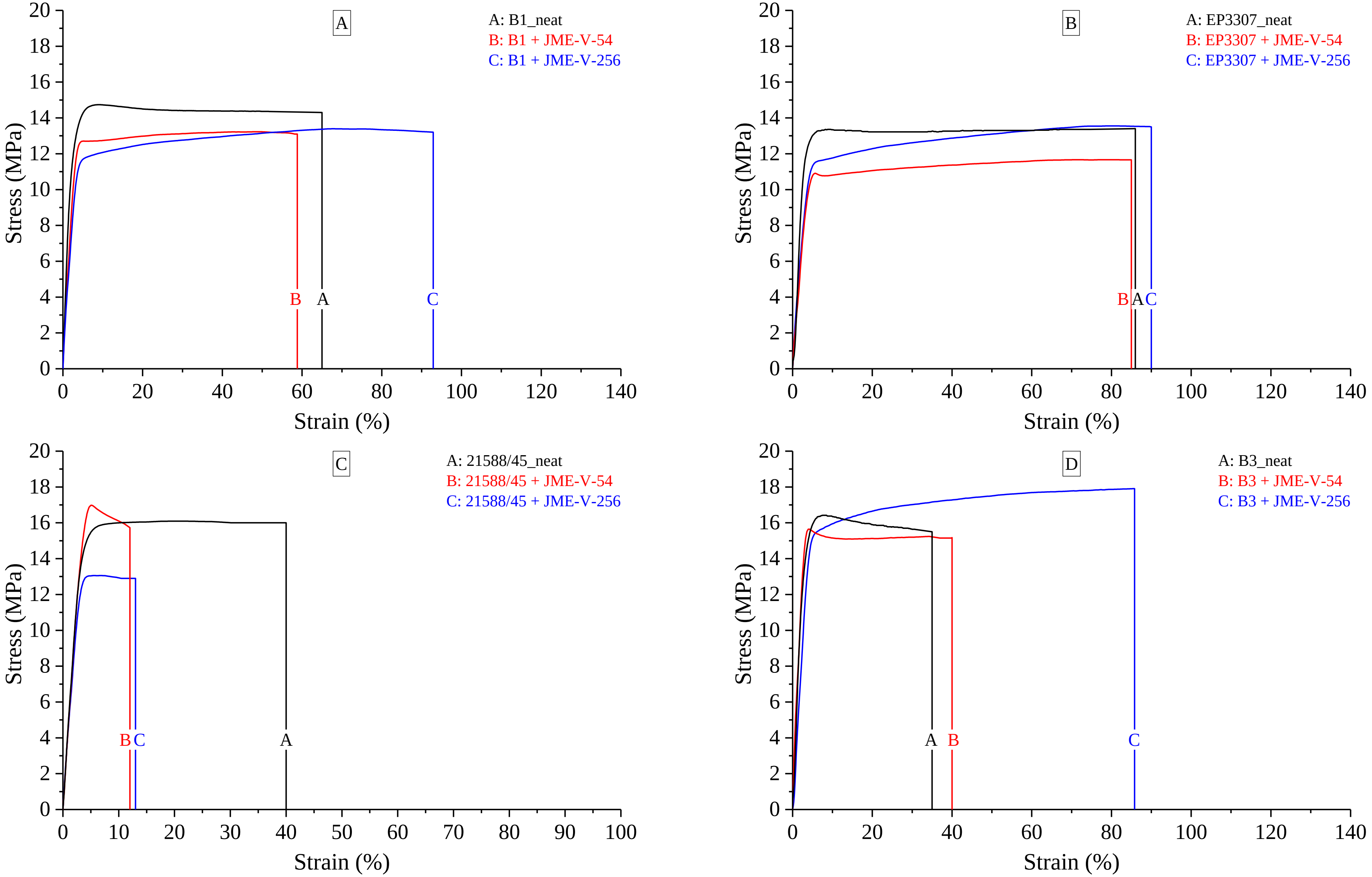

Figure 3.13. Stress-strain curves recorded at *T* = 25°C of compression-molded films of B1 (A), EP3307 (B), 21588/45 (C), and B3 (D) samples, pure, and in blends with iPP-*b*-LLDPE samples.

Table 3.5. Values of strain (ε_b) and stress (σ_b) at break, Young's modulus (E), strain (ε_y) and stress (σ_y) at the yield point and degree of crystallinity (x_c) of compression-molded films crystallized by slow cooling from the melt of iPP-*b*-LLDPE copolymer samples, non-compatibilized HECO samples and blends of HECOs with block copolymer samples.

Sample	ε_b (%)	σ_b (MPa)	ε_y (%)	σ_y (MPa)	E (MPa)	x_c[a] (%)
JME-V-54	1805 ± 95	41 ± 1	16.0 ± 0.5	21.0 ± 0.4	300 ± 20	51
JME-V-256	1055 ± 90	22.0 ± 1.5	-	-	110 ± 5	-
B1	65 ± 8	14.3 ± 0.2	-	-	525 ± 25	55
B1 + JME-V-54	60 ± 5	13.1 ± 0.5	4.7 ± 0.1	12.7 ± 0.4	450 ± 30	58
B1 + JME-V-256	95 ± 25	13.6 ± 0.7	-	-	400 ± 15	50
EP3307	85 ± 5	13.4 ± 0.2	-	-	550 ± 25	57
EP3307 + JME-V-54	85 ± 15	11.7 ± 1.1	5.4 ± 0.5	11.0 ± 1.5	460 ± 30	53
EP3307 + JME-V-256	90 ± 20	15.7 ± 1.6	-	-	450 ± 60	54
21588/45	40 ± 15	16.7 ± 0.3	-	-	520 ± 30	54
21588/45 + JME-V-54	12 ± 2	15.8 ± 0.2	5.1 ± 0.3	17.0 ± 0.2	505 ± 5	53
21588/45 + JME-V-256	13 ± 4	12.9 ± 0.3	-	-	470 ± 50	53
B3	35 ± 3	15.5 ± 0.2	-	-	620 ± 30	56
B3 + JME-V-54	40 ± 5	15.2 ± 0.4	4.2 ± 0.5	15.6 ± 0.6	505 ± 40	54
B3 + JME-V-256	90 ± 25	18.0 ± 0.5	-	-	450 ± 30	55

a) Values evaluated from X-ray powder diffraction profiles of Figure 3.8B, Figure 3.12, and Figure 1.7.

3.3. Multi-block copolymers by chain-shuttling technology

As previously discussed, block copolymers are widely produced by different synthesis strategies involving, for example, ionic (anionic and cationic) or radical type polymerization, which we said are catalysis not capable of creating BCPs with stereoregular polyolefins as building blocks resulting in polyolefins without microstructural control. However, the introduction of living catalysis has in fact overcome this problem by allowing semi-crystalline BCPs to be obtained. Nevertheless, these polymerization methods share the ability to create block-copolymers by adding several monomers one at a time to the same polymerization mixture. Therefore, preserving the living nature of the process during synthesis is essential to linking chemically distinct monomers together in a chain and preventing the creation of a physical mixture of homopolymers. The fact that each active center may propagate only one polymer chain, resulting in just one macromolecule per catalyst molecule at the termination of the polymerization process, is another shortcoming of these types of synthetic techniques that is significant to the industry. As a result, efficiency is strongly penalized with consequences in the process costs.

In order to get over these problems, researchers have recently created a new synthetic method based on coordination catalysis with the goal of producing ethylene-based (or propylene-based) block copolymers (OBCs) from a common combination of ethylene (or propylene) and higher α-olefins (such as 1-octene, 1-hexene).[12] The mechanism for chain-shutting polymerization was created and is well-discussed in ref. 12. In summary, this process relies on reversible trans-alkylation reactions, which are carried out using a dual catalytic system in conjunction with a substance known as a "chain shuttling agent" (CSA). The (pyridylamido)Hf[25] and bis(phenoxyimine)Zr[26] catalysts (see Figure 3.14), as well as alkyl Zinc species as CSA, make up the catalytic system. The two catalysts have a different selectivity towards α-olefin incorporation at fixed comonomer contents of the reactor feed.

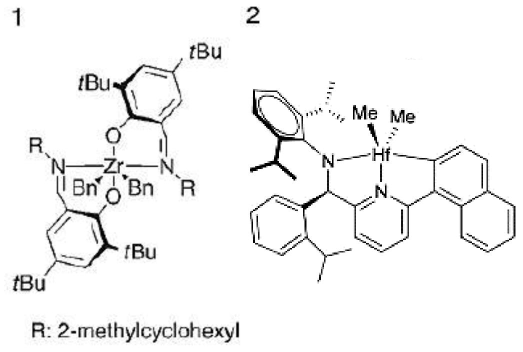

Figure 3.14. Zirconium bis(phenoxyimine) complex (1) and Hafnium pyridylamido complex (2). Bn ligand of complex 1 corresponds to Benzyl.

The role of the CSA is to switch the propagating chains growing on the two catalysts providing the formation of chains made by hard (lower α-olefins content, i.e., crystalline) and soft (higher α-olefins content, i.e., amorphous) alternating segments chemically linked. The first block exhibits thermoplastic properties, whereas the second exhibits elastomeric properties. This mechanism has several advantages over the traditional methods of synthesizing block-copolymers (anionic, radical, and cationic polymerizations), including better performance in terms of catalyst activity and efficiency, the ability to afford stereoregular polymers, and the ability to precisely tune the polymer microstructure by changing the process operating variables.

Table 3.6 shows the main characteristics of the multi-block copolymers (OBCs) used for the preparation of blends (5wt% of compatibilizer). The necessity of using OBCs from chain-shuttling catalysis arises directly from the fact that BCPs copolymers produced by living catalysis have high production costs and are not very easy to synthesize industrially. This drives up the cost of the compatibilizer with a consequent increase in the price of the starting HECO material, which itself, has low production costs. Moreover, all OBC copolymers are commercial samples marketed by the Dow Chemical Company under the trade names INTUNE (PP-based OBCs) and INFUSE (PE-based OBCs).

INFUSE samples consist of ethylene/1-octene copolymers and show similar values of the average content of 1-octene units f(C8) (≈ 13−14 mol%), weight-average molecular masses ($155 < M_w < 180$ kDa) and PDI (≈ 2.5). The two samples differ in the percentage of hard segments; in particular, sample D9000 has a w_H of roughly 28wt%, whereas sample D9007 of about 15.5wt%.

INTUNE samples, on the other hand, consist of blocks of isotactic polypropylene linked to rubbery ethylene-propylene copolymer blocks in which there is a significant difference in the ethylene content of the elastomeric block. Indeed, sample D5545 (made of Hard/Hard blocks) has an ethylene content in the EPR block of about 91wt%, while sample D5535 (made of Hard/Soft blocks) has 68wt% of the average content of ethylene units f(C2). The molecular mass values (M_w) are still high, in the range of 140-170kDa.

Table 3.6. Main characteristics of multi-block copolymers used as compatibilizers for HECOs.

Sample	Type	M_n (kDa)	M_w (kDa)	PDI	f(C8) (mol%)	f(C2) (wt%)	w_H (wt%)
D9000	INFUSE Ethylene/1-octene	60	155	2.6	13.1	61.6	27.7
D9007		70	177	2.5	14.6	58.6	15.4
D5545 H/H 50/50	INTUNE iPP/EPR	59	142	2.4	-	90.8 (EPR) 1.8 (iPP)	-
D5535 H/S 55/45		73	170	2.3	-	68 (EPR) 2.7 (iPP)	-

3.3.1. Blends of HECOs with iPP/EPR copolymers (INTUNE)

Figure 3.15 shows DSC thermograms (Figure 3.15A), X-ray diffraction profiles of samples crystallized from the melt (Figure 3.15B), and stress-strain curves (Figure 3.15C) of samples of the iPP/EPR multi-block copolymers, D5535 and D5545, before being blended with HECOs. The thermal analysis (Figure 3.15A) shows that the two samples have different thermal behavior only in the two heating curves. In fact, sample D5545 shows two main endothermic peaks at about 115 and 135°C for both the first and second heating scans. Peaks at higher temperature values are due to the melting of the iPP block, whereas peaks at lower temperatures correspond to the melting of PE-like crystals. These data are consistent with the fact that this sample is made up of a hard iPP-block and a hard EPR-block with an ethylene content of about 90wt%. Thus, the EPR block roughly behaves like a polyethylene block since its ethylene concentration is very high. On the other hand, sample D5535 presents one main endothermic peak at about 140°C both in the first and in the second heating thermograms. Accordingly with the compositional data (see Table 3.6) this endothermic phenomenon is just related to the melting of the crystalline iPP block since the EPR block has an ethylene content of about 60wt% and is amorphous.

The DSC thermograms recorded during the cooling from the melt present only one exothermic phenomenon indicating that, in the case of sample D5535, correspond to the crystallization of the iPP block, while for sample D5545 it means that the two blocks co-crystallize at the same temperature.

The X-ray diffraction profiles of the compression-molded film slowly crystallized from the melt (Figure 3.15B) confirms that the sample D5535 exhibits crystallinity only from isotactic polypropylene in the α form with a low crystallinity index (due to the amorphous EPR block) and the sample D5545 exhibits crystallinity from both isotactic polypropylene, in the α and γ forms, and polyethylene in the orthorhombic form, as indicated by the presence of the only

$(130)_{\alpha}$ reflection at $2\theta = 18.6°$ for the sample D5535 and the presence of both $(130)_{\alpha}$ and $(117)_{\gamma}$ reflections at $2\theta = 18.6°$ and $20.1°$, respectively, in the sample D5545.

The stress-strain curves reported in Figure 3.15C indicate that the two OBC samples exhibit good mechanical properties with high values of stress and strain at break.

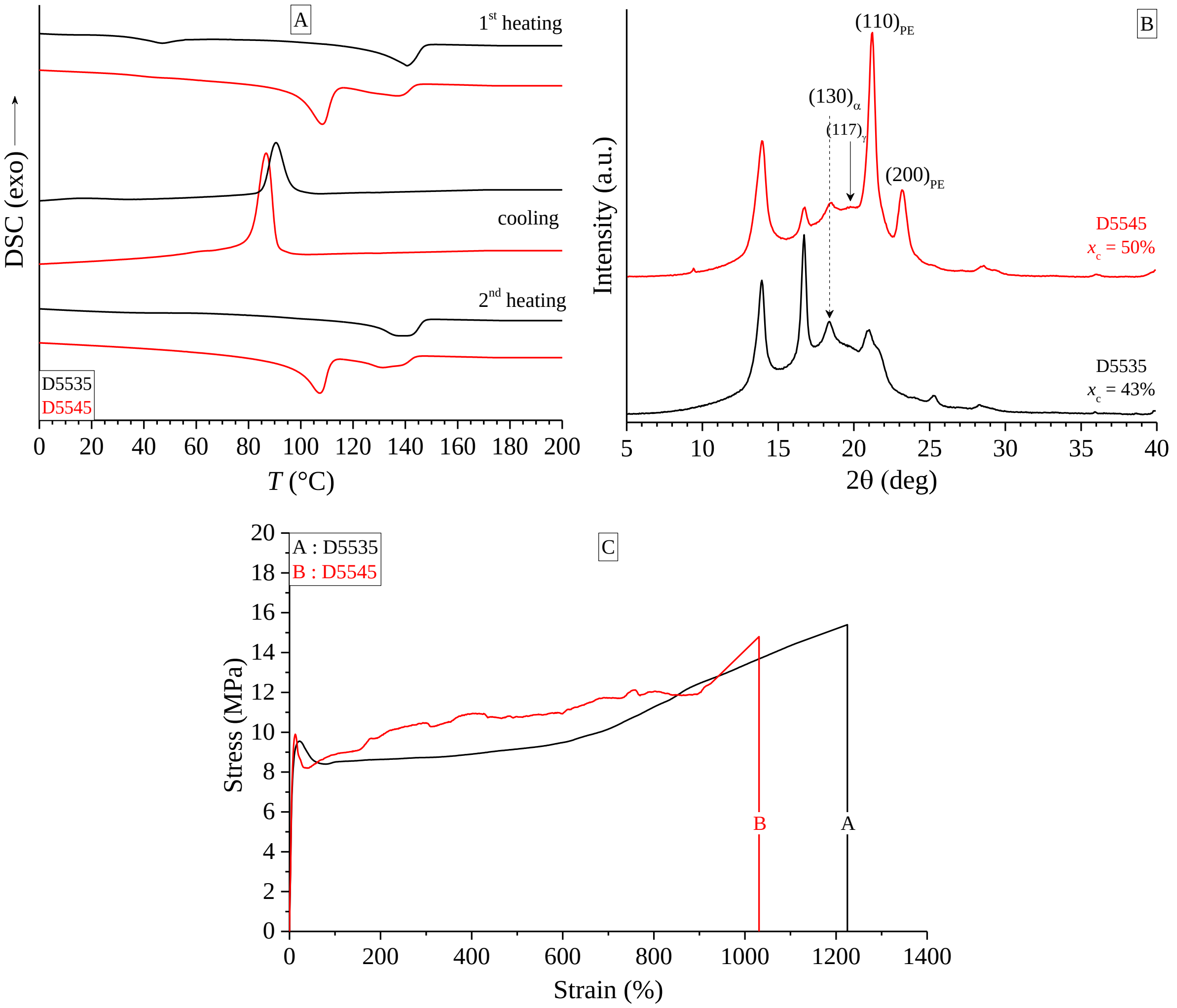

Figure 3.15. DSC thermograms (A), X-ray powder diffraction profiles of compression-molded films (B), and stress-strain curves (C) of iPP/EPR multi-block copolymer samples D5535 and D5545.

The X-ray powder diffraction profiles recorded on all blends of HECOs with the iPP/EPR multi-block copolymers, as obtained immediately after the blending process, are reported in Figure 3.16. The diffraction profiles show that all samples crystallize basically in the α-form of isotactic polypropylene. In addition, especially in samples blended with the sample D5545, a low-intensity peak at $2\theta \approx 23.5°$ corresponding to the reflection $(200)_{PE}$ of the orthorhombic form of polyethylene is also present. Also in this case, this indicates the crystallization of PE from the EPR phase of the HECO samples, favored by the presence of the iPP/EPR block copolymers, and the crystallization of PE from the block copolymer containing the crystallizable EPR block.

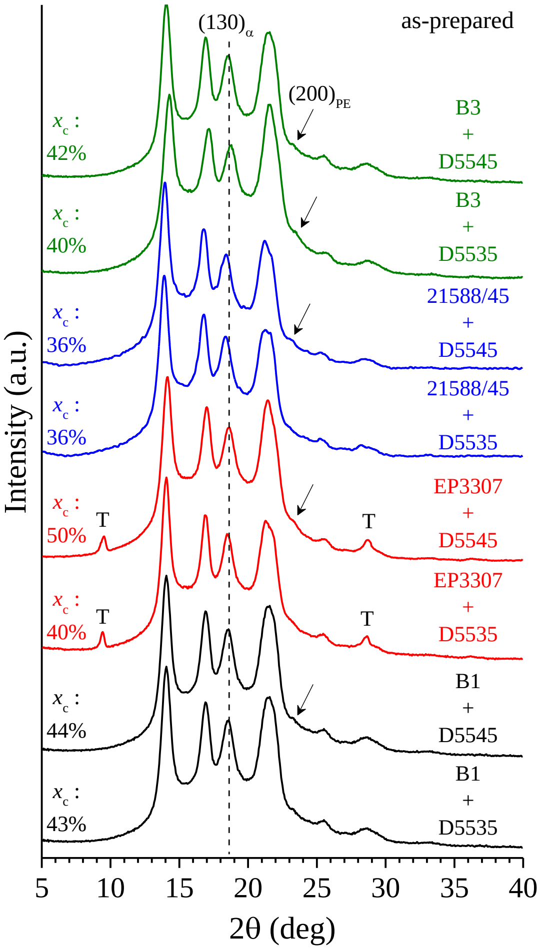

Figure 3.16. X-ray powder diffraction patterns of all the “as-prepared” blends with iPP/EPR (INTUNE) copolymers.

Figure 3.17 shows the DSC thermograms of the first heating (A), cooling (B), and second heating (C) of the analyzed blends of HECOs with iPP/EPR (INTUNE) copolymers. In the thermograms of all blends, in addition to the main melting peaks at about 160-165°C and crystallization peaks at about 115-120°C, corresponding to the melting and crystallization of the α-crystals of the thermoplastic matrix of iPP, a low-enthalpy peak at lower temperatures ($T_m \approx$ 115-120°C, $T_c \approx$ 95-105°C), corresponding to the melting and crystallization of defective polyethylene crystals belonging to the EPR rubbery phase, is present.

Table 3.7 shows the thermal parameters obtained from DSC thermograms of Figure 3.17, while Figure 3.18 reports the crystallization temperatures of the EPR phase of all HECOs before and after the addition of 5wt% of iPP/EPR multi-block copolymers.

From the data shown in Table 3.7, it is evident that after the addition of the compatibilizers, the values of crystallization and melting temperatures of the thermoplastic iPP matrix of the investigated samples do not significantly change. Instead, the introduction of 5wt% of the block copolymer sample D5545, containing the crystalline EPR block, leads to an increase of the crystallization temperature of the EPR phase of the HECO samples of nearly 3-8 °C compared to samples without compatibilizer (Figure 3.18). This result confirms that polyethylene crystals (from HECOs) originate earlier due to an effect of the compatibilizer. On the other hand, the presence of sample D5535, containing the amorphous EPR block, does not produce any significant changes in the thermal behavior of the HECO samples.

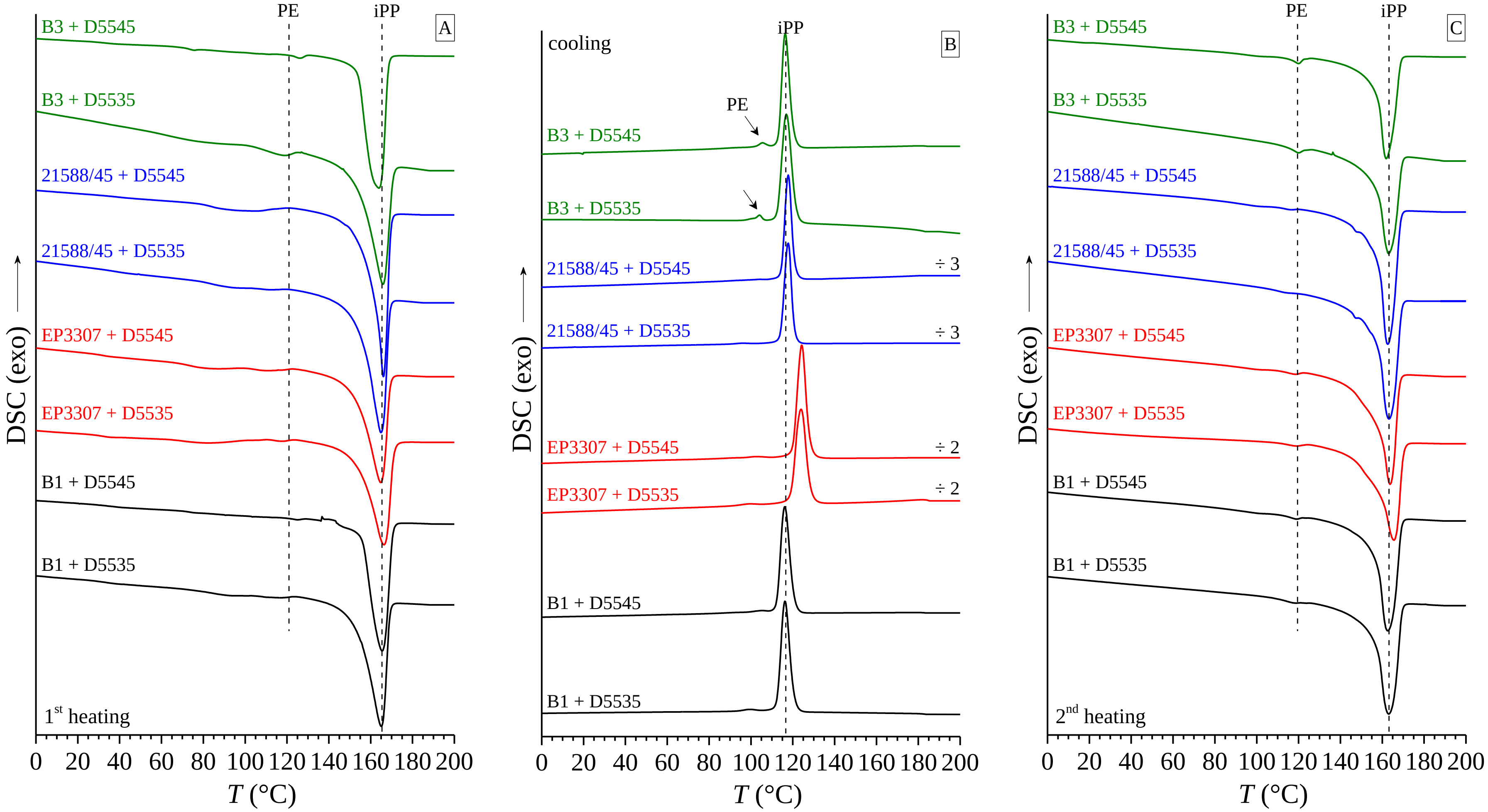

Figure 3.17. Comparison of DSC thermograms of first heating (A), cooling (B), and second heating (C) of all "as-prepared" blends of HECOs with iPP/EPR (INTUNE) copolymers.

Table 3.7. Values of melting temperatures and enthalpies recorded in first heating (T_m^I and ΔH_{mTOT}^I), crystallization temperatures and enthalpies (T_c, ΔH_c), and melting temperatures and enthalpies recorded in second heating (T_m^{II}, ΔH_{mTOT}^{II}) of INTUNE copolymer samples, non-compatibilized HECO samples and blends of HECOs with multi-block iPP/EPR copolymer samples. Subscripts "1" and "2" refer to values for PE and α-form crystals, respectively.

Sample	T_{m1}^I (°C)	T_{m2}^I (°C)	ΔH_{mTOT}^I (J/g)	T_{c1} (°C)	T_{c2} (°C)	ΔH_c (J/g)	T_{m1}^{II} (°C)	T_{m2}^{II} (°C)	ΔH_{mTOT}^{II} (J/g)
D5535	46.8	140.7	38.1	-	90.5	39.1	-	138.0	22.6
D5545	108.2	136.9	61.3	86.8	86.8	67.9	107.2	131.4	60.4
B1	-	165.4	72.0	99.8	116.1	82.4	118.2	163.2	85.8
B1 + D5535	92.6	165.2	76.5	99.4	116.3	74.4	118.3	163.0	78.6
B1 + D5545	124.8	165.5	96.4	105.4	116.2	76.2	118.9	162.6	80.3
EP3307	117.6	165.6	68.2	100.4	124.8	81.0	118.6	164.4	79.6
EP3307 + D5535	117.8	166.4	66.6	99.9	124.0	70.5	119.4	165.6	72.4
EP3307 + D5545	110.2	164.8	61.9	102.9	124.2	67.2	118.8	163.8	73.3
21588/45	113.3	168.6	73.9	96.0	120.2	78.9	114.6	163.7	89.4
21588/45 + D5535	95.0	164.8	78.1	96.0	117.9	75.5	115.0	163.2	81.6
21588/45 + D5545	97.0	166.1	84.9	104.0	117.8	76.6	116.5	162.6	80.0
B3	119.3	166.8	75.3	100.4	116.2	85.7	120.1	163.6	88.2
B3 + D5535	117.9	165.8	83.9	104.1	116.9	86.8	119.9	162.8	80.1
B3 + D5545	126.1	163.9	88.2	105.6	116.4	75.6	119.9	161.8	71.0

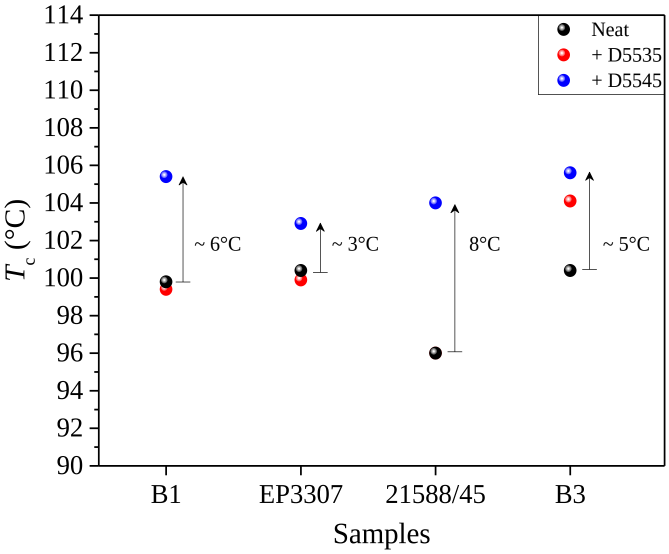

Figure 3.18. Crystallization temperatures of the EPR phase of all HECO samples before and after adding iPP/EPR (INTUNE) samples as compatibilizers.

The X-ray powder diffraction profiles of compression molded films obtained by slow cooling from the melt of the blends of HECOs with the INTUNE block copolymers are reported in Figure 3.19. All samples crystallize in the α-form of isotactic polypropylene, as evidenced by the presence of peaks at $2\theta = 14°$, 16.9°, 18.6°, and 21.3° corresponding to the $(110)\alpha$, $(040)\alpha$, $(130)\alpha$ and $(111)\alpha$ reflections of the α-form of the iPP. In addition, for the sample of blend B3 with D5545 is also possible to notice the presence of the peak at $2\theta = 16°$, corresponding to the reflection $(110)_\beta$ of the β-form of iPP.

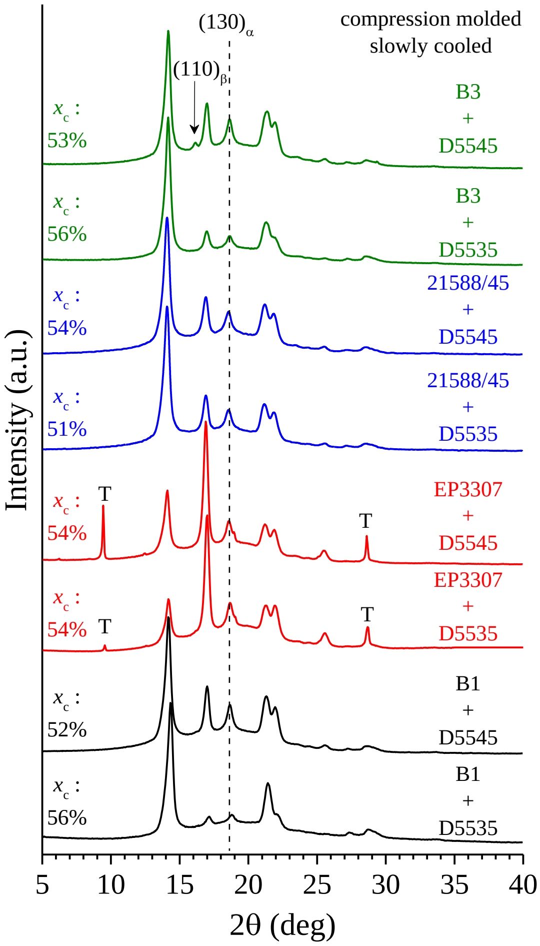

Figure 3.19. X-ray powder diffraction patterns of the compression molded films of blends of HECOs with iPP/EPR (INTUNE) copolymers.

Figure 3.20 shows the stress-strain curves of HECO samples and of blends of HECOs with INTUNE copolymer samples, recorded at room temperature on films obtained by slow cooling from the melt. The values of the mechanical parameters evaluated from the stress-strain curves of Figure 3.20 are reported in Table 3.8.

The analysis of mechanical properties, in almost all cases, revealed that the introduction of 5wt% of iPP/EPR copolymers is not sufficient to produce improvements in the final properties of HECO samples. In fact, it is evident that almost all stress-strain curves of blends exhibit lower ductility values than those of the starting HECO samples.

The only exception is the blends of sample 21588/45 (Figure 3.20C) for which slight improvements in ductility are observed when compared with the starting sample. In particular, it appears that the greatest enhancements are obtained with sample D5545, which is characterized by an EPR block that is chemically more similar to a defective polyethylene block of the EPR phase of the HECO samples.

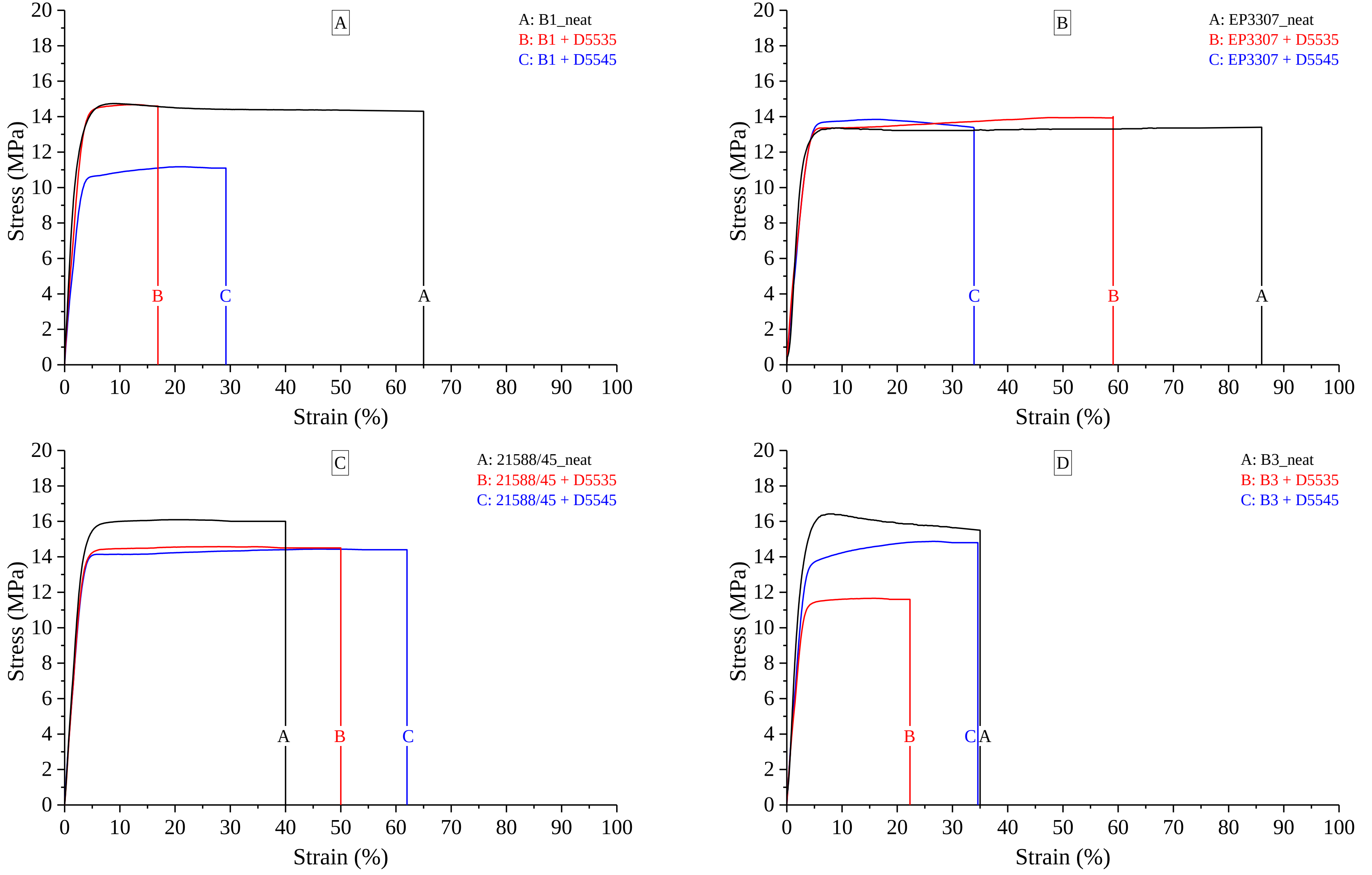

Figure 3.20. Stress-strain curves recorded at *T* = 25°C of compression-molded films of the pure HECO samples B1 (A), EP3307 (B), 21588/45 (C), and B3 (D) and of their blends with iPP/EPR (INTUNE) samples.

Table 3.8. Values of strain (ε_b) and stress (σ_b) at break, Young's modulus (E), and degree of crystallinity (x_c) of compression-molded films crystallized by slow cooling from the melt of iPP/EPR (INTUNE) copolymer samples, non-compatibilized HECO samples and blends of HECOs with multi-block copolymer samples.

Sample	ε_b **(%)**	σ_b **(MPa)**	E **(MPa)**	x_c[a] **(%)**
D5535	1225 ± 100	15.4 ± 2.8	180 ± 10	43
D5545	1030 ± 95	15 ± 3	255 ± 25	50
B1	65 ± 8	14.3 ± 0.2	525 ± 25	55
B1 + D5535	17 ± 2	14.6 ± 0.4	490 ± 50	56
B1 + D5545	30 ± 8	11 ± 2	390 ± 50	52
EP3307	85 ± 5	13.4 ± 0.2	550 ± 25	57
EP3307 + D5535	60 ± 7	14.0 ± 0.9	425 ± 25	54
EP3307 + D5545	35 ± 5	13.9 ± 0.8	350 ± 20	54
21588/45	40 ± 15	16.7 ± 0.3	520 ± 30	54
21588/45 + D5535	50 ± 12	14.5 ± 0.3	470 ± 20	51
21588/45 + D5545	60 ± 12	14.4 ± 0.4	430 ± 15	54
B3	35 ± 3	15.5 ± 0.2	620 ± 30	56
B3 + D5535	22 ± 1	11.5 ± 0.1	430 ± 20	56
B3 + D5545	35 ± 5	14.8 ± 0.5	470 ± 20	53

a) Values evaluated from X-ray powder diffraction profiles of Figure 3.15B, Figure 3.19, and Figure 1.7.

3.3.2. Blends of HECOs with Ethylene/1-octene copolymers (INFUSE)

Figure 3.21 shows DSC thermograms (Figure 3.21A), X-ray diffraction profiles of samples crystallized from the melt (Figure 3.21B), and stress-strain curves (Figure 3.21C) of samples of the ethylene/1-octene multi-block copolymers, D9000 and D9007. The thermal analysis (Figure 3.21A) shows that the two samples present only one main endothermic and exothermic peak in the temperatures range of 120-123 °C and 91-97 °C, respectively, associated with the melting and crystallization of polyethylene crystals. In particular, sample D9000 shows higher melting and crystallization temperatures according to the higher weight fraction of the semicrystalline hard block (see Table 3.6).

The X-ray diffraction profiles performed on samples slowly crystallized from the melt (Figure 3.21B) confirm that the two samples crystallize in the orthorhombic form of polyethylene as evidenced by the presence of the (110) and (200) reflections at $2\theta = 21.4°$ and $23.9°$, respectively.

Finally, the stress-strain curves reported in Figure 3.21C, indicate that the two OBC samples exhibit good mechanical properties of high ductility and quite high values of stress at break. Sample D9000 shows higher values of stress at any strain and at break higher than those of sample D9007, according to the presence of a higher weight fraction of semicrystalline hard block.

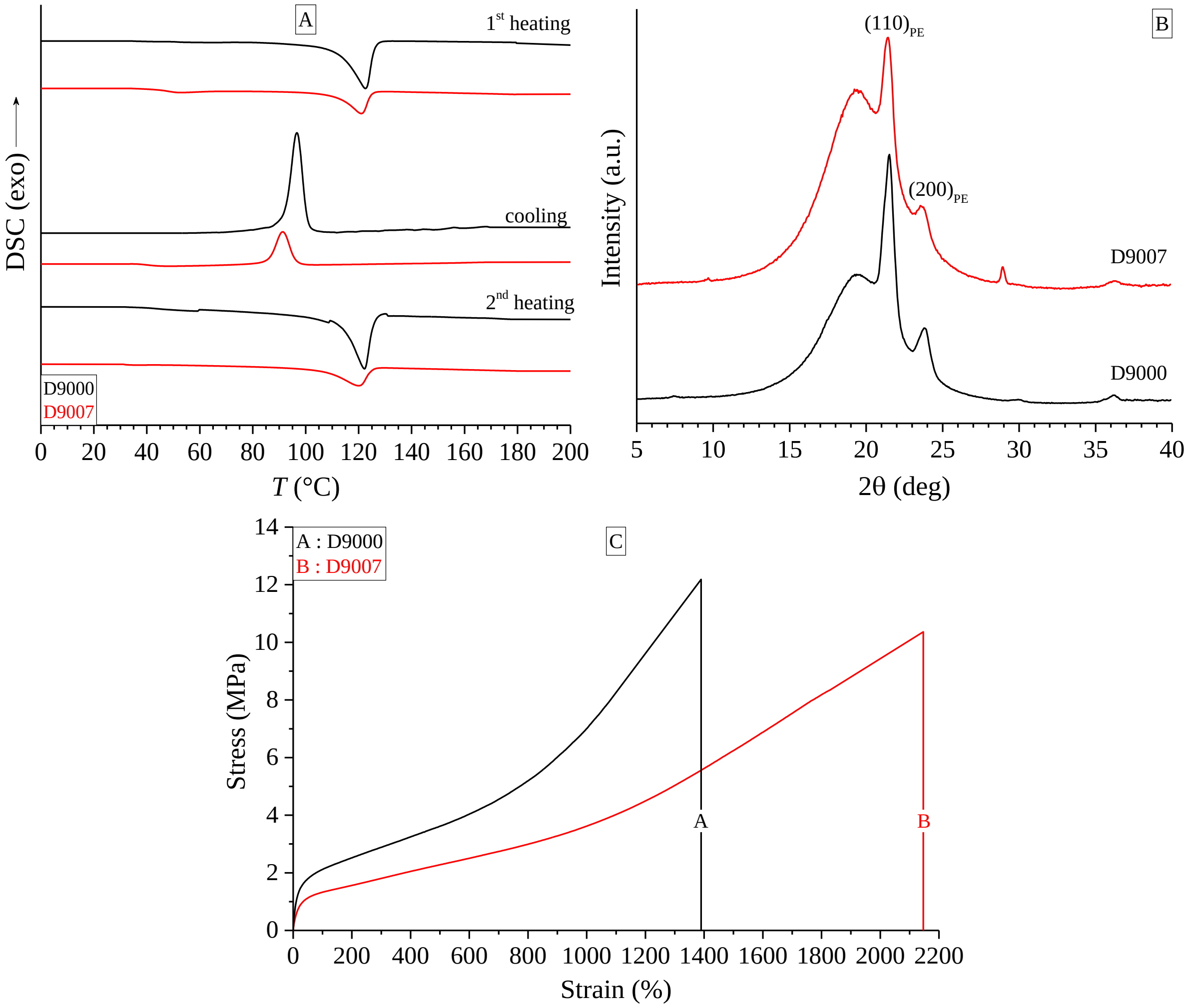

Figure 3.21. DSC thermograms (A), X-ray powder diffraction profiles of compression-molded films (B), and stress-strain curves (C) of ethylene/1-octene multi-block copolymer samples D9000 and D9007 (INFUSE).

The X-ray powder diffraction profiles of all blends of HECOs with ethylene/1-octene multi-block copolymers, as obtained immediately after the blending process, are reported in Figure 3.22. The diffraction profiles show that all samples crystallize in the α-form of isotactic polypropylene. In all samples also a small number of crystals of PE is present due to the crystallization of the EPR phase and/or of PE from the ethylene-octene hard block of the block copolymer.

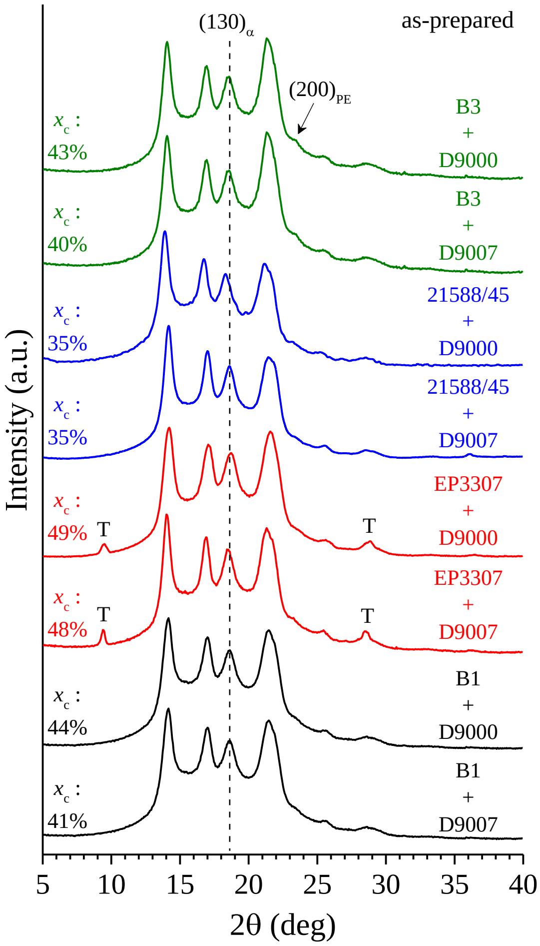

Figure 3.22. X-ray powder diffraction patterns of all the "as-prepared" blends of HECO samples with ethylene/1-octene (INFUSE) copolymers.

Figure 3.23 shows the DSC thermograms of the first heating (A), cooling (B), and second heating (C) of the analyzed blends of HECOs with ethylene/1-octene (INFUSE) copolymers. In the thermograms of all blends, in addition to the main melting peaks at about 160-165°C and crystallization peaks at about 115-120°C, corresponding to the melting and crystallization of the α-crystals of the thermoplastic matrix of iPP, a low-enthalpy peak at lower temperatures ($T_m \approx$ 115-120°C, $T_c \approx$ 95-105°C), corresponding to the melting and crystallization of defective polyethylene crystals belonging to the EPR rubbery phase, are present.

Table 3.9 shows the thermal parameters obtained from DSC thermograms of Figure 3.23, while Figure 3.24 reports the crystallization temperatures of the EPR phase of all HECOs before and after the addition of 5wt% of ethylene/1-octene multi-block copolymers.

It is clear from the data in Table 3.9 that the values of the crystallization and melting temperatures of the thermoplastic iPP matrices are not modified by the presence of the block copolymers, whereas-the crystallization temperature of the EPR phase increases of the 2–8 °C range in the blends, in particular with the sample D9000 having the higher content of the crystalline hard block. This indicates that also in this case the crystallization of the EPR phase of the HECO samples is favored by the presence of the crystallizable block of the block copolymer.

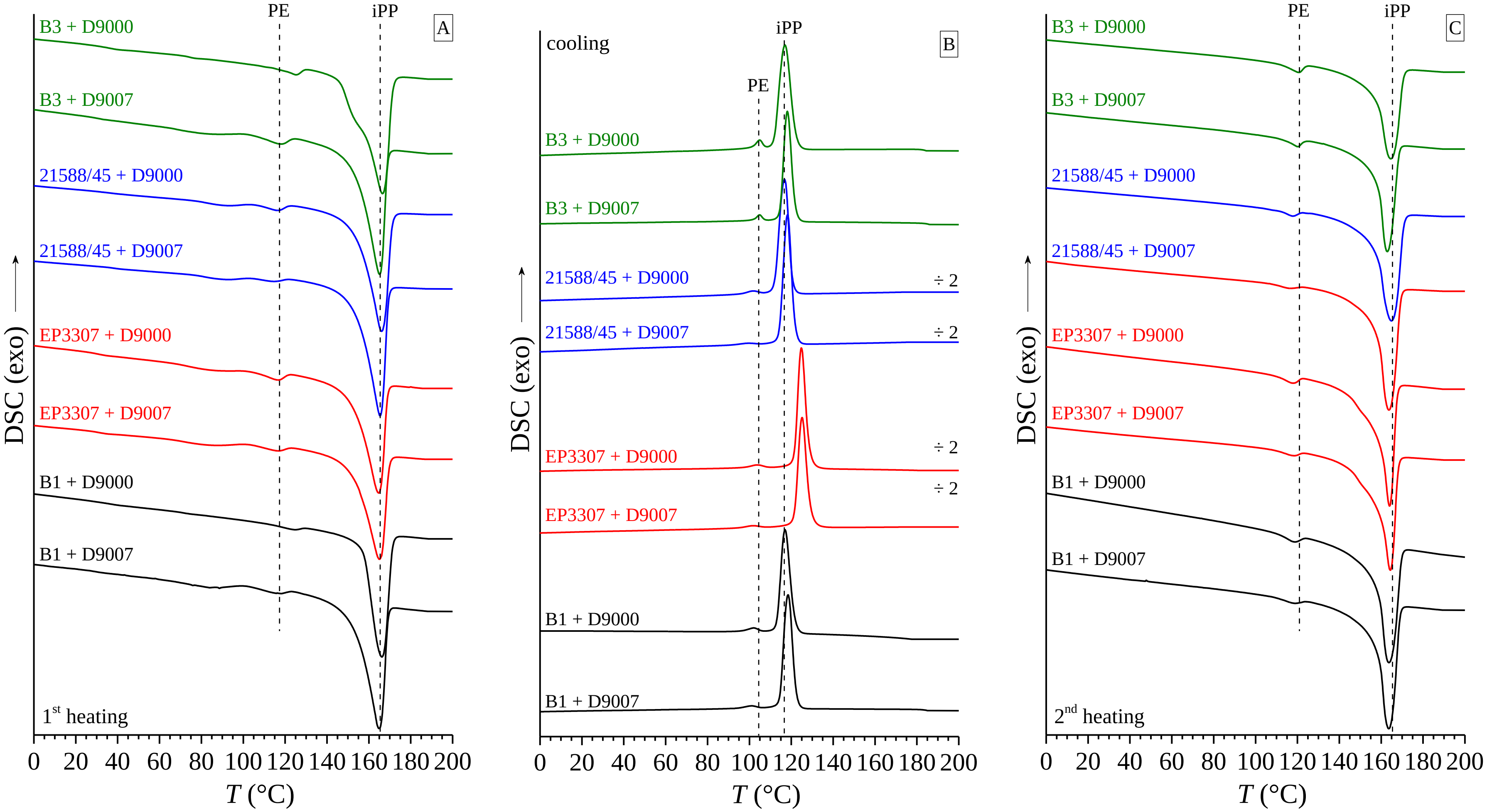

Figure 3.23. Comparison of DSC thermograms of first heating (A), cooling (B), and second heating (C) of all "as-prepared" blends of HECOs with ethylene/1-octene (INFUSE) copolymers.

Table 3.9. Values of melting temperatures and enthalpies recorded in first heating ($T_{\mathrm{m}}^{\mathrm{I}}$ and $\Delta H_{\mathrm{mTOT}}^{\mathrm{I}}$), crystallization temperatures and enthalpies (T_{c}, ΔH_{c}), and melting temperatures and enthalpies recorded in second heating ($T_{\mathrm{m}}^{\mathrm{II}}$, $\Delta H_{\mathrm{mTOT}}^{\mathrm{II}}$) of INFUSE copolymer samples, non-compatibilized HECO samples and blends of HECOs with multi-block ethylene/1-octene copolymer samples. Subscripts “1” and “2” refer to values for PE and α-form crystals, respectively.

Sample	$T_{\mathrm{m1}}^{\mathrm{I}}$ **(°C)**	$T_{\mathrm{m2}}^{\mathrm{I}}$ **(°C)**	$\Delta H_{\mathrm{mTOT}}^{\mathrm{I}}$ **(J/g)**	T_{c1} **(°C)**	T_{c2} **(°C)**	ΔH_{c} **(J/g)**	$T_{\mathrm{m1}}^{\mathrm{II}}$ **(°C)**	$T_{\mathrm{m2}}^{\mathrm{II}}$ **(°C)**	$\Delta H_{\mathrm{mTOT}}^{\mathrm{II}}$ **(J/g)**
D9000	122.5	-	36.4	96.8	-	37.1	122.3	-	38.1
D9007	51.6; 120.8	-	16.7	91.0	-	17.4	120.2	-	17.4
B1	-	165.4	72.0	99.8	116.1	82.4	118.2	163.2	85.8
B1 + D9000	123.8	166.2	94.8	102.1	116.9	73.5	118.3	163.6	74.1
B1 + D9007	115.8	164.8	70.6	101.1	118.5	75.2	118.6	163.6	74.9
EP3307	117.6	165.6	68.2	100.4	124.8	81.0	118.6	164.4	79.6
EP3307 + D9000	117.4	164.6	66.3	108.8	128.7	74.9	117.7	163.9	73.6
EP3307 + D9007	116.7	165.1	61.2	102.0	125.2	69.0	118.6	164.4	70.5
21588/45	113.3	168.6	73.9	96.0	120.2	78.9	114.6	163.7	89.4
21588/45 + D9000	116.1	166.0	73.1	101.8	116.8	75.0	117.2	165.0	83.0
21588/45 + D9007	114.0	165.3	77.3	99.3	118.2	74.1	116.0	163.7	81.0
B3	119.3	166.8	75.3	100.4	116.2	85.7	120.1	163.6	88.2
B3 + D9000	125.2	166.4	85.9	104.9	116.9	77.9	120.6	164.6	76.4
B3 + D9007	117.6	165.1	73.9	104.9	118.1	75.2	120.1	163.0	76.1

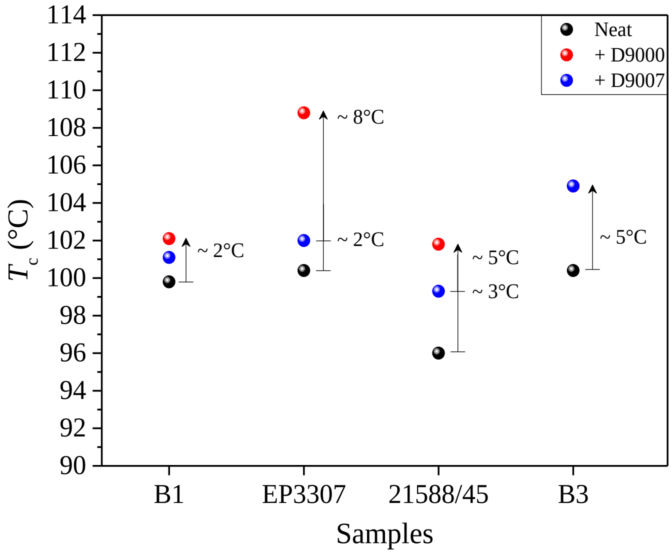

Figure 3.24. Crystallization temperatures of the EPR phase of all HECO samples before and after adding ethylene/1-octene (INFUSE) samples as compatibilizers.

The X-ray powder diffraction profiles of all compression molded films obtained by slow cooling from the melt are reported in Figure 3.25. The diffraction profiles show that all samples crystallize in the α-form of isotactic polypropylene. In addition, for blends of B3 with both ethylene/1-octene copolymer samples is also possible to note the presence of the peak at $2\theta = 16°$, corresponding to the reflection $(110)_\beta$ of the β-form of iPP.

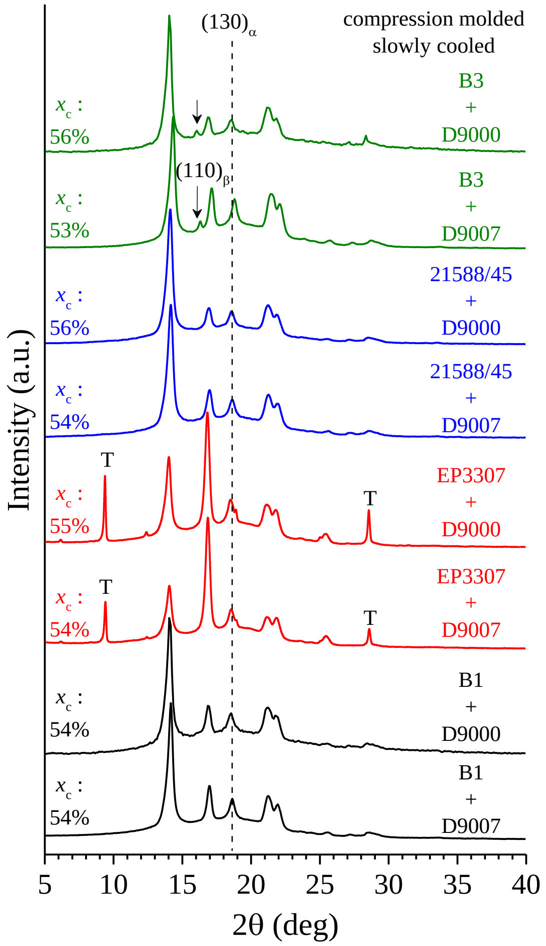

Figure 3.25. X-ray powder diffraction patterns of the compression molded films of blends of HECOs with ethylene/1-octene (INFUSE) copolymers.

Figure 3.26 shows the stress-strain curves of blends of HECOs with INFUSE copolymer samples, recorded at room temperature on films obtained by slow cooling from the melt. The values of the mechanical parameters evaluated from the stress-strain curves of Figure 3.26 are reported in Table 3.10. In all cases no improvement of the mechanical properties is observed.

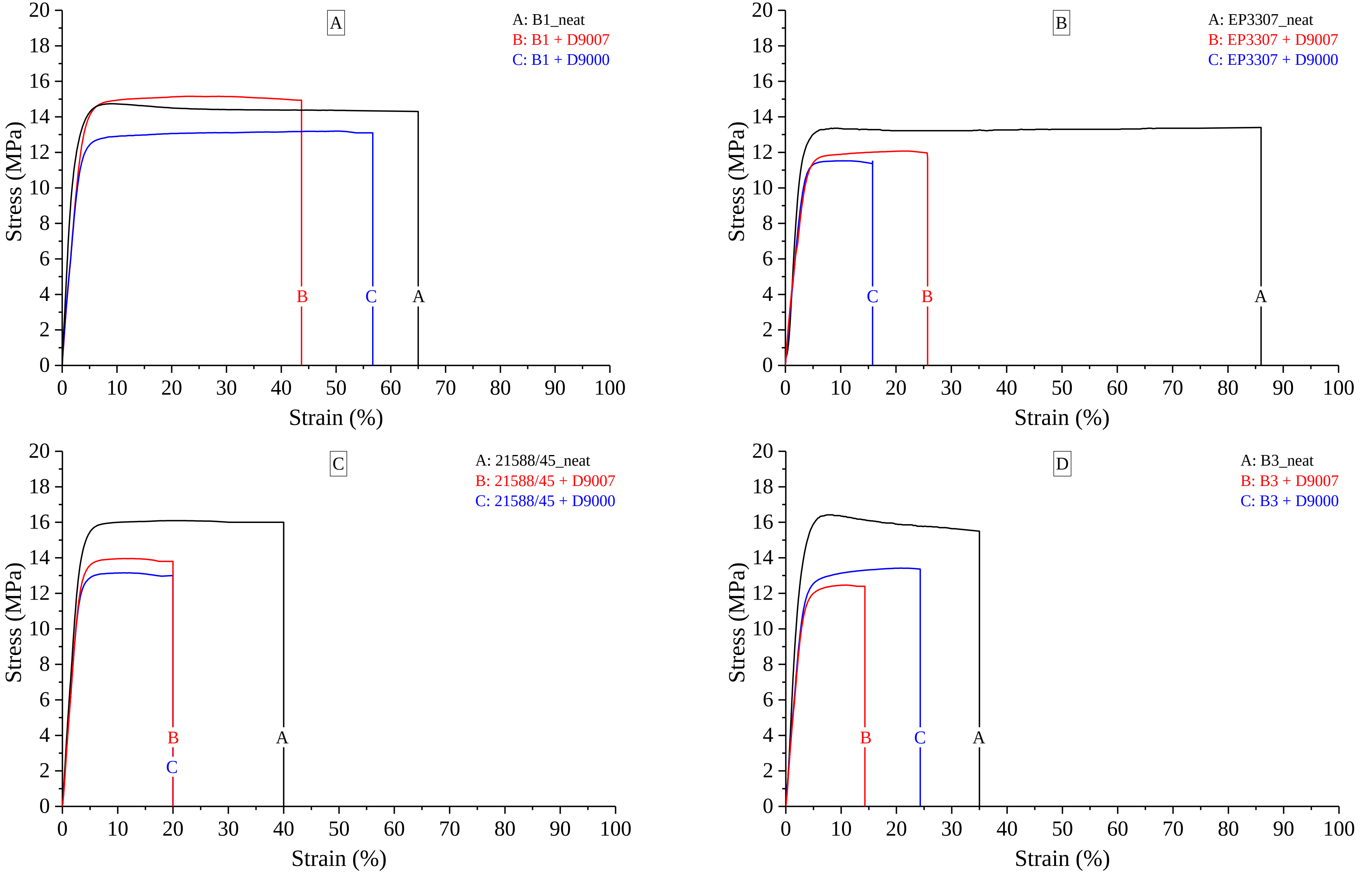

Figure 3.26. Stress-strain curves recorded at *T* = 25°C of compression-molded films of pure HECO samples B1 (A), EP3307 (B), 21588/45 (C), and B3 (D) samples, and of their blends with ethylene/1-octene (INFUSE) samples.

Table 3.10. Values of strain (ε_b) and stress (σ_b) at break, Young's modulus (E), and degree of crystallinity (x_c) of compression-molded films crystallized by slow cooling from the melt of ethylene/1-octene (INFUSE) copolymer samples, non-compatibilized HECO samples and blends of HECOs with multi-block copolymer samples.

Sample	ε_b (%)	σ_b (MPa)	E (MPa)	x_c^{a} (%)
D9000	1390 ± 200	12.2 ± 1.2	15.5 ± 0.5	-
D9007	2100 ± 300	10 ± 2	6.0 ± 1.0	-
B1	65 ± 8	14.3 ± 0.2	525 ± 25	55
B1 + D9000	60 ± 5	13.1 ± 0.6	415 ± 5	54
B1 + D9007	45 ± 10	15.1 ± 0.2	420 ± 10	54
EP3307	85 ± 5	13.4 ± 0.2	550 ± 25	57
EP3307 + D9000	16 ± 6	11.7 ± 0.8	365 ± 5	55
EP3307 + D9007	25 ± 3	11.7 ± 1.0	310 ± 50	54
21588/45	40 ± 15	16.7 ± 0.3	520 ± 30	54
21588/45 + D9000	20 ± 5	13.0 ± 0.3	455 ± 5	56
21588/45 + D9007	20 ± 2	13.8 ± 0.4	455 ± 10	54
B3	35 ± 3	15.5 ± 0.2	620 ± 30	56
B3 + D9000	25 ± 3	13.3 ± 0.7	440 ± 35	56
B3 + D9007	15 ± 5	12.4 ± 0.6	435 ± 15	53

a) Values evaluated from X-ray powder diffraction profiles of Figure 3.21B, Figure 3.25, and Figure 1.7.

3.4. Blends of HECO samples with isotactic propene-ethylene random copolymers from metallocene catalyst

The compatibilization effect of block copolymers in blends with HECO samples has been compared with that of random crystalline propene-ethylene copolymers, similar to the EPR phase of HECOs but with lower ethylene concentrations, such as to ensure crystallization of the copolymers in the iPP crystalline forms (α or γ forms) rather than in the PE orthorhombic form.

In particular, the strategy of using random C3C2 copolymers synthesized with metallocene catalysts was chosen. Figure 3.27 shows the molecular structure of the zirconocene catalytic precursor used for the synthesis of random C3C2 copolymers.

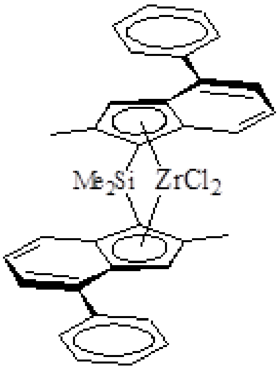

Figure 3.27. C2-symmetric zirconocene catalytic precursor (dimethylsilyl(2,2’-dimethyl-4,4’-diphenylindenyl)ZrCl$_2$) used to synthesize propylene-ethylene random copolymers before being activated with MAO.

This catalyst is highly stereo- and regio-selective and produces high-molecular-weight ethylene-propylene copolymers with very small amounts of stereo-defects (about [rr] = 0.2 mol%) and regio-defects (secondary insertions of 2,1-erythro units of propylene, [2,1e] < 1 mol %).

Table 3.11 shows the main characteristics of the two samples of C3C2 copolymers, provided by Lyondell Basell Polyolefins laboratories, used in blends with all the HECO samples listed in Table 1.1. The two samples contain only 10.1 wt% and 16.3 wt% of ethylene. Blends with 10 wt% of the two samples of random copolymers have been prepared.

Table 3.11 Concentration of ethylene (C2) (wt% and mol%), products of reactivity ratios (r_1r_2), and intrinsic viscosity (IV) of propylene-ethylene random copolymers prepared with the highly stereo- and regio-selective zirconocene catalyst of Figure 3.27.

Sample	**Type**	**C2 (wt%)**	**C2 (mol%)**	r_1r_2	**IV (dL/g)**
S15080	Random copolymers	10.1	14.4	1.5	2.4
S15071		16.3	22.5	1.6	2.8

3.4.1. Blends of HECO samples with isotactic propene-ethylene random copolymers prepared by solution mixing

Figure 3.28 shows DSC thermograms (Figure 3.28A), X-ray diffraction profiles of samples crystallized from the melt (Figure 3.28B), and stress-strain curves (Figure 3.28C) of samples of random C3C2 copolymer samples, S15080 and S15071. It is apparent that the sample S15080 with 10.1wt% of ethylene exhibits crystallinity from isotactic polypropylene in mixture of α and γ form with a low crystallinity, whereas the sample S15071 with 16wt% of ethylene is completely amorphous when cooled from the melt (Figure 3.28B). Accordingly, the DSC curves indicate that the sample S15080 shows two main endothermic peaks at 60 and 80°C in the first heating and a broad melting peak in the second heating scan, and crystallizes during the cooling at 10°C/min at nearly 54°C. On the other hand, sample S15071 shows a melting peak in the DSC curve of the as-prepared sample, but does not crystallize upon cooling from the melt. In addition, both samples are characterized by medium-low T_g values in the temperature range of -25/-30°C.

The analysis of mechanical properties (Figure 3.28C) shows that the two copolymer samples are characterized by high ductility with remarkable strain-hardening at high deformation.

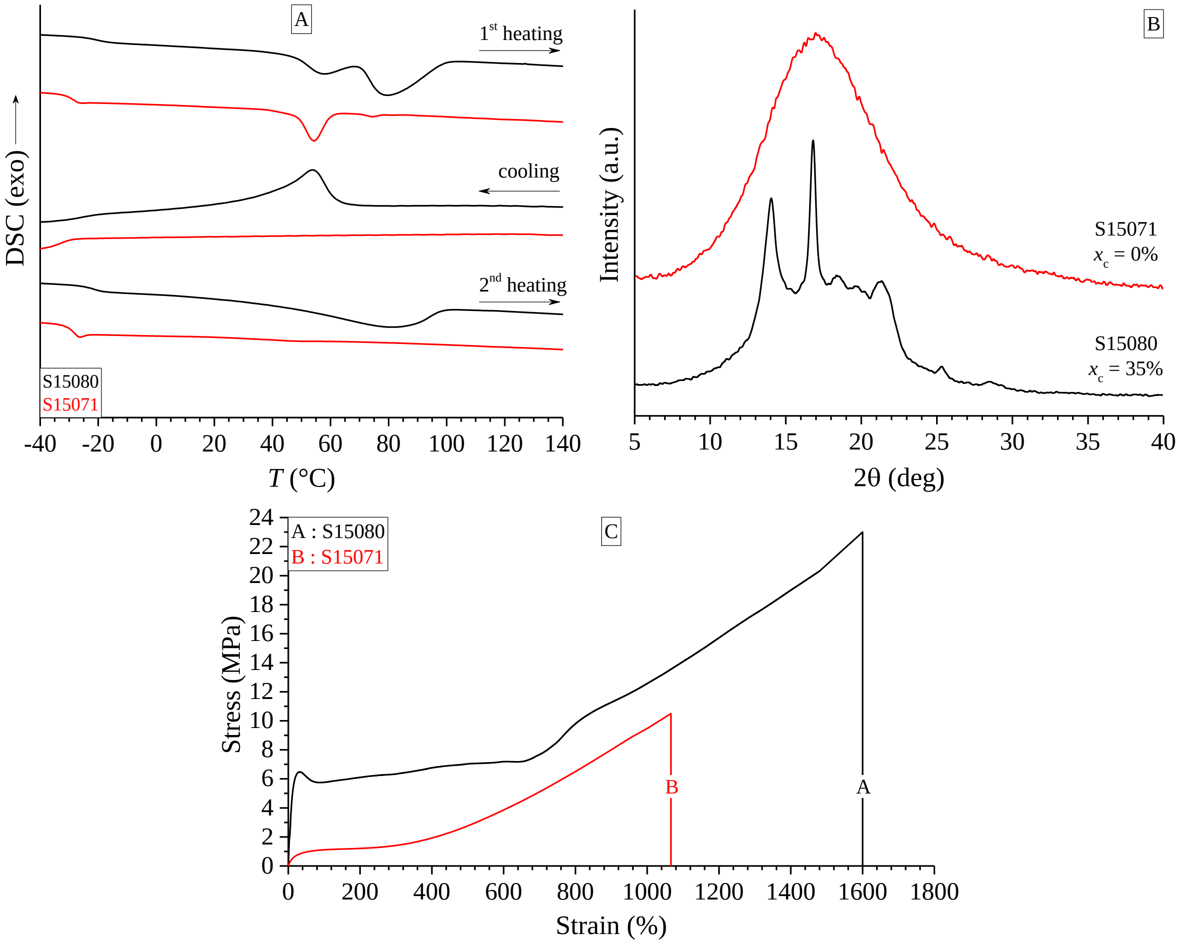

Figure 3.28. DSC thermograms (A), X-ray powder diffraction patterns of compression-molded films (B), and stress-strain curves (C) of random C3C2 copolymer samples S15080 and S15071.

The X-ray powder diffraction patterns of blends of HECOs with S15080 and S15071 samples, as obtained immediately after the blending process, are reported in Figure 3.29. All samples are crystallized in the α-form of isotactic polypropylene. In addition for the blends of samples B2 and B3, it is also possible to notice a low-intensity peak at 2θ ≈ 23.5° corresponding to the reflection $(200)_{PE}$ of the orthorhombic form of polyethylene.

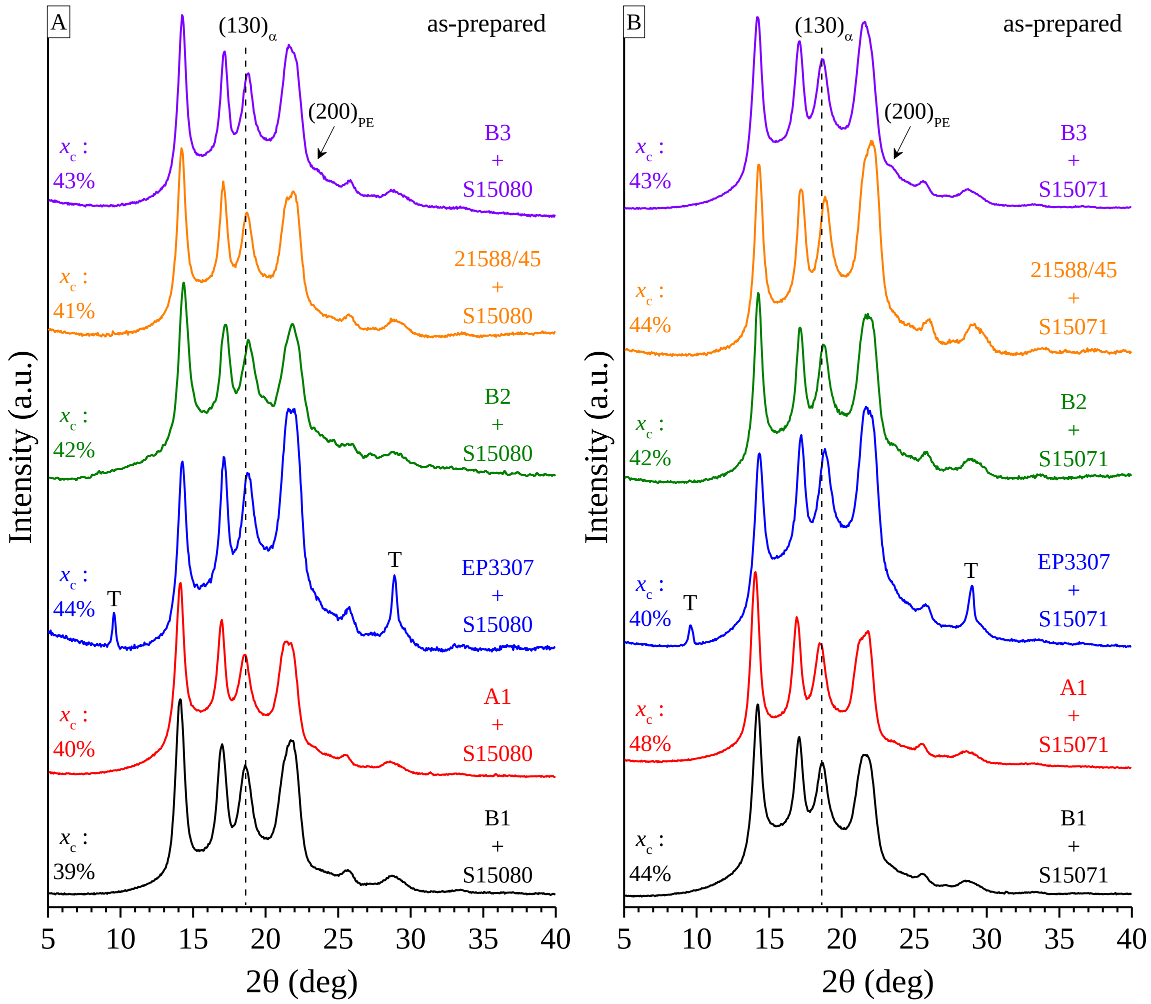

Figure 3.29. X-ray powder diffraction profiles of “as-prepared” blends of HECO samples with random C3C2 copolymer samples S15080 (A) and S15071 (B).

Figures 3.30-3.31 show the DSC thermograms of the first heating (A), cooling (B), and second heating (C) of blends of HECOs with S15080 and S15071 random copolymer samples, respectively. In the thermograms of all blends, in addition to the main melting peaks at about 160-165°C and crystallization peaks at about 115-120°C, corresponding to the melting and crystallization of the α-crystals of the thermoplastic matrix of iPP, a low-enthalpy peak at lower temperatures ($T_m \approx$ 115-120°C, $T_c \approx$ 95-105°C), corresponding to the melting and crystallization of defective polyethylene crystals belonging to the EPR phase, is present.

Table 3.12 shows the thermal parameters obtained from DSC thermograms of Figures 3.30-3.31. The presence of 10wt% of the random copolymers does not modify the melting and crystallization temperatures of both the iPP matrix and the elastomeric EPR phase of the HECO samples.

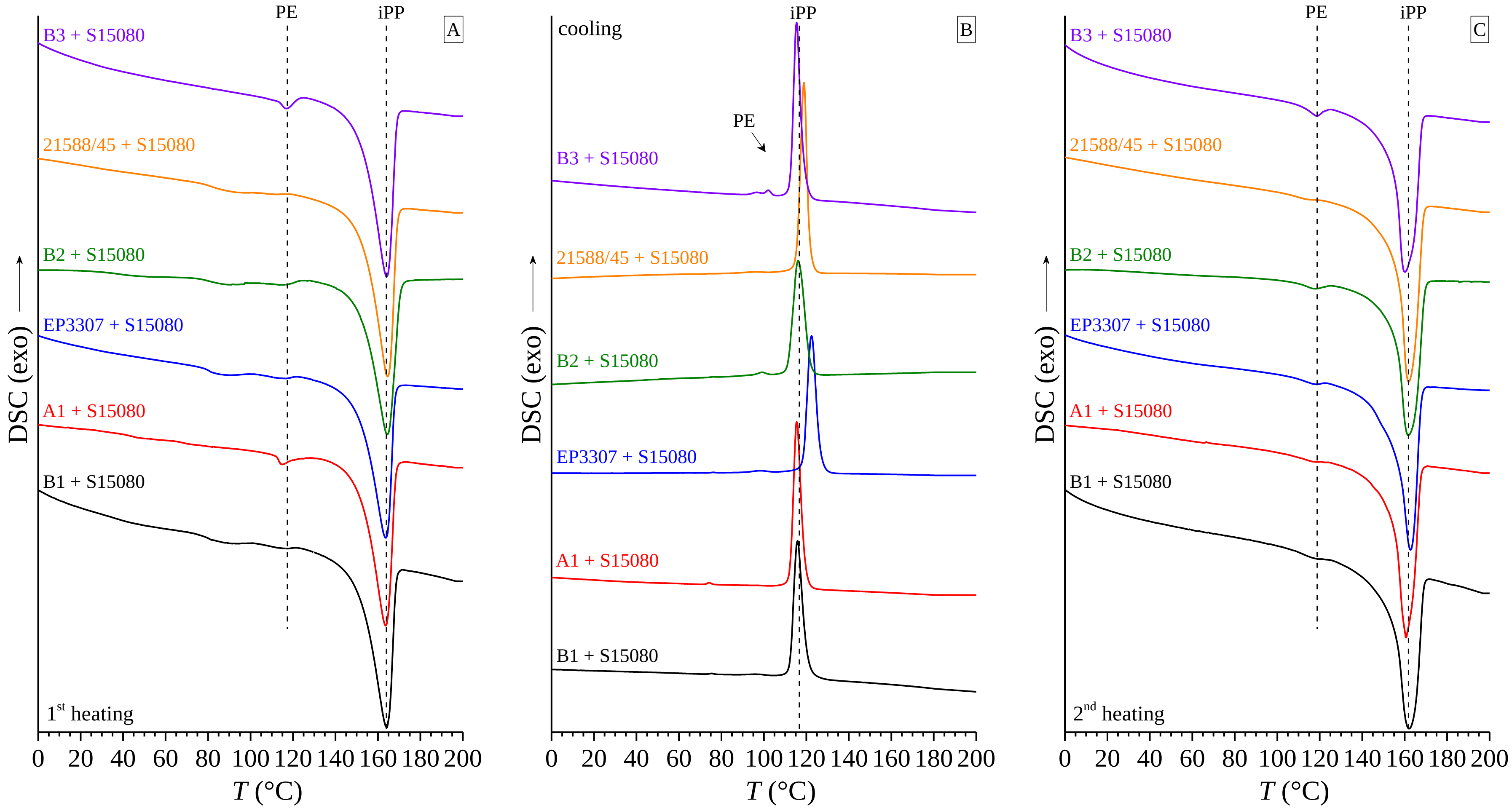

Figure 3.30. Comparison of DSC thermograms of first heating (A), cooling (B), and second heating (C) of the "as-prepared" blends of HECO samples with the random copolymer sample S15080.

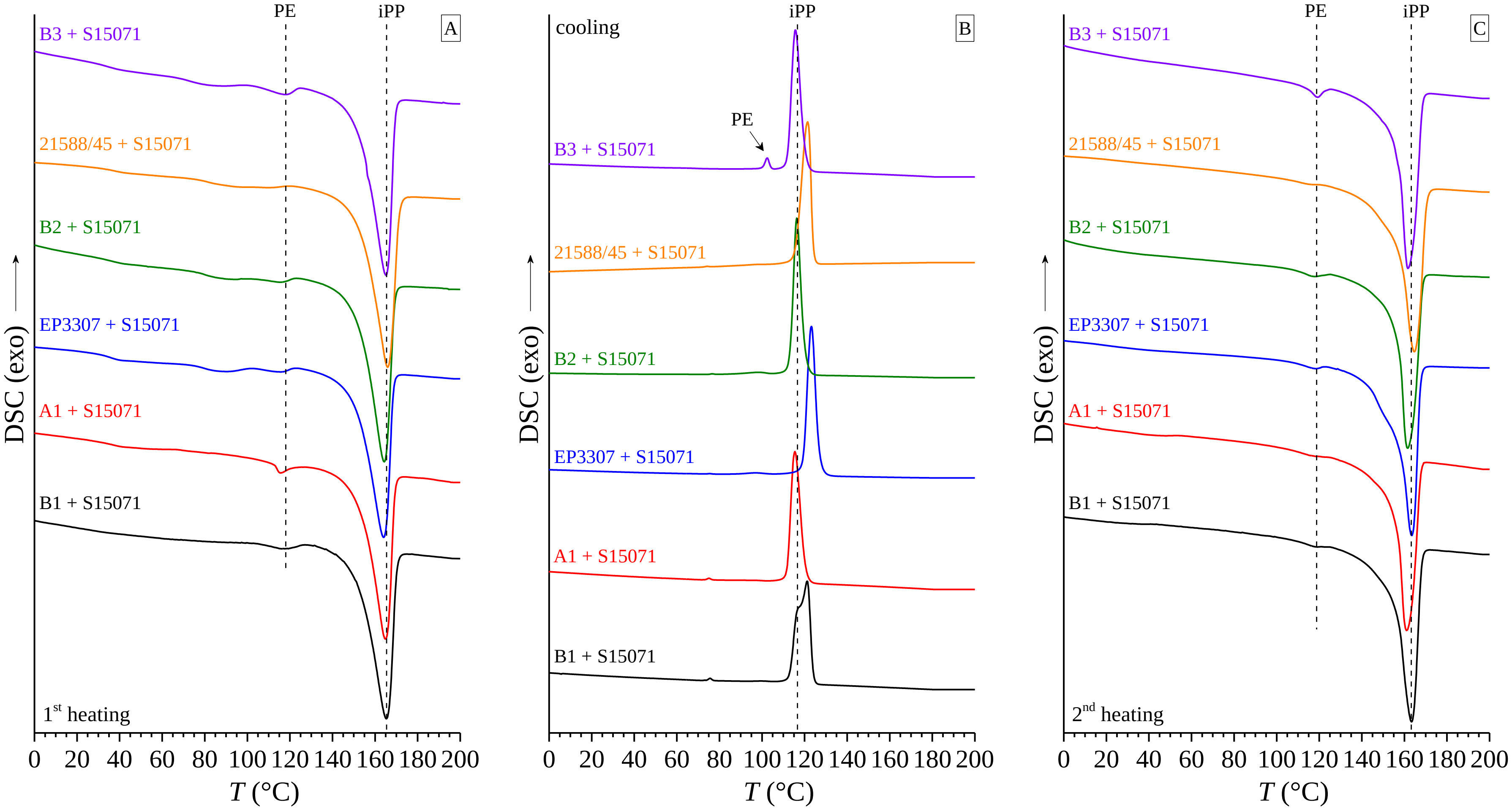

Figure 3.31. Comparison of DSC thermograms of first heating (A), cooling (B), and second heating (C) of as-prepared" blends of HECO samples with the random copolymer sample S15071.

Table 3.12. Values of melting temperatures and enthalpies recorded in first heating ($T_{\mathrm{m}}^{\mathrm{I}}$ and $\Delta H_{\mathrm{mTOT}}^{\mathrm{I}}$), crystallization temperatures and enthalpies (T_{c}, ΔH_{c}), and melting temperatures and enthalpies recorded in second heating ($T_{\mathrm{m}}^{\mathrm{II}}$, $\Delta H_{\mathrm{mTOT}}^{\mathrm{II}}$) of random C3C2 copolymer samples, non-compatibilized HECO samples and blends of HECOs with random C3C2 copolymer samples. Subscripts “1” and “2” refer to values for PE and α-form crystals, respectively.

Sample	$T_{\mathrm{m1}}^{\mathrm{I}}$ **(°C)**	$T_{\mathrm{m2}}^{\mathrm{I}}$ **(°C)**	$\Delta H_{\mathrm{mTOT}}^{\mathrm{I}}$ **(J/g)**	T_{c1} **(°C)**	T_{c2} **(°C)**	ΔH_{c} **(J/g)**	$T_{\mathrm{m1}}^{\mathrm{II}}$ **(°C)**	$T_{\mathrm{m2}}^{\mathrm{II}}$ **(°C)**	$\Delta H_{\mathrm{mTOT}}^{\mathrm{II}}$ **(J/g)**
S15080	-	58.1; 79.1	47.7	-	53.8	38.5	-	79.9	40.0
S15071	-	54.3; 74.1	11.4	-	-	-	-	-	-
B1	-	165.4	72.0	99.8	116.1	82.4	118.2	163.2	85.8
B1 + S15080	112.3	164.2	64.1	97.7	115.9	72.3	119.1	161.8	66.6
B1 + S15071	116.0	165.3	66.0	99.6	117.0; 121.3	70.0	118.6	163.4	63.0
A1	-	165.3	74.7	99.4	115.4	86.6	120.1	163.6	91.2
A1 + S15080	115.0	163.4	70.8	99.0	115.4	74.0	117.4	160.6	68.4
A1 + S15071	115.4	164.8	66.2	98.0	115.4	68.0	118.3	161.0	63.0
EP3307	117.6	165.6	68.2	100.4	124.8	81.0	118.6	164.4	79.6
EP3307 + S15080	116.4	163.7	66.5	98.4	122.5	71.6	118.0	162.8	69.6
EP3307 + S15071	89.2; 115.2	164.1	62.1	96.9	123.2	67.1	118.6	163.6	71.0
B2	118.0	166.6	74.2	101.4	116.4	84.3	118.2	162.6	87.6
B2 + S15080	113.6	164.5	69.4	99.0	116.0	71.9	117.6	161.8	70.1
B2 + S15071	114.8	164.3	67.0	98.5	116.3	70.3	117.8	161.5	67.8
21588/45	113.3	168.6	73.9	96.0	120.2	78.9	114.6	163.7	89.4
21588/45 + S15080	110.0	164.6	71.2	96.0	118.9	70.2	114.3	161.9	67.5
21588/45 + S15071	100.0	165.9	72.0	97.0	121.5	69.9	115.0	164.4	64.6
B3	119.3	166.8	75.3	100.4	116.2	85.7	120.1	163.6	88.2
B3 + S15080	116.7	164.0	69.7	102.1	115.4	75.4	118.4	160.1	68.7
B3 + S15071	117.6	165.2	67.1	102.4	115.6	74.1	119.0	161.7	68.6

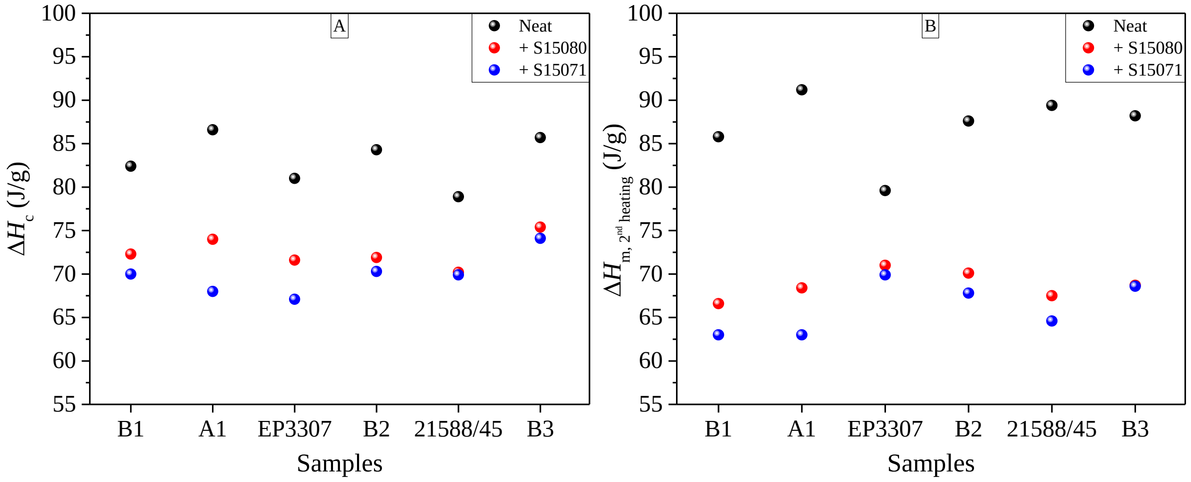

Figure 3.32. Overall crystallization (A) and second melting (B) enthalpies of all HECO samples before and after the addition of random C3C2 copolymer samples.

Figure 3.33 reports the X-ray powder diffraction patterns of all compression molded films that were obtained by slow cooling from the melt and Figure 3.34 show the corresponding stress-strain curves. The values of the mechanical parameters are reported in Table 3.13. Finally, Figure 3.35 shows the strain (Figure 3.35A) and stress (Figure 3.35B) at break and Young's modulus (Figure 3.35C) values before and after the addition of the polymeric additive. All samples are crystallized in the α-form of isotactic polypropylene, and great enhancements of the ductility and a decrease of Young's modulus are observed for blends compared to the pure HECO samples.

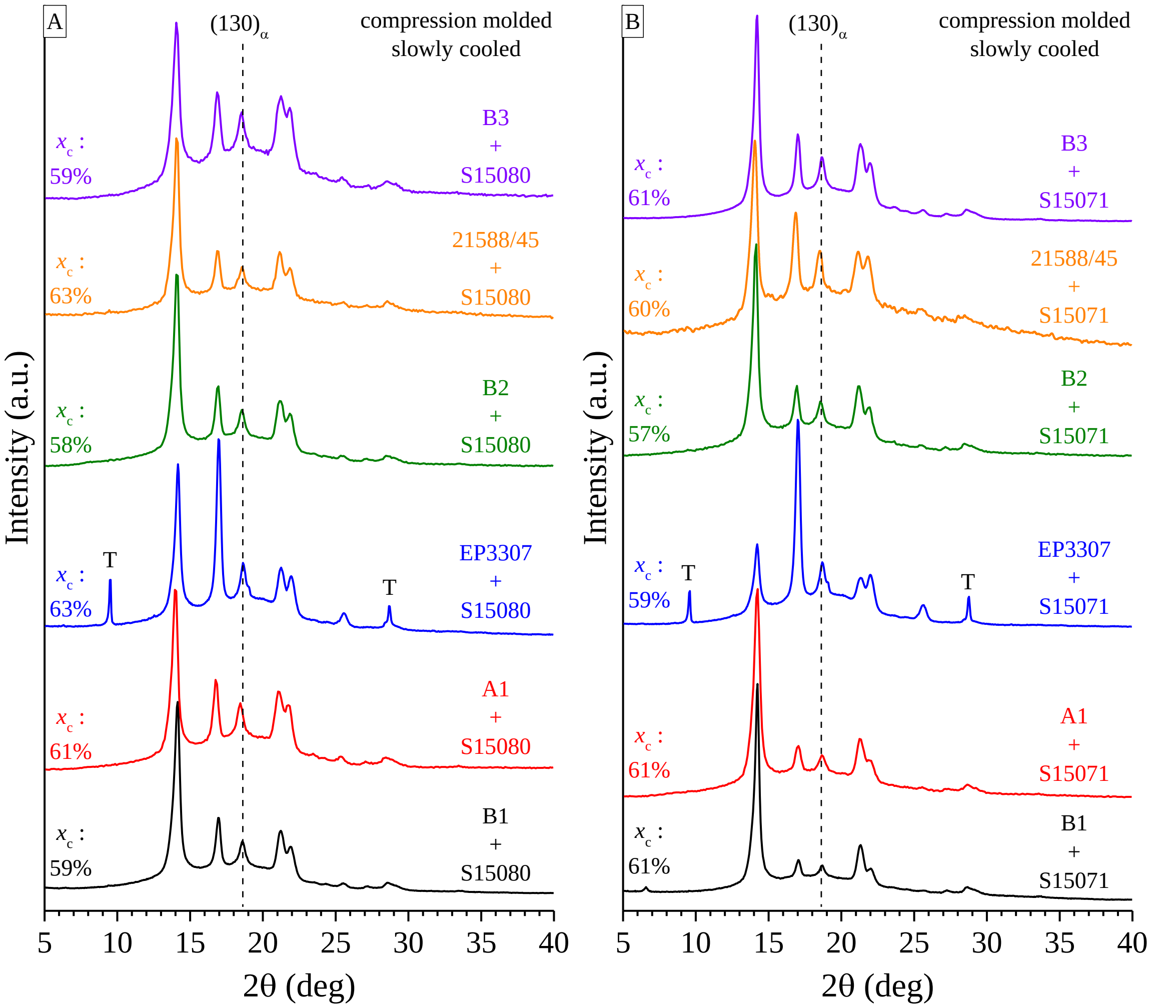

Figure 3.33. X-ray powder diffraction patterns of the compression-molded films of blends of HECO samples with the random copolymer samples S15080 (A) and S15071 (B).

Figure 3.34 shows the stress-strain curves of blends of HECOs with random C3C2 copolymer samples, recorded at room temperature on films obtained by slow cooling from the melt. For completeness, the stress-strain curves of the non-compatibilized samples are also reported in Figure 3.34. The values of the mechanical parameters evaluated from the stress-strain curves of Figure 3.34 are reported in Table 3.13. Finally, Figure 3.35 shows the strain (Figure 3.35A) and stress (Figure 3.35B) at break and Young's modulus (Figure 3.35C) values before and after the addition of the random C3C2 copolymers.

For samples B1 and A1, which are characterized by lower ethylene concentrations of the rubbery phase, the best results are obtained with the semicrystalline sample S15080, while for all the remaining samples, with gradually increasing ethylene content of the EPR phase, the best results are obtained with the amorphous sample S15071. A possible explanation for these results could lie in the fact that the addition of copolymers with low or no crystallinity acts as a "diluent" for the ethylene-rich macromolecules belonging to the starting elastomeric phase.

In fact, as seen in the previous Chapter 2, such heterophasic copolymers are characterized by varying weight percentages of fractions with high ethylene concentrations that crystallize giving PE crystals. Such fractions can be highly incompatible with the thermoplastic iPP matrix generating weak interphase interactions resulting in brittle mechanical behavior.

Since the random C3C2 copolymers with low ethylene concentration crystallize in iPP crystals and not in PE-like crystals it would be not plausible that compatibilization occurs through interaction between chemically identical blocks according to the model described in Refs. 8 and 28. Therefore, the improvement observed in the HECO copolymers examined could be due to the fact that the chemically incompatible macromolecules interact less with each other due to a higher concentration of rubbery component (resulting from the C3C2 copolymer by metallocene catalysis) that dilutes the system overall and interposes itself in the middle between the P-rich and E-rich macromolecules, according to the model involving the formation of droplets in a core-shell structure.[29,30]

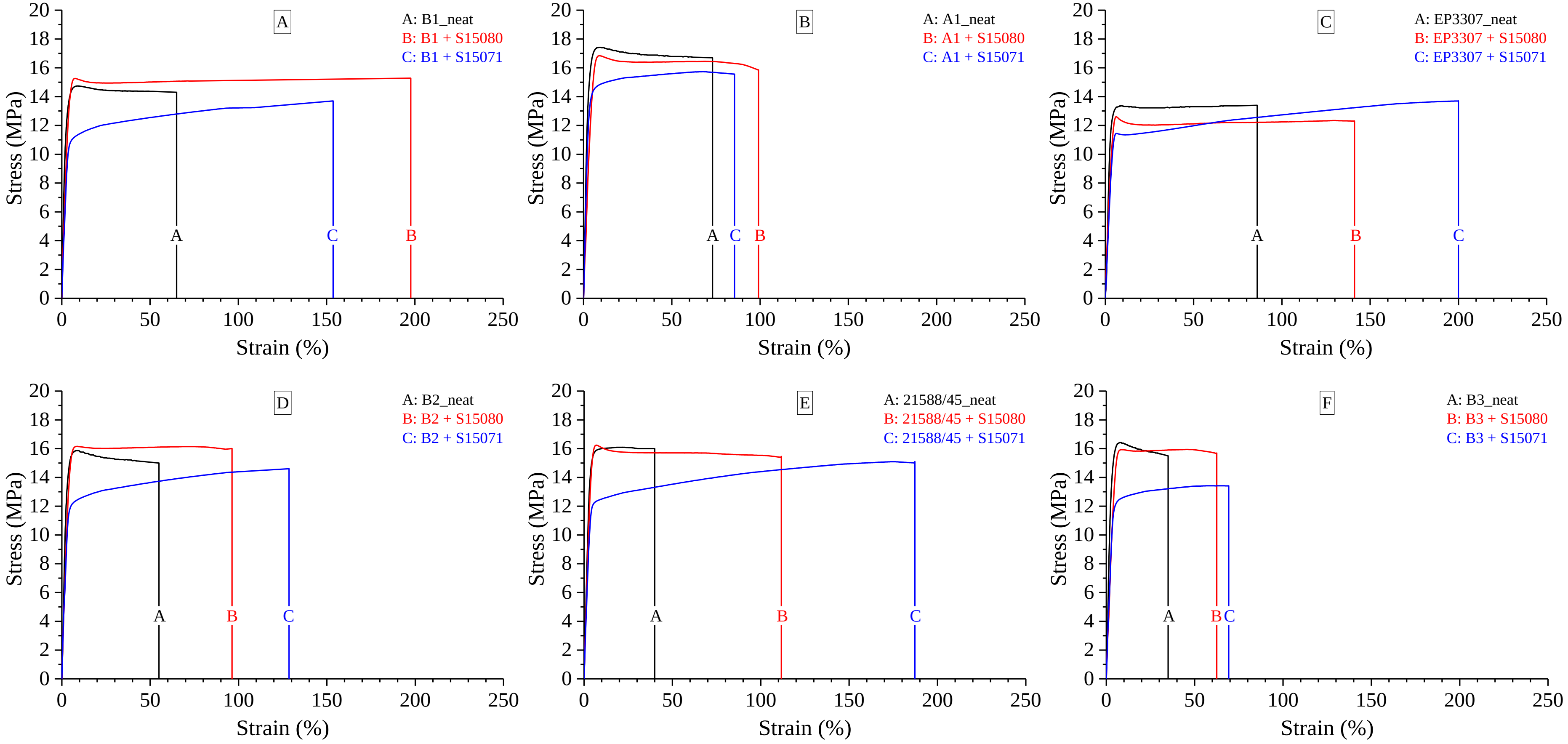

Figure 3.34. Stress-strain curves recorded at *T* = 25°C of compression-molded films of HECO samples B1 (A), A1 (B), EP3307 (C), B2 (D), 21588/45 (E), and B3 (F) and of their blends with random C3C2 copolymer samples.

Table 3.13. Values of strain (ε_b) and stress (σ_b) at break, Young's modulus (E), strain (ε_y) and stress (σ_y) at the yield point and degree of crystallinity (x_c) of compression-molded films crystallized by slow cooling from the melt of random C3C2 copolymer samples, non-compatibilized HECO samples and blends of HECOs with C3C2 copolymer samples.

Sample	**ε_b (%)**	**σ_b (MPa)**	**ε_y (%)**	**σ_y (MPa)**	**E (MPa)**	**x_c^a (%)**
S15080	1620 ± 120	23 ± 2	32 ± 3	6.5 ± 0.3	75 ± 5	35
S15071	1065 ± 95	10 ± 1	90 ± 10	1.1 ± 0.1	5.6 ± 0.6	0
B1	65 ± 8	14.3 ± 0.2	-	-	525 ± 25	55
B1 + S15080	200 ± 40	15.0 ± 0.8	8.0 ± 0.5	15.0 ± 0.8	410 ± 30	59
B1 + S15071	150 ± 60	14.0 ± 0.8	-	-	330 ± 25	61
A1	75 ± 5	16.4 ± 0.3	-	-	620 ± 25	57
A1 + S15080	100 ± 20	16.0 ± 0.2	9.0 ± 1.3	17.0 ± 0.5	400 ± 30	61
A1 + S15071	90 ± 20	15.6 ± 0.1	-	-	310 ± 20	61
EP3307	85 ± 5	13.4 ± 0.2	-	-	550 ± 25	57
EP3307 + S15080	140 ± 30	12.0 ± 0.3	6.0 ± 0.5	13.0 ± 0.4	350 ± 15	63
EP3307 + S15071	200 ± 50	14.0 ± 0.4	6.0 ± 0.8	12.0 ± 0.2	290 ± 10	59
B2	55 ± 10	15.0 ± 0.4	-	-	520 ± 25	55
B2 + S15080	100 ± 15	16.0 ± 0.5	9.0 ± 1.5	16.0 ± 0.5	430 ± 30	58
B2 + S15071	130 ± 30	15.0 ± 0.5	-	-	370 ± 20	57
21588/45	40 ± 15	16.7 ± 0.3	-	-	520 ± 30	54
21588/45 + S15080	110 ± 5	16.0 ± 0.2	7.0 ± 0.7	16.0 ± 0.3	370 ± 15	63
21588/45 + S15071	190 ± 30	15.0 ± 0.3	-	-	320 ± 20	60
B3	35 ± 3	15.5 ± 0.2	-	-	620 ± 30	56
B3 + S15080	65 ± 5	16.0 ± 0.1	8.0 ± 0.9	16.0 ± 0.3	350 ± 25	59
B3 + S15071	70 ± 10	13.0 ± 0.3	-	-	320 ± 15	61

a) Values evaluated from X-ray powder diffraction profiles of Figure 3.28B, Figure 3.33, and Figure 1.7.

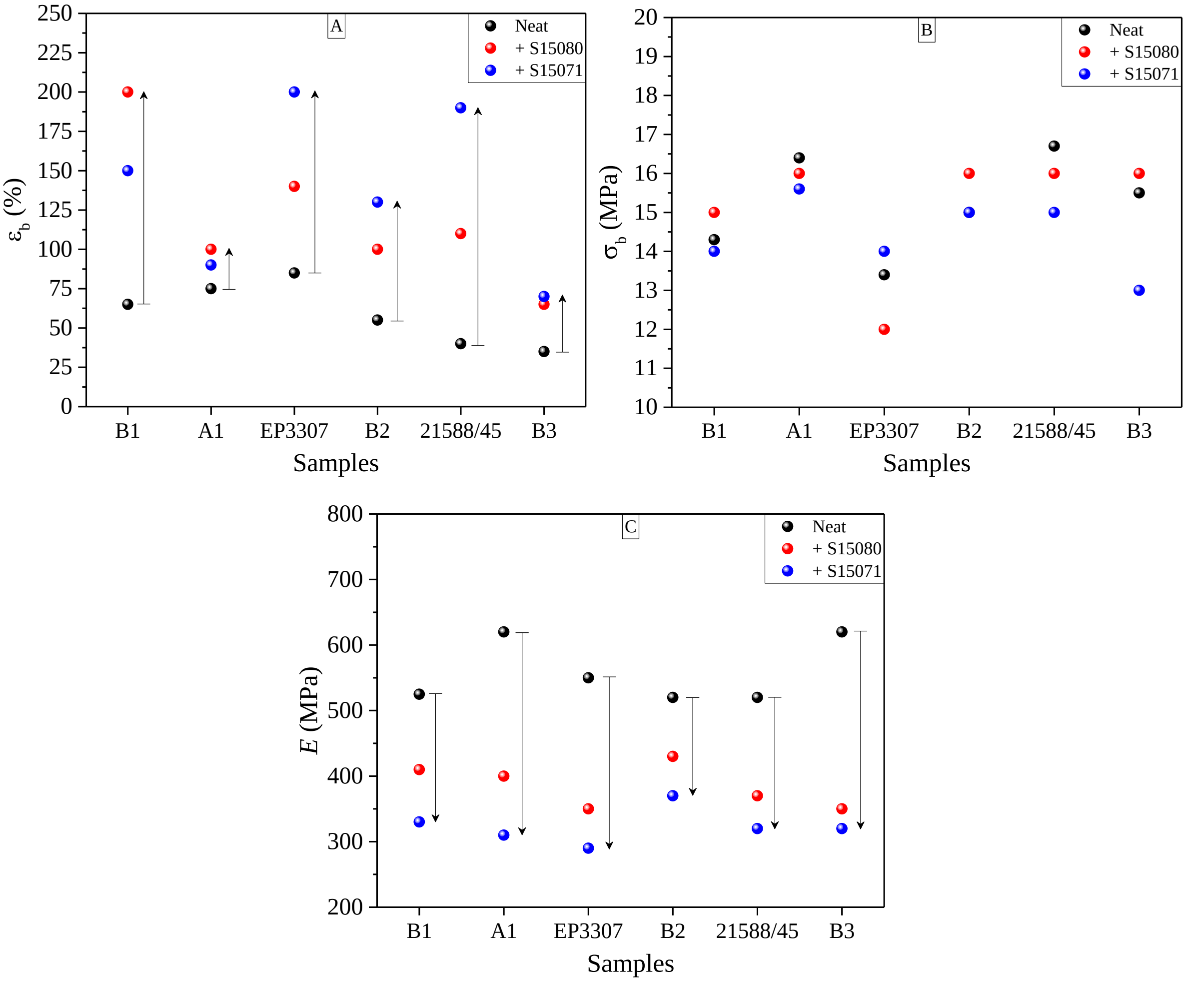

Figure 3.35. Strain (A) and stress (B) at break, and Young's modulus (C) values of all HECO samples before and after the addition of random C3C2 copolymer samples.

3.4.2. Blends of HECO samples with isotactic propene-ethylene random copolymers prepared by extruder mixing

Considering the promising results obtained with the random C3C2 copolymers with low ethylene concentrations, blends of HECO samples with metallocene C3C2 copolymers have been prepared by melt mixing in an extruder to improve the dispersion of the two components in the blends. Six samples of blends of one sample of HECO with three different samples of C3C2 copolymers having different ethylene concentrations in the range of 10-20wt% have been prepared. For each C3C2 copolymer sample, two blends with 95:5wt% and 90:10wt% HECO/C3C2 ratios have been prepared.

The main characteristics of the random C3C2 copolymer samples, prepared with the same metallocene catalyst of Figure 3.27, used for preparing blends in the extruder are shown in Table 3.14. These three samples are very similar to those described in the previous section (samples S15080 and S15071).

Table 3.14. Concentration of ethylene (C2) (wt% and mol%), melt flow index (MFI), density, and stress at break (ε_b) of propylene-ethylene random copolymers prepared with the highly stereo- and regio-selective zirconocene catalyst of Figure 3.27 and used for the preparation of extruder blends.

Sample	Type	C2 (wt%)	C2 (mol%)	MFI (g/10')	Density (Kg/dm^3)	ε_b (%)
Copo10	Random copolymers	10.4	14.4	2.95	0.879	680
Copo15		15.1	21.1	2.98	0.867	710
Copo20		19.4	26.5	2.80	0.856	780

The main characteristics of the pure HECO sample, labeled LYBA, and those of the blends prepared with the random C3C2 copolymers of Table 3.14 are listed in Table 3.15. The sample LYBA is characterized by an XS fraction of 26.3wt% and an average total ethylene concentration of 12.6 wt%. Assuming that the XS fractions roughly correspond to the percentage of the elastomeric EPR phase, the HECO sample LYBA is characterized by an EPR rubbery phase with an ethylene concentration of about 50 wt% ($C2_{EPR} = (C2_{average} / XS)*100$). Therefore, this new HECO sample is similar to the samples analyzed so far and shown in Table 1.1.

Table 3.15. Percentage and type of additive, average ethylene concentration ($C2_{average}$) evaluated from IR analysis, percentage of xylene soluble fraction (XS), and intrinsic viscosity (IV) of the new HECO sample and its blends with propylene-ethylene random copolymers of Table 3.14.

Sample	**Additive (wt%)**	**Additive**	**$C2_{average}$ (wt%)**	**XS (%)**	**IV (dL/g)**
LYBA	-	-	12.8	26.3	3.33
BLEND 5	5	Copo10	12.8	26.5	3.20
BLEND 3		Copo15	12.9	28.4	3.09
BLEND 1		Copo20	12.9	29.9	3.16
BLEND 6	10	Copo10	12.6	28.5	3.14
BLEND 4		Copo15	13.1	31.5	2.90
BLEND 2		Copo20	13.4	33.7	2.83

It is noticeable that the addition of the random copolymers does not result in great changes in the average ethylene concentration of the samples. However, as the ethylene concentration of the added random copolymer increases as well as its weight percentage in the blend increases, the fraction of sample soluble in xylene increases and the intrinsic viscosity value decreases.

The X-ray powder diffraction profiles of the neat HECO LYBA sample and of all blends reported in Figure 3.36 indicate that all samples crystallize in the α-form of isotactic polypropylene. In addition, all samples show the characteristic Bragg reflection at $2\theta \approx 16°$ corresponding to the $(110)_\beta$ plane of the β-form of iPP.

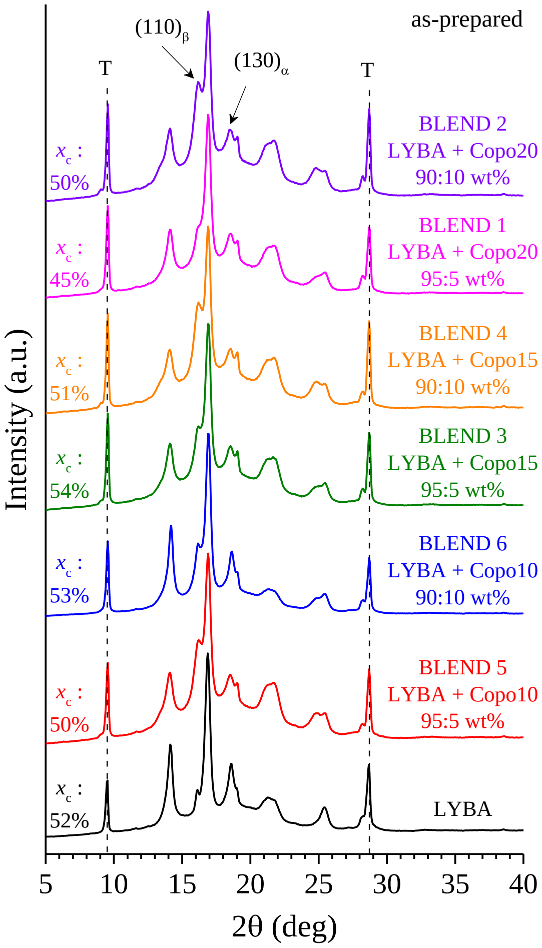

Figure 3.36. X-ray powder diffraction profiles of the "as-prepared" HECO sample and all "as-prepared" blends of HECO with random C3C2 copolymer samples.

Figure 3.37 shows the DSC thermograms of the first heating (A), cooling (B), and second heating (C) recorded on the neat HECO LYBA sample and on all its blends with random C3C2 copolymers. In addition to the primary melting peaks at approximately 160-165°C and crystallization peaks at about 125°C, which correspond to the melting and crystallization of the α-crystals of the thermoplastic matrix of iPP, all blends also exhibit a low-enthalpy peak at lower temperatures ($T_m \approx$ 115-120°C, $T_c \approx$ 100°C) generated by the melting and crystallization of defective polyethylene crystals belonging to the rubbery EPR phase.

Table 3.16 shows the thermal parameters obtained from DSC thermograms of Figure 3.37. As can be noticed, the melting and crystallization temperatures of the thermoplastic iPP matrix and the elastomeric phase of the HECO samples are not affected by the addition of 5-10wt% of these random copolymers, whereas both the values of the crystallization and melting enthalpy and, hence, of crystallinity decrease with increasing ethylene concentration of the C3C2 copolymer (Figure 3.38).

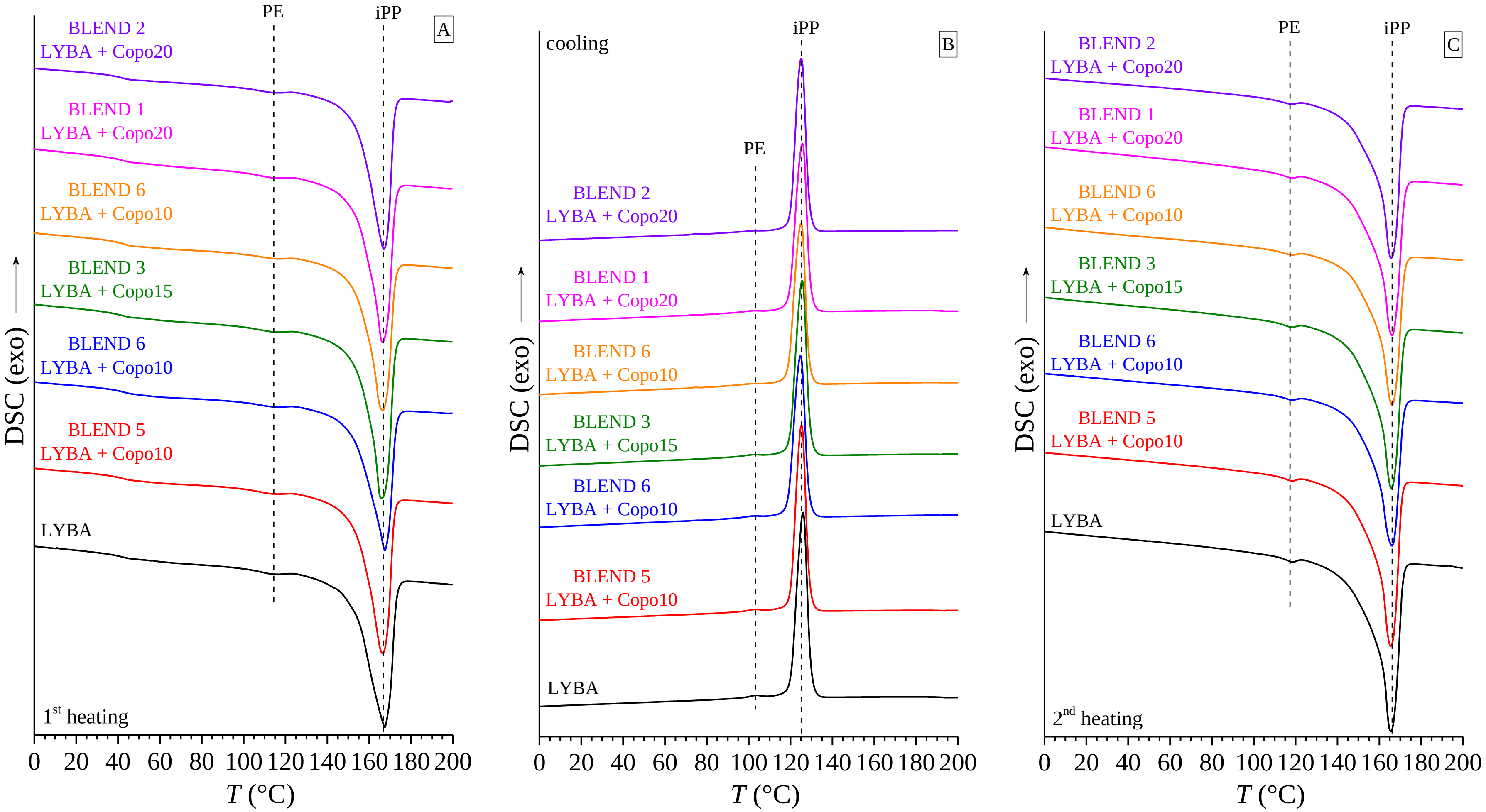

Figure 3.37. Comparison of DSC thermograms of first heating (A), cooling (B), and second heating (C) of the “as-prepared” HECO sample and all “as-prepared” blends of the HECO sample with random C3C2 copolymer samples.

Table 3.16. Values of melting temperatures and enthalpies recorded in first heating ($T_{\mathrm{m}}^{\mathrm{I}}$ and $\Delta H_{\mathrm{mTOT}}^{\mathrm{I}}$), crystallization temperatures and enthalpies (T_{c}, ΔH_{c}), and melting temperatures and enthalpies recorded in second heating ($T_{\mathrm{m}}^{\mathrm{II}}$, $\Delta H_{\mathrm{mTOT}}^{\mathrm{II}}$) of HECO sample and blends of HECO with random C3C2 copolymer samples. Subscripts “1” and “2” refer to values for PE and α-form crystals, respectively.

Sample	$T_{\mathrm{m1}}^{\mathrm{I}}$ **(°C)**	$T_{\mathrm{m2}}^{\mathrm{I}}$ **(°C)**	$\Delta H_{\mathrm{mTOT}}^{\mathrm{I}}$ **(J/g)**	T_{c1} **(°C)**	T_{c2} **(°C)**	ΔH_{c} **(J/g)**	$T_{\mathrm{m1}}^{\mathrm{II}}$ **(°C)**	$T_{\mathrm{m2}}^{\mathrm{II}}$ **(°C)**	$\Delta H_{\mathrm{mTOT}}^{\mathrm{II}}$ **(J/g)**
LYBA	113.7	167.5	88.8	103.4	126.0	90.0	118.4	165.4	92.0
BLEND 5	113.1	166.4	87.0	102.9	125.3	88.1	118.4	165.6	85.0
BLEND 6	114.1	167.5	90.7	102.8	124.8	83.6	118.0	166.1	82.4
BLEND 3	113.7	165.9	89.8	102.9	125.5	84.3	118.2	165.9	84.0
BLEND 4	114.0	166.4	86.6	102.3	125.0	82.5	118.2	166.0	80.6
BLEND 1	113.7	166.3	89.2	102.8	125.6	83.0	118.2	166.0	82.0
BLEND 2	113.8	166.9	82.5	102.9	125.2	80.6	117.6	165.6	80.0

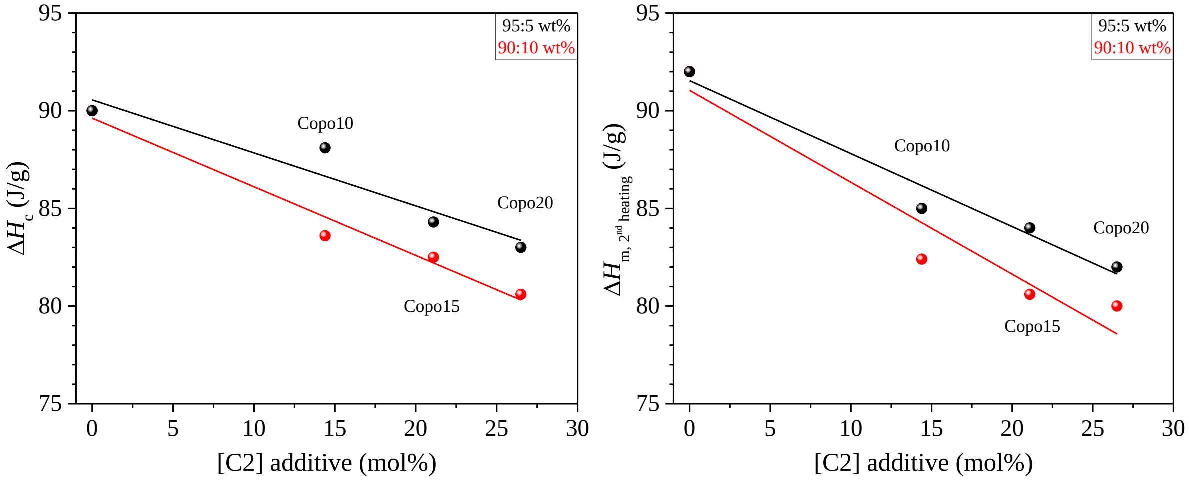

Figure 3.38. Overall crystallization (A) and second melting (B) enthalpies of the HECO LYBA sample before and after the addition of 5 and 10wt% of random C3C2 copolymer samples as a function of the ethylene concentration in the C3C2 copolymer.

The X-ray powder diffraction profiles of all compression molded films crystallized by slow cooling from the melt are shown in Figure 3.39. All samples crystallize in the α-form of isotactic polypropylene with a small amount of crystals of γ form.

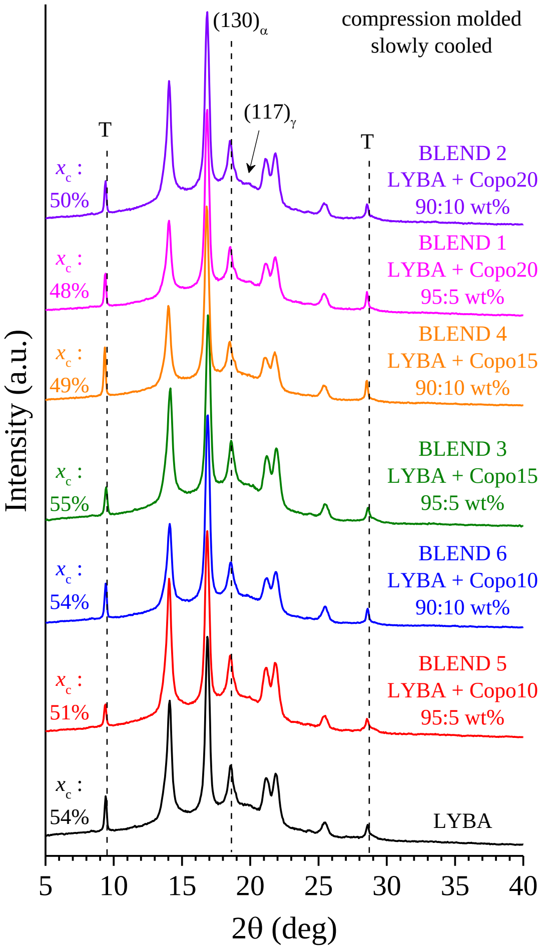

Figure 3.39. X-ray powder diffraction profiles of the compression molded films of LYBA HECO sample and of all blends of HECO with random C3C2 copolymer samples.

Figure 3.40 shows the stress-strain curves of blends of HECO and its blends with random C3C2 copolymer samples, recorded at room temperature on films obtained by slow cooling from the melt. The values of the mechanical parameters evaluated from the stress-strain curves of Figure 3.40 are reported in Table 3.17, whereas Figure 3.41 shows the strain (Figure 3.41A) and stress (Figure 3.41B) at break and Young's modulus (Figure 3.41C) values before and after the addition of the polymeric additives.

From the analysis of the mechanical properties, it is well evident that the presence of the C3C2 copolymers results in ductility improvements compared to the pure HECO sample and a decrease of modulus and strength. In general, as the ethylene concentration of the added copolymer increases, better performance is obtained and the specimen achieves higher values of strain at break. In addition, the ductility of the samples improves as the content of the C3C2 copolymer incorporated in the HECO system increases. In fact, specimens with a lower weight percentage of additive are more brittle than specimens with 10wt% of random C3C2 copolymer.

As shown in Figure 3.41, for samples with a HECO/C3C2 ratio of 95:5wt%, ductility increases as the ethylene concentration of the additive increases. On the other hand, for blends with a 90:10wt% ratio, it is observed that the best performance is achieved in the presence of the Copo15 sample with an ethylene concentration of about 20mol%. From this result, it can be inferred that high concentrations of an amorphous copolymer with high ethylene concentration (as in the case of Copo20) produce a worsening of the mechanical properties.

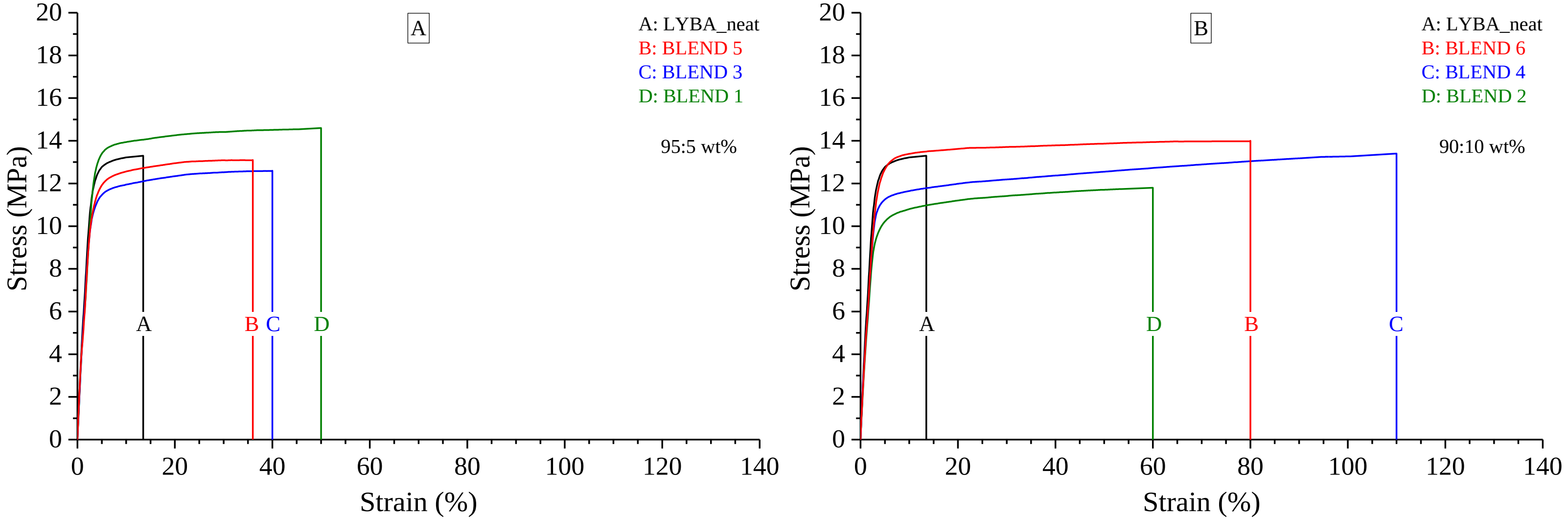

Figure 3.40. Stress-strain curves recorded at *T* = 25°C of compression-molded films of HECO sample and all blends at 95:5wt% (A) and 90:10wt% (B) of HECO with random C3C2 copolymer samples.

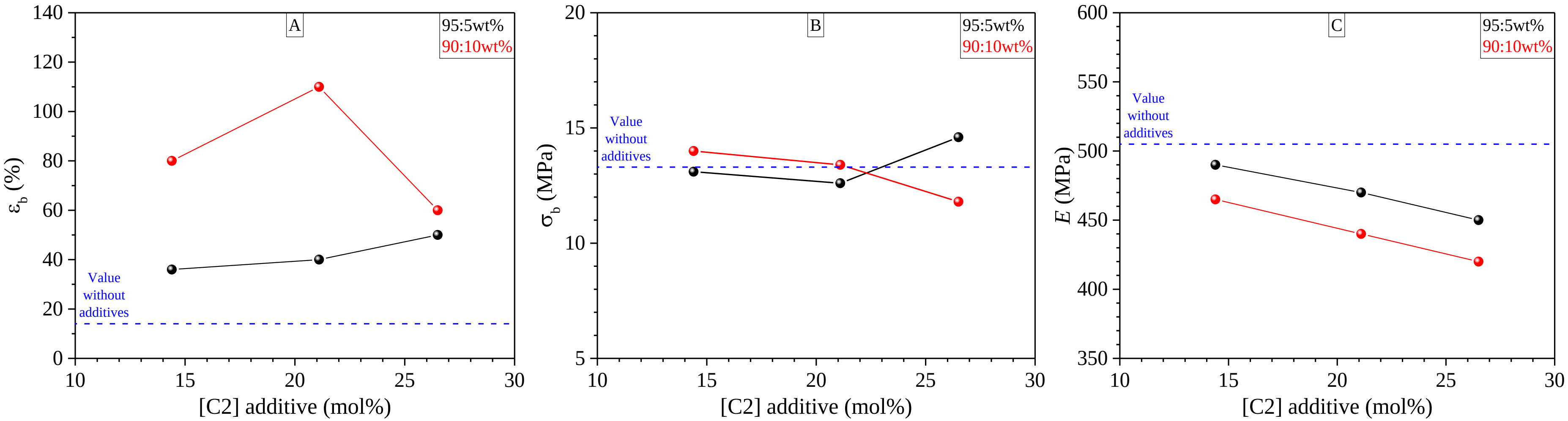

Figure 3.41. Strain (A) and stress (B) at break, and Young's modulus (C) values of HECO sample before and after the addition of random C3C2 copolymer samples.

Table 3.17. Values of strain (ε_b) and stress (σ_b) at break, Young's modulus (E), and degree of crystallinity (x_c) of compression-molded films crystallized by slow cooling from the melt of the HECO sample and of all blends with random C3C2 copolymer samples.

Sample	**ε_b (%)**	**σ_b (MPa)**	**E (MPa)**	**x_c[a] (%)**
LYBA	14 ± 2	13.3 ± 1.3	505 ± 25	54
BLEND 5	36 ± 8	13.1 ± 0.6	490 ± 20	51
BLEND 6	80 ± 20	14.0 ± 0.5	465 ± 20	54
BLEND 3	40 ± 10	12.6 ± 0.8	470 ± 20	55
BLEND 4	110 ± 20	13.4 ± 0.6	440 ± 25	49
BLEND 1	50 ± 10	14.6 ± 0.5	450 ± 10	48
BLEND 2	60 ± 10	11.8 ± 0.7	420 ± 10	50

a) Values evaluated from X-ray powder diffraction patterns of Figure 3.39.

3.5. Blends of isotactic polypropylene with other rubbery phases

Although HECO copolymers are already widely used in various industries, we have studied the possibility to replace the EPR phase with alternative rubbery components. To this aim, we have studied the properties of blends of iPP with samples of random ethylene-butene copolymers (C2C4) or with a sample of high molecular mass isotactic poly(1-octene).

Samples of the iPP homopolymer (sample X19875) prepared with Ziegler-Natta catalyst and samples of C2C4 copolymers with butene concentration in the range 15-30 mol%, prepared with a metallocene catalyst, and the sample of poly(1-octene) were provided by Lyondell Basell. All samples are reported in Table 3.18. The metallocene catalyst used for the synthesis of the C2C4 copolymers is shown in Figure 3.42.

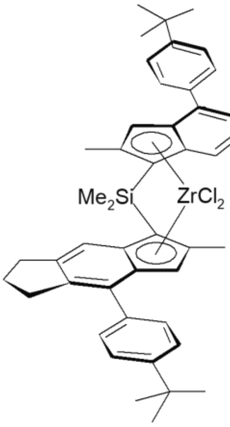

Figure 3.42. C2-symmetric zirconocene catalytic precursor dimethylsilyl bis [2-methyl-4-(4'-tert-butylphenyl)-1,5,6,7-tetrahydro-s-indacen-1-yl]$ZrCl_2$) used to synthesize ethylene-butene random copolymers before being activated with MAO.

Table 3.18. Butene concentration (C4) (wt% and mol%), products of reactivity ratios (r_1r_2), intrinsic viscosity (IV), average molecular weights (M_w), and polydispersity index (PDI) of ethylene-butene random copolymers prepared with the highly stereo- and regio-selective zirconocene catalyst of Figure 3.42 and concentration of the *mmmm* pentad and molecular mass of poly(1-octene).

Sample	**Type**	**C4 (wt%)**	**C4 (mol%)**	r_1r_2	**IV (dL/g)**	M_w **(Kg/mol)**	**PDI**
S09057	Random copolymers	29.5	17.3	0.93	1.5	-	-
S09033		31.2	18.5	0.89	2.3	-	-
S09062		38.7	24.0	0.75	1.4	-	-
S09066		41.1	25.9	0.71	1.8	-	-
Poly(1-octene) (PO)	Homopolymer mmmm = 95%	-	-	-	-	1400	2.7

In order to directly compare the results of the new blends with the HECO copolymers presented in Table 1.1 (Chapter 1), iPP/C2C4 blends were prepared by keeping a constant ratio of 70:30wt% and varying the butene concentration of the copolymer. On the other hand, blends of iPP with 10, 30, and 40wt% of poly(1-octene) have been prepared.

Figures 3.43-3.44 show DSC thermograms (Figures 3.43A,3.44A), X-ray diffraction profiles of samples crystallized from the melt (Figures 3.43B,3.44B), and the correspondent stress-strain curves (Figures 3.43C,3.44C) of the pure samples of random C2C4 copolymers and isotactic PO sample, respectively.

The X-ray diffraction profiles of the C2C4 copolymers indicate that all samples are almost amorphous with the presence of a small number of crystals of the orthorhombic form of PE (Figure 3.43B), as demonstrated by the presence of the (110) reflection of PE at $2\theta = 21.5°$. Accordingly, the DSC heating and cooling curves show very small melting and crystallization peaks (Figure 3.43A).

The stress-strain curves (Figure 3.43C) indicate that all C2C4 copolymers samples show great ductility with high deformation at break and different tensile strengths depending on the butene concentration.

Regarding the isotactic poly(1-octene) sample, the diffraction profile (Figure 3.44B) and the DSC curves (Figure 3.44A) show that the sample is completely amorphous, despite the high percentage of pentads "*mmmm*" (95%), with a very low glass transition temperature of -65°.

The analysis of mechanical properties (Figure 3.44C) shows that the PO sample is characterized by good ductility, low mechanical strength, and elastic properties, according to the very low values of the tension set after breaking.

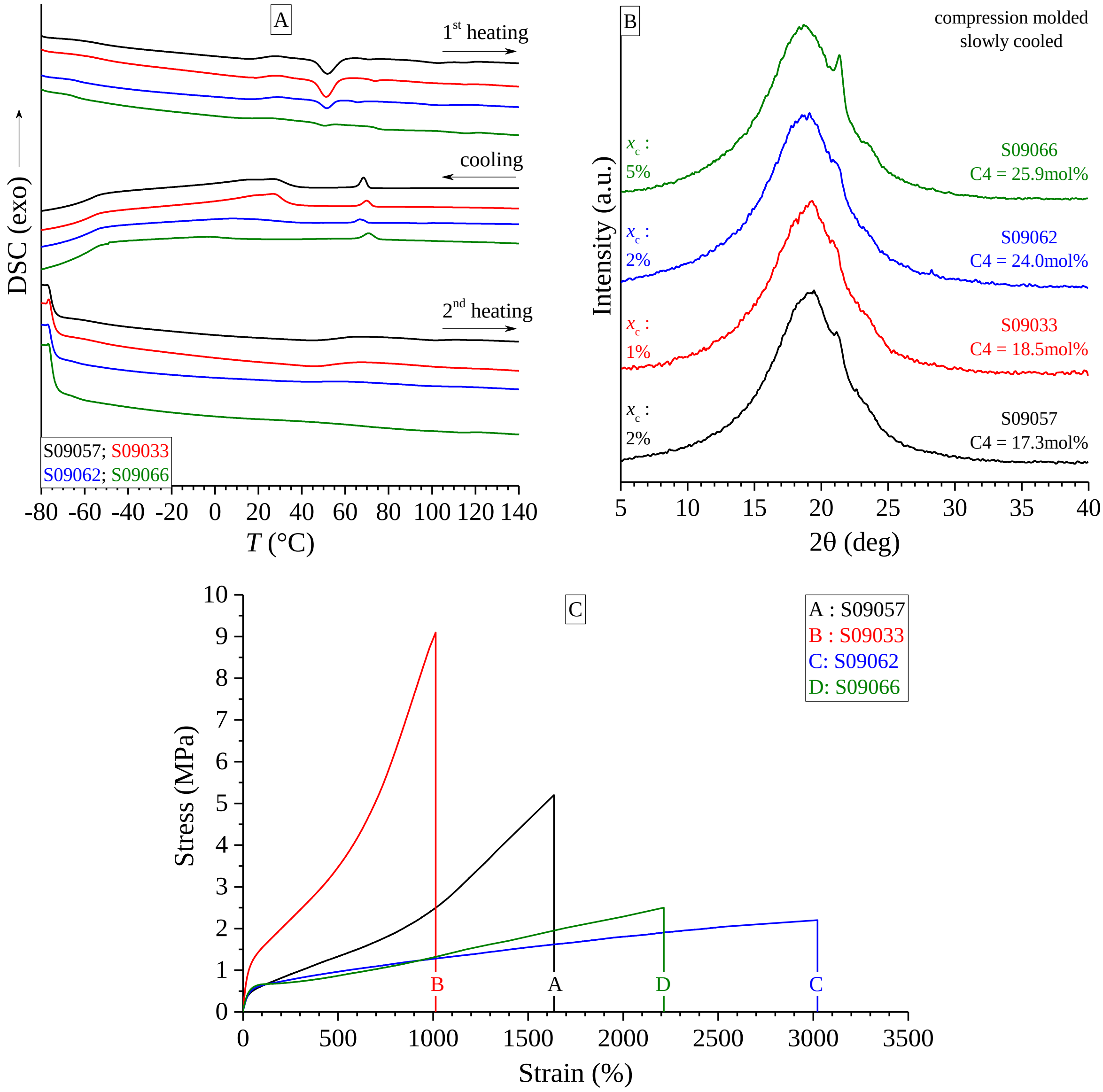

Figure 3.43. DSC thermograms (A), X-ray powder diffraction patterns of compression-molded films (B), and stress-strain curves (C) of random C2C4 copolymer samples.

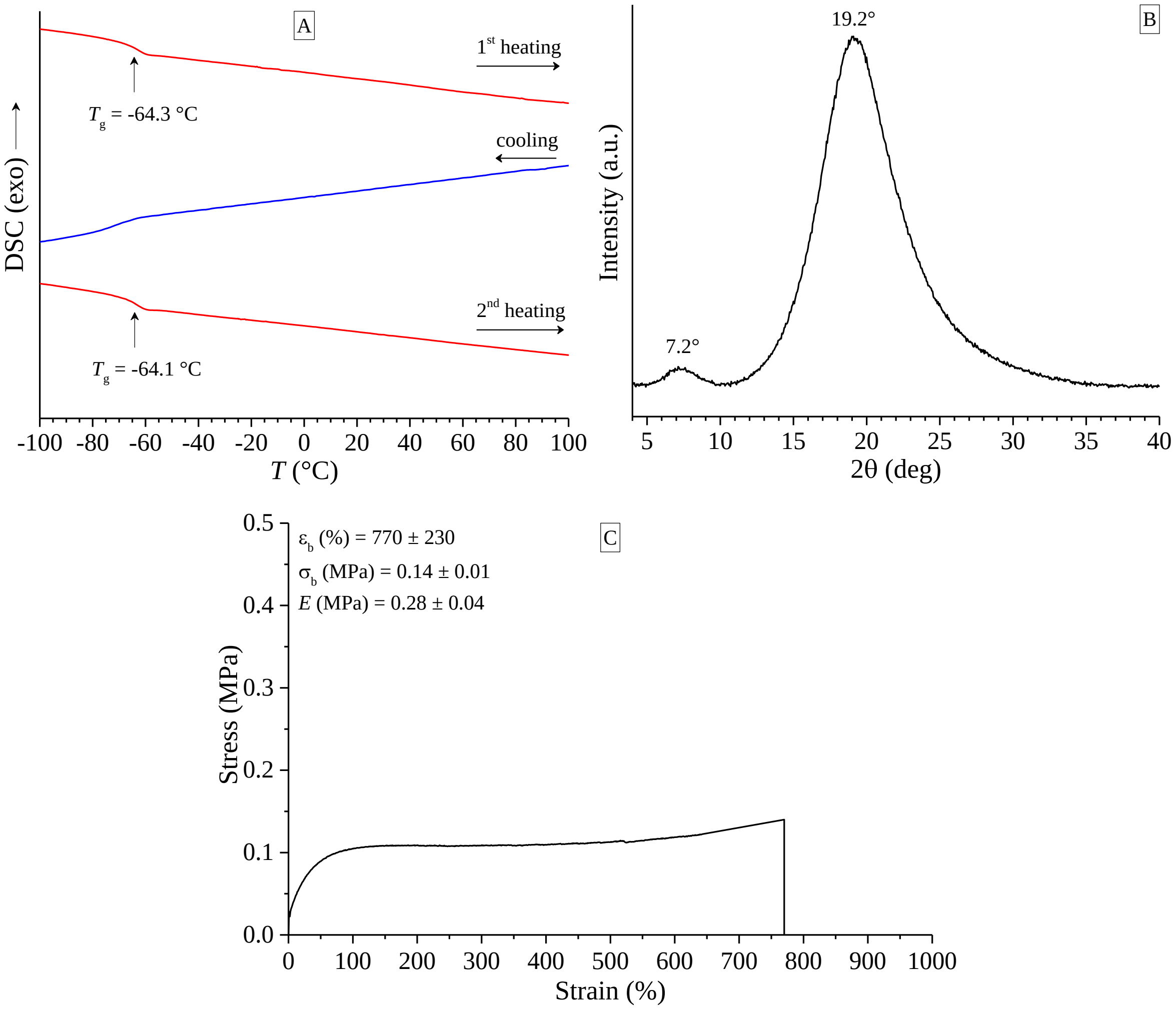

Figure 3.44. DSC thermograms (A), X-ray powder diffraction patterns of compression-molded films (B), and stress-strain curves (C) of the poly(1-octene) sample.

The X-ray powder diffraction patterns recorded on all blends of iPP with C2C4 copolymers and the PO sample, as obtained immediately after the blending process, are reported in Figure 3.45. The diffraction profiles show that all samples crystallize in the α-form of isotactic polypropylene. For all samples of blend with PO (Figure 3.45B), is also visible the low-intensity halo at $2\theta \approx 7°$ which intensity increases with the increasing of poly(1-octene) content.

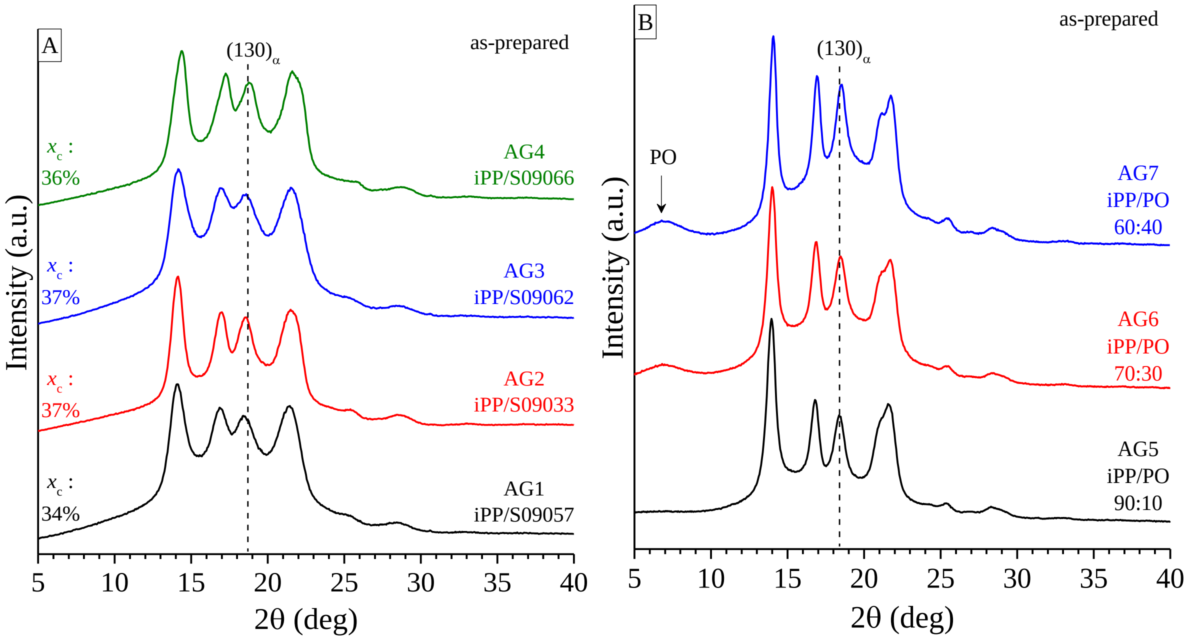

Figure 3.45. X-ray powder diffraction patterns of the “as-prepared” blends of iPP homopolymer with random C2C4 copolymer samples (A) and the homopolymer PO sample (B).

Figure 3.46 shows the DSC thermograms of the first heating (A, A’), cooling (B, B’), and second heating (C, C’) recorded on blends of iPP with random C2C4 copolymers and the PO sample. All DSC curves show one main endothermic and exothermic peak associated with the melting and crystallization of the α-crystals of the thermoplastic matrix of iPP. In addition, only in the first heating scans of blends with C2C4 copolymers (Figure 3.46A), two further low-intensity endothermic peaks ($T_m \approx 40°C$ and 90-120°C) related to the melting of small crystals belonging to the random C2C4 copolymers are visible.

Table 3.19 shows the thermal parameters extracted from the DSC thermograms of Figures 3.43A, and 3.46. According to the diffraction profiles, a decrease in the crystallinity and melting and crystallization enthalpies (Figure 3.47) is observed in the blends, in particular with increasing PO concentration.

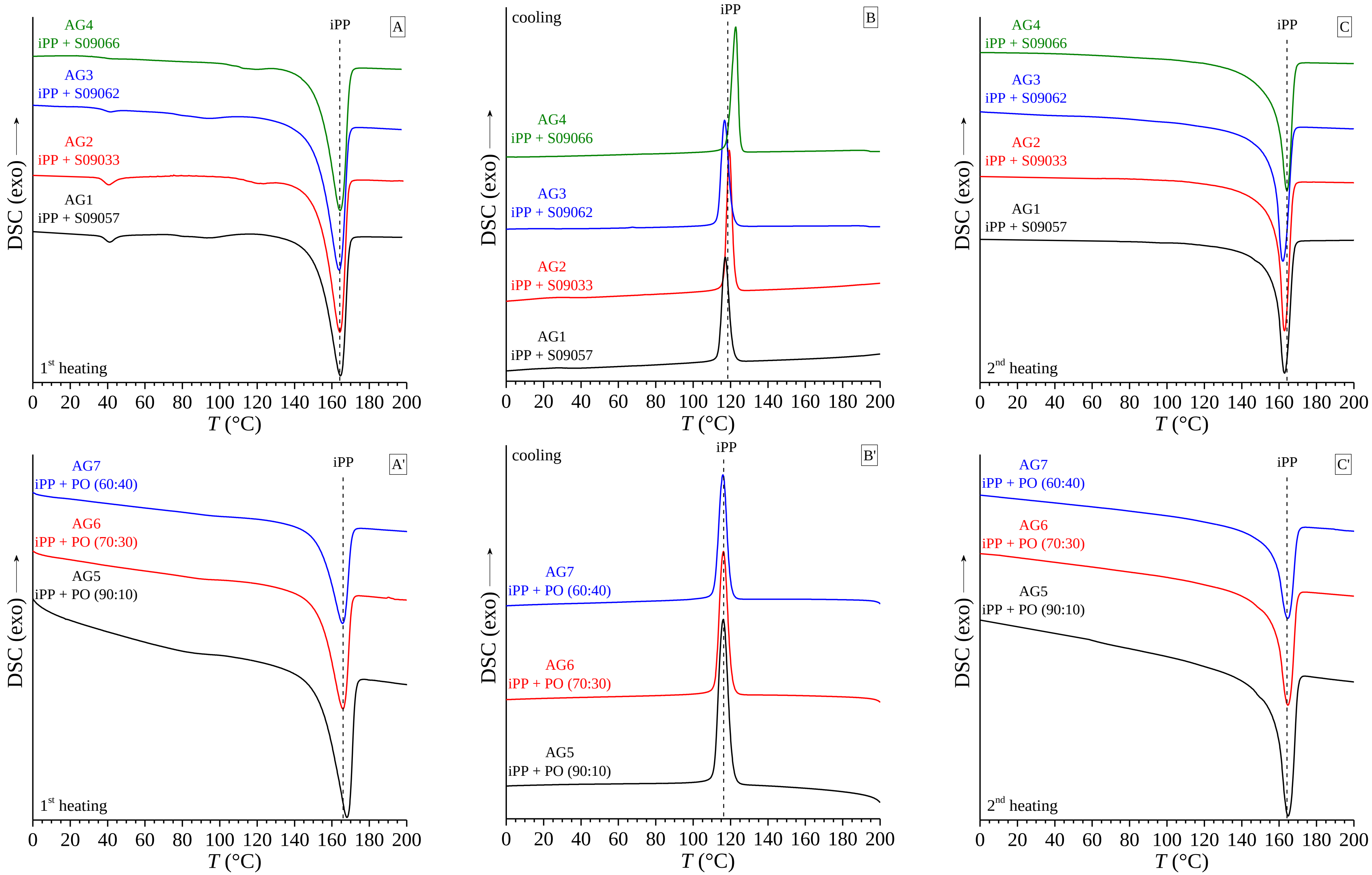

Figure 3.46. Comparison of DSC thermograms of first heating (A, A'), cooling (B, B'), and second heating (C,C') of all "as-prepared" blends of iPP with random C2C4 copolymer samples (A,B,C) and the poly(1-octene) sample (A', B', C').

Table 3.19. Values of melting temperatures and enthalpies recorded in first heating (T_m^I and ΔH_{mTOT}^I), crystallization temperatures and enthalpies (T_c, ΔH_c), and melting temperatures and enthalpies recorded in second heating (T_m^{II}, ΔH_{mTOT}^{II}) of iPP homopolymer, random C2C4 copolymer samples, poly(1-octene) sample, and blends of iPP with C2C4 and PO samples used as new rubbery phases.

Sample	**T_m^I (°C)**	**ΔH_m^I (J/g)**	**T_c (°C)**	**ΔH_c (J/g)**	**T_m^{II} (°C)**	**ΔH_m^{II} (J/g)**
iPP	168.3	98.8	118.2	112.4	166.3	112.6
S09057	15; 51.7; 70.7; 102.5; 114	29.6	15.4; 26.4; 68.5	40.5	40; 100	36.0
S09033	18.5; 51.3; 73.4	26.0	18.9; 26.7; 69.9	30.7	45.8	28.9
S09062	13.4; 51.6; 65.6; 104.1	20.4	8.6; 66.7	18.0	30.1; 97.2	11.0
S09066	11.3; 49.9; 77.3; 116	15.0	-3.5; 70.6	10.5	0.7; 114.5	9.0
Poly(1-octene)	/	/	/	/	/	/
AG1 **iPP + S09057**	41; 92.6; 164.0	69.0	121.0	71.0	162.0	74.0
AG2 **iPP + S09033**	40.7; 121; 164.0	76.0	119.0	72.0	163.0	73.0
AG3 **iPP + S09062**	41.8; 94.1; 164.0	73.0	117.0	72.0	162.0	74.0
AG4 **iPP + S09066**	41; 120.8; 164.0	76.0	123.0	75.0	164.0	77.0
AG5 **iPP/PO 90:10**	168.0	96.8	116.2	95.0	164.9	98.8
AG6 **iPP/PO 70:30**	165.9	74.2	116.2	74.0	164.7	77.1
AG7 **iPP/PO 60:40**	165.6	62.0	116.0	62.4	164.5	65.3

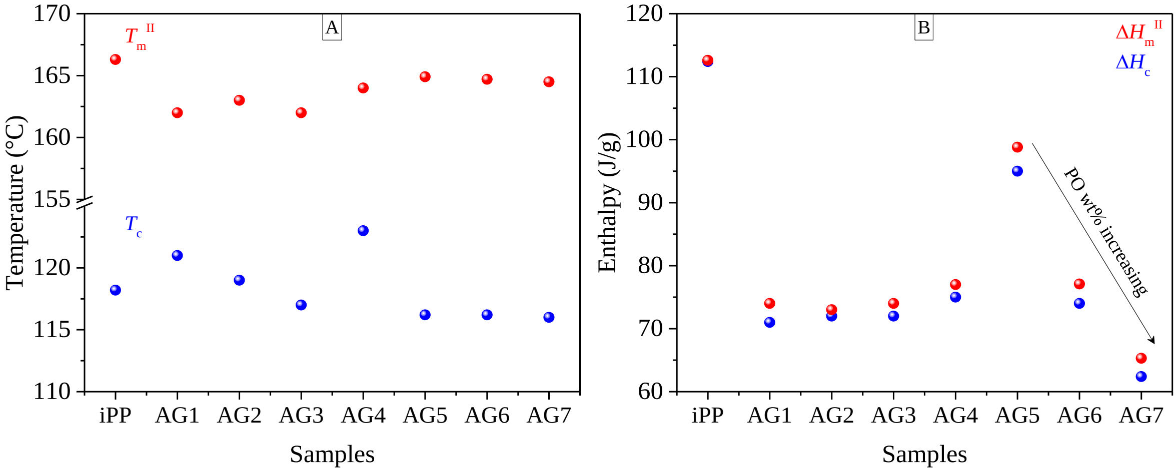

Figure 3.47. Crystallization and second melting temperatures (A) and crystallization and second melting enthalpies (B) of the iPP sample before and after the addition of C2C4 copolymers and poly(1-octene) samples.

The X-ray powder diffraction profiles of compression molded films of all blends, obtained by slow cooling from the melt, are shown in Figure 3.48. All samples crystallize in the α-form of isotactic polypropylene.

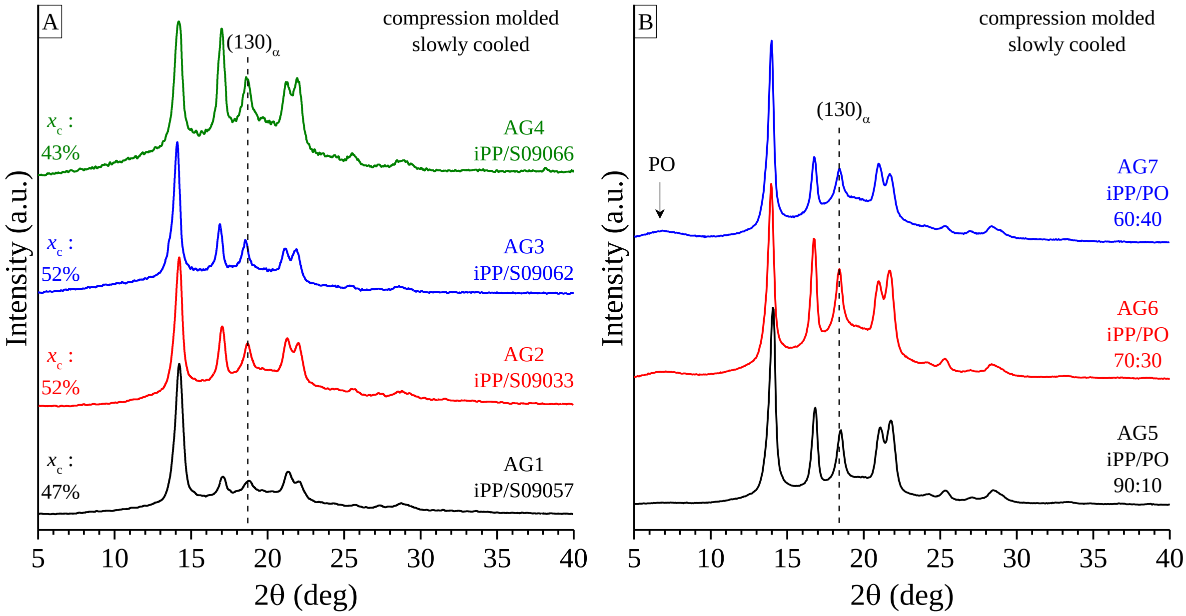

Figure 3.48. X-ray powder diffraction profiles of the compression molded film of blends of iPP homopolymer with random C2C4 copolymer samples (A) and the homopolymer PO sample (B).

Figure 3.49 shows the stress-strain curves of compression molded films of all iPP/C2C4 and iPP/PO blends. Table 3.20 displays the mechanical parameters of the pure components C2C4 copolymers and PO and of all blends evaluated from the curves in Figures 3.43, 3.44, and 3.49. Figure 3.50 shows the mechanical parameters of blends as a function of butene concentration, in the case of C2C4 copolymers, and as a function of the weight percentage of poly(1-octene) in the case of the blends with PO.

The analysis of the mechanical properties performed on the iPP/C2C4 blends (Figure 3.49A) shows that the incorporation of a random copolymer C2C4 copolymer results in an overall improvement of ductility compared to the iPP homopolymer sample, in particular in the case of blends with the C2C4 copolymers with higher butene concentration. This result depends partly on the excellent mechanical properties exhibited by the original samples (see Figure 3.43C) but also, probably, on better compatibility between the iPP phase and the added elastomeric phase. However, the increase in ductility is accompanied by a decrease of the mechanical strength (Figure 3.50C), and, in general, of the stresses involved at any deformations, including the tensile strength values (Figure 3.50B). This decrease seems to be more pronounced for higher concentrations of butene in the copolymer in agreement, probably, with a lower crystallinity of the blended sample.

As for the blends with poly(1-octene), again, the incorporation of the new elastomeric phase results in improvements of the strain at break values of iPP homopolymer, especially for the blend with 40wt% PO. Again, as expected, the addition of this rubbery phase reduces the mechanical strength and stress values involved throughout the deformation when compared to the iPP homopolymer sample.

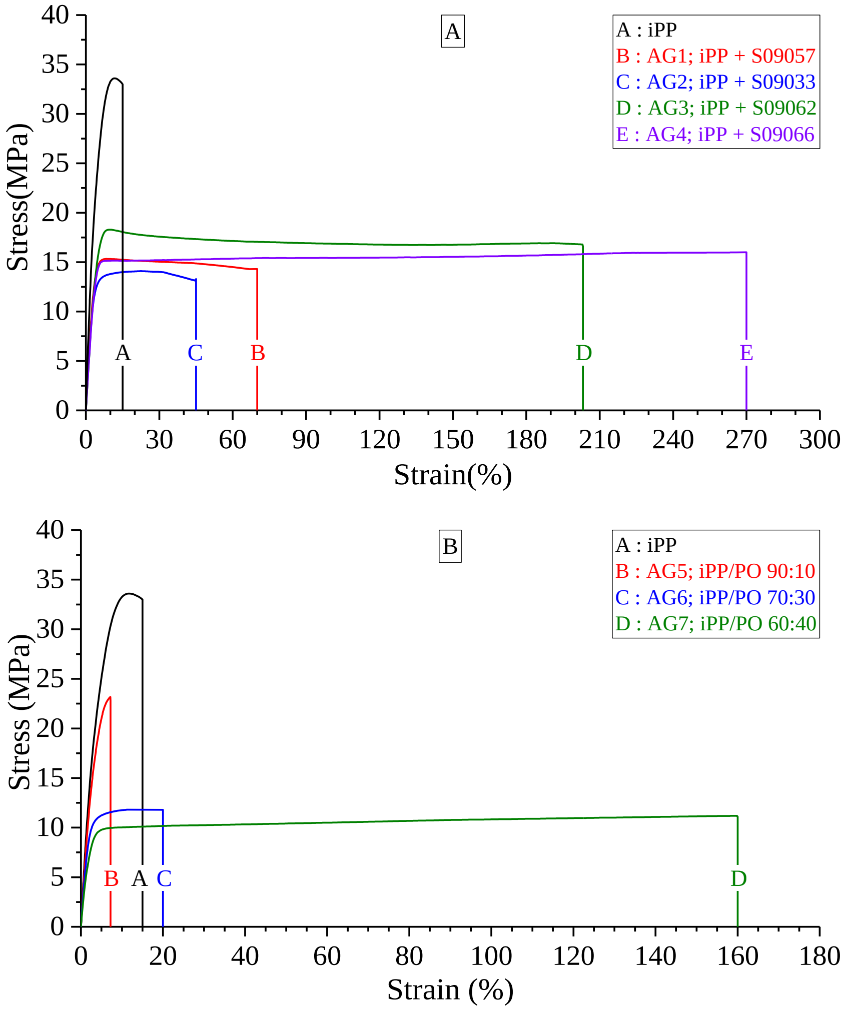

Figure 3.50. Stress-strain curves recorded at *T* = 25°C of compression-molded films of blends of iPP homopolymer with random C2C4 copolymer samples (A) and the homopolymer PO sample (B).

Table 3.20. Values of strain (ε_b) and stress (σ_b) at break, Young's modulus (E), and degree of crystallinity (x_c) of compression-molded films crystallized by slow cooling from the melt of iPP homopolymer, random C2C4 copolymer samples, poly(1-octene) sample, and blends of iPP with C2C4 and PO samples used as new rubbery phases.

Sample	**ε_b (%)**	**σ_b (MPa)**	**E (MPa)**	**x_c[a] (%)**
iPP	15 ± 1.2	31.0 ± 1.5	770 ± 20	65
S09057	1635 ± 285	5.2 ± 0.4	1.7 ± 0.4	2
S09033	1015 ± 30	9.0 ± 1.0	4.3 ± 0.5	1
S09062	3020 ± 285	2.2 ± 0.2	0.8 ± 0.2	2
S09066	2215 ± 500	2.5 ± 0.3	1.2 ± 0.2	5
Poly(1-octene)	770 ± 230	0.14 ± 0.01	0.28 ± 0.04	0
AG1 iPP + S09057	70 ± 15	15.0 ± 1.0	450 ± 35	53
AG2 iPP + S09033	45 ± 10	13.3 ± 1.4	420 ± 30	43
AG3 iPP + S09062	200 ± 50	17.0 ± 1.9	420 ± 40	52
AG4 iPP + S09066	270 ± 20	16.2 ± 0.4	410 ± 20	47
AG5 iPP/PO 90:10	7.2 ± 1.2	22.8 ± 1.2	620 ± 20	-
AG6 iPP/PO 70:30	20 ± 5	11.8 ± 0.4	600 ± 20	-
AG7 iPP/PO 60:40	160 ± 15	11.1 ± 0.5	420 ± 20	-

a) Values evaluated from X-ray powder diffraction profiles of Figure 3.43B, Figure 3.48, and Figure 1.7.

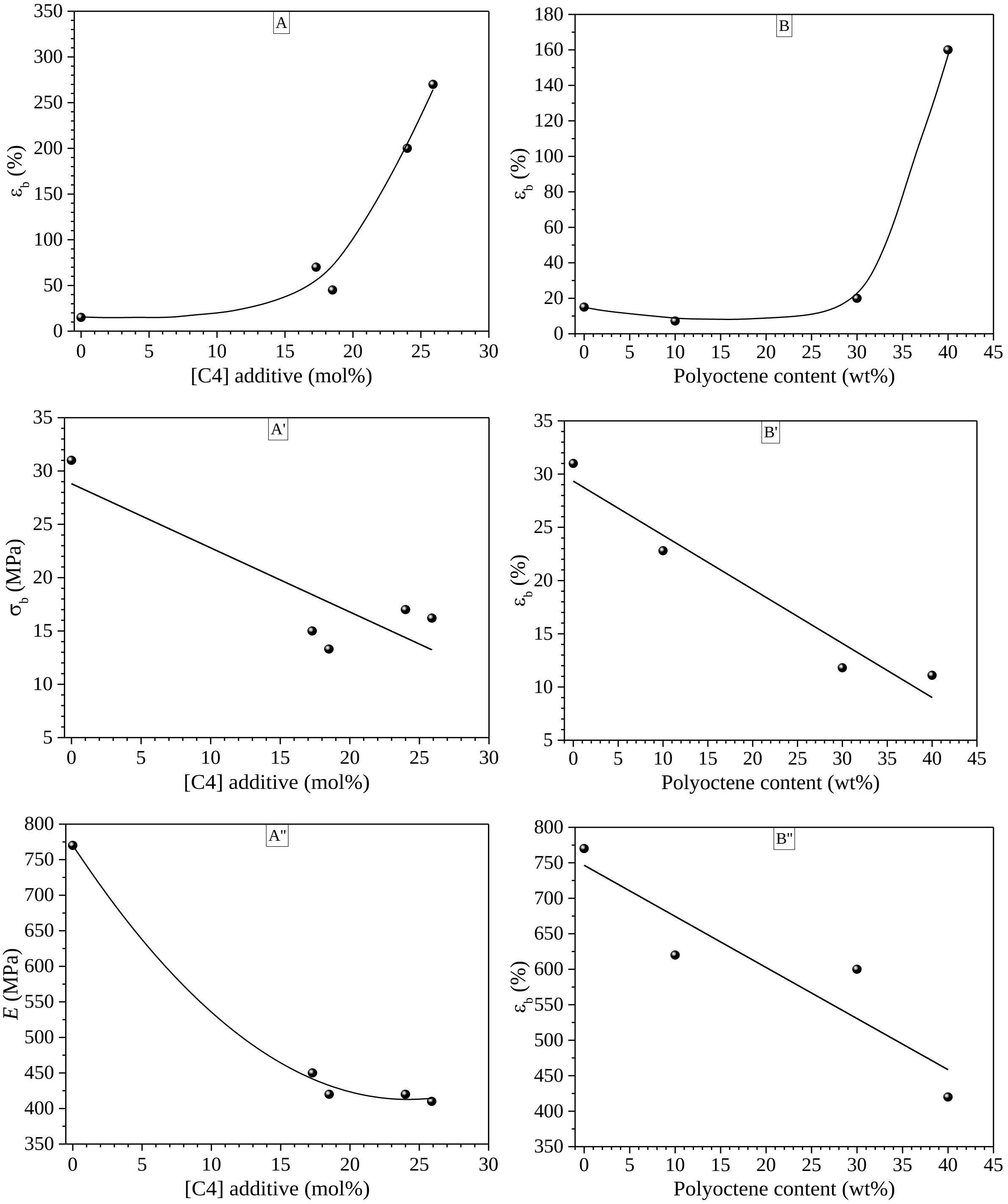

Figure 3.50. Strain (A, B) and stress (A', B') at break, and Young's modulus (A'', B'') values of blends of iPP homopolymer with random C2C4 copolymer samples (A, A', A'') and the homopolymer PO sample (B, B', B''). The lines are only a guide for eyes.

Figure 3.51 shows a direct comparison between the stress-strain curves (Figure 3.51A) and mechanical parameters, such as strain at break (Figure 3.51B) and Young's modulus (Figure 3.51C), of the HECO samples and the blends iPP/C2C4 and iPP/PO produced by solution mixing. In particular, in order to assess the direct effect of the different rubbery phases on the iPP sample, only samples with the content of the rubbery phase of about 30wt% have been compared. It is apparent that the incorporation of a heterogeneous phase results, in the range of weight percentages investigated, in an improvement of the ductility of the iPP sample. In more detail, it has been observed that the strain at break values increase as the weight percentage of ethylene in the EPR rubbery phase of HECO samples decreases. Sample EP3307, despite having a higher average ethylene concentration than sample B1 and more similar to sample B2, still exhibits better performance than all the other HECO samples. It is worth mentioning that sample EP3307 is a triphasic sample, that is, it consists of the iPP matrix and two different C3C2 copolymers and namely, one copolymer with an ethylene concentration of 30wt% (EPR1 at 11wt%) and one at a concentration of 60wt% (EPR2 at 20wt%). We have already justified in Chapter 1 that this improvement could be the result of a compatibilizing effect of the heterogeneous system due to the presence of the EPR1 component. This hypothesis is supported by the results shown in Section 3.4 in which the effect of adding 10wt% of metallocene C3C2 copolymers with low ethylene content on HECO samples was evaluated. Improvements in the mechanical properties could be achieved even in the presence of C2C4 copolymers. In general, all iPP/C2C4 copolymers blends show good mechanical properties and Figure 3.51B shows that, for butene concentrations around 30wt%, the strain-at-break values are similar to those of the classical HECO systems studied although lower than for sample EP3307. Excellent results, and considerably superior to conventional HECO materials, are achieved with ethylene-butene copolymers with a comonomer concentration of around 40wt%. This result may depend, in part, on the fact that the added C2C4 copolymers were synthesized with metallocene catalysts that guarantee obtaining macromolecules with a controlled distribution of molecular masses also characterized by a perfectly random distribution of comonomer. Thus, the synthesis process results in the formation of macromolecules more homogeneous than those of the C3C2 copolymer incorporated in conventional HECO systems produced with Ziegler-Natta catalysts. Thus, this result could be the consequence of better compatibility between the thermoplastic matrix of iPP and the macromolecules of C2C4 random copolymer samples. Finally, the addition of 30wt% PO also produces improvement of the ductility of the iPP homopolymer.

However, despite the improvements of the strain at break values, all the blends suffer from a worsening of mechanical strength due to the introduction of an elastomeric amorphous phase. It is evident from Figure 3.51C that the greatest losses in mechanical strength occur with the incorporation of C2C4 amorphous copolymers.

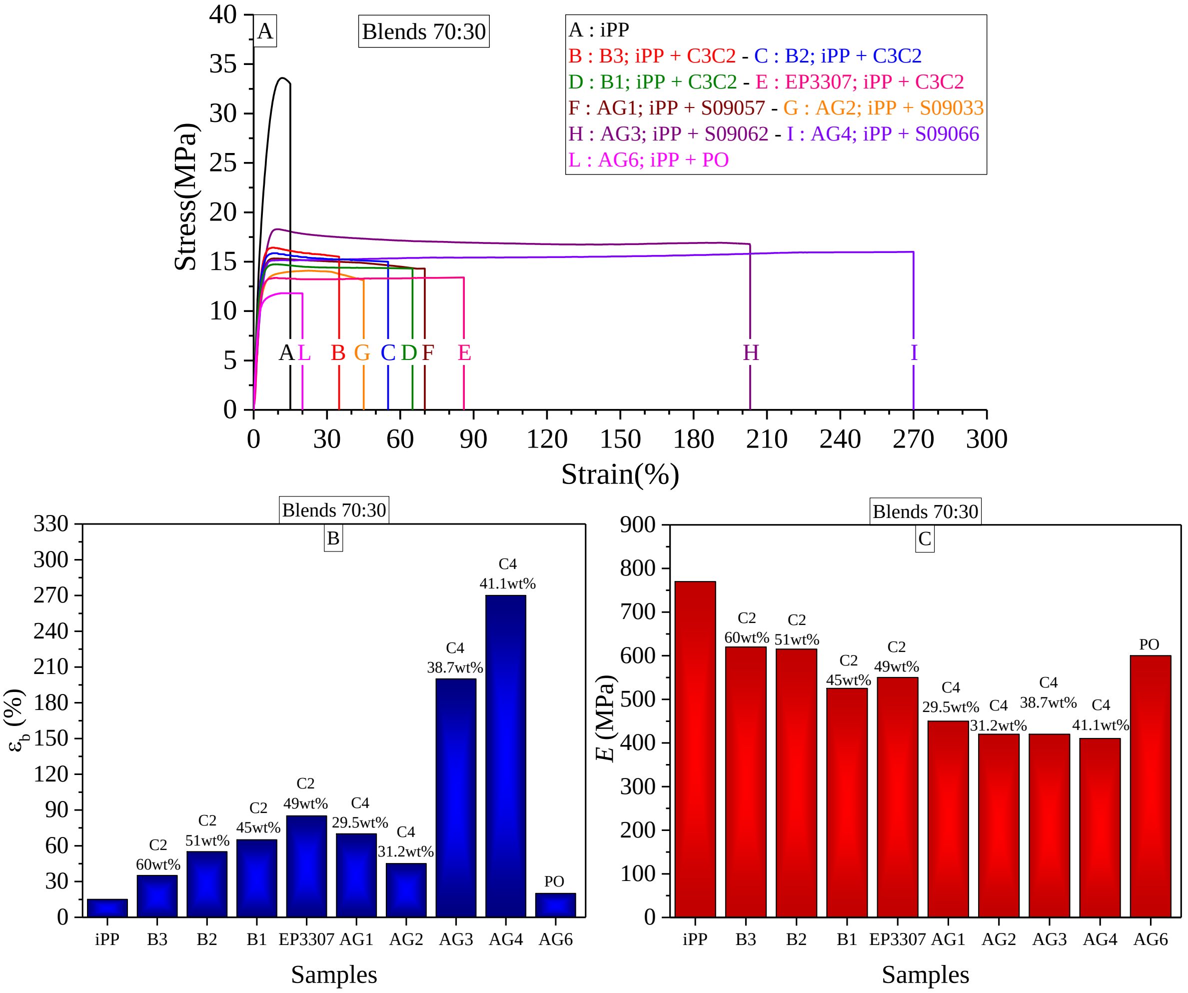

Figure 3.51. Stress-strain curves (A), strain at break (B), and Young's modulus (C) values of HECO samples with about 30wt% of EPR phase and blends of iPP with C2C4 copolymers and the PO sample at a ratio 70:30wt%.

References for Chapter 3

1. F.S. Bates, G.H. Fredrickson, *Macromolecules* **1994**, *27*, 1065-1067.

2. F.S. Bates, *Science* **1991**, *251*, 898-905.

3.W. Kaminsky, Ed., Polyolefins: 50 Years After Ziegler and Natta I (Advances in Polymer Science Series, Springer, **2013**).

4. D. Nwabunma, T. Kyu, Eds., Polyolefin Blends (Wiley, **2008**).

5 J. W. Teh, A. Rudin, J. C. Keung, *Adv. Polym. Technol.* **1994**, *13,* 1–23.

6. Y. Lin, V. Yakovleva, H. Chen, A. Hiltner, E. Baer, *J. Appl. Polym. Sci.* **2009**, *113*, 1945–1952.

7. A. Colbeaux, F. Fenouillot, J.-F. Gérard, M. Taha, H. Wautier, *J. Appl. Polym. Sci.* **2005**, *95*, 312–320.

8. J. M. Eagan, J. Xu, R. Di Girolamo, C. M. Thurber, C. W. Macosko, A. M. LaPointe, F. S. Bates, G. W. Coates, *Science* **2017**, *355,* 814–816

9. K. A. Chaffin, J. S. Knutsen, P. Brant, F. S. Bates, *Science* **2000**, *288,* 2187–2190

10. J. J. Benkoski, P. Flores, E. J. Kramer, *Macromolecules* **2003**, *36*, 3289–3302.

11. C. Laurens, C. Creton, L. Léger, *Macromolecules* **2004**, *37*, 6814–6822.

12. D. J. Arriola, E. M. Carnahan, P. D. Hustad, R. L. Kuhlman, T. T. Wenzel1, *Science* **2006**, *312*, 714-719.

13. F. S. Bates, G. H. Fredrickson, *Annu. Rev. Phys. Chem*. **1990**, *41*, 525.

14. L. Leibler, *Macromolecules* **1980**, *13*, 1602.

15. B. D. Olsen, X. Li, J. Wang, R. A. Segalman, *Macromolecules* **2007**, *40*, 3287.

16. W. van Zoelen, G. ten Brinke, *Soft Matter* **2009**, *5*, 1568.

17. M. Park, C. Harrison, P. M. Chaikin, R. A. Register, D. H. Adamson, *Science* **1997**, *276*, 1401.

18. G. W. Coates, P. D. Hustad, S. Reinartz *Angew. Chem*. Int. Ed. **2002**, *41*, 2236.

19. G. J. Domski, J. M. Rose, G. W. Coates, A. D. Bolig, M. Brookhart *Prog. Polym. Sci.* **2007**, *32,* 30.

20. J. Tian, P. D. Hustad, G. W. Coates *J. Am. Chem. Soc.* **2001**, *123*, 5134.

21. A. F. Mason, G. W. Coates *J. Am. Chem. Soc* **2004**, *126*, 16326.

22. A. E. Cherian, J. M. Rose , E. B. Lobkovsky , G. W. Coates *J. Am. Chem. Soc* **2005**, *127*, 13770.

23. V. Busico, R. Cipullo, N. Friederichs, S. Ronca, M. Togrou, *Macromolecules* **2003**, *36*, 3806.

24. V. Busico, R. Cipullo, N. Friederichs, S. Ronca, G. Talarico, M. Togrou, B. Wang *Macromolecules* **2004**, *37*, 8201.

25. K.A. Frazier, H.W. Boone, P. C. Vosejpka, J. C. Stevens, U.S. Patent Appl. 0220050A1, 2004.

26. M. Mitani, J. Saito, S. Ishii, Y. Nakayama, H. Makio, N. Matsukawa, S. Matsui, J. Mohri, R. Furuyama, H. Terao, H. Bando, H. Tanaka, T. Fujita, *Chem. Rec.* **2004**, *4*, 137–158.

27. J. Xu, J. M. Eagan, S.-S. Kim, S. Pan, B. Lee, K. Klimovica, K. Jin, T.-W. Lin, M. J. Howard, C. J. Ellison, A. M. LaPointe, G. W. Coates, F. S. Bates, *Macromolecules* **2018**, *51*, 8585−8596.

28. C. Paulik, C. Tranninger, J. Wang, P. Shutov, D. Mileva, M. Gahleitner, *Macromol. Chem. Phys.* **2021**, *222*, 2100302.

29. F. Luo, C. Xu, K. Wang, H. Deng, F. Chen, Q. Fu, *Polymer* **2012**, *53*, 1783-1790.

30. F. Chen, Y. Shangguan, Y. Jiang, B. Qiu, G. Luo, Q. Zheng, *Polymer* **2015**, *65*, 81-92.

Conclusions

This work reports an extensive study of the structure, composition, and physical properties of heterophasic copolymers (HECOs) of isotactic polypropylene (iPP), which are reactor blends of a highly crystalline thermoplastic phase of iPP homopolymer and an elastomeric phase constituted by a propene-ethylene random copolymer (EPR). The aim was to investigate the mechanisms responsible for the toughness of these materials and develop methods for improving toughness without losing mechanical strength. The incorporation of an elastomeric phase in the iPP matrix results in a marked drop in stiffness and mechanical strength with an increase in impact resistance (toughness). The main objective of this work was to identify the ideal composition of the HECO materials, in particular the composition of the elastomeric C3C2 copolymer, that can reconcile the apparent conflict between toughness and mechanical strength. The study was conducted through the analysis of the structure, microstructure, morphology, thermal, rheological, and mechanical properties of HECO samples industrially obtained by Ziegler-Natta catalysts and characterized by an EPR content in the range 22-32wt% and with different ethylene concentrations in the range 40-60wt%. The research activities have been divided into three sections in order to adequately address the complexity of these reactor blend systems.

In Chapter 1 it was illustrated a detailed study of the structural, thermal, mechanical, and rheological behavior of these complex HECO materials. The X-ray diffraction and DSC analyses have shown that all samples basically crystallize in the α-form of isotactic polypropylene (iPP) with the presence of a small amount of crystals of PE, at least for the samples with high ethylene concentration in the EPR phase. This suggests the presence of quite long ethylene sequences in the EPR phase able to crystallize forming PE-like crystals. This is due to the use of a Ziegler-Natta catalyst, which, because of multiple heterogeneous sites, produces a mixture of copolymer chains having different compositions and a non-uniform distribution of comonomer units. Hence, fractions with high ethylene concentration able to crystallize are present even in an apparently amorphous rubbery copolymer having an average ethylene concentration of 50wt%.

The analysis of mechanical properties performed on the film of samples crystallized by slow cooling from the melt revealed that the introduction of a rubbery phase leads to an improvement of the ductility and a reduction of the strength in comparison with the mechanical behavior exhibited by a highly isotactic polypropylene sample. Overall, the mechanical parameters depend both on the EPR content and on the ethylene concentration of the rubbery phase. Indeed, the ductility increases with increasing the EPR content but decreases with the increase of the ethylene concentration of the elastomeric phase.

The morphological analysis was conducted both by polarized optical microscopy (POM) and scanning electron microscopy (SEM) on samples slowly and rapidly crystallized from the melt. POM analysis performed on slowly crystallized samples has evidenced that the HECO systems crystallize in a spherulitic-like morphology, characterized by lamellae radiating from a central nucleus, often organized in fan-like structures, due to the crystallization of the iPP matrix. This morphology is similar to that of the pure iPP but, contrary to the homopolymer which shows well-formed big spherulites with sharp boundaries, in the HECO systems, spherulites are organized to form a unique pattern in which it is barely possible to identify their boundaries. In addition, all HECO samples show, both within and between the spherulites, circular dark areas, probably corresponding to non-birefringent particles presumably attributable to the amorphous fractions of the elastomeric phase rejected from crystals. On the other hand, POM images of samples quenched from the melt showed the presence of needle-like crystals, namely the presence of small birefringent needle-shaped entities. Unlike the spherulitic morphology presented by the samples obtained by slow cooling, the needle-like morphology appears to be undisturbed by the presence of rubbery particles.

The SEM analysis was performed on non-etched specimens, and on samples treated at the surface with xylene to dissolve the amorphous phase. SEM analysis revealed that the morphology of the iPP sample does not change after the solution etching because xylene is not able to dissolve the intra-lamellar amorphous phase of iPP. On the other hand, HECO samples present some voids already on the specimens before etching. After xylene treatment, the specimens appear with a major number of cavities, uniformly dispersed in the thermoplastic phase, due to the dissolution of the EPR domains. The sizes and distances of these voids are mostly affected by the ethylene concentration of the rubbery phase and, specifically, they increase as the ethylene content increases. The SEM analysis revealed a uniform distribution of the EPR particles in the shape of spherical-like droplets with a size in the range of 1.5-3.5 μm, placed at an average distance of 1.5-3 μm, revealing a good dispersion of the rubbery phase, with small domains, in the thermoplastic matrix with the consequent positive effect on the toughness of HECO samples. Nevertheless, the bigger the droplet dimensions the worst the mechanical performance. Indeed, samples that show the most brittle mechanical behavior are characterized by the highest dimension of embedded particles.

Therefore, according to the SEM investigation results, the size of the rubbery domains on the order of a few micrometers and a good dispersion of the EPR phase within the thermoplastic matrix, generating a network, is critical for improving the mechanical behavior of the iPP. However, the chemical composition of the rubbery phase is equally important.

Through analyses performed with fast scanning chip calorimetry (FSC), we were able to determine that the presence of the EPR phase can modify the crystallization behavior and crystallization kinetics of the homopolymer. First, these experiments allowed us to confirm the presence of crystalline components belonging to the elastomeric phase (EPC), which may also have a nucleating effect on the thermoplastic iPP matrix by promoting complete crystal formation, sometimes inhibited in the homopolymer sample. This analysis also showed that, although the rubbery phases of the different samples are characterized by different ethylene concentrations, the crystalline components develop at about the same crystallization temperature suggesting that the average length of the crystallizable ethylene units is roughly the same. Finally, isothermal crystallization experiments have shown that EPC particles are able to modify the crystallization kinetics of the thermoplastic iPP matrix, anticipating the development of α-form crystals, i.e., increasing their crystallization rate.

From rheological experiments, it was observed that the introduction of the elastomeric component has a strong effect on the relaxation times. In fact, HECO samples show relaxation times much lower than that of the iPP homopolymer.

Finally, possible strategies to improve the mechanical properties of HECO through the use of compatibilizers of the iPP matrix and the EPR phase have been studied. To this aim blends of HECO samples with different random and block copolymers of different molecular architecture and composition have been prepared and characterized. In particular, block copolymers containing crystalline blocks of isotactic polypropylene linked to crystalline polyethylene or LLDPE blocks or to amorphous blocks of propylene-ethylene copolymers have been used as additives. Random C3C2 copolymers with low ethylene concentration (10-20 wt%) have also been blended with HECO samples.

These studies have revealed that the addition of iPP-b-PE block copolymers, characterized by a long PE block, and random C3C2 copolymers of low ethylene concentrations, gives a remarkable improvement in ductility and toughness of HECOs. The beneficial effect was generally found in HECO systems with higher ethylene concentrations of the rubbery phase. This result confirms, therefore, that the presence of macromolecules highly rich in long ethylene sequences may be a disruptive element in HECO copolymers resulting in increased brittleness of the analyzed systems.

Concluding, this thesis work has contributed to expanding the knowledge in the field of heterophasic copolymers illustrating the influence of the multiple fractions belonging to the elastomeric phase over the morphology, rheological properties, crystallization behavior, and mechanical properties of the thermoplastic matrix of a complex HECO system.

Annex 1

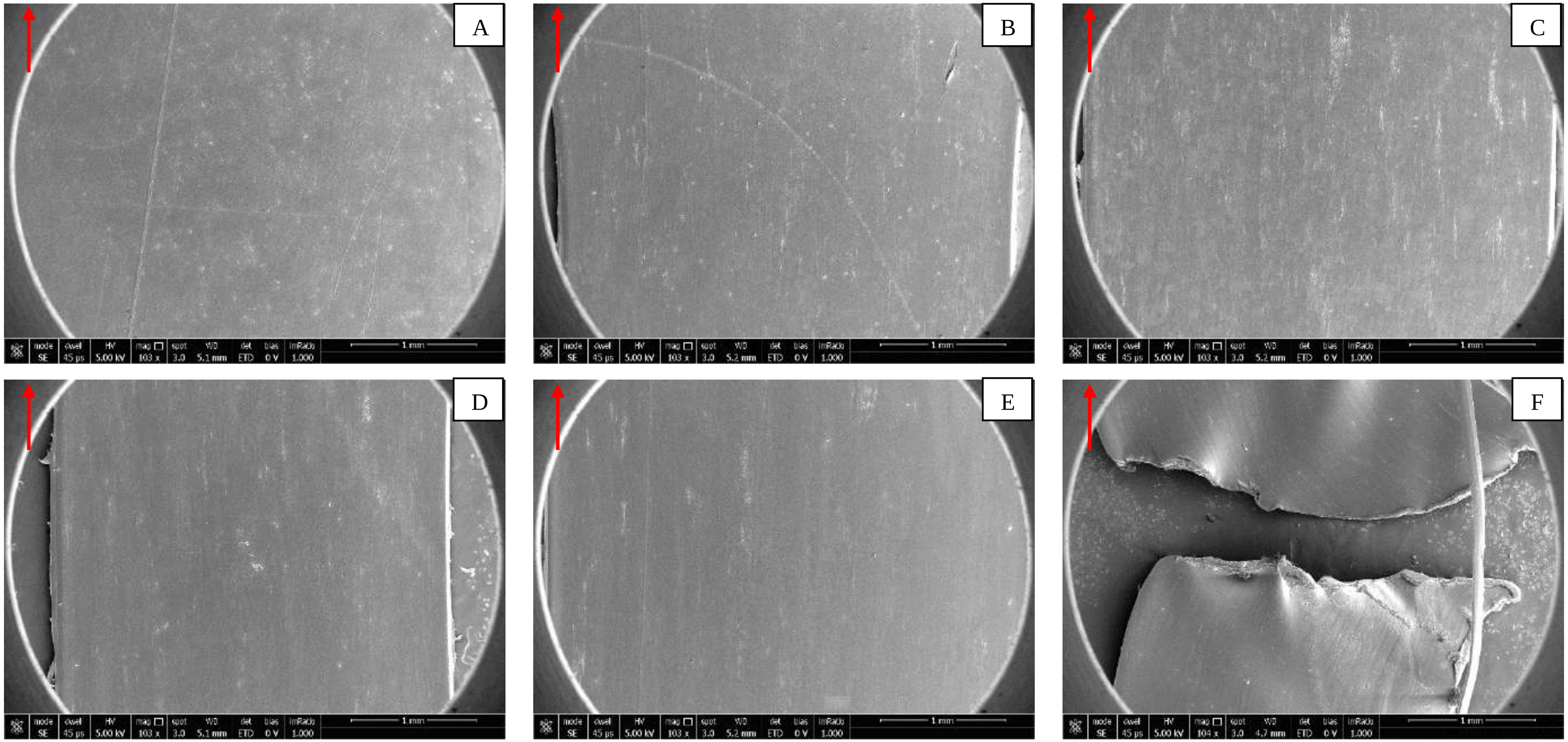
iPP; [*mmmm*] = 98%

Figure A1.1. FESEM images of surfaces of compression-molded films of the homopolymer undeformed (A) and after deformation at 70% (B), 150% (C), 400% (D), 750% (E), at break (F). All the images were acquired at the same magnification of 100X. The vertical red arrow indicates the stretching direction.

iPP; [*mmmm*] = 98%

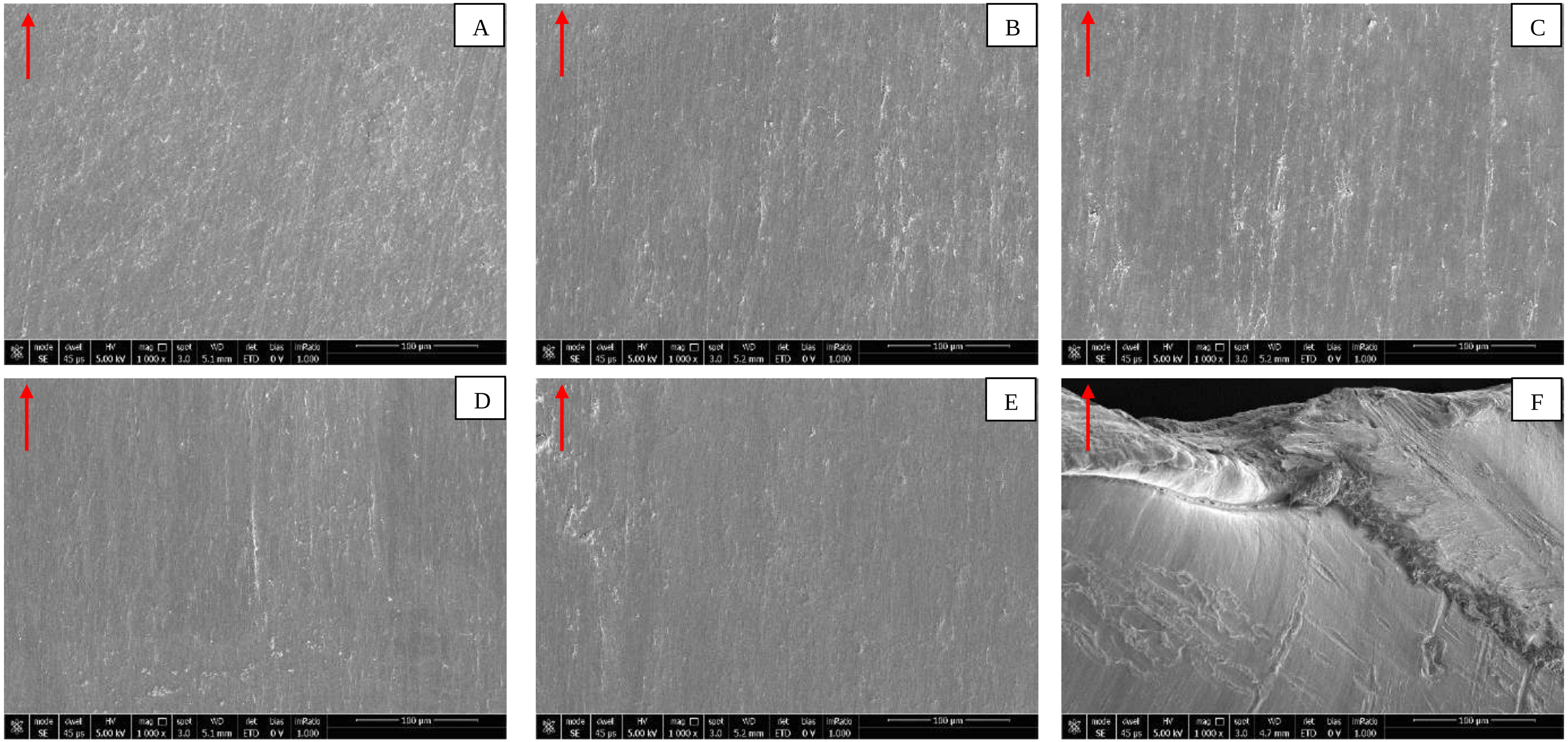

Figure A1.2. FESEM images of surfaces of compression-molded films of the homopolymer undeformed (A) and after deformation at 70% (B), 150% (C), 400% (D), 750% (E), at break (F). All the images were acquired at the same magnification of 1000X. The vertical red arrow indicates the stretching direction.

21588\45; EPR = 22.0wt%, C2(EPR) = 54.0wt%

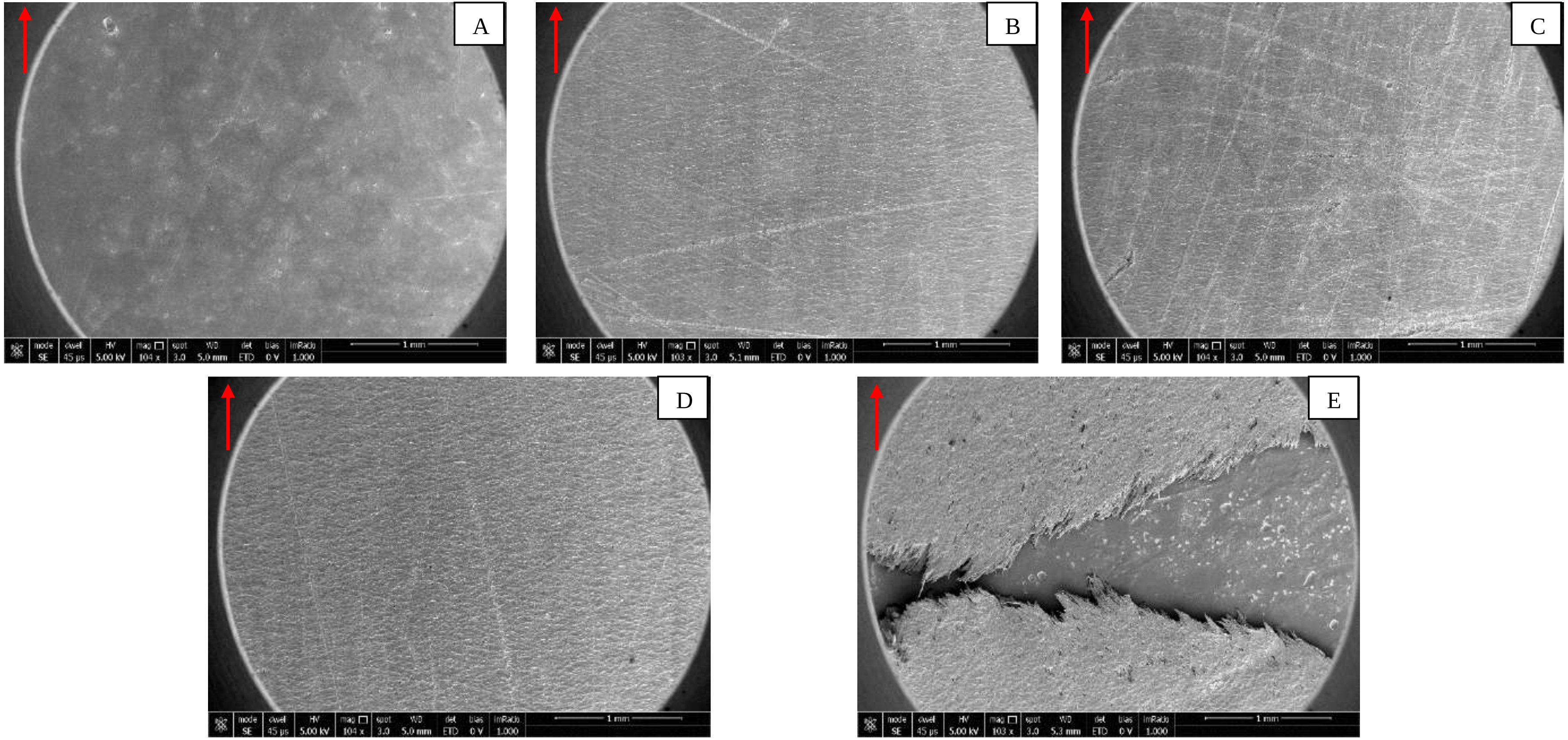

Figure A1.3. FESEM images of surfaces of compression-molded films of the sample 21588/45 undeformed (A) and after deformation at 30% (B), 70% (C), 110% (D), at break (E). All the images were acquired at the same magnification of 100X. The vertical red arrow indicates the stretching direction.

21588\45; EPR = 22.0wt%, C2(EPR) = 54.0wt%

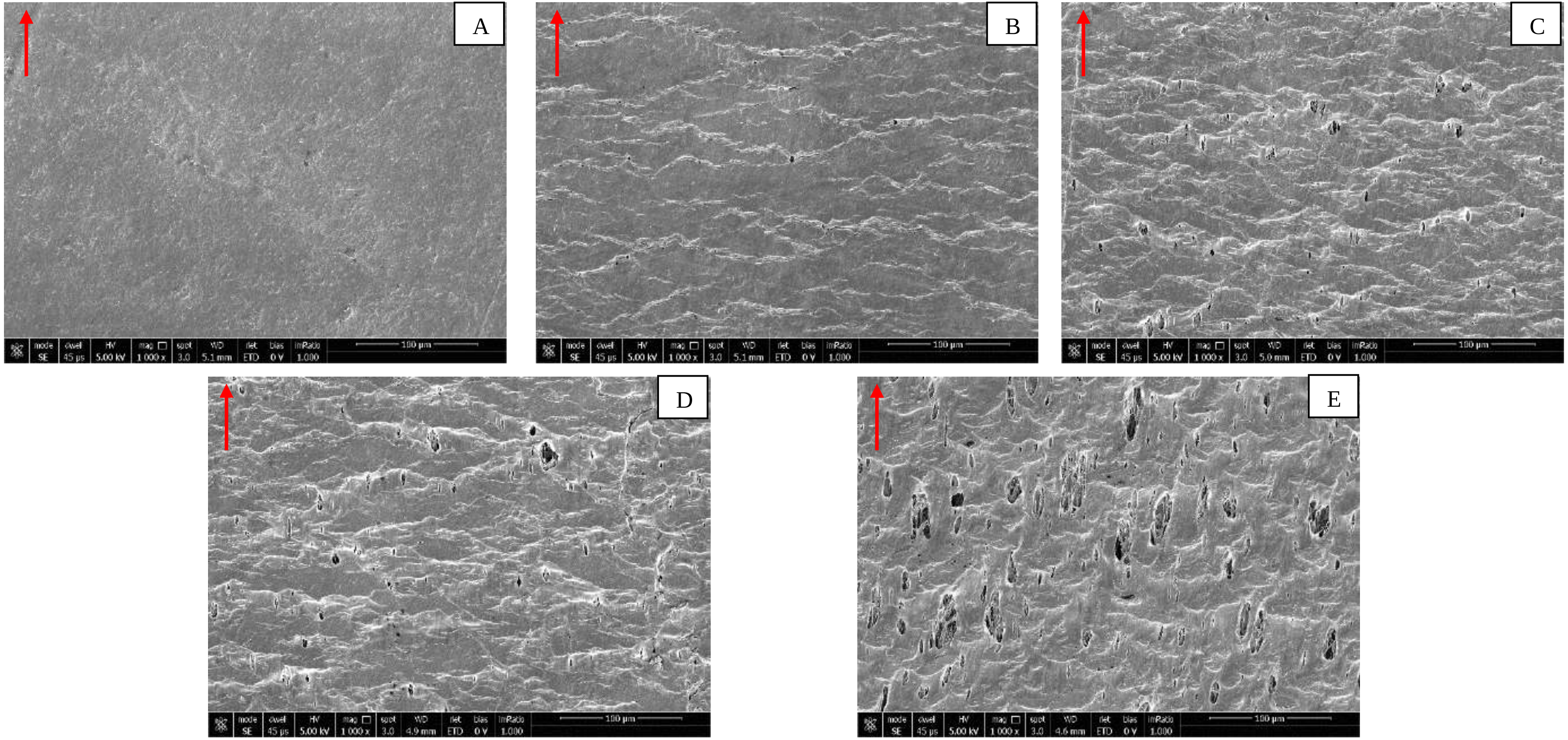

Figure A1.4. FESEM images of surfaces of compression-molded films of the sample 21588/45 undeformed (A) and after deformation at 30% (B), 70% (C), 110% (D), at break (E). All the images were acquired at the same magnification of 1000X. The vertical red arrow indicates the stretching direction.

A1; EPR = 24.6wt%, C2(EPR) = 45.6wt%

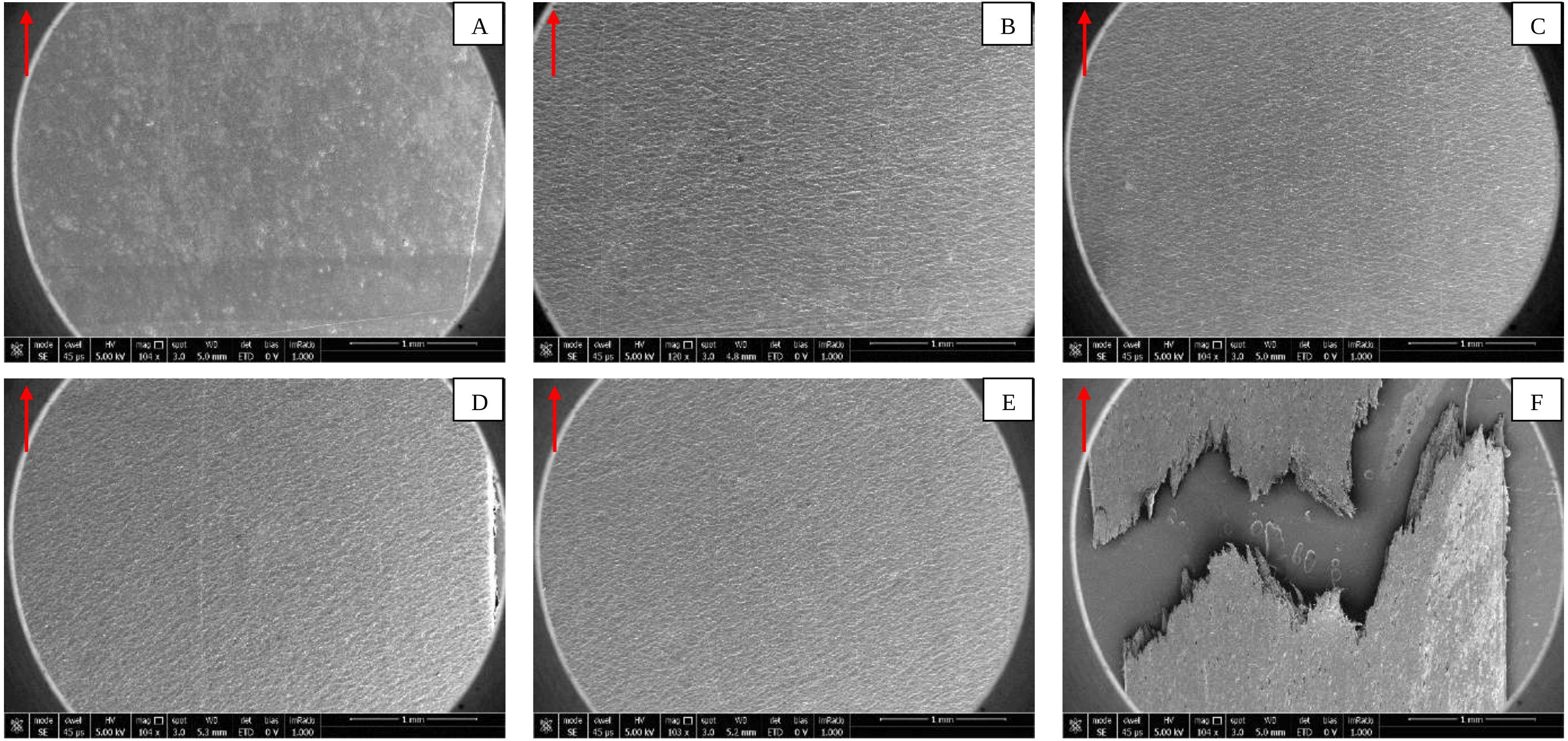

Figure A1.5. FESEM images of surfaces of compression-molded films of the sample A1 undeformed (A) and after deformation at 30% (B), 70% (C), 110% (D), 150% (E), at break (F). All the images were acquired at the same magnification of 100X. The vertical red arrow indicates the stretching direction.

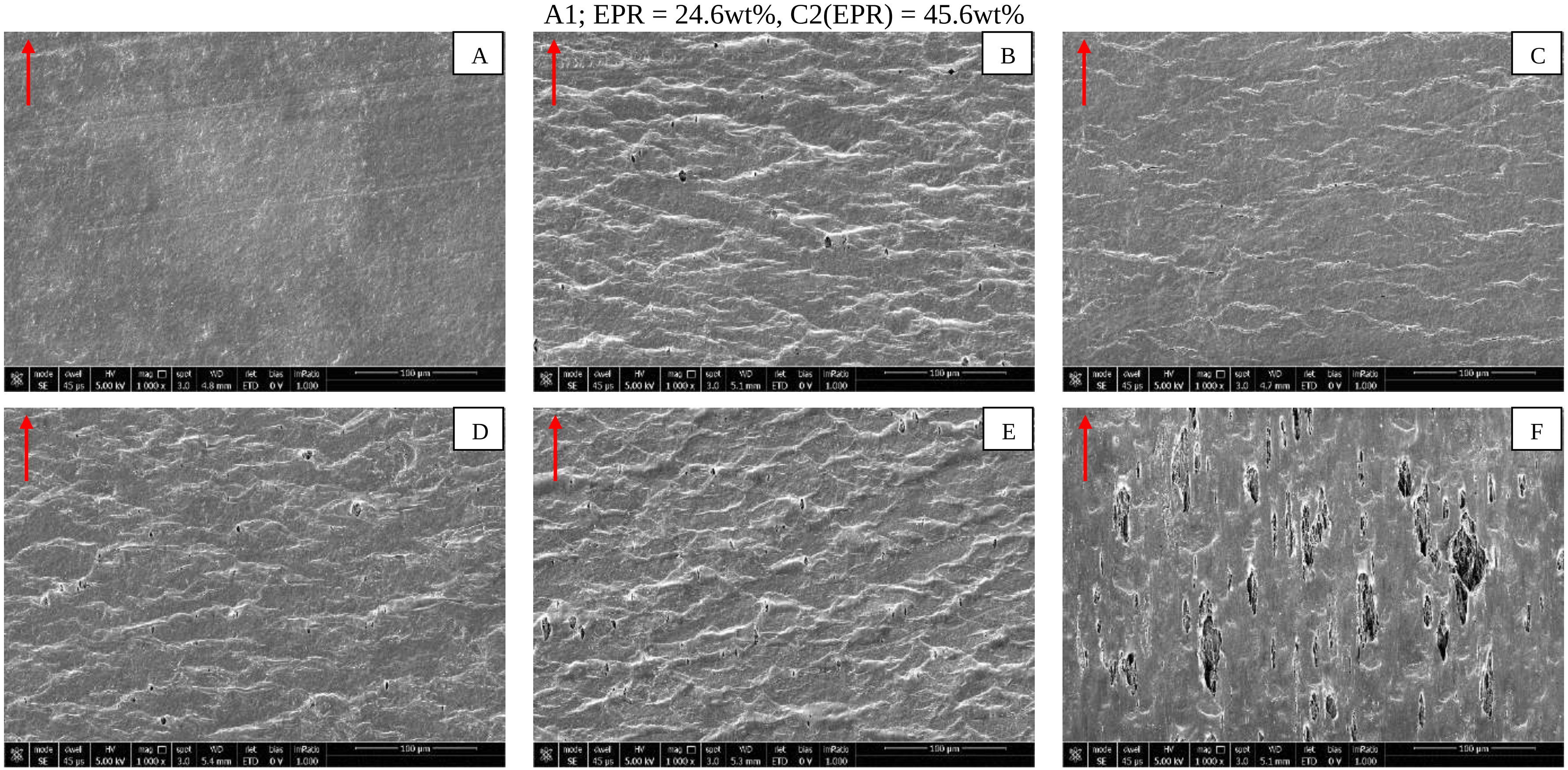

Figure A1.6. FESEM images of surfaces of compression-molded films of the sample A1 undeformed (A) and after deformation at 30% (B), 70% (C), 110% (D), 150% (E), at break (F). All the images were acquired at the same magnification of 1000X. The vertical red arrow indicates the stretching direction.

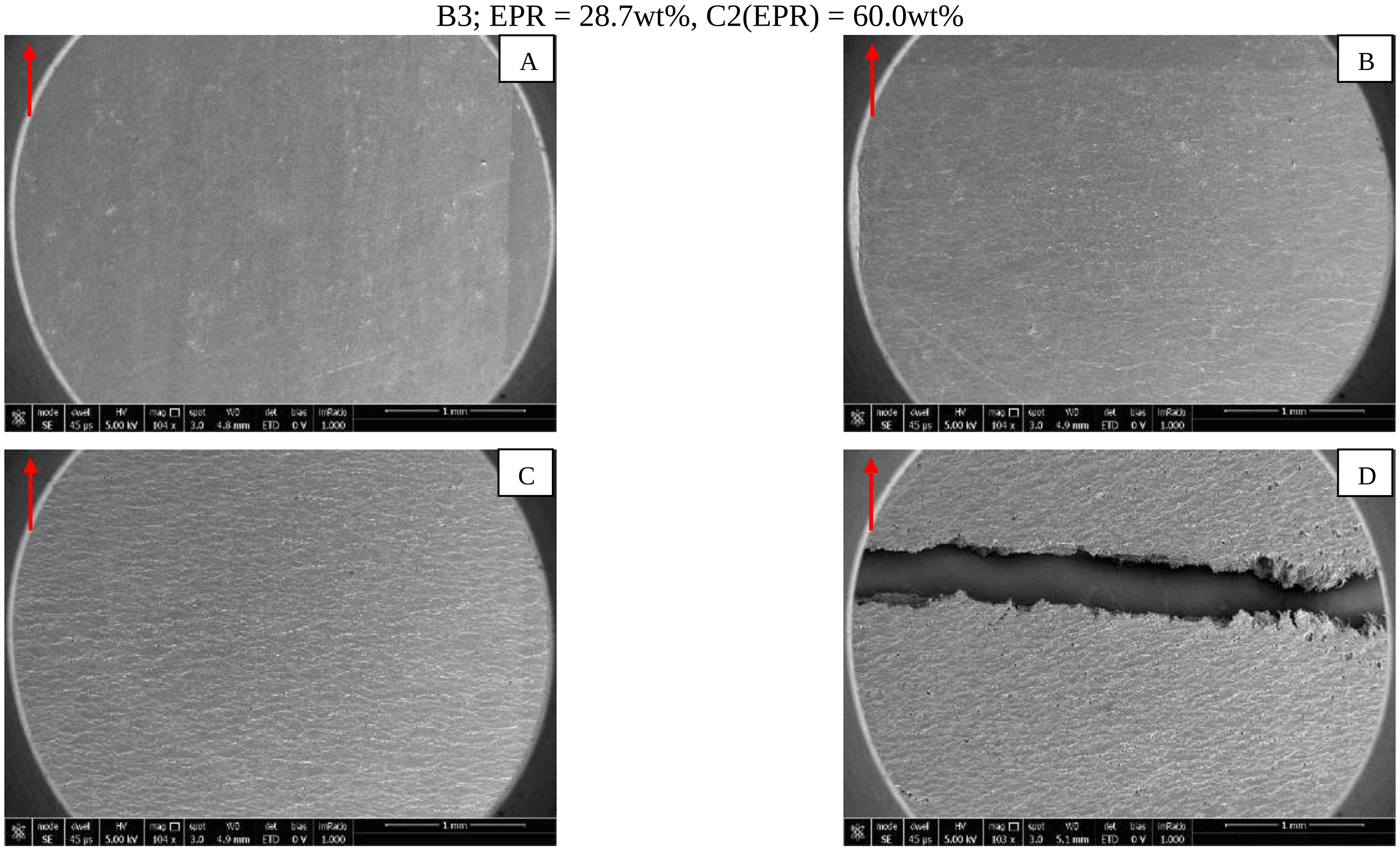

B3; EPR = 28.7wt%, C2(EPR) = 60.0wt%

Figure A1.7. FESEM images of surfaces of compression-molded films of the sample B3 undeformed (A) and after deformation at 20% (B), 40% (C), at break (D). All the images were acquired at the same magnification of 100X. The vertical red arrow indicates the stretching direction.

B3; EPR = 28.7wt%, C2(EPR) = 60.0wt%

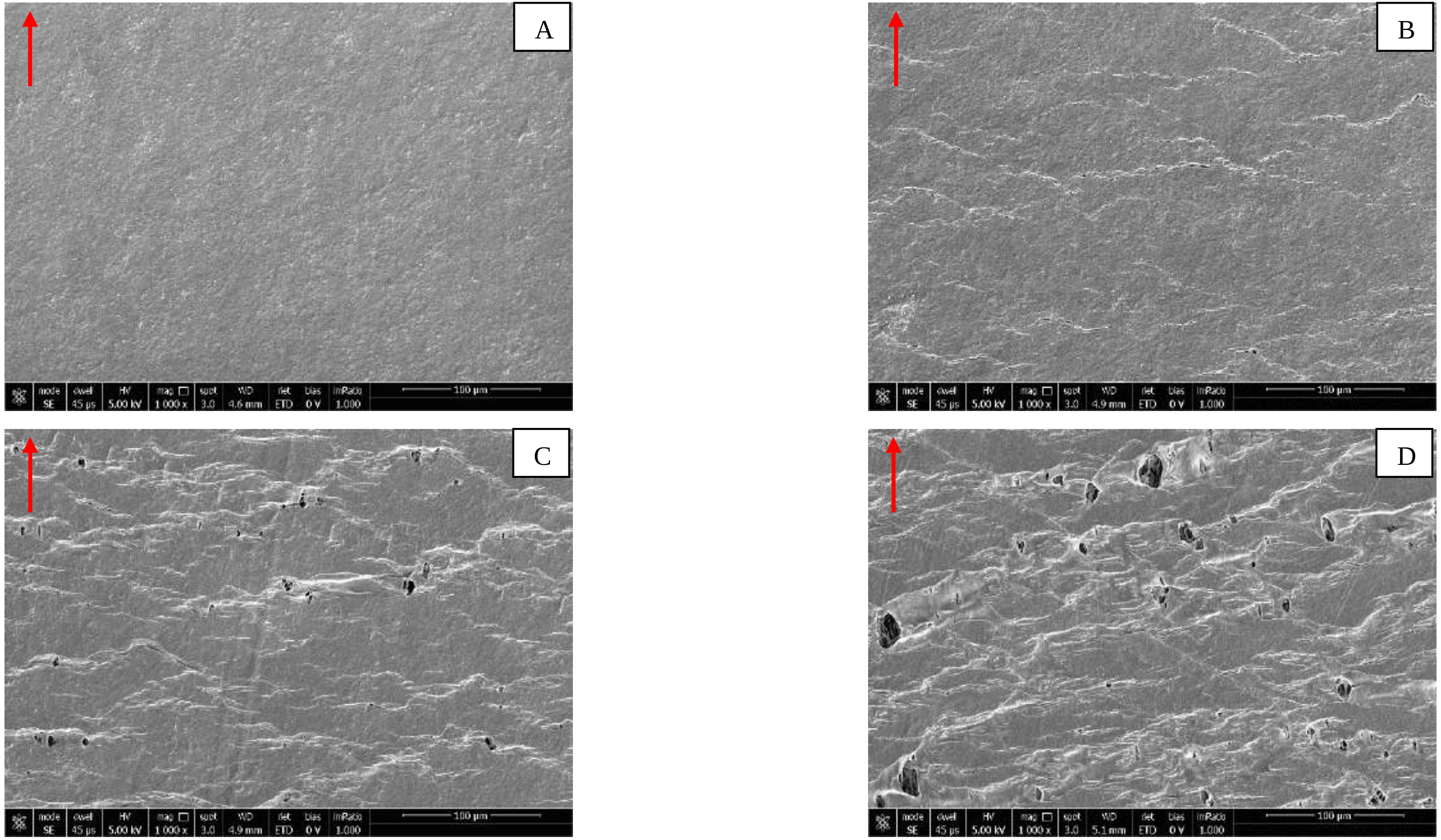

Figure A1.8. FESEM images of surfaces of compression-molded films of the sample B3 undeformed (A) and after deformation at 20% (B), 40% (C), at break (D). All the images were acquired at the same magnification of 1000X. The vertical red arrow indicates the stretching direction.

B2; EPR = 29.0wt%, C2(EPR) = 51.0wt%

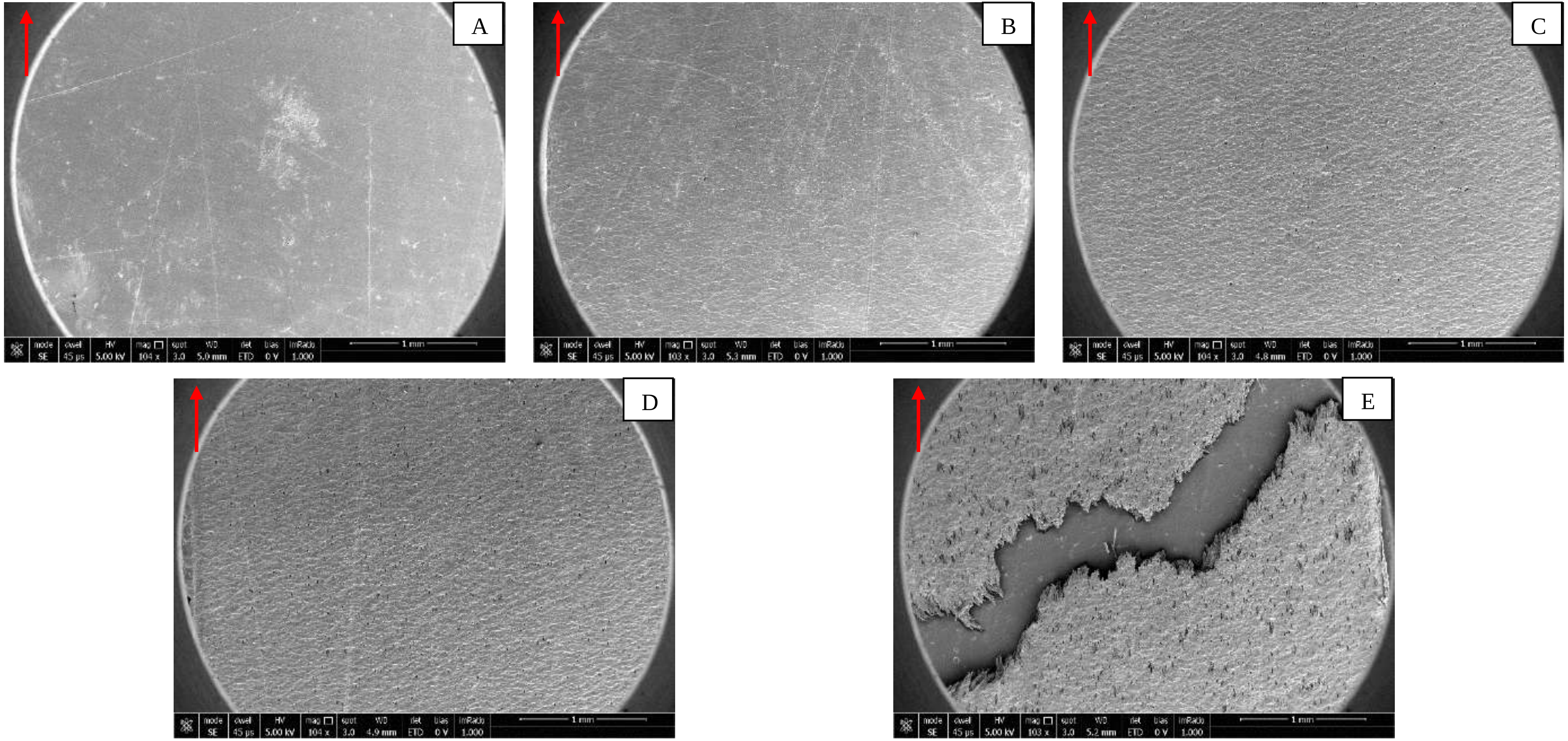

Figure A1.9. FESEM images of surfaces of compression-molded films of the sample B2 undeformed (A) and after deformation at 30% (B), 70% (C), 110% (D), at break (E). All the images were acquired at the same magnification of 100X. The vertical red arrow indicates the stretching direction.

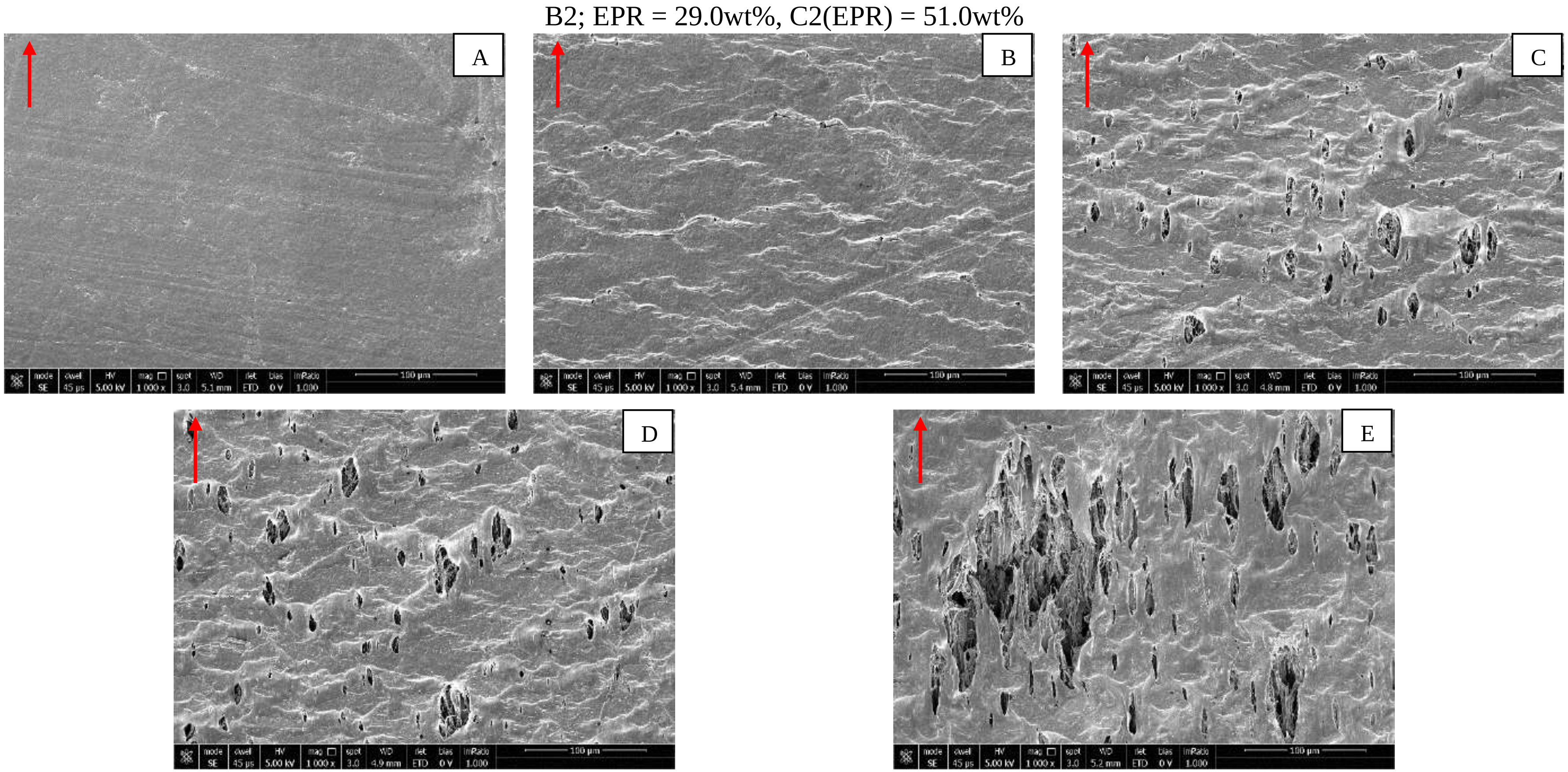
B2; EPR = 29.0wt%, C2(EPR) = 51.0wt%

Figure A1.10. FESEM images of surfaces of compression-molded films of the sample B2 undeformed (A) and after deformation at 30% (B), 70% (C), 110% (D), at break (E). All the images were acquired at the same magnification of 1000X. The vertical red arrow indicates the stretching direction.

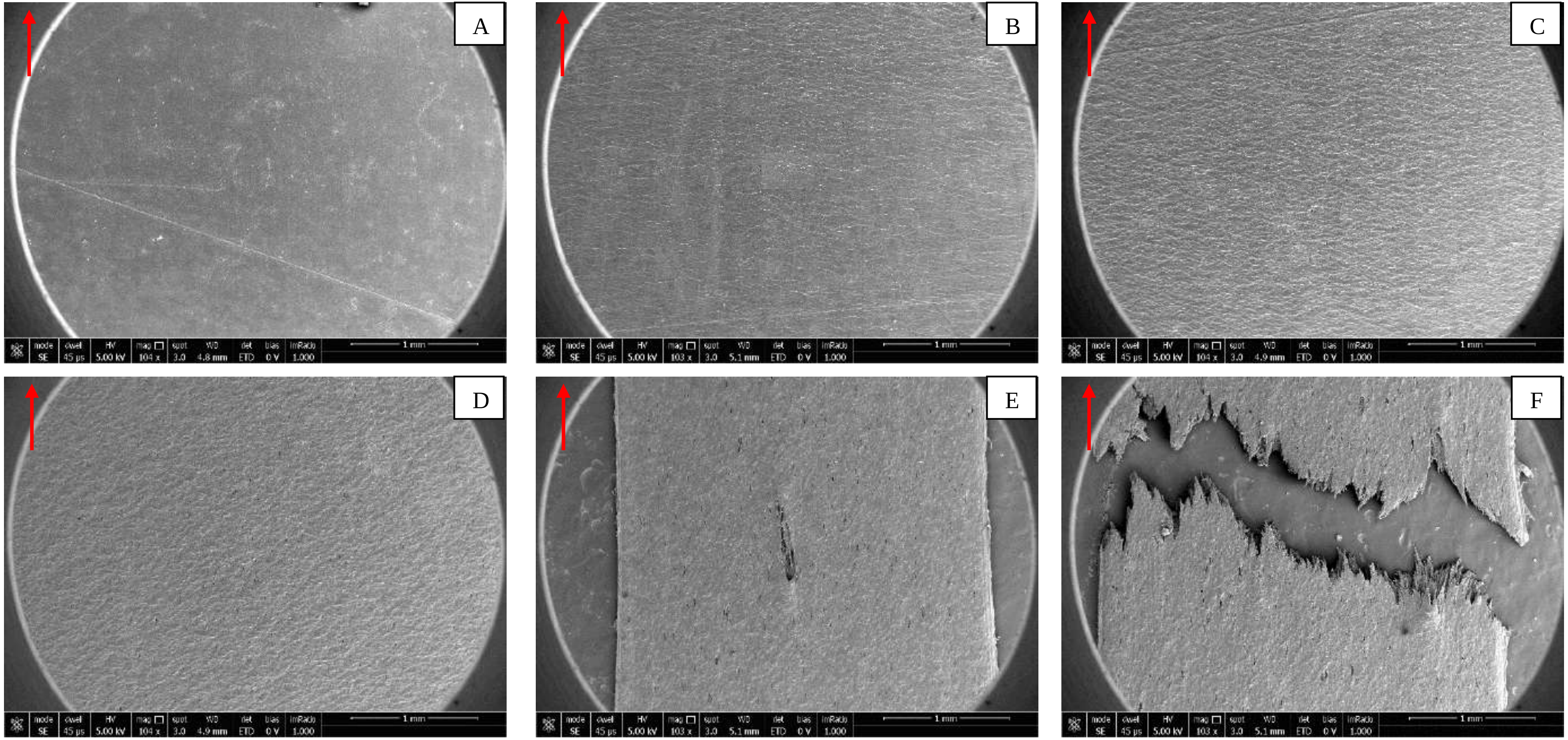

B1; EPR = 29.6wt%, C2(EPR) = 45.0wt%

Figure A1.11. FESEM images of surfaces of compression-molded films of the sample B1 undeformed (A) and after deformation at 30% (B), 70% (C), 110% (D), 150% (E), at break (F). All the images were acquired at the same magnification of 100X. The vertical red arrow indicates the stretching direction.

B1; EPR = 29.6wt%, C2(EPR) = 45.0wt%

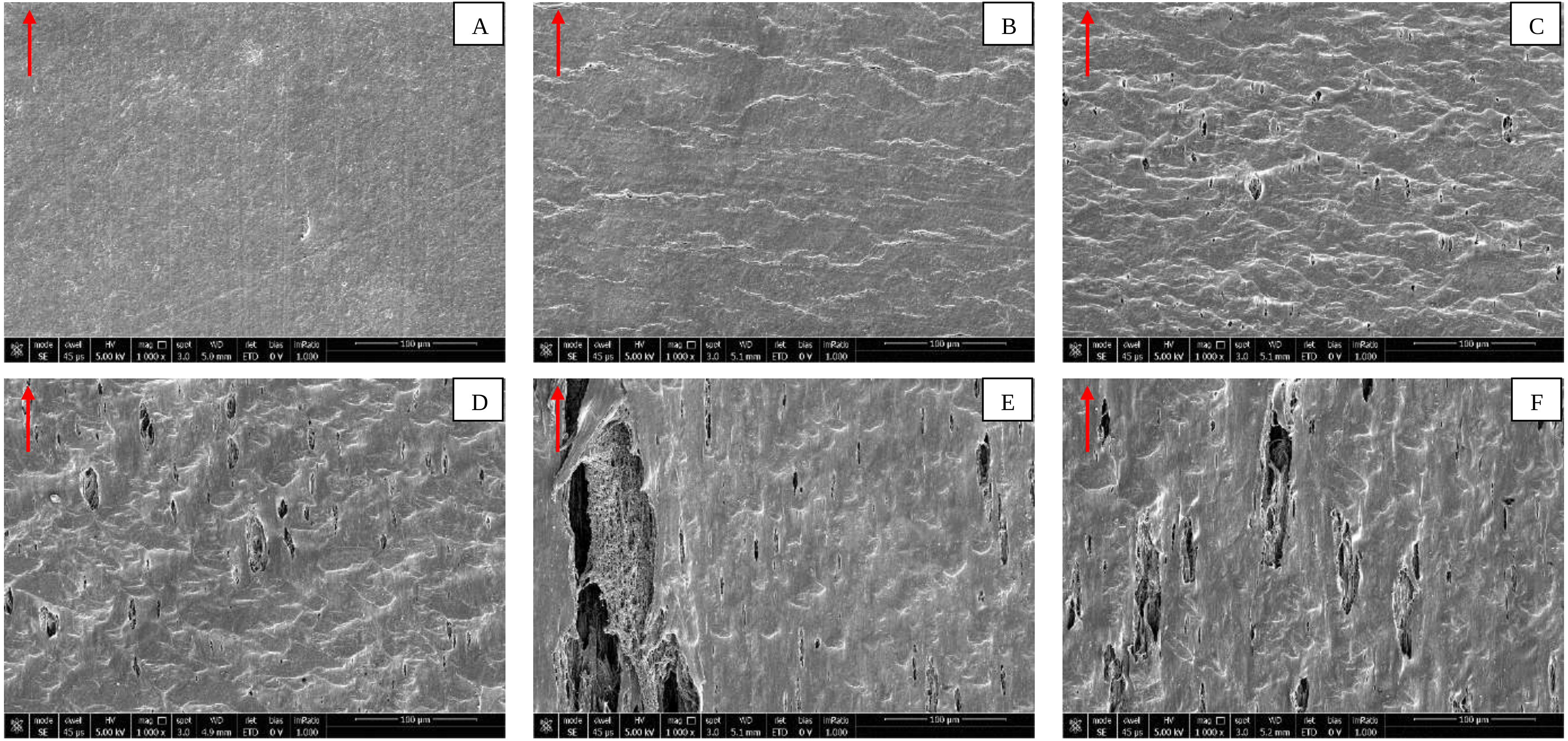

Figure A1.12. FESEM images of surfaces of compression-molded films of the sample B1 undeformed (A) and after deformation at 30% (B), 70% (C), 110% (D), 150% (E), at break (F). All the images were acquired at the same magnification of 1000X. The vertical red arrow indicates the stretching direction.

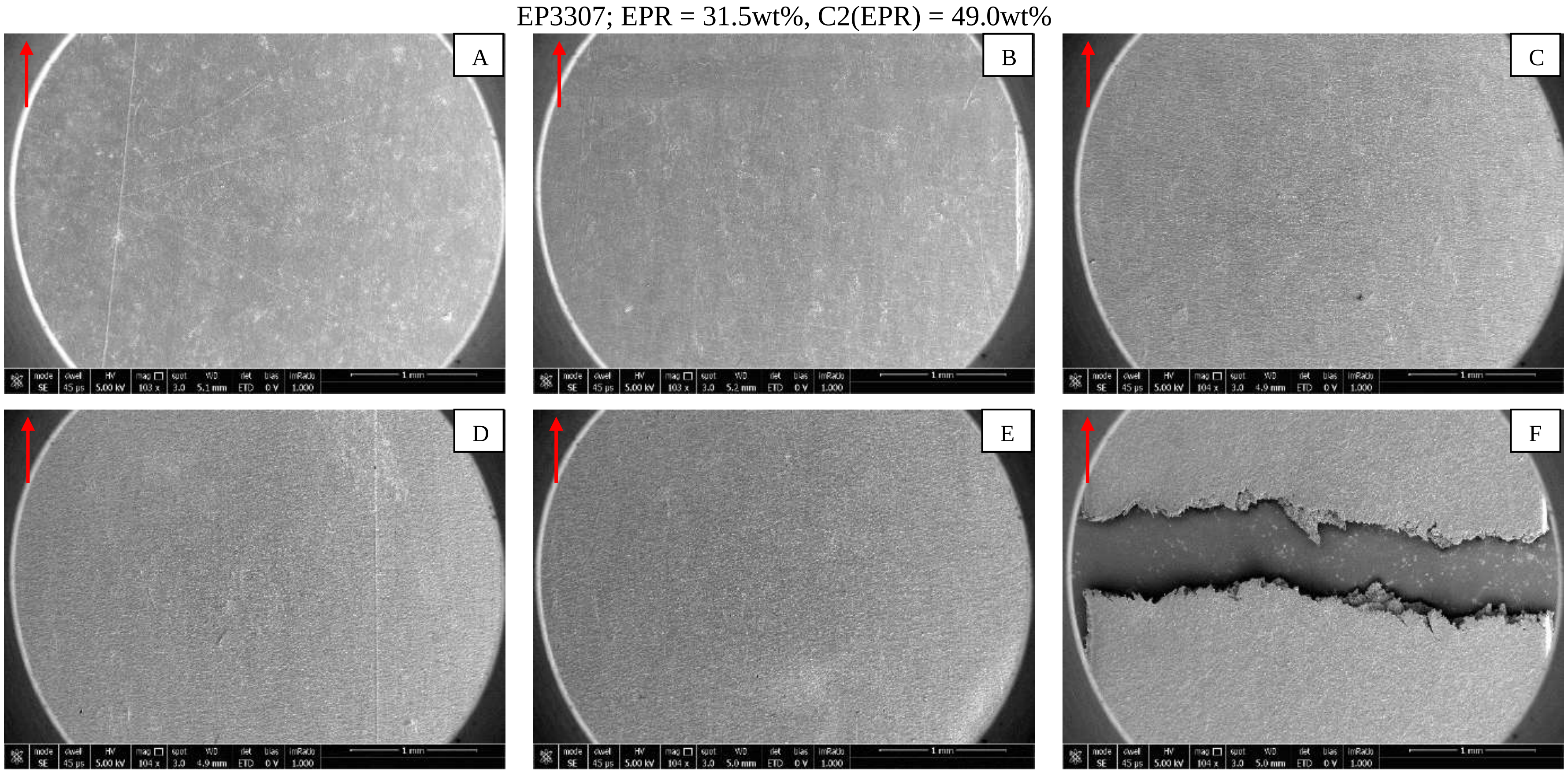

Figure A1.13. FESEM images of surfaces of compression-molded films of the sample EP3307 undeformed (A) and after deformation at 30% (B), 70% (C), 110% (D), 150% (E), at break (F). All the images were acquired at the same magnification of 100X. The vertical red arrow indicates the stretching direction.

EP3307; EPR = 31.5wt%, C2(EPR) = 49.0wt%

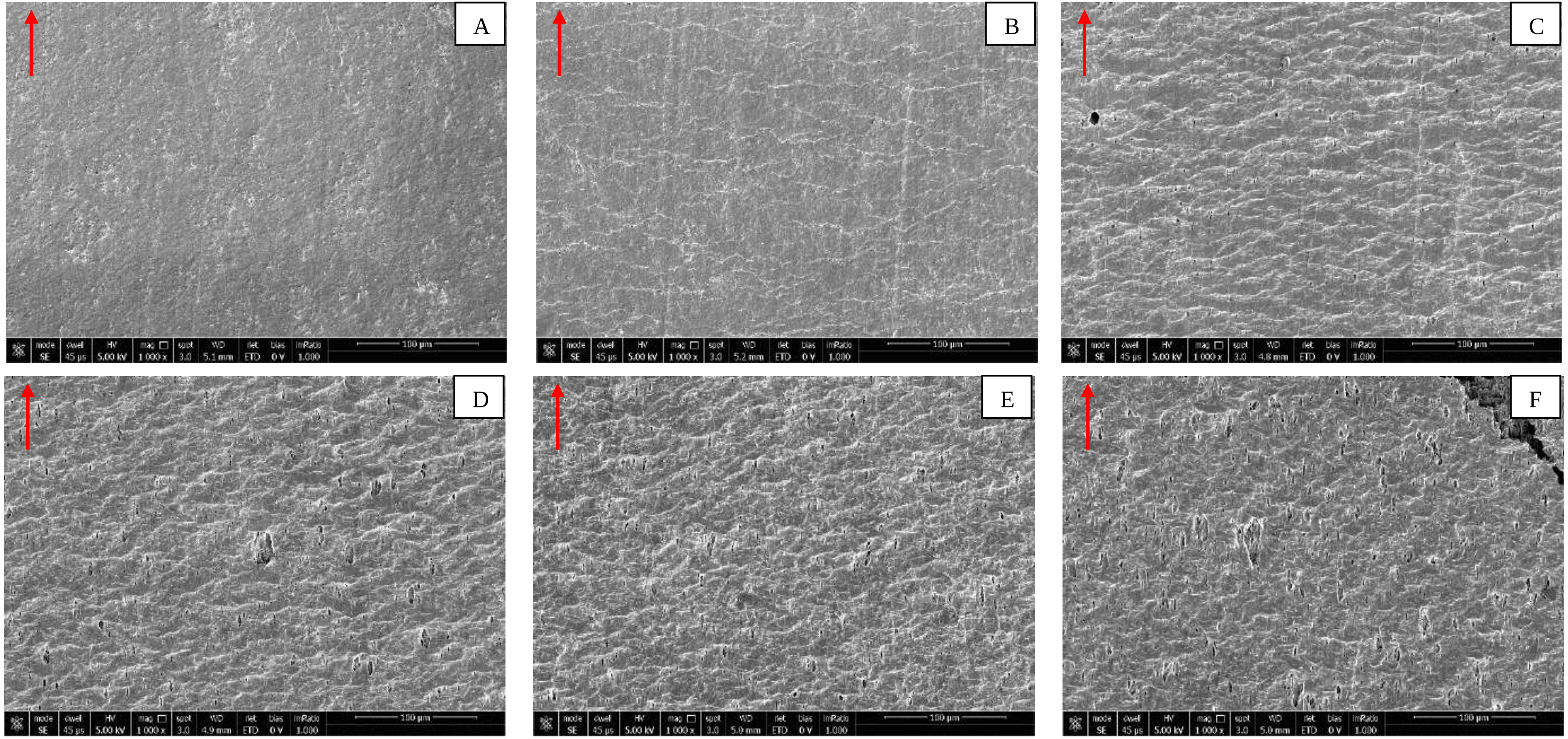

Figure A1.14. FESEM images of surfaces of compression-molded films of the sample EP3307 undeformed (A) and after deformation at 30% (B), 70% (C), 110% (D), 150% (E), at break (F). All the images were acquired at the same magnification of 1000X. The vertical red arrow indicates the stretching direction.